UNIVERSITY OF LIVERPOOL

Thin Film Components For Solid Oxide Fuel Cells (SOFCs)

Thesis submitted in accordance with the requirements of the University of Liverpool for the degree of Doctor in Philosophy by:

Natasha Louise Olenka Flack

September 2014

Supervised by:

Professor Matthew Rosseinsky
Professor Paul Chalker

Contents Page

Abstract

Thin film components for solid oxide fuel cells (SOFCs) have been investigated in this thesis. This work focuses on electrolyte materials such as samarium doped ceria (SDC) and cathode materials including neodymium barium cobalt oxide (NBCO) and barium calcium yttrium iron oxide.

Single layer growth of NBCO or SDC is achieved on single crystal strontium titanate (001) before these materials were grown via pulsed laser deposition as a bi-layer and multilayers. Ordered NBCO required deposition at 850°C, whereas it was found that the SDC grew with a lower surface roughness at lower temperatures of around 650°C. The motivation was to investigate how the conductivity is affected by the interfaces between these layers, as motivated by previous studies of yttrium stabilised zirconia (YSZ) with strontium titanate (STO). NBCO was found to be unstable at the temperatures required for AC impedance measurements. From the transmission electron microscopy (TEM) and Energy Dispersive X-ray (EDX) data there is likely migration of Nd into the SDC layers. The interfaces are also less sharp for the multilayer films deposited at the higher temperature for the SDC growth. However, in all cases the SDC growth appears more favourable in the TEM when compared to the NBCO, with some regions even showing Co-metal and fluorite structures potentially attributed to $Co\text{-}O_x$ where we would expect to see the perovskite block.

Thin films of barium calcium yttrium iron oxide were grown on single crystal strontium titanate (001). The material is a candidate cathode for solid oxide fuel cells (SOFCs) and in the intermediate temperature (IT) region at 600°C the in-plane AC conductivity of the thin film is found to be $30.0 Scm^{-1}$, significantly enhanced over $3.5 Scm^{-1}$ found for the polycrystalline form. This is assigned to reduction of the grain boundary density and alignment of the planes predicted to have the highest electronic and ionic conductivities. The symmetry of the film appears to be tetragonal within the resolution of the measurements employed, as opposed to the orthorhombic symmetry of the bulk phase, which may be attributed to the in-plane structural match between the cubic STO substrate and the grown layer.

Three potential geometries investigating both single and double-sided growth for measuring the area specific resistance of thin films are discussed and an experimental prototype constructed and tested.

Acknowledgements

I would like to thank my supervisors Professor Matthew Rosseinsky and Professor Paul Chalker for allowing me the opportunity to undertake this PhD.

Throughout the course of my PhD I have worked with several inspirational post-docs; I would like to thank Dr. Sean McMitchell, Dr. Robert Palgrave, Dr. Pavel Borisov, Dr. Ruth Sayers, Dr. Jonathan Alaria, Dr. Ming Li, Dr. Marco Zanella, Dr. Marita O'Sullivan, Dr. Paritosh Wadekar, Dr. Troy Manning and Dr. Matthew Werner.

I would also like to thank Darren Hodgeman for his help and support throughout the PhD, and especially for assisting with his 10 layer ink in the ASR project.

Thanks also to everyone in the MJR group past and present, particularly the thin film sub group, and my colleagues in our office 3.14. I would also like to thank Jane Remmer, Dr. Hongjun Niu and Mike Chatterton for their continual support throughout the PhD. I would like to thank the Engineering and Physical Sciences Research Council for providing funding.

I will be eternally grateful to my fiancé David G. for his everlasting love and support, and for sticking by me through the rollercoaster ride which is a PhD!

Family is by far the most important part of my life and without my parents, Hugh and Michelle, and my siblings, Gemma and David, I'm sure I would have given up a long time ago! I am really grateful for their unconditional love and support. I would also like to thank Wendy, Alastair and Iain for their love and understanding.

One of the most relaxing parts of the journey was coming home to our two happy, not so little, guinea pigs Coconut and Liquorice, and I would love to thank them for their calming influences in times of stress. The continual love and support of all my family and friends throughout the journey makes reaching the end all the more satisfying.

The work presented in this thesis was carried out by myself, except where stated, at the Chemistry Department, University of Liverpool between October 2010 and September 2014 under the supervision of Prof. M.J. Rosseinsky and Prof. P. Chalker. This work has not been submitted for any other degree at this or any other university.

Name Date

List of Abbreviations

10 layer	$Ba_{1.7}Ca_{2.4}Y_{0.9}Fe_5O_{13}$ (10 a_p)
AC	Alternating Current
AC-AFM	Alternating Contact Atomic Force Microscopy
AFC	Alkaline Fuel Cell
AFM	Atomic Force Microscopy
ALD	Atomic Layer Deposition
a_p	Single Perovskite Unit Cell Length
ASR	Area Specific Resistance
CIP	Cold Isostatic Press
CMD	Centre of Materials Discovery
CVD	Chemical Vapour Deposition
DMFC	Direct Methanol Fuel Cell
DP	Double Perovskite ($a_p/a_p/2a_p$)
ECM	Equivalent Circuit Model
EDX	Energy Dispersive X-ray
EELS	Electron Energy Loss Spectroscopy
EIS	Electrochemical Impedance Spectroscopy
EMAT	Electron Microscopy for Materials Science
FFT	Fast Fourier Transform
FRA	Frequency Response Analyser
FWHM	Full Width Half Maximum
GBCO	$GdBaCo_2O_5$
GDC	Gadolinium Doped Ceria
HAADF	High Angle Annular Dark Field
HR	High Resolution
IT	Intermediate Temperature
LSC	$La_{0.8}Sr_{0.2}CoO_{(3-\delta)}$
LSM	$La_{(1-x)}Sr_xMnO_{(3-\delta)}$
MIEC	Mixed Ionic Electronic Conductor
MBE	Molecular Beam Epitaxy
MOCVD	Metal-Organic Chemical Vapour Deposition
MOMBE	Metal-Organic Molecular Beam Epitaxy
NASA	National Aeronautics and Space Administration
NBCO	$NdBaCo_2O_5$
NiCaL	Nanoinvestigation Centre at Liverpool
ORR	Oxygen Reduction Reaction
PAFC	Phosphoric Acid Fuel Cell
PEMFC	Proton Exchange Membrane Fuel Cell
PLD	Pulsed Laser Deposition
PPM	Parts Per Million
PVD	Physical Vapour Deposition
RC	Rocking Curve
RE	Rare Earth
RSM	Reciprocal Space Maps
SCCM	Standard Cubic Centimetres per Minute

SDC	Samarium Doped Ceria
SEM	Scanning Electron Microscopy
SOFC	Solid Oxide Fuel Cell
SP	Single Perovskite ($a_p/a_p/a_p$)
STO	Strontium Titanate
SuperSTEM	Aberration-Corrected Scanning Transmission Electron Microscopy
TEM	Transmission Electron Microscopy
UV	Ultra Violet
XRD	X-ray Diffraction
XRR	X-ray Reflectivity
YSZ	Yttrium-stabilized Zirconia

Chapter 1: Introduction

1.1 Fuel Cells

Fuel cells were originally conceived in 1839 by Sir William Robert Grove, who discovered that reversing the electrolytic process could result in the generation of electricity.[1] Grove's discovery was generally overlooked due to the more popular fossil fuel-powered engines until the National Aeronautics and Space Administration (NASA) started to use the technology in the 1960s. NASA promoted the use of this fuel cell technology over other options because fuel cell systems are of relatively low weight and low toxicity.[2]

All fuel cells operate on the same basic concept of reacting fuel and oxygen to produce electricity. The essential components of a fuel cell are an anode, cathode, electrolyte. An oxidant is delivered to the cathode, while a fuel is supplied to the anode. The generated electrons are able to flow through an external circuit, which can be used to power electrical devices.[3]

There are various types of fuel cells, with some examples including: proton exchange membrane fuel cells (PEMFCs), direct methanol fuel cells (DMFCs), alkaline fuel cells (AFCs), phosphoric acid fuel cells (PAFCs), molten carbonate fuel cells and solid oxide fuel cells (SOFCs).[4] The main focus of this thesis is concerned with investigating new materials for use in SOFCs.

1.2 Solid Oxide Fuel Cells

The Solid Oxide Fuel Cell was originally derived from the Nernst lamp (also called the Nernst 'glower'), which was developed by Walther Nernst in 1897.[5] Nernst lamps used a ceramic rod composed of yttria-stabilised zirconia (YSZ) that was heated to incandescence instead of a glowing tungsten filament. In 1943 it was recognised that the conduction mechanism of the Nernst lamp stemmed from the vacancies in the anion sublattice of the YSZ, and so the Nernst lamp is considered to be one of the first commercially produced solid electrolyte gas cell.[6]

The SOFC is a high-temperature fuel cell that typically operates over a wide temperature range from 800°C – 1000°C.[7] As the electrolyte is a solid, high operating temperatures are required in order to have sufficient ionic mobility through the electrolyte so that ohmic losses are acceptably low. A schematic of a SOFC is shown in Figure 1.1.

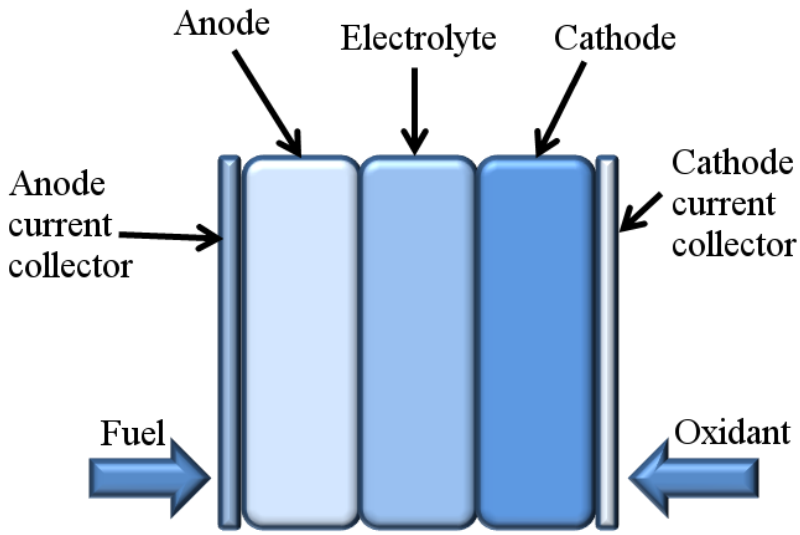

Figure 1.1: Schematic of a solid oxide fuel cell.

CeO_2 is a promising electrolyte in SOFC technology. The high performance of CeO_2 in this capacity is related to its high ionic conductivity,[8] and has been reported to become more effective when doped with a trivalent ion.[9] The underlying mechanism is thought to be increased mobility of oxygen ions through the extrinsic oxygen vacancy defects created in ceria's doped fluorite lattice to maintain charge neutrality.[10] In recent studies, Sm and Gd were found to be the best trivalent dopant atoms for ceria in this regard[11,12] and have since become a focal point of fuel cell research intent on verifying and shedding light on the underlying principles responsible for this enhanced oxygen mobility.[12-14]

Recently, considerable efforts have also been directed to intermediate-temperature (500-700°C) SOFCs based on thin film electrolytes of Rare-Earth doped ceria, $Re_xCe_{1-x}O_{(2-\delta)}$.[15] Gadolinium doped ceria (GDC), for example, has been shown to have improved conductivity over yttria stabilised zirconia (YSZ).[16] Zirconia-based electrolytes, such as YSZ, have traditionally been used because of their nearly pure oxygen ionic conductivity in both oxidizing and reducing atmospheres, as well as good mechanical properties. However they require high operating temperatures of over 900°C to maintain high oxygen ionic conductivity. Such high operating temperatures result in high fabrication cost and accelerate degradation of the fuel cell systems. Yttrium doped ceria, or just yttrium oxide have also been shown to be possibilities for use as an electrolyte in intermediate-temperature SOFCs.[17]

SOFCs operate under the general principle that oxygen is reduced to oxygen ions at the cathode (see Equation 1.1) and these oxygen ions then migrate through the electrolyte, which needs to be ionically conducting.

$$O_2 + 4e^- \rightarrow 2O^{2-} \qquad \text{Eqn. (1.1)}$$

The rate limiting step tends to be the surface oxygen exchange reaction, as is typically the case for mixed ionic-electronic conductors.[18] This reaction comprises several steps, including gas phase diffusion, adsorption, dissociation, surface diffusion of intermediate oxygen species, and oxygen incorporation. The presence of surface atoms not terminated with oxygen (onto which O_2 can be chemisorbed) and surface oxygen vacancies are considered to play an essential role in the reaction pathway for oxygen ion incorporation.[19]

The anode is required to be porous to allow the fuel to infiltrate into the anode and to increase the surface area maximising fuel oxidation, forming water, electrons and heat (see Equation 1.2).

$$2H_2 + 2O^{2-} \rightarrow 2H_2O + 4e^- \qquad \text{Eqn. (1.2)}$$

Typically, anode materials are required to be stable in reducing atmospheres and transition metals are typically chosen due to their high catalytic activity, e.g. nickel-based cermets.[3] These exhibit good compatibility with electrolytes

composed of doped ceria or stabilized zirconia, in conjunction with high activity toward the oxidation of hydrogen, and high electronic conductivity.[20]

Micro-solid oxide fuel cells (μ-SOFCs) are on a much smaller scale, with thin films being utilised to dramatically decrease the thickness of the single cells.[21]

SOFCs have been rapidly developed for clean and efficient power generation. A major advantage of SOFCs over other fuel cell types is the ability to use a variety of fuels including, but not limited to many common hydrocarbon fuels such as natural gas, diesel, gasoline, alcohol and coal gas.[22] Another advantage with SOFCs is that all the components are solid, and so fuel cells can be fabricated in very thin layers, and cell components can be configured into unique shapes and orientations unachievable in fuel cell systems that have a liquid electrolyte.[3] With the development of thin film technology, efforts have been made to progress miniaturisation.[23,24]

1.2.1 μ-Solid Oxide Fuel Cells

Micro-solid oxide fuel cells (μ-SOFCs) are potentially highly efficient, and would be useful as high energy-density replacements for batteries in the mW to W power generation for portable consumer and military electronic devices.[21] μ-SOFCs offer great advantages over their macroscopic counterparts, such as lower operating temperatures (approximately 550°C), easy integration with the required electrical components, small size and reduced weight.[25] This leads to further

application in the portable electronic device market. A schematic of a μ-SOFC is shown in Figure 1.2.

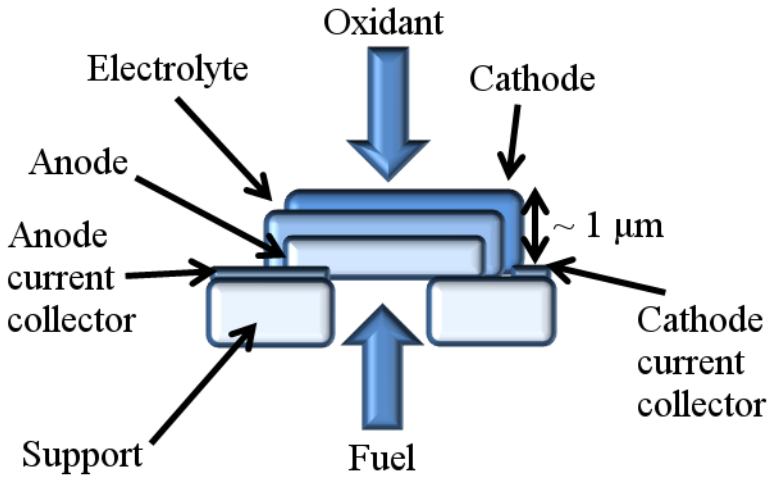

Figure 1.2: Schematic of a μ-SOFC adapted from.[26]

1.3 Thin Film Components for SOFCs

In the methodology, Chapter 2, more detail can be found on pulsed laser deposition (PLD) as a technique for thin film growth. Here a literature review of PLD is discussed where other groups are also using it as a technique to study thin film components for SOFCs.

PLD has been shown to be a suitable method for depositing a wide range of cathode materials such as lanthanum strontium cobaltite, $La_{1-x}Sr_xCoO_{(3-\delta)}$,[27-31] lanthanum cobalt iron oxide, $La_xCo_yFe_{1-y}O_{(3-\delta)}$,[32] and La_x-$Sr_{1-x}MnO_3$ (LSM);[29,30,33,34] electrolytes including yttrium stabilised zirconia (YSZ),[35-37] lanthanum gallate;[38-40] and lanthanum chromite-based electrical interconnects.[41-44]

YSZ was the first fuel cell relevant material to be deposited as a thin film by PLD. Murray *et al.* deposited YSZ from an oxide target with deposition rates of less than 0.15μmh^{-1}.[37] Later work by Kokai and co-workers employed a YSZ target to prepare well-adhered, fully dense thin films up to 2μm in thickness.[35,36]

PLD is not generally considered as a manufacturing method for cathodes due to a lack of scalability for industry however SolMateS,[45] based in the Netherlands, is starting to manufacture PLD systems for industrial clients so this may prove viable in the near future. Currently more readily scalable methods of thin film deposition include chemical vapour deposition and sputtering.[46] PLD has proven to be a valuable tool in preparing novel electrode compositions and structures for use in fundamental reaction mechanism studies.[27-34] PLD allows thin, fully dense, and oriented cathode films to be deposited onto various electrolytes, which enables the role of mixed electron and oxygen ion conductivity to be assessed.[47] Endo and co-workers studied the performance of dense lanthanum manganite cathodes over a range of thicknesses, temperature, and oxygen partial pressure, concluding that reaction rates were controlled by oxygen transport through the dense electrode layers.[29,33,34] It would not have been possible to assess this contribution to the cathodic reaction without the formation of high quality thin films by PLD. Similar studies with strontium-substituted lanthanum cobaltite and lanthanum iron cobaltite allowed an assessment of the role of mixed conduction on electrocatalytic activity to be made.[27-32,34] Chen *et al*. found that the orientation of lanthanum cobaltite films was affected by the oxygen partial pressure in the deposition chamber,[27,28] which also affected electrochemical properties. Kawada

et al. studied oxygen isotope surface exchange and bulk migration in PLD-deposited lanthanum cobaltite thin films, and showed that surface processes, such as adsorption and dissociation dominated electrochemical performance.[31]

The most recent studies where PLD has been applied to fuel cell materials involved the deposition of alternative electrolytes and electrodes. Mathews *et al*. first reported the deposition of a number of lanthanum strontium gallium magnesium oxide (LSGM), $La_{1-x}Sr_xGa_{1-y}Mg_yO_{(3-\delta)}$ ($0.1 \leq x \leq 0.2$, $0.1 \leq y \leq 0.2$), thin films onto quartz and silicon substrates.[39] The lanthanum gallates are of interest because they have a considerably higher ionic conductivity than YSZ and good stability in oxidizing and reducing atmospheres.[39] The as-deposited films were amorphous, and converted to single phase orthorhombic or cubic perovskite structures after annealing at 1500°C.[39] Multiple ion and neutral species were found in the evaporated plume; major species that were detected included O^+, Ga^+, O, and Ga. Kanazawa *et al*. used PLD to deposit dense LSGM films onto porous nickel oxide, and studied plume dynamics as well as film composition and structure.[40] As-deposited films were amorphous in that study as well, but were fully crystallized by annealing in air at 1000°C. Small differences in composition were noted between the target and deposit. Deposited films tended to be enhanced with respect to Sr and depleted with respect to Ga, compared to the target. Manoravi *et al*. were able to fully crystallize laser-ablated LSGM at 730°C in air. These authors reported a factor of 10 higher ionic conductivity for LSGM films on sapphire than on strontium titanate.[38]

1.4 Superlattice Growth

Novel structures comprising layers of different materials can be grown as superlattices. Superlattices made of strontium titanate, $SrTiO_3$, (STO) and 8mol% Y_2O_3 doped ZrO_2 (YSZ) layers have been investigated, and have been found to possess a colossal enhancement of ionic conductivity, which was eight orders of magnitude larger than the YSZ conductivity, even at room temperature.[48] However, these findings were successively questioned because the researchers omitted to consider the ionic and electronic conductivity contribution from the much thicker STO substrates they used.[49]

Sanna *et al*.[50] have investigated the electrochemical properties of superlattices made of alternate layers of 20mol% SDC and 8mol% YSZ, fabricated by pulsed laser deposition (PLD). Doped ceria films having a fluorite structure can be deposited on several non-fluorite substrates by PLD, starting from a polycrystalline target and maintaining the correct stoichiometry.[51] In particular, doped ceria has been shown to grow on {001} $LaAlO_3$ (LAO), {110} $NdGaO_3$ (NGO), and {001} STO perovskite substrates.[52,53] Perovskite-type substrates provide the correct lattice match for ceria, and induce the growth of epitaxial monocrystalline films with a low degree of structural disorder.[52] STO, NGO, and LAO have a cubic (pseudocubic for NGO) structure with lattice parameter values a_p = 3.91Å (STO), 3.86Å (NGO), and 3.79Å (LAO). On the other hand, the lattice parameter of highly doped SDC, a = 5.44Å, does not allow a cube-on-cube, epitaxial relationship (see Chapter 3, Section 3.5.5) between (001)-oriented perovskite substrates and SDC films. The interplanar distance along the in-plane

(110) direction for STO is 5.52Å, which gives a good match with the SDC cubic parameter (1.5%) and even smaller for NGO and LAO, encouraging growth along this direction.[54]

1.5 Materials of Interest

1.5.1 Strontium Titanate

Strontium titanate (STO), $SrTiO_3$, is a simple cubic perovskite with no distortions of the oxygen octahedra. Perovskite materials have the formula ABX_3, with the structure including one 12-coordinate cubo-octahedral site occupied by a large cation, A, one 6-coordinate octahedral site occupied by a smaller cation, B, and a 6-coordinate site occupied by an anion, X, which is typically oxygen or a halide.[55] The perovskite structure is shown in Figure 1.3. A-site cations are usually members of group II or lanthanides, e.g. Sr/La, while B-site cations are typically transition metals, e.g. Ti. Typically cubic perovskites possess lattice parameters, denoted a_p, of approximately 4Å.[55] For example, STO has an a_p of 3.91Å.[56]

The structure of STO was verified by Tegze *et al.* who obtained direct images of the three dimensional arrangement.[57] STO is used as a single crystal substrate for the growth of many films,[56] including those in this thesis where (001) STO is used from PI-KEM.

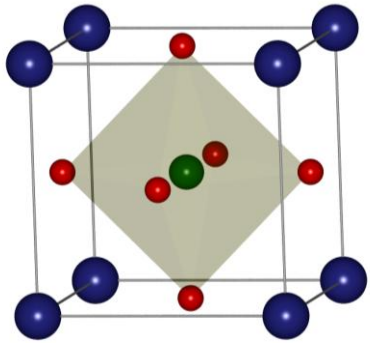

Figure 1.3: Undistorted perovskite structure ABO_3. With the blue atoms showing the A site, the green atom showing the B site and the oxygen atoms in red.

1.5.2 Electrolyte Material

The electrolyte requires a *high* ionic conductivity and a *negligible* electronic conductivity. It also needs to be stable in redox environments. The electrolyte materials need to be selected with care as it was important to select a material that would not react with the chosen cathode material when heated to SOFC operating and fabrication temperatures.

Materials with the fluorite structure, such as samarium doped and gadolinium doped ceria, are typically used as electrolytes in SOFCs. The fluorite structure (see Figure 1.4) is represented by the formula AX_2, where X is typically oxygen or a halide. When X is oxygen, A is typically a 4+ cation such as Ce and when X is a halide, A is usually a 2+ cation e.g. Ca. The A-site cation can be substituted with a lower charged cation which incurs oxygen deficiencies in the structure to balance the overall charge. These oxygen vacancies generally improve the overall oxide ion conductivity and are therefore of great interest for these electrolyte materials.[58]

1.5.2.1 Samarium Doped Ceria

Ceria (CeO_2) has the standard fluorite structure, and does not possess a high ionic conductivity. Replacing Ce^{4+} with Sm^{3+} introduces oxygen vacancies and the resultant samarium doped ceria (SDC), $Ce_{(1-x)}Sm_xO_{(2-\delta)}$, possesses a much higher ionic conductivity.[59] Doping ceria with cations that have similar ionic radii to Ce^{4+}, e.g. Sm^{3+}, produces materials with low activation energies for oxide diffusion.[60] One of the disadvantages of this material is that Ce^{4+} is easily reducible creating an electrical component to the conductivity.

Samarium doped ceria (SDC), $Sm_{0.2}Ce_{0.8}O_{2-\delta}$, has the face centred cubic fluorite structure (see Figure 1.4) and has a lattice parameter of 5.44Å.

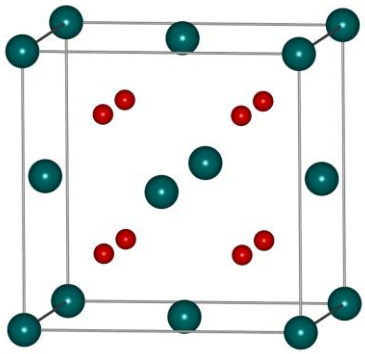

Figure 1.4: Schematic of the SDC's fluorite structure, the green spheres represent Ce/Sm and the red spheres represent oxygen.

Films of SDC grown in this work are discussed in Chapter 3 and 5.

1.5.2.2 Yttria-stabilised Zirconia

Zirconia (ZrO_2) only adopts the cubic fluorite structure shown in Figure 1.4 above 2300°C.[61] Doping zirconia with yttria stabilises the cubic fluorite structure at room temperature, and has the additional benefit that substituting the Zr^{4+} with the

lower charged Y^{3+} results in oxygen vacancies, as discussed with SDC, thereby increasing the ionic conductivity.[62]

One potential issue with using yttria-stabilised zirconia (YSZ) is that it has the potential to react with cathode materials such as $La_{(1-x)}Sr_xMnO_{(3-\delta)}$ (LSM) producing unwanted species such as $La_2Zr_2O_7$ [63-67] and $SrZrO_3$ [68,69] and resulting in a loss in performance.

SDC/GDC, on the other hand, has been found to be more chemically stable than YSZ,[70] and has been used as a buffer layer between YSZ and the cathode material both in the bulk[71,72] and as a thin film.[73]

In this work, YSZ is used as a single crystal (001) substrate procured from PI-KEM, upon which SDC buffer layers and cathode materials are deposited. Films grown on YSZ are discussed in Chapter 5.

1.5.3 Cathode Materials

A cathode must have *high* electronic *and* ionic conductivity for intermediate temperature SOFCs (IT-SOFCs) operating at 500-700°C. This work focuses on two cathode materials, neodymium barium cobalt oxide (discussed in Section 1.5.3.1) and barium calcium yttrium iron oxide (discussed in Section 1.5.3.2).

1.5.3.1 Neodymium Barium Cobalt Oxide

$LnBaCo_2O_{(5+\delta)}$ is an A-site layered perovskite which has been extensively researched in the literature, where Ln = Gd, Pr.[74-78] These materials are of interest because of the A-site cation ordering in the double perovskite (DP), and it has been found that the oxygen ion diffusivity was greater in the DP than in the single perovskite (SP) materials. SP $GdBaCo_2O_{(5+\delta)}$ (GBCO) was found to be unstable degrading into $GdCoO_3$ and $BaCO_3$ in low concentrations of CO_2. However DP GBCO structure was found to be stable in air conditions for 100 hours at 500-700°C and with < 500ppm of CO_2.[79] Neodymium barium cobalt oxide (NBCO), $NdBaCo_2O_{(5+\delta)}$, has a perovskite based structure and can be found in multiple forms depending on the degree of cationic/oxygen vacancy order. NBCO thin films have been previously grown by Grygiel *et al*. via PLD.[80]

Completely disordered NBCO is a simple cubic perovskite shown in Figure 1.3 with a random mixture of Nd and Ba on the A-site and Co on the B-site. Any oxygen vacancies are randomly positioned. A composition of $NdBaCo_2O_{(5+\delta)}$ can lead to ordering of oxygen vacancies as shown in Figure 1.5. Here, oxygen vacancy channels occur in alternating a_p rows along the *b*-direction running parallel to *a*. Cationic order is driven by this process with Nd positioned in the A-site of the layers containing oxygen vacancies and Ba on the alternate layer positions. Films of NBCO grown in this work are discussed in Chapter 3.

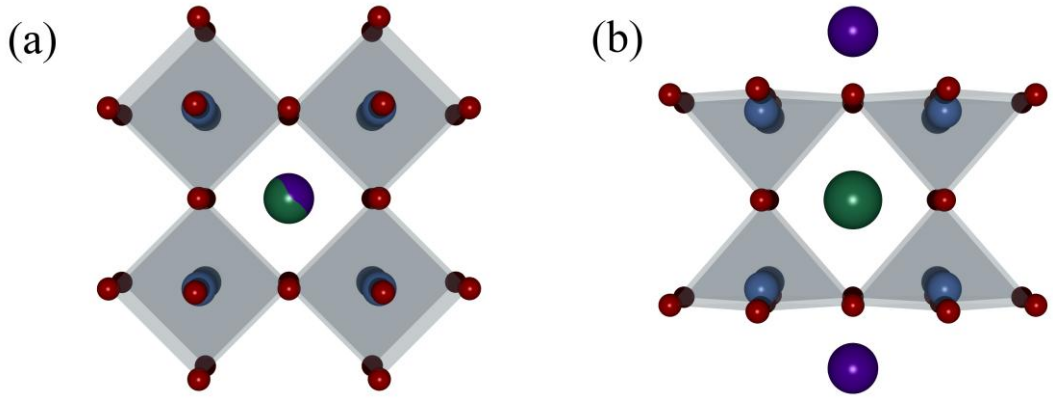

Figure 1.5: Structural depiction of (a) random occupancy of cation site indicated by mixed colour central atom, the disordered perovskite $NdBaCo_2O_5$, (b) the ordered double perovskite $NdBaCo_2O_5$. Nd in purple, Ba in green, Co in blue and O in red.

1.5.3.2 Barium Calcium Yttrium Iron Oxide

The barium calcium yttrium iron oxide (10 layer), $Ba_{1.7}Ca_{2.4}Y_{0.9}Fe_5O_{13}$, material can be described as a regular intergrowth between $Ca_2Fe_2O_5$ [81] and $YBa_2Fe_3O_8$ [82,83] building blocks in a one to one ratio. The 10 layer structure has similarities to that of $LnBaCo_2O_{(5+\delta)}$, as discussed in section 1.5.3.1, and possesses channels of ordered oxygen vacancies forming between square pyramidal sites, with additional oxygen vacancies at the tetrahedral sites.

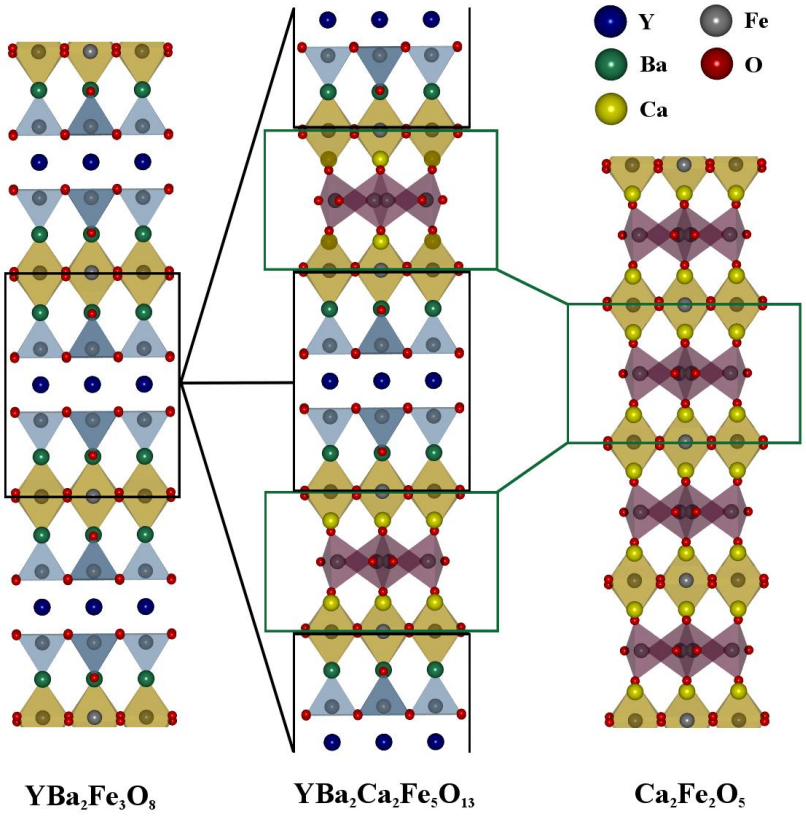

Figure 1.6**:** Crystal structure showing the intergrowth between $Ca_2Fe_2O_5$ and $YBa_2Fe_3O_8$ building blocks. The iron sites in the purple polyhedra are disordered.

Previously the 10 layer material has been reported in the literature in the bulk form by Demont *et al*.[84] Sayers *et al*. report an improved ASR for the bulk 10 layer material having modified the cathode processing technique.[85] A related 16 a_p phase has also been reported.[86] In addition Darren Hodgeman has also conducted further studies with doping the 10 layer material which is reported in his thesis.[87] The publication on thin films of the 10 layer material is based on the work presented in Chapter 4.[88] Films of the 10 layer grown in this work are discussed in both Chapters 4 and 5.

1.6 Thesis Overview

This thesis is concerned with the pulsed laser deposition (PLD) growth of thin films for use as electrolytes and cathodes in solid oxide fuel cell applications. Thin film growth of samarium doped ceria (SDC) was initially optimised on a strontium titanate (STO) {001} substrate. Samarium doped ceria was used as an electrolyte for solid oxide fuel cells due to its high ionic conductivity.[54] Neodymium barium cobalt oxide (NBCO) was grown as a bilayer with the SDC, as NBCO is a cathode material. SDC and NBCO were also grown in multilayers, and these SDC and NBCO growths are discussed in Chapter 3.

Barium calcium yttrium iron oxide (10 layer), $Ba_{1.7}Ca_{2.4}Y_{0.9}Fe_5O_{13}$, material was also grown in thin film form. The 10 layer is a potential cathode material for SOFCs and was grown as a thin film in an attempt to improve the conductivity. The 10 layer growths are discussed in Chapter 4, and are later used as the motivation for the area specific resistance (ASR) measurements discussed in Chapter 5.

1.7 References

1 Grove, W. R. LVI. On a new voltaic combination. *Philosophical Magazine Series 3* **13**, 430-431, doi:10.1080/14786443808649618 (1838).

2 Exarchakos, L., Hawkes, A. D. & Leach, M. A. in *The European Union, 25 different countries, 25 different energy policies…? An overview* (VGB Powertech, Essen, 2006).

3 Minh, N. Q. Ceramic Fuel Cells. *J. Am. Ceram. Soc.* **76**, 563-588 (1993).

4 Aricò, A. S., Bruce, P., Scrosati, B., Tarascon, J.-M. & van Schalkwijk, W. Nanostructured materials for advanced energy conversion and storage devices. *Nature Materials* **4**, 366-377, doi:10.1038/nmat1368 (2005).

5 H. Monmouth Smith. The Nernst lamp. *Science* **11**, 689-690 (1898).

6 Möbius, H.-H. On the history of solid electrolyte fuel cells. *J Solid State Electrochem* **1**, 2-16, doi:10.1007/s100080050018 (1997).

7 Singhal, S. in *High-temperature Solid Oxide Fuel Cells: Fundamentals, Design and Applications* (Elsevier, Oxford, 2006).

8 Eguchi, K., Setoguchi, T., Inoue, T. & Arai, H. Electrical properties of ceria-based oxides and their application to solid oxide fuel cells. *Solid State Ionics* **52**, 165-172 (1992).

9 Mori, T. & Drennan, J. Influence of microstructure on oxide ionic conductivity in doped CeO_2 electrolytes. *Journal of Electroceramics* **17**, 749-757, doi:10.1007/s10832-006-6311-7 (2006).

10 Yahiro, H., Eguchi, K. & Arai, H. Electrical properties and reducibilities of ceria-rare earth oxide systems and their application to solid oxide fuel

cell. *Solid State Ionics* **36**, 71-75, doi:Doi: 10.1016/0167-2738(89)90061-1 (1989).

11 Hooper, J., Ismail, A., Giorgi, J. B. & Woo, T. K. Computational insights into the nature of increased ionic conductivity in concentrated samarium-doped ceria: a genetic algorithm study. *Phys. Chem. Chem. Phys.* **12**, 12969-12972, doi:10.1039/c0cp00863j (2010).

12 Andersson, D. A., Simak, S. I., Skorodumova, N. V., Abrikosov, I. A. & Johansson, B. Optimization of ionic conductivity in doped ceria. *Proceedings of the National Academy of Sciences of the United States of America* **103**, 3518-3521 (2006).

13 Wei, X., Pan, W., Cheng, L. F. & Li, B. Atomistic calculation of association energy in doped ceria. *Solid State Ionics* **180**, 13-17, doi:10.1016/j.ssi.2008.10.019 (2009).

14 Nakayama, M. & Martin, M. First-principles study on defect chemistry and migration of oxide ions in ceria doped with rare-earth cations. *Phys. Chem. Chem. Phys.* **11**, 3241-3249 (2009).

15 Steele, B. C. H. Appraisal of $Ce_{1-y}Gd_yO_{2-y/2}$ electrolytes for IT-SOFC operation at 500 ^{o}C. *Solid State Ionics* **129**, 95-110 (2000).

16 Joo, J. H. & Choi, G. M. Electrical conductivity of thin film ceria grown by pulsed laser deposition. *Journal of the European Ceramic Society* **27**, 4273-4277, doi:DOI: 10.1016/j.jeurceramsoc.2007.02.135 (2007).

17 Ballée, E., Ringuedé, A., Cassir, M., Putkonen, M. & Niinistö, L. Synthesis of a Thin-Layered Ionic Conductor, $CeO_2{-}Y_2O_3$, by Atomic Layer Deposition in View of Solid Oxide Fuel Cell Applications. *Chemistry of Materials* **21**, 4614-4619, doi:10.1021/cm9016968 (2009).

18 Jung, W. & Tuller, H. L. Investigation of Cathode Behavior of Model Thin-Film $SrTi_{1-x}$ $Fe_xO_{3-\delta}$ ($x = 0.35$ and 0.5) Mixed Ionic-Electronic Conducting Electrodes. *J. Electrochem. Soc.* **155**, B1194-B1201, doi:10.1149/1.2976212 (2008).

19 Jung, W. & Tuller, H. L. Impedance study of $SrTi_{1-x}Fe_xO_{3-\delta}$ (x=0.05 to 0.80) mixed ionic-electronic conducting model cathode. *Solid State Ionics* **180**, 843-847, doi:http://dx.doi.org/10.1016/j.ssi.2009.02.008 (2009).

20 Jiang, S. & Chan, S. A review of anode materials development in solid oxide fuel cells. *J Mater Sci* **39**, 4405-4439, doi:10.1023/B:JMSC.0000034135.52164.6b (2004).

21 Nikbin, D. Micro SOFCs: why small is beautiful. *Fuel Cell Rev.*, 21-24 (2006).

22 Pomfret, M. B. *et al.* Hydrocarbon Fuels in Solid Oxide Fuel Cells: In Situ Raman Studies of Graphite Formation and Oxidation. *The Journal of Physical Chemistry C* **112**, 5232-5240, doi:10.1021/jp711312p (2008).

23 La, G. J., Hertz, J., Tuller, H. & Shao-Horn, Y. Microstructural. features of RF-sputtered SOFC anode and electrolyte materials. *Journal of Electroceramics* **13**, 691-695 (2004).

24 Hertz, J. L. & Tuller, H. L. Electrochemical characterization of thin films for a micro-solid oxide fuel cell. *Journal of Electroceramics* **13**, 663-668 (2004).

25 Baertsch, C. D. *et al.* Fabrication and structural characterization of self-supporting electrolyte membranes for a micro solid-oxide fuel cell. *Journal of Materials Research* **19**, 2604-2615, doi:10.1557/jmr.2004.0350 (2004).

26 Heiroth, S. *Pulsed laser deposition of functional electroceramic thin films for micro solid oxide fuel cell applications*, ETH ZURICH, (2010).

27 Chen, X., Wu, N. J., Ignatiev, A., Zhang, Z. H. & Chu, W. K. Structure and conducting properties of $La_{0.5}Sr_{0.5}CoO_{3-delta}$ films on YSZ. *Thin Solid Films* **350**, 130-137 (1999).

28 Chen, X., Wu, N. J., Ritums, D. L. & Ignatiev, A. Pulsed laser deposition of conducting porous La-Sr-Co-O films. *Thin Solid Films* **342**, 61-66 (1999).

29 Endo, A., Fukunaga, H., Wen, C. & Yamada, K. Cathodic reaction mechanism of dense $La_{0.6}Sr_{0.4}CoO_3$ and $La_{0.81}Sr_{0.09}MnO_3$ electrodes for solid oxide fuel cells. *Solid State Ionics* **135**, 353-358, doi:Doi: 10.1016/s0167-2738(00)00466-5 (2000).

30 Imanishi, N. *et al.* Impedance spectroscopy of perovskite air electrodes for SOFC prepared by laser ablation method. *Solid State Ionics* **174**, 245-252, doi:DOI: 10.1016/j.ssi.2004.06.019 (2004).

31 Kawada, T. *et al.* Oxygen isotope exchange with a dense $La_{0.6}Sr_{0.4}CoO_{3-[delta]}$ electrode on a $Ce_{0.9}Ca_{0.1}O_{1.9}$ electrolyte. *Solid State Ionics* **121**, 271-279, doi:Doi: 10.1016/s0167-2738(99)00046-6 (1999).

32 Coocia, L. G. *et al.* Pulsed laser deposition of novel materials for thin film solid oxide fuel cell applications: $Ce_{0.9}Gd_{0.1}O_{1.95}$, $La_{0.7}Sr_{0.3}CoO_y$ and $La_{0.7}Sr_{0.3}Co_{0.2}Fe_{0.8}O_y$. *Applied Surface Science* **96-98**, 795-801, doi:Doi: 10.1016/0169-4332(96)00000-1 (1996).

33 Endo, A., Ihara, M., Komiyama, H. & Yamada, K. Cathodic reaction mechanism for dense Sr-doped lanthanum manganite electrodes. *Solid State Ionics* **86-88**, 1191-1195, doi:Doi: 10.1016/0167-2738(96)00286-x (1996).

34 Endo, A., Wada, S., Wen, C.-J., Komiyama, H. & Yamada, K. Low Overvoltage Mechanism of High Ionic Conducting Cathode for Solid Oxide Fuel Cell. *J. Electrochem. Soc.* **145**, L35-L37, doi:10.1149/1.1838332 (1998).

35 Kokai, F., Amano, K., Ota, H., Ochiai, Y. & Umemura, F. XeCl laser ablative deposition and characterization of yttria-stabilized zirconia thin films on glass and CeO_2-Sm_2O_3. *J. Appl. Phys.* **72**, 699-704 (1992).

36 Kokai, F., Amano, K., Ota, H. & Umemura, F. XeCl laser ablation of yttria stabilized zirconia. *Applied Physics a-Materials Science & Processing* **54**, 340-342 (1992).

37 Murray, P. T., Wolf, J. D., Mescher, J. A., Grant, J. T. & McDevitt, N. T. Growth of yttria-stabilized cubic zirconia films on GaAs (100) by pulsed laser evaporation. *Materials Letters* **5**, 250-254 (1987).

38 Manoravi, P., Sivakumar, N., Joseph, M. & Mathews, T. Laser ablation of $La_{0.9}Sr_{0.1}Ga_{0.8}Mg_{0.2}O_{2.85}$ - Plume and film characterization. *Ionics* **10**, 32-38 (2004).

39 Mathews, T., Manoravi, P., Antony, M. P., Sellar, J. R. & Muddle, B. C. Fabrication of $La_{1-x}Sr_xGa_{1-y}Mg_yO_{3-(x\ plus\ y)/2}$ thin films by pulsed laser ablation. *Solid State Ionics* **135**, 397-402 (2000).

40 Kanazawa, S. *et al.* Preparation of doped $LaGaO_3$ films by pulsed laser deposition. *Surface & Coatings Technology* **169**, 508-511 (2003).

41 Sasaki, H. *et al.* Fabrication of high power density tabular type solid oxide fuel cells. *Solid State Ionics* **72**, 253-256, doi:Doi: 10.1016/0167-2738(94)90155-4 (1994).

42 Kajimura, A. *et al.* Preparation of La(Sr)$CrO_{3-delta}$ thin-film interconnector by high deposition rate laser-ablation method. *Solid State Ionics* **82**, 107-111 (1995).

43 Kajimura, A. *et al.* Preparation of $La_{1-x}Sr_xCrO_{3-delta}$ film by laser ablation method. *Solid State Ionics* **76**, 41-46 (1995).

44 Suzuki, M., Sasaki, H. & Kajimura, A. Oxide ionic conductivity of doped lanthanum chromite thin film interconnectors. *Solid State Ionics* **96**, 83-88 (1997).

45 *SolMateS Solutions in Material Science*. (http://www.solmates.nl).

46 Baxamusa, S. H., Im, S. G. & Gleason, K. K. Initiated and oxidative chemical vapor deposition: a scalable method for conformal and functional polymer films on real substrates. *Phys. Chem. Chem. Phys.* **11**, 5227-5240, doi:10.1039/b900455f (2009).

47 Eason, R. in *Pulsed Laser Deposition of Thin Films* (Wiley and Sons, 2007).

48 Garcia-Barriocanal, J. *et al.* Colossal Ionic Conductivity at Interfaces of Epitaxial ZrO_2:Y_2O_3/$SrTiO_3$ Heterostructures. *Science* **321**, 676-680, doi:10.1126/science.1156393 (2008).

49 Guo, X. Comment on "Colossal Ionic Conductivity at Interfaces of Epitaxial ZrO_2:Y_2O_3/$SrTiO_3$ Heterostructures". *Science* **324**, doi:10.1126/science.1168940 (2009).

50 Sanna, S. *et al.* Enhancement of Ionic Conductivity in Sm-Doped Ceria/Yttria-Stabilized Zirconia Heteroepitaxial Structures. *Small* **6**, 1863-1867, doi:10.1002/smll.200902348 (2010).

51 Infortuna, A., Harvey, A. S. & Gauckler, L. J. Microstructures of CGO and YSZ thin films by pulsed laser deposition. *Advanced Functional Materials* **18**, 127-135, doi:10.1002/adfm.200700136 (2008).

52 Huang, D. X., Chen, C. L. & Jacobson, A. J. Interface structures and periodic film distortions induced by substrate-surface steps in Gd-doped ceria thin-film growth. *J. Appl. Phys.* **97**, doi:10.1063/1.1845576 (2005).

53 Chen, L. *et al.* High temperature electrical conductivity of epitaxial Gd-doped CeO_2 thin films. *Solid State Ionics* **175**, 103-106, doi:10.1016/j.ssi.2004.09.034 (2004).

54 Sanna, S. *et al.* Fabrication and Electrochemical Properties of Epitaxial Samarium-Doped Ceria Films on $SrTiO_3$-Buffered MgO Substrates. *Advanced Functional Materials* **19**, 1713-1719, doi:10.1002/adfm.200801768 (2009).

55 Mitchell, R. H. *Perovskites, Modern and Ancient*. (Almaz Press, 2002).

56 Wan, X. J., Wang, L., Su, X. Q., Chen, J. B. & Kong, L. in *5th International Symposium on Advanced Optical Manufacturing and Testing Technologies: Optoelectronic Materials and Devices for Detector, Imager, Display, and Energy Conversion Technology* Vol. 7658 *Proceedings of SPIE-The International Society for Optical Engineering* (eds Y. Jiang, B. Kippelen, & J. Yu) (Spie-Int Soc Optical Engineering, 2010).

57 Tegze, M. & Faigel, G. X-ray holography with atomic resolution. *Nature* **380**, 49-51 (1996).

58 Malavasi, L., Fisher, C. A. J. & Islam, M. S. Oxide-ion and proton conducting electrolyte materials for clean energy applications: structural and mechanistic features. *Chemical Society Reviews* **39**, 4370-4387, doi:10.1039/b915141a (2010).

59 Inaba, H. & Tagawa, H. Ceria-based solid electrolytes. *Solid State Ionics* **83**, 1-16, doi:http://dx.doi.org/10.1016/0167-2738(95)00229-4 (1996).

60 Fergus J.W., Hui R., Li X., Wilkinson D.P. & J., Z. in *Solid Oxide Fuel Cells - Material Properties and Performance* (CRC Press, Boca Raton, 2009).

61 Scott, H. G. Phase relationships in the zirconia-yttria system. *J Mater Sci* **10**, 1527-1535, doi:10.1007/bf01031853 (1975).

62 Fergus, J. W. Electrolytes for solid oxide fuel cells. *Journal of Power Sources* **162**, 30-40, doi:http://dx.doi.org/10.1016/j.jpowsour.2006.06.062 (2006).

63 Kuščer, D. *et al.* Interactions between a thick film $LaMnO_3$ cathode and YSZ SOFC electrolyte during high temperature ageing. *Solid State Ionics* **78**, 79-85, doi:http://dx.doi.org/10.1016/0167-2738(95)00010-4 (1995).

64 Ji, Y., Kilner, J. A. & Carolan, M. F. Electrical properties and oxygen diffusion in yttria-stabilised zirconia (YSZ)–$La_{0.8}Sr_{0.2}MnO_{3\pm\delta}$ (LSM) composites. *Solid State Ionics* **176**, 937-943, doi:http://dx.doi.org/10.1016/j.ssi.2004.11.019 (2005).

65 Clausen, C., Bagger, C., Bilde-Sørensen, J. B. & Horsewell, A. Microstructural and microchemical characterization of the interface between $La_{0.85}Sr_{0.15}MnO_3$ and Y_2O_3-stabilized ZrO_2. *Solid State Ionics* **70–71, Part 1**, 59-64, doi:http://dx.doi.org/10.1016/0167-2738(94)90287-9 (1994).

66 Chiodelli, G. & Scagliotti, M. Electrical characterization of lanthanum zirconate reaction layers by impedance spectroscopy. *Solid State Ionics* **73**, 265-271, doi:http://dx.doi.org/10.1016/0167-2738(94)90043-4 (1994).

67 Brugnoni, C., Ducati, U. & Scagliotti, M. SOFC cathode/electrolyte interface. Part I: Reactivity between $La_{0.85}Sr_{0.15}MnO_3$ and ZrO_2-Y_2O_3. *Solid State Ionics* **76**, 177-182, doi:http://dx.doi.org/10.1016/0167-2738(94)00299-8 (1995).

68 Tu, H. Y. *et al.* Chemical compatibility of $RE_{0.6}M_{0.4}Mn_{0.8}Co_{0.2}O_{3-\delta}$ (RE=La, Pr, Nd, Sm and Gd; M=Sr and Ca) with yttria stabilized zirconia. *Journal of the European Ceramic Society* **20**, 2421-2425, doi:http://dx.doi.org/10.1016/S0955-2219(00)00126-6 (2000).

69 Stochniol, G., Syskakis, E. & Naoumidis, A. Chemical Compatibility between Strontium-Doped Lanthanum Manganite and Yttria-Stabilized Zirconia. *J. Am. Ceram. Soc.* **78**, 929-932, doi:10.1111/j.1151-2916.1995.tb08416.x (1995).

70 Waller, D., Lane, J. A., Kilner, J. A. & Steele, B. C. H. The effect of thermal treatment on the resistance of LSCF electrodes on gadolinia doped ceria electrolytes. *Solid State Ionics* **86–88, Part 2**, 767-772, doi:http://dx.doi.org/10.1016/0167-2738(96)00362-1 (1996).

71 Martínez-Amesti, A. *et al.* Reactivity between La(Sr)FeO_3 cathode, doped CeO_2 interlayer and yttria-stabilized zirconia electrolyte for solid oxide fuel cell applications. *Journal of Power Sources* **185**, 401-410, doi:http://dx.doi.org/10.1016/j.jpowsour.2008.06.049 (2008).

72 Tsoga, A., Gupta, A., Naoumidis, A. & Nikolopoulos, P. Gadolinia-doped ceria and yttria stabilized zirconia interfaces: regarding their application for SOFC technology. *Acta Materialia* **48**, 4709-4714, doi:http://dx.doi.org/10.1016/S1359-6454(00)00261-5 (2000).

73 Qian, J., Tao, Z., Xiao, J., Jiang, G. & Liu, W. Performance improvement of ceria-based solid oxide fuel cells with yttria-stabilized zirconia as an electronic blocking layer by pulsed laser deposition. *International Journal*

of Hydrogen Energy **38**, 2407-2412, doi:http://dx.doi.org/10.1016/j.ijhydene.2012.11.112 (2013).

74 Taskin, A. A., Lavrov, A. N. & Ando, Y. Achieving fast oxygen diffusion in perovskites by cation ordering. *Applied Physics Letters* **86**, -, doi:doi:http://dx.doi.org/10.1063/1.1864244 (2005).

75 Taskin, A. A., Lavrov, A. N. & Ando, Y. Transport and magnetic properties of $GdBaCo_2O_5$ single crystals: A cobalt oxide with square-lattice CoO_2 planes over a wide range of electron and hole doping. *Physical Review B* **71**, 134414 (2005).

76 Burriel, M. *et al.* Anisotropic Oxygen Ion Diffusion in Layered $PrBaCo_2O_{5+\delta}$. *Chemistry of Materials* **24**, 613-621, doi:10.1021/cm203502s (2012).

77 Tarancon, A., Burriel, M., Santiso, J., Skinner, S. J. & Kilner, J. A. Advances in layered oxide cathodes for intermediate temperature solid oxide fuel cells. *Journal of Materials Chemistry* **20**, 3799-3813, doi:10.1039/b922430k (2010).

78 Parfitt, D., Chroneos, A., Tarancon, A. & Kilner, J. A. Oxygen ion diffusion in cation ordered/disordered $GdBaCo_2O_{5+[delta]}$. *Journal of Materials Chemistry* **21**, 2183-2186, doi:10.1039/c0jm02924f (2011).

79 Tarancón, A., Marrero-López, D., Peña-Martínez, J., Ruiz-Morales, J. C. & Núñez, P. Effect of phase transition on high-temperature electrical properties of $GdBaCo_2O_{5+delta}$ layered perovskite. *Solid State Ionics* **179**, 611-618, doi:http://dx.doi.org/10.1016/j.ssi.2008.04.028 (2008).

80 Grygiel, C. *et al.* A-Site Order Control in Mixed Conductor $NdBaCo_2O_{5+\delta}$ Films through Manipulation of Growth Kinetics. *Chemistry of Materials* **22**, 1955-1957, doi:10.1021/cm9037022 (2010).

81 Bertaut, E. F., Blum, P. & Sagnieres, A. Structure du ferrite bicalcique et de la brownmillerite. *Acta Crystallographica* **12**, 149-159, doi:doi:10.1107/S0365110X59000433 (1959).

82 Huang, Q. *et al.* Neutron-powder-diffraction study of the nuclear and magnetic structures of $YBa_2Fe_3O_8$ at room temperature. *Physical Review B* **45**, 9611-9619 (1992).

83 Karen, P., Suard, E. & Fauth, F. Crystal Structure of Stoichiometric $YBa_2Fe_3O_8$. *Inorganic Chemistry* **44**, 8170-8172, doi:10.1021/ic048746b (2005).

84 Demont, A. *et al.* Stabilization of a Complex Perovskite Superstructure under Ambient Conditions: Influence of Cation Composition and Ordering, and Evaluation as an SOFC Cathode. *Chemistry of Materials* **22**, 6598-6615, doi:10.1021/cm102475n (2010).

85 Sayers, R. *et al.* Internal Activation Strain and Oxygen Mobility in a Thermally Stable Layered Fe^{3+} Oxide. *Chemistry of Materials* **25**, 3441-3457, doi:10.1021/cm4013359 (2013).

86 Dyer, M. S. *et al.* Computationally Assisted Identification of Functional Inorganic Materials. *Science* **340**, 847-852, doi:10.1126/science.1226558 (2013).

87 Hodgeman, D. W. *New cathodes for intermediate temperature solid oxide fuel cells (IT-SOFCs).* PhD thesis, University of Liverpool, (2014).

88 Sayers, R. *et al.* Epitaxial growth and enhanced conductivity of an IT-SOFC cathode based on a complex perovskite superstructure with six distinct cation sites. *Chemical Science* **4**, 2403-2412, doi:10.1039/c3sc21931c (2013).

Chapter 2: Methodology

2.1 Film Growth Techniques

Typically, deposition techniques fall into two broad categories, chemical vapour deposition (CVD) or physical vapour deposition (PVD). If material is deposited from the product of a chemical reaction then the process is classified as CVD. Alternatively, if a vapour is created via physical means with no chemical reaction then it is classified as PVD. Several variations of these techniques have been implemented to balance the various advantages and disadvantages depending on the requirements for film purity, structural quality, growth rate and temperature constraints. Examples of CVD techniques include atomic layer deposition (ALD), which is able to be used at low temperatures using gaseous precursors, and metal-organic molecular beam epitaxy (MOMBE), which is described as a hybrid of metal-organic chemical vapor deposition (MOCVD) and molecular beam epitaxy (MBE) that exploits the advantages of both the techniques. PVD techniques include sputtering, which is a low temperature technique involving the bombardment of a target with Ar^+ ions, and pulsed laser deposition (PLD), which uses a laser to vaporise the surface of a target material producing a plasma.[1]

2.1.1 Pulsed Laser Deposition

2.1.1.1 History of PLD

PLD has been used for evaporative film growth for over 40 years, practically since the discovery of lasers themselves.[2,3] In the 1980s PLD became more popular as a fast and reproducible technique for growing oxide films, with key

success in epitaxial high temperature superconducting films.[4] Further laser developments occurring in the 1990s, such as development of lasers with shorter pulse durations and higher frequencies, enabling the use of PLD for the growth of thin films with complex stoichiometry.

2.1.1.2 PLD Growth Mechanism

Pulsed laser deposition is a vacuum deposition technique which uses a high powered (0.1 - 10Jcm^{-2})[5] laser to vaporise (or ablate) material from a target to create a plasma plume. This plume then condenses onto a heated substrate, forming a film.[5-7] The thin film formation process takes place in the following stages:

1. Laser radiation interaction with the target (vaporisation and ionisation)

Initially the laser beam is focused onto the surface of the target, via a series of optical components. All elements in the target surface are rapidly heated up to their evaporation temperature. This leads to dissociation of materials from the target, which are then ablated with the stoichiometry of the target. Typically bulk ceramic targets are used for PLD, however single crystals can also be used, providing the material is not a wide bandgap insulator such as Al_2O_3 which would have insufficient optical absorption.[5]

2. Plasma expansion of the ionised species

During the second stage the emitted materials from the target move towards the substrate. Various factors such as the substrate temperature and the laser spot size have an effect on the deposited film's surface morphology. The shape and size of

the plume can be affected by the partial pressure of oxygen. To achieve thicker films at higher oxygen pressures a smaller target-to-substrate distance is desirable to increase the deposition rate.

3. Deposition of the adatoms

The third stage is important to determine the quality of thin film. It is possible that the ejected high-energy species (up to 120eV)[8] may affect the substrate surface potentially causing damage to the substrate.[9] Energetic species can sputter some of the surface atoms and between the incident flow and the sputtered atoms a collision region becomes established. A film grows immediately upon formation of this collision region and the region serves as a source for the condensation of particles. When the condensation rate is higher than the rate of particles supplied by the sputtering, thermal equilibrium condition can be reached quickly and film grows on the substrate surface at the expense of the direct flow of the ablation particles.

4. Nucleation and thin film growth

The fourth stage is the growth mode of the thin film. The growth mode affects the microstructure of the film. There are three types of growth modes as seen in Figure 2.1:

1. 2D layer by layer (Frank-van der Merwe)
2. 3D island (Volmer-Weber)
3. Layer by layer superseded by 3D growth (Stranski-Krastanov)[10]

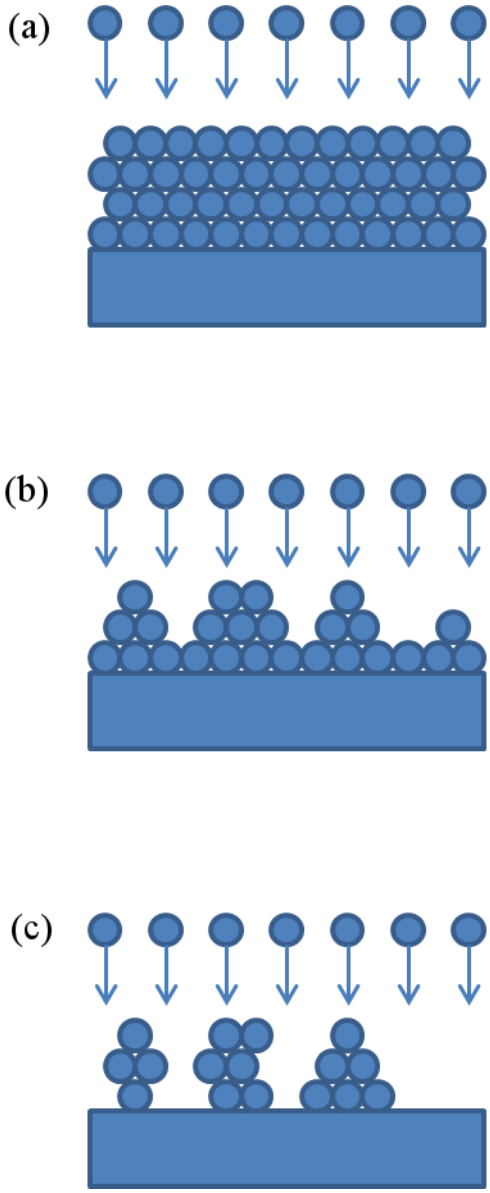

Figure 2.1: Schematic of growth modes (a) 2D layer by layer (Frank-van der Merwe), (b) Layer by layer superseded by 3D growth (Stranski-Krastanov), (c) 3D island (Volmer-Weber).[11]

In Frank van der Merwe growth (Figure 2.1 (a)), adatoms attach preferentially to step edges of growing islands over nucleation of new islands on top resulting in atomically smooth, fully formed layers. This layer-by-layer growth is two dimensional, so complete layers form prior to nucleation of subsequent layers. In Volmer-Weber growth (Figure 2.1 (c)), the interactions between the adatoms are

stronger than those between the surface and the adatoms, leading to the formation of three-dimensional adatom clusters or islands. Growth of these clusters will cause rough multi-layer films to grow on the substrate surface. Finally, Stranski-Krastanov (Figure 2.1 (b)) growth is an intermediate process characterized by both 2D layer and 3D island growth. Transition from the layer-by-layer to island-based growth occurs at a critical layer thickness which is highly dependent on the chemical and physical properties, such as surface and strain energies.[7,10]

The growth mode affects whether the film is granular or a single crystal as well as determining the strain in the structure. The film's structural morphology is determined by the growth mode altering defect density and type, as well as controlling the quality of the interfaces between layers. Surface mobility, deposition rate, interface compatibility and lattice mismatch all can affect the growth mode.

2.1.1.3 PLD Setup

In this work a Nano PVD chamber was used for thin film deposition via PLD. An excimer laser typically uses a mixture of a noble and a reactive gas such as a halide and has a typical pulse width of 10-70ns. For this work a KrF excimer laser with a wavelength of 248nm from Coherent was used.

A schematic of the PLD chamber is shown in Figure 2.2.

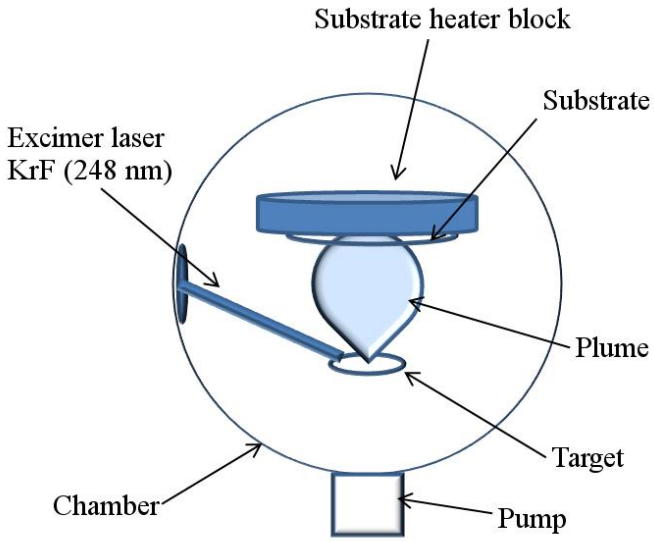

Figure 2.2: Schematic of a PLD chamber.

In PLD, the growth of the thin films is strongly affected by the size and shape of the plasma plume. The plasma plume's shape and size is dependent on the partial pressure of oxygen, the laser energy, the spot size and the angular distribution of the kinetic energy of the ablated particles (which in turn is dependent on the aforementioned parameters).[10] The plume shape was observed for each deposition, and any noticeable changes in the plume resulted in re-cleaning and re-aligning the laser optics.

One of the main advantages of PLD over other deposition techniques is the ability to deposit stoichiometric films. It is possible to deposit complex multi-cation films from targets with the correct cation ratios, however phase purity of the target is not essential.[5] In this work dense ceramic targets were used, as in Section 2.1 Table 2.1.

The optimised growth conditions for the thin films grown in this work are summarised in Table 2.2.

Table 2.2: Summary of material growth conditions.

Growth conditions	**$Sm_{0.2}Ce_{0.8}O_2$ (SDC)**	**$NdBaCo_2O_5$ (NBCO)**	**$Ba_{1.7}Ca_{2.4}Y_{0.9}Fe_5O_{13}$ (10 layer)**
Substrate Temperature (°C)	600-850	850	850
Growth pressure (mTorr)	1	1	1
Laser energy (mJ)	195	195	300
Frequency (Hz)	4-5	4-5	5

2.2 Target Preparation

Ceramic targets were produced via a conventional solid state reaction for use as targets for pulsed laser deposition (PLD). The precursors were dried for 2 hours at 200°C, except for lanthanide-containing compounds which were dried at 950°C due to their highly hygroscopic nature. The starting materials were then ground together in a pestle and mortar to give a homogeneous powder with uniform small particle size before being pressed into a pellet using a pellet die. The formation of pellets increases the contact between crystallite faces decreasing the reaction timescale.[12] The pellet was then calcined, before being re-ground and sintered under conditions reported in Table 2.1, in an air atmosphere. After each heating step the phase of the pellet was examined by X-ray diffraction. Once a phase pure material was achieved the powder was again ground and pressed into a pellet,

before being isostatically pressed using Autoclave Engineers cold isostatic press (CIP) at 200MPa. This pressed pellet was then returned to the furnace for sintering under conditions reported in Table 2.1.

A Sartorius extend balance ED124S with density determination kit YDP01LP was used to perform density measurements on the targets using Archimedes's principle. Initially, the mass of the sample is measured (m_1) following which the sample is immersed in water and its mass measured again (m_2). The surface of the sample is then carefully dried with a non-absorbent material before its mass is measured a final time (m_3). The density of the sample can then be calculated using the following equation:

$$\rho = \left(\frac{m_1}{(m_3 - m_2)}\right) \times \rho_{H_2O} \qquad \text{Eqn. (2.1)}$$

ρ_{H_2O} is the density of water, 0.997gcm^{-3} at 25°C. This measured value of the density is then divided by the theoretical density of the sample to provide a value of the percentage of theoretical density for the pellet.

The density of the targets is important for PLD as the density of the target affects the surface morphology of the films grown. Kim *et al.* found that using higher density TiO_2 targets resulted in a smoother film with fewer particulates.[13] In addition to this Willmott *et al*. discuss problems associated with target surface morphology resulting in the formation of droplets on the film surface.[14] To prevent these problems the targets were polished by hand to achieve a flat surface

using silicon carbide paper (203mm P1200 from Agar Scientific) and each target was pre-ablated in the chamber prior to film growth after it had been polished.

Pre-ablation is critical to maintain the homogeneity of the target stoichiometry, as during the ablation process favourable ion segregation to the surface is likely to occur.[7] In this work when the targets were pre-ablated they were subjected to 5000 pulses at 195mJ and 5Hz to expose fresh material and attain a steady state composition at the target surface.

In each of the results chapters the precise conditions for each target material used in this work is discussed, and a summary is shown in Table 2.1.

Table 2.1: Summary of the target preparation conditions.

Target material	**$Sm_{0.2}Ce_{0.8}O_2$ (SDC)**	**$NdBaCo_2O_5$ (NBCO)**	**$Ba_{1.7}Ca_{2.4}Y_{0.9}Fe_5O_{13}$ (10 layer)**
Starting materials	Commercially available SDC powder (from fuel cell materials (FCM)	Dried Nd_2O_3, $BaCO_3$ and Co_3O_4 from Sigma-Aldrich	Dried Y_2O_3, $BaCO_3$, $CaCO_3$, Fe_2O_3 from Alfa Aesar
Sintering Conditions	1400°C for 10 hours	1000°C for 12 hours, re-ground and second sintering at 1000°C for 12 hours, and finally at 1100°C for 24 hours	1200°C for 12 hours, with cycles of re-grinding and firing until phase purity was achieved
Percentage theoretical density	98%	85%	> 90%

The $Ba_{1.7}Ca_{2.4}Y_{0.9}Fe_5O_{13}$ target used for the growths in Chapter 4 and 5 was synthesised by Dr. Ruth Sayers, University of Liverpool, using conditions described in the Demont *et al*.[15] publication, and listed in Table 2.1.

2.2.1 Substrate Considerations

It is important to consider the lattice mismatch between the film and the substrate when choosing which substrate to grow the film on (Figure 2.3). Materials with well matched lattice parameters are more likely to grow epitaxially,[10] and the presence of strain may force the film into metastable structures and affect the morphology.[10] When a film with a different lattice parameter to the substrate is grown, the initial layer(s) may suppress the internal defects and form a flat surface. However the increase in strain energy that results with increasing film thickness will eventually result in the introduction of strain relief mechanisms. Such methods of relieving stress include, for example, dewetting, or the formation of defects such as dislocations[16,17] in the film, by island formation or by the roughening of its surface.[18]

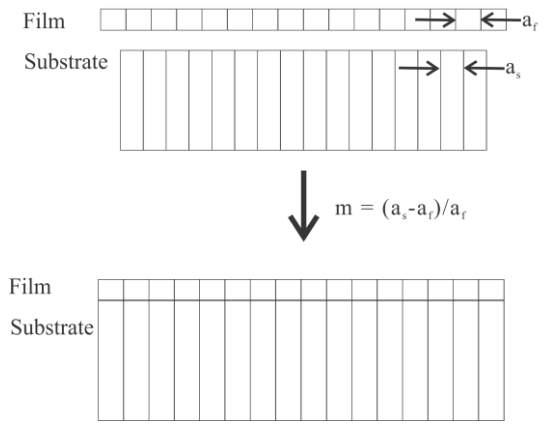

Figure 2.3: A heteroepitaxial thin-film structure. The mismatch between the lattice parameters of the film (a_f) and substrate (a_s) is accommodated by an elastic strain (m) in the film. Adapted from.[19]

The substrates were cleaned prior to thin film deposition in acetone ≥99.8% (Sigma-Aldrich) for 15 mins in an Agar Scientific ultrasonic cleaning bath, Sonomatic® T80 and subsequently sonicated in ethanol ≥99.5% (Sigma-Aldrich) for 15 mins. The substrates were dried with BOC CP grade nitrogen gas to ensure no residue from the solvents dried onto the substrate surface. The substrates were adhered onto the sample holder with silver DAG from Agar Scientific, before being loaded into the PLD chamber.

2.3 Crystal Structure

The unit cell of a crystal is the basic repeating unit which can be used to build the whole crystal lattice. The unit cells are classified into 7 crystal systems based on the symmetry the systems exhibit under rotations about different axes. A lattice can be described by defining a unit cell with edges *a*, *b* and *c* and angles α, β and γ, and the seven crystal systems and their corresponding essential symmetries are summarised in Table 2.3.

Table 2.3: Summary of the seven crystal systems and their associated essential symmetries.

System	Essential symmetries	Cell edge	Cell angle
Triclinic	None	$a \neq b \neq c$	$\alpha \neq \beta \neq \gamma \neq 90°$
Monoclinic	One twofold axis	$a \neq b \neq c$	$\alpha = \gamma = 90°, \beta \neq 90°$
Orthorhombic	Three perpendicular twofold axes	$a \neq b \neq c$	$\alpha = \beta = \gamma = 90°$
Rhombohedral	One threefold axis	$a = b = c$	$\alpha = \beta = \gamma \neq 90°$
Tetragonal	One fourfold axis	$a = b \neq c$	$\alpha = \beta = \gamma = 90°$
Hexagonal	One sixfold axis	$a = b \neq c$	$\alpha = \beta = 90°, \gamma = 120°$
Cubic	Four threefold axes in a tetrahedral arrangement	$a = b = c$	$\alpha = \beta = \gamma = 90°$

Combining these seven systems with lattice centerings (primitive, body centred, face centred, and base) generate 14 types of unit cell Bravais lattices.[20]

2.3.1 Miller Indices

The Miller indices are used as a labeling mechanism to effectively describe the different planes in a crystal lattice and use the notation *hkl*. Firstly we will look at the {00*l*} family, these planes runs parallel to the coordinates *a* and *b*, but in a cubic system *a*, *b* and *c* are all equal and are labeled as a_1, a_2 and a_3 in the following Figure 2.4 to illustrate this.[21]

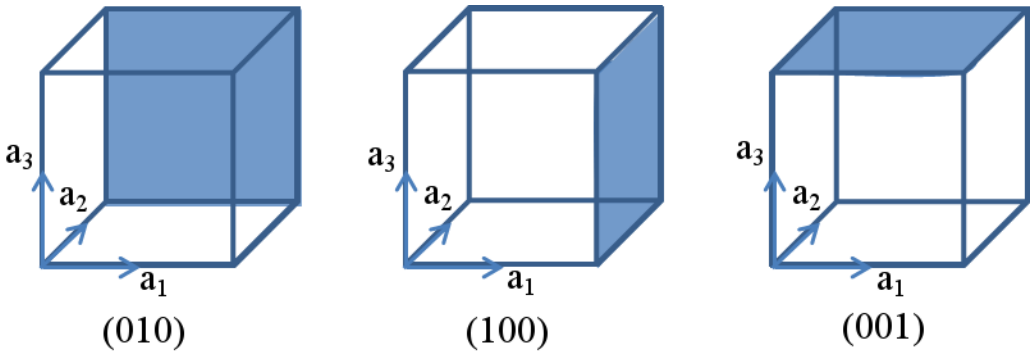

Figure 2.4: *hkl* Miller indices. Shaded planes are those represented by their respective Miller indices below.

The Miller indices are also used for calculating the plane separation as shown in Table 2.4.

Table 2.4: The relationship between the Miller indices and the lattice separation.

Crystal system	**d_{hkl}, lattice parameters and Miller indices**
Cubic	$\frac{1}{d^2} = \frac{h^2 + k^2 + l^2}{a^2}$
Tetragonal	$\frac{1}{d^2} = \frac{h^2 + k^2}{a^2} + \frac{l^2}{c^2}$
Orthorhombic	$\frac{1}{d^2} = \frac{h^2}{a^2} + \frac{k^2}{b^2} + \frac{l^2}{c^2}$

Table 2.4 gives formulae that can be used to calculate the lattice parameters from the *d*-spacing and the *h*, *k*, *l* values for cubic, tetragonal and orthorhombic structures. Different equations are used, depending on the structure of the crystal system of interest.[20] Throughout this work the films have been grown on (001) oriented single crystal substrates.

2.4 Characterisation

Characterising thin films is fundamentally important to determine the quality of the film and to help optimise the growth conditions. A variety of techniques have been employed to analyse film quality, and this section will briefly describe them.

2.4.1 X-ray Scattering

2.4.1.1 History of X-ray Diffraction

Wilhelm Röntgen discovered X-rays in 1895, and later in 1912 Max von Laue suggested that a crystal would be a good 3-dimensional diffraction grating for X-rays. Friederich, Knipping and von Laue carried out the first diffraction experiments; these experiments showed that X-rays have wave-like properties, and that the atoms in crystals are arranged in a regular pattern.[22]

2.4.1.2 Fundamental Concepts

Two distinct processes are involved in X-ray emission. In the first process, electrons are slowed down or stopped by a target, and part or all of their kinetic energy is converted directly to a continuous spectrum of photons, including X-rays - this radiation is termed bremsstrahlung. The second process gives peaks in the X-ray spectrum at characteristic wavelengths that depend on the target material. Here electrons, if they have enough kinetic energy, can transfer their energy partly or completely into individual atoms within the target. These atoms are left in excited states, creating core-hole pairs; when they decay back to their ground state they emit X-ray photons.[22] Typical targets include copper (Cu, $\lambda = 0.154$nm) and cobalt

(Co, λ = 0.178nm) for laboratory based diffractometers, both of which were utilized for this work.

In a copper source, X-rays are generated by positioning a negatively charged W filament in close proximity to a piece of positively charged Cu with all components under vacuum. This results in Cu emitting X-rays through a beryllium window. Beryllium is a light element and is minimally absorbent for X-rays. When electrons are removed from Cu holes are formed, and electrons from higher energy states drop down to these holes, or vacant lower energy states, emitting *hv* (*h* being Planck's constant, and *v* the frequency) energy in the form of X-rays.

Sir William Bragg and his son Laurence Bragg carried out extensive work in X-ray analysis and derived the Braggs Law equation:

$$n\lambda = 2d \sin\theta \qquad \text{Eqn. (2.2)}$$

Where *n* is the order of the reflection and must always be an integer number, λ is the wavelength, *d* is the *interplanar* spacing, and θ is the angle of incidence.[23]

When looking at the schematic in Figure 2.5 one can observe two X-rays being reflected by a surface. If these two X-rays are in-phase with each other, then X-rays are detected. In order for this to be the case the difference in path length between position A and B, and position B and C are required to be an integer number multiple of λ. However if the path length was instead 0.5 λ for example, then

destructive interference would occur and both rays would cancel each other out and no X-rays would therefore be detected. In an experiment one would observe the intensity versus theta plots, and peaks would be visible in 2 theta scans/diffractograms where the constructive interference conditions were satisfied, i.e. where n is equal to an integer number of λ.[23]

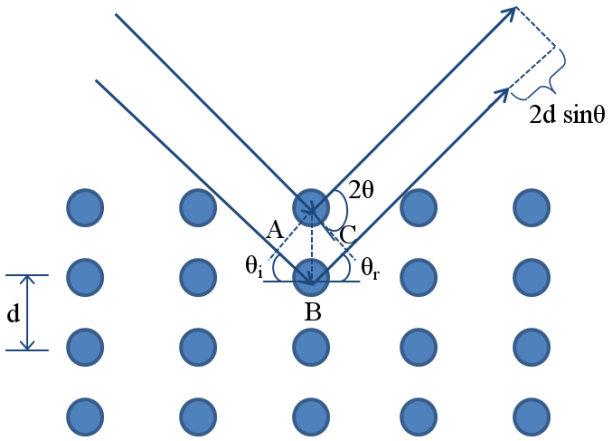

Figure 2.5: Schematic of Bragg's Law adapted from.[24] Where θ_i is the angle of incidence, θ_r is the angle of reflection, *d* is the distance between the planes. Positions A, B and C are labeled to indicate the path length.

2.4.2 Thin Film X-ray Scattering Techniques

2.4.2.1 X-ray Diffraction

Theta/2 theta (θ/2θ) measurements give information regarding the material structure, phase, orientation, crystallinity and particle size. In addition to this it also allows us to observe any impurity phases present in the sample. Figure 2.6 shows a schematic of the setup for a θ/2θ scan.

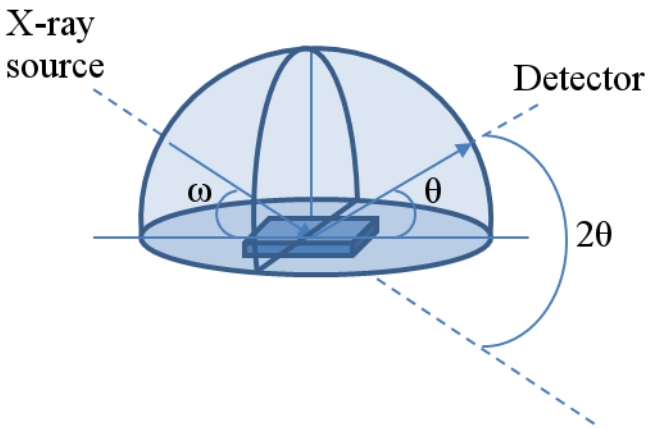

Figure 2.6: Schematic to show the θ/2θ diffractometer geometry. ω == θ in symmetric geometry.

In the θ/2θ scan, θ and 2θ are moved simultaneously, and the out of plane lattice parameter can be determined from this type of scan.[25]

In this work different diffractometers with different targets have been used. XRD measurements in this work were performed using either a PANalytical X'Pert diffractometer with Co $K_{\alpha 1}$ radiation λ = 0.179nm, or a Philips X'Pert diffractometer equipped with a Cu $K_{\alpha 1}$ X-ray source (λ = 0.154nm) and a four bounce Ge monochromator. The Philips X'Pert diffractometer was also used for all subsequent scans described in the following sections.

2.4.2.2 Omega Scans

Omega scans, or rocking curves (RC), provide information on the crystalline quality of the films. By fixing the detector at the centre of the expected Bragg reflection and following the diffracted intensity as the sample is independently rotated (or "rocked") through this angle, one can gain information concerning the growth coherence and crystallinity. The geometry used for omega scans is shown in the schematic in Figure 2.7.

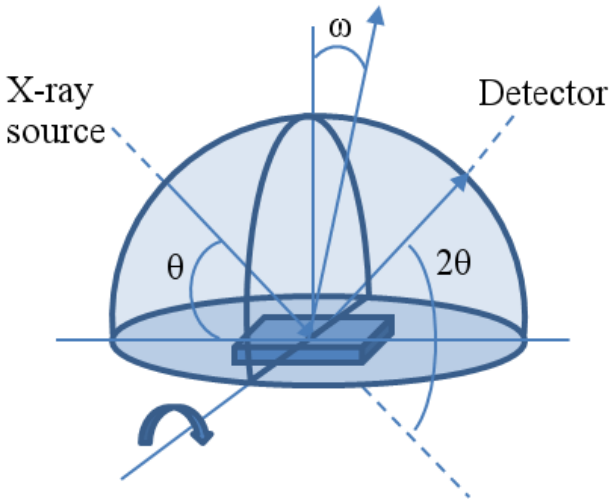

Figure 2.7: Schematic showing the diffractometer geometry for an omega scan.

The full width of the peak at half maximum intensity (FWHM) is related to the dislocation density in the film. Figure 2.8 shows how the microstructure of the film surface can give rise to a broadening of the rocking curve.

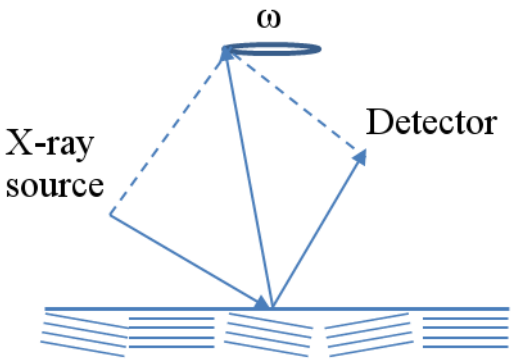

Figure 2.8: Schematic showing how the small differences in film orientation can be observed through the omega scan.

High Resolution variations of the method also allow us to determine misfit strain, the periodicity in artificial superlattices, the quality of the interfacial region and degree of mosaicity.[25]

The film FWHM is limited by the substrate's FWHM; the narrowness of the film's FWHM is indicative of a film that has few defects and good crystalline quality. Typically films with FWHMs of less than 1° would be considered to be of good quality.

2.4.2.3 Phi Scan

Phi scans in this work were performed at the University of Liverpool with Dr. Robert Palgrave. Phi (see Figure 2.9) is altered and the scan measures the change in diffracted X-ray intensity in-plane. This scan is used to investigate the epitaxial relationship of the film to the substrate.

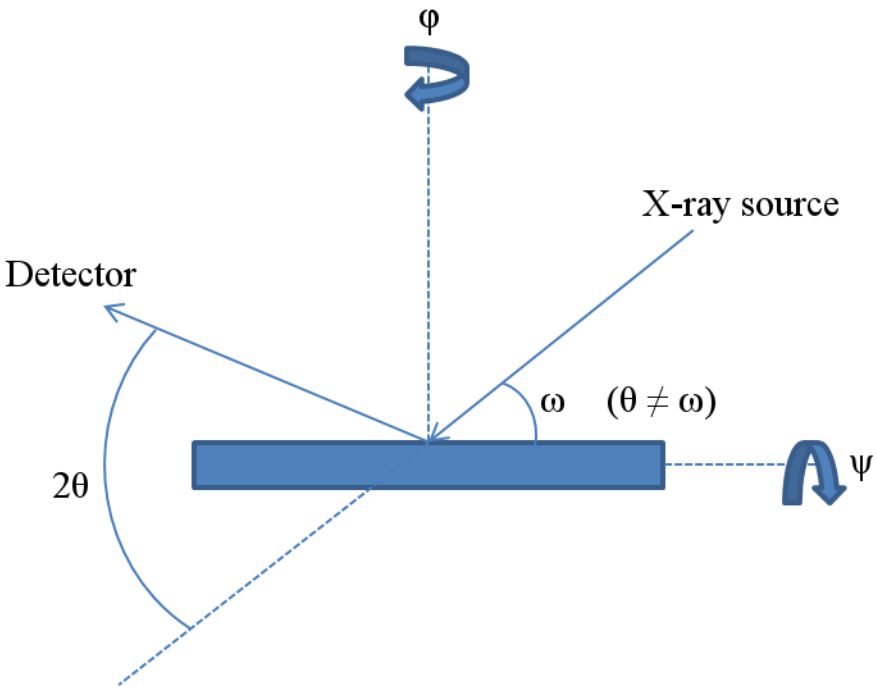

Figure 2.9: Schematic of a phi scan. ω is the angle between incident X-rays and sample surface and is not equal to θ, 2θ is the angle between incident X-rays and detector, ψ is the sample tilt, φ is the in-plane sample rotation.

Off axis peaks are used to determine in plane lattice parameters This can be useful for seeing how the film grows on the substrate and can be used to determine lattice mismatch.[26]

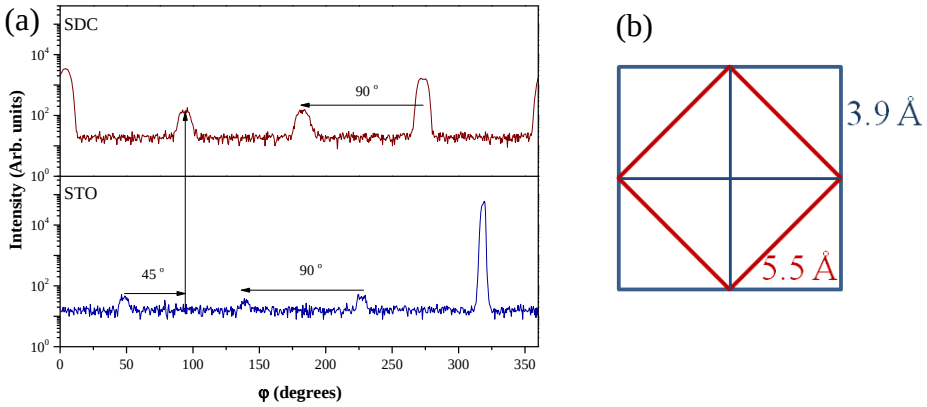

Figure 2.10: (a) Representative phi scan of SDC on STO and (b) 2-dimensional representation of the unit cell arrangement of SDC, shown in red, grown over four STO unit cells, shown in blue, offset at 45°.

The phi scan results in a pattern of 4 peaks that are 90° apart in a cubic system. In this example where the scan is aligned around the (311) orientation, the response from the (311) peak is joined by peaks from three further reflections that are caused by the equally probable scattering of the incoming X-ray beam at lattice planes $(1\bar{3}1)$, $(\bar{1}31)$ and $(\bar{3}\bar{1}1)$. The number of equivalent lattice planes that cause reflections is referred to as the multiplicity. If the film is grown offset on the unit cell of the substrate then 4 film peaks at an offset angle to those of the substrate are observed (Figure 2.10 (a)). For example, samarium doped ceria (SDC) can be grown on strontium titanate (STO), 45° rotated, and the unit cells would appear as shown in the diagram Figure 2.10 (b).

2.4.2.4 Pole Figures

Pole figures in this work were performed at the University of Liverpool with Dr. Jonathan Alaria. Pole figures are utilised to provide information about the films texture or preferred orientation.[25]

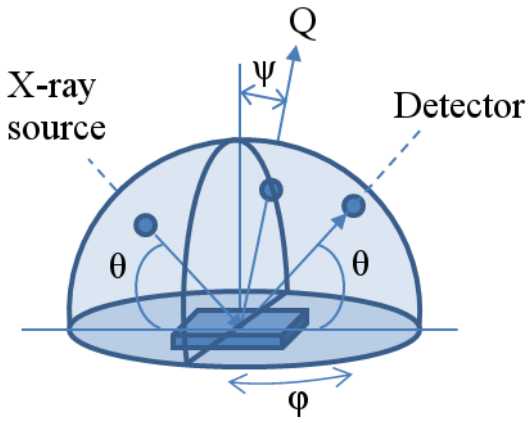

Figure 2.11: Schematic of the diffractometer geometry required for a pole figure.

The representation of the geometry required for a pole figure is shown in Figure 2.11. Individual phi scans are measured at incremental azimuthal angle, ψ. ψ is a measure of the angle between the surface normal of the sample and the scattering vector, Q as the sample is tilted in-plane and φ is the azimuth angle of the sample in the surface plane.[25] Q is the scattering vector for the momentum transfer and Q-space is related to θ by the Equation 2.3.

$$Q = \frac{4\pi \sin\theta}{\lambda} \qquad \text{Eqn. (2.3)}$$

2.4.2.5 Reciprocal Space Maps

Reciprocal space maps (RSMs) in this work were performed at the University of Liverpool with Dr. Jonathan Alaria. RSMs are obtained by collecting ω scans at incremental 2θ or running (ω + ω_0)/ 2θ scans for different offset angles ω_0 and plotting the recorded intensities in a contour plot. The results of these scans are plotted to produce a 'map' such as the one shown in Figure 2.12.

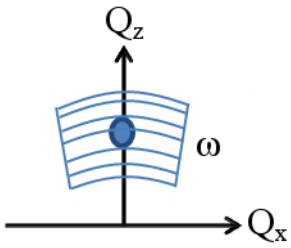

Figure 2.12: Schematic showing a reciprocal space map acquired by measuring several omega scans. Adapted from.[25]

Reciprocal space mapping generally operates at a much higher resolution and in a more restricted Q area than pole figures, and so are useful for obtaining additional structural information.

2.4.2.6 X-ray Reflectivity

X-ray reflectivity (XRR) is a technique that can be used to determine the thickness of thin films. The principle is based on the reflection of X-rays at very low angles of incidence (θ_i), and a schematic representation of this is shown in Figure 2.13.[27]

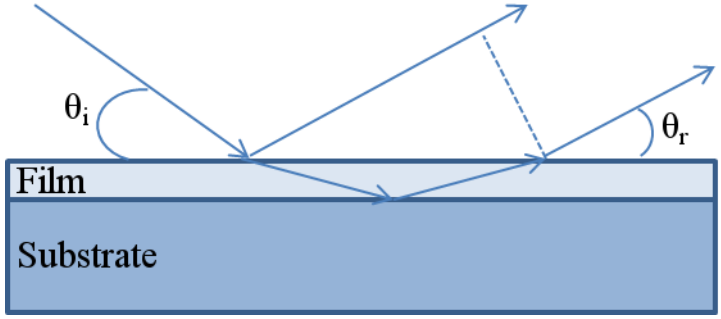

Figure 2.13: Schematic representation of XRR. θ_i is the angle of incidence and θ_r is the angle of reflection. Adapted from.[25]

The film is deposited on top of a single crystal substrate, which creates a film-substrate interface. At the interface some of the X-rays are reflected and the interference of these partially reflected X-ray beams generates a reflectometry pattern. This pattern appears by having X-rays of fixed wavelength, and changing the angle of incidence. As the angle of incidence changes, the pathlength of the X-rays change and when the difference in pathlength between two X-rays equals a whole number at the fixed wavelength then you see a maximum in the intensity. When the path difference is not equal to a whole number of wavelengths then it is out-of-phase and leads to a minimum.[25,26]

The geometry of the diffractometer which is required for XRR is shown in the schematic in Figure 2.14.

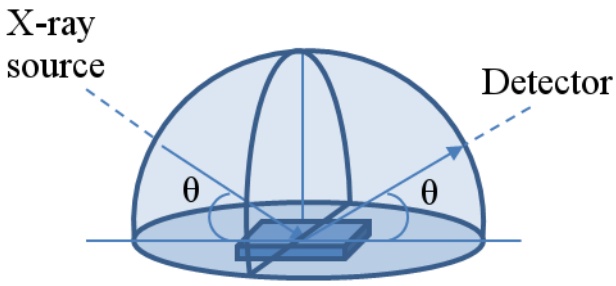

Figure 2.14: Schematic of XRR geometry.

Interpretation of XRR curves can be separated into 3 regions, as shown in Figure 2.15. These regions are: 1) increasing intensity, 2) intensity plateau and 3) steeply decreasing intensity. Regions 2 and 3 are separated by the critical angle. Region 3 provides an indication of the film's roughness as the slope depends on the surface roughness.

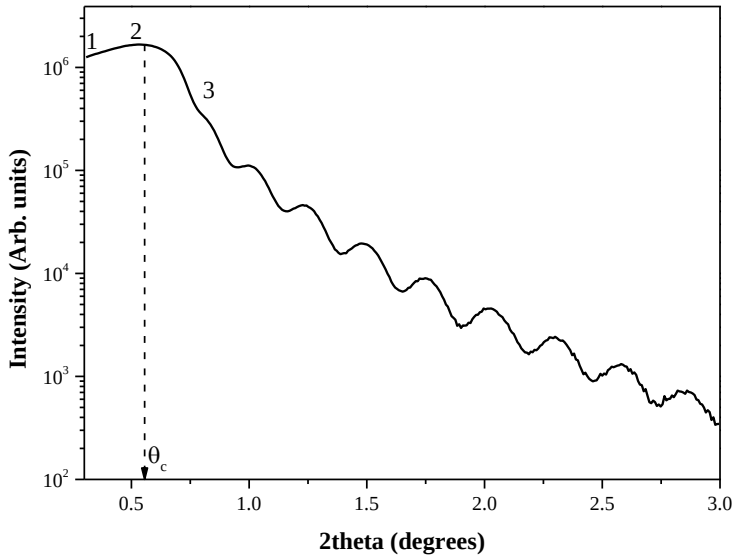

Figure 2.15: A typical XRR, with the three regions labeled 1 increasing intensity, 2 intensity plateau and 3 steeply decreasing intensity. θ_c is the critical angle.

The critical angle depends on the electron density of the substrate and film – the larger the number of electronic scatterers the higher the critical angle. Intensity oscillations are called Kiessig oscillations or Kiessig fringes, named after H. Kiessig, as published in 1931.[28,29] Maximum intensities are observed whenever the phase difference between the reflected and refracted beam is a multiple of the wavelength.

X'Pert Reflectivity Software was used to simulate the XRR pattern and determine the thickness. The model takes into account all interfaces and also the substrate and film's density, thickness and roughness. There are three fitting procedure options available within the X'Pert Reflectivity Software including segmented fitting, genetic algorithm fitting and a combined genetic algorithm and segmented fitting.[30]

The procedure for segmented fitting initially begins by fitting the first part of the curve, around position 2 in Figure 2.15. Having obtained a good fit for this region it progressively fits the curve over the full measured range. This function allows automatic fitting of simulated scans to measured scans and is particularly useful when the film's target values for thickness etc. are relatively accurate.

Genetic algorithm fitting on the other hand generates multiple fits where random modifications of the selected parameters (ie. roughness, thickness) within a set range are automatically tested until the best fit is achieved. This fit is considered complete when the simulated data matches the experimental data within set tolerances. If there is a large difference between the films targeted parameters and

the fit then this method is particularly useful as it allows for a large deviation, which can be further refined with the segmented fitting method.

The combined genetic algorithm and segmented fitting firstly generates a initial approximation using the genetic algorithm before refining with the segmented fitting method.

These procedures all perform multiple simulations to refine the experimental data and also take into account the instrumental parameters. The simulations are based on established dispersion theory and the fitting takes divergence and background into account as well as the irradiated area determined by the substrate length and beam dimensions.

2.4.3 Atomic Force Microscopy

Binnig and Quate first demonstrated an atomic force microscope in 1986 as a method to image the topography of a surface.[31] For imaging the topography of the films the AFM can be used in contact mode or alternating contact mode (ACAFM), and both of these have been used in this work. In contact mode, the AFM tip, mounted on a soft cantilever spring, is brought into gentle contact with the sample and then scanned across the surface. A laser, as in Figure 2.16, senses the cantilever deflection as the tip moves across the surface of the material. The tip is rastered across the surface in a pendulum – like manner.[32] There is a feedback system to monitor and control the cantilever's height, and software converts the height position into an image.[10] Typically the system maintains a constant force on the tip, however the system can also maintain the tip at a

constant height, for high resolution imaging of very flat surfaces. Contact mode tips are designed specifically for this application, with lower resonance frequency and with softer cantilevers.

In ACAFM the cantilever oscillates in sinusoidal fashion at or near one of its resonance frequencies with intermittent contact between the sample and the tip. During the oscillation cycle, the tip and sample become close, moving the tip through an interaction potential that includes long-range attractive and short term repulsive components. The complex forces between the tip and the sample cause changes in the amplitude, phase and resonance frequency of the oscillating cantilever.

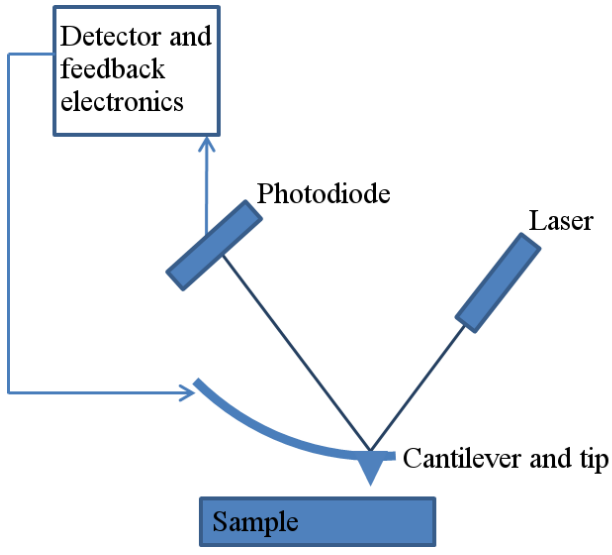

Figure 2.16: Schematic of AFM showing the beam deflection system, using a laser and detector to measure the beam position.

AFM images are particularly important in thin film characterisation, as the quality of the surfaces can be used as an indication of microstructure and growth mode.[33]

An Agilent 5600LS AFM was used; the images were acquired using a μ-masch cantilever and tip with the product code LS15/AlBS, they are long-scanning scanning probe microscopy (SPM) probes with an Al coating on the back and have a resonant frequency of 325kHz and a force constant $46Nm^{-1}$. These were typically used for ACAFM in air at room temperature at a scan speed of 1line/s. Later in the work these tips were discontinued and were replaced with new equivalent tips with the product code HQ:NSC15/Al BS-15, supplied from Windsor Scientific.

All the AFM images were obtained using PicoView 1.10.7 software in conjunction with a 512 x 512 pixel camera, used to position the AFM tip and sample before scanning. The processing and analysis of the images was performed using the PicoImage Software.

2.4.4 Optical Microscopy

The optical microscope, uses visible light and a system of lenses to magnify images of small sample. A Meiji Techno RZ Zoom Stereo Microscope was used to image the electrodes in Chapter 5.

2.4.5 Transmission Electron Microscopy and Scanning Electron Microscopy

2.4.5.1 Transmission Electron Microscopy

Transmission electron microscopy (TEM) in this work was performed by Prof. Joke Hadermann (Electron Microscopy for Materials Science (EMAT), University of Antwerp), Dr. Simon Romani (NiCaL, University of Liverpool), Dr. Quentin Ramasse (SuperSTEM, Daresbury) and Dr. Timothy Pennycook (SuperSTEM, Daresbury and University of Oxford). TEM, uses a beam of electrons focussed through electromagnetic lenses to image the sample. By varying the strength of these electromagnets, the magnification of the image formed can be changed. TEM can be used to image cross sections of films, and can therefore be used for microstructural analysis, crystallographic analysis on a local scale and interface quality analysis on an atomic scale.

The quality of TEM images is directly dependent on the sample preparation process, a destructive technique that involves cleaving, grinding, polishing, and ion milling the material to electron transparency.

2.4.5.2 Scanning Transmission Electron Microscopy

In the scanning transmission electron microscopy (STEM) mode, the microscope lenses are adjusted to create a focused convergent electron beam at the sample surface. This focused probe is then scanned across the sample and signals are collected to form an image. The nature of the images obtained in the STEM can

differ in significant ways from those formed by the conventional TEM, in particular, multiple signals can be acquired in the STEM including bright field, annular dark field (ADF) images, and spectroscopic images using either electrons that have lost energy by exciting specific inner shell or valence band levels or by detecting emitted characteristic X-rays.[34] STEM was performed by Dr. Quentin Ramasse (SuperSTEM, Daresbury) and Dr. Timothy Pennycook (SuperSTEM, Daresbury and University of Oxford).

2.4.5.3 Scanning Electron Microscopy and Energy Dispersive X-Ray Analysis

Scanning electron microscopy (SEM) in this work was performed at the University of Liverpool with the assistance of Dr. Ruth Sayers and Dr. Marco Zanella in the centre of materials discovery (CMD) on a Hitachi S-4800 SEM. SEM is another electron microscopy technique similar to TEM, and images a sample by scanning it with a high-energy beam of electrons in a raster scan pattern (a systematic process of covering the area progressively, one line at a time). The electrons interact with the atoms that make up the sample producing signals that contain information about the sample's surface topography. If the sample is not sufficiently electrically conductive, then sample charging can occur and some samples may be required to have a gold coating to limit this. SEM is used to establish an estimate of thicknesses of films when films are too thick for XRR analysis (typically when film thickness is > 100nm). From the thickness, the deposition rate for the films can be calculated.

SEM/ Energy dispersive X-ray analysis (EDX) was used for compositional analysis. When an incident electron or X-ray beam passes through a sample, electrons in the sample are excited from their ground state energy levels to higher ones creating an electron-hole pair. When these excited electrons decay back into their ground state, X-rays are emitted which are characteristic not only of the parent atom, but also of the energy levels involved in the excitation and decay process.

2.4.5.4 Raman Spectroscopy

Raman spectroscopy is a technique that is used to observe vibrational and rotational modes in a sample. Laser light excites the sample vibrational or rotational modes, which then decay resulting in emitted radiation. The majority of the energy emitted has the same magnitude as that absorbed, and this is termed Rayleigh scattering. However, some of the modes decay to higher or lower states than the original ground state and so the emitted radiation of higher or lower energy than the incident radiation. This difference in energy gives information about the vibrational and rotational modes of the system.[35] Dr. Marco Zanella at the University of Liverpool collected Raman data using a Reinshaw inVia Raman Microscope with WiRE software.

2.4.6 AC Impedance Spectroscopy

AC impedance spectroscopy in this work was performed at the University of Liverpool with the assistance of Dr. Ruth Sayers. For use in SOFCs, cathodes should have *high* electronic and ionic conductivity. To measure the total conductivity of the thin film cathodes, alternating current (AC) impedance spectroscopy was used. The theory behind this technique is briefly described as follows, and more information can be found elsewhere.[36-38]

Ohm's Law is shown in Equation 2.4:

$$R = \frac{V}{I} \qquad \text{Eqn. (2.4)}$$

R is the resistance, V is the voltage and I is the current. This law is limited in its use to the ideal resistor, where the resistance is independent of the frequency and the potential and current are in phase with each other. Impedance is the measure of how resistant the circuit is to the flow of current, and these assumptions of an ideal resistor do not hold true in most situations where there are circuit elements which possess more complex behaviour.[37]

The relationship between the resistance and the resistivity of a sample can be described by Equation 2.5:

$$\rho = \frac{R.A}{L} \qquad \text{Eqn. (2.5)}$$

ρ is the resistivity, R is the resistance, A is the cross sectional area and L is the length. The conductivity (σ) of the sample is simply the reciprocal of the resistivity (ρ):

$$\sigma = \frac{1}{\rho} \quad \text{Eqn. (2.6)}$$

Therefore due to the reciprocal relationship between the conductivity and the resistivity:

$$\sigma = \frac{L}{R.A} \quad \text{Eqn. (2.7)}$$

To measure the impedance, an AC potential is applied across an electrochemical cell, and the current measured through the cell. Typically an equivalent circuit model is used to interpret the data, using components such as resistors, capacitors and inductors.

Impedance is a more general concept than resistance because it takes phase differences into account. Impedance can be written as Z(ω) and comprises a real and an imaginary part. The real part is typically expressed as (Z', or Re(Z)) and is resistive, whereas the imaginary part is (Z", or Im(Z)) and is capacitive. These two components can be plotted on a Nyquist plot as in Figure 2.17, with a Z' x-axis, and -Z" y-axis.[38] In general, *Z* is frequency-dependent and typically measured over a wide frequency range (e.g. 0.01Hz to 1MHz).

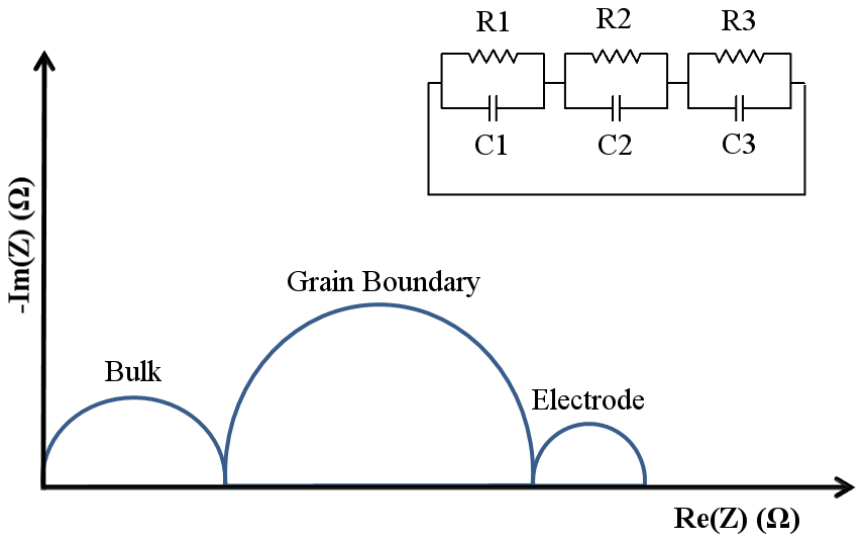

Figure 2.17: Schematic of a typical Nyquist plot showing individual contributions to the impedance from the bulk, grain boundary and electrode. The inset shows an equivalent circuit model.

The plot shown in Figure 2.17 shows characteristic arcs for a simple circuit with a response which can be described by a set of three parallel equivalent circuits of resistors (R1, R2, R3) and capacitors (C1, C2, C3) in series.

Once the electrochemical processes have been identified and assigned in an equivalent circuit, the bulk and grain boundary conductivity of the electrolyte/electrode can be calculated using the sample dimensions, from Equation 2.7.

The individual electrochemical processes can be identified from their respective capacitances. Capacitance (C) is measured in Farads, and can be calculated from Equation 2.8.

$$C = \varepsilon_r \varepsilon_0 \frac{A}{L} \qquad \text{Eqn. (2.8)}$$

ε_r is the relative static permittivity, ε_0 is the dielectric constant of a vacuum, A is the cross sectional area and L is the length. Typical values for each process are shown in Table 2.5.

Table 2.5: Capacitance values and their possible interpretation from Irvine *et al.*[36]

Capacitance (F)	**Phenomenon responsible**
10^{-12}	Bulk
10^{-11}	Minor, second phase
10^{-11}-10^{-8}	Grain boundary
10^{-10}-10^{-9}	Bulk ferroelectric
10^{-9}-10^{-7}	Surface layer
10^{-7}-10^{-5}	Sample- electrode interface
10^{-4}	Electrochemical reactions

Studies on single crystal materials have the advantage that grain boundary phenomena should be absent and a more detailed analysis of bulk properties may be made. Throughout this work the impedance analysis was carried out on thin films with reduced grain boundary contributions.

The conductivity of materials is affected by the temperature; the resistivity of metallic materials increases with temperature, whereas that of intrinsic semiconductors decreases. In this work, AC impedance measurements were performed over a range of temperatures from 200 - 600°C.

The schematic in Figure 2.18 is designed to show the geometry of the electrodes used for the AC impedance measurement of thin films, where the impedance is measured in-plane. Gold electrodes are sputtered onto the film, and gold wires are

attached using gold paste. AC impedance measurements were performed using a Solartron 1260 with SMaRT software.

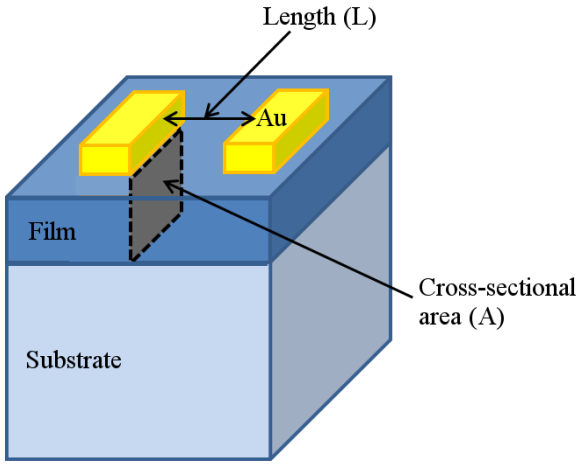

Figure 2.18: Schematic showing the geometry of the contacts used for the AC-impedance measurement of thin films.

In addition to this, the area specific resistance (ASR) of the cathode materials was also calculated from resistance values obtained from cathode films on electrolytes (Equation 2.9).

$$ASR = R.A \qquad \text{Eqn. (2.9)}$$

R is the measured resistance, and A is the sample surface area.

The ASR measurements of the cathode material are discussed in Chapter 5. The electrode patterning work performed by Dr. Plamen Stanislavov's group at the University of Dublin used a plasma etching process using a Millatron argon ion beam vacuum etching milling system. The etching process faithfully reproduces the mask pattern on the substrate. An argon ion beam is used to etch material exposed by a mask to obtain the desired pattern. Two sets of masks were produced for positive and negative etching. A Ti layer was deposited between the

Au and the 10 layer to improve the adhesion. Later a Cr later was deposited between the Pt and the 10 layer was used instead of the Ti|Au layer.

2.5 References

1 L. B. Freund & Suresh, S. in *Thin Film Materials: Stress, Defect Formation and Surface Evolution* (Cambridge University Press, Cambridge, 2003).

2 Hass, G. & Ramsey, J. B. Vacuum Deposition of Dielectric and Semiconductor Films by a CO_2 Laser. *Appl. Opt.* **8**, 1115-1118, doi:10.1364/ao.8.001115 (1969).

3 Smith, H. M. & Turner, A. F. Vacuum Deposited Thin Films Using a Ruby Laser. *Appl. Opt.* **4**, 147-148, doi:10.1364/ao.4.000147 (1965).

4 Inam, A. *et al.* As-deposited high T_c and J_c superconducting thin films made at low temperatures. *Appl. Phys. Lett.* **53**, 908-910, doi:doi:http://dx.doi.org/10.1063/1.100155 (1988).

5 Eason, R. in *Pulsed Laser Deposition of Thin Films* (Wiley and Sons, 2007).

6 Tagawa, H. & Igarashi, K. Reaction of Strontium Carbonate with Anatase and Rutile. *Journal of the American Ceramic Society* **69**, 310-314, doi:10.1111/j.1151-2916.1986.tb04737.x (1986).

7 Douglas B. Chrisey & Hubler, G. K. in *Pulsed Laser Deposition of Thin Films* (John Wiley and Sons, INC., 1994).

8 Taylor, M. E., Atwater, H. A. & Murty, M. V. R. Role of energetic flux in low temperature Si epitaxy on dihydride-terminated Si (001). *Thin Solid Films* **324**, 85-88, doi:http://dx.doi.org/10.1016/S0040-6090(97)01212-1 (1998).

9 Mayr, S. G., Moske, M., Samwer, K., Taylor, M. E. & Atwater, H. A. The role of particle energy and pulsed particle flux in physical vapor deposition and pulsed–laser deposition. *Appl. Phys. Lett.* **75**, 4091-4093, doi:doi:http://dx.doi.org/10.1063/1.125546 (1999).

10 Ohring, M. in *Materials Science of Thin Films, Deposition and Structure* (Academic Press, 2002).

11 Lee, Y. H. *et al.* in *Pricm 7, Pts 1-3* Vol. 654-656 *Materials Science Forum* (eds J. F. Nie & A. Morton) 2787-2790 (Trans Tech Publications Ltd, 2010).

12 Lesley E. Smart & Moore, E. A. in *Solid State Chemistry an Introduction* (Taylor and Francis, Boca Raton, 2012).

13 Kim, J.-H., Lee, S. & Im, H.-S. The effect of target density and its morphology on TiO_2 thin films grown on Si(100) by PLD. *Applied Surface Science* **151**, 6-16, doi:http://dx.doi.org/10.1016/S0169-4332(99)00269-X (1999).

14 Willmott, P. R. & Huber, J. R. Pulsed laser vaporization and deposition. *Reviews of Modern Physics* **72**, 315-328 (2000).

15 Demont, A. *et al.* Stabilization of a Complex Perovskite Superstructure under Ambient Conditions: Influence of Cation Composition and Ordering, and Evaluation as an SOFC Cathode. *Chem. Mat.* **22**, 6598-6615, doi:10.1021/cm102475n (2010).

16 Frank, F. C. & van der Merwe, J. H. One-Dimensional Dislocations. I. Static Theory. *Proceedings of the Royal Society of London. Series A. Mathematical and Physical Sciences* **198**, 205-216, doi:10.1098/rspa.1949.0095 (1949).

17 Matthews, J. W. & Blakeslee, A. E. Defects in epitaxial multilayers: I. Misfit dislocations. *Journal of Crystal Growth* **27**, 118-125, doi:http://dx.doi.org/10.1016/S0022-0248(74)80055-2 (1974).

18 Asaro, R. J. & Tiller, W. A. Interface morphology development during stress corrosion cracking: Part I. Via surface diffusion. *MT* **3**, 1789-1796, doi:10.1007/bf02642562 (1972).

19 Gao, H. J. & Nix, W. D. Surface roughening of heteroepitaxial thin films. *Annual Review of Materials Science* **29**, 173-209 (1999).

20 Peter Atkins & Paula, J. d. *Elements of physical chemistry* 4edn, (Oxford University Press, 2006).

21 Gao, W. L., Deng, H. M., Huang, D. J., Yang, P. X. & Chu, J. H. in *3rd International Photonics and Optoelectronics Meetings* Vol. 276 *Journal of Physics Conference Series* (eds C. Ye, Z. L. Wang, & B. Zhou) (Iop Publishing Ltd, 2011).

22 Aksenova, T. V., Gavrilova, L. Y., Tsvetkov, D. S., Voronin, V. I. & Cherepanov, V. A. Crystal structure and physicochemical properties of

layered perovskite-like phases $LnBaCo_2O_{5+delta}$. *Russ. J. Phys. Chem. A* **85**, 427-432, doi:10.1134/s0036024411030022 (2011).

23 Cherepanov, V. A., Aksenova, T. V., Gavrilova, L. Y. & Mikhaleva, K. N. Structure, nonstoichiometry and thermal expansion of the $NdBa(Co,Fe)_2O_{5+[delta]}$ layered perovskite. *Solid State Ionics* **188**, 53-57, doi:DOI: 10.1016/j.ssi.2010.10.021 (2011).

24 Necas, D., Franta, D., Bursikova, V. & Ohlidal, I. Ellipsometric characterisation of thin films non-uniform in thickness. *Thin Solid Films* **519**, 2715-2717, doi:10.1016/j.tsf.2010.12.065 (2011).

25 Birkholz, M. *Thin Film Analysis by X-Ray Scattering*. (Wiley-VCH, 2006).

26 Burriel, M. *et al.* Influence of the Microstructure on the High-Temperature Transport Properties of $GdBaCo_2O_{5.5+delta}$ Epitaxial Films. *Chem. Mat.* **22**, 5512-5520, doi:10.1021/cm101423z (2010).

27 Ramana, C. V. *et al.* Enhanced optical constants of nanocrystalline yttrium oxide thin films. *Appl. Phys. Lett.* **98**, doi:10.1063/1.3524202 (2011).

28 Kiessig, H. Untersuchungen zur Totalreflexion von Röntgenstrahlen. *Annalen der Physik* **402**, 715-768, doi:10.1002/andp.19314020607 (1931).

29 Kiessig, H. Interferenz von Röntgenstrahlen an dünnen Schichten. *Annalen der Physik* **402**, 769-788, doi:10.1002/andp.19314020702 (1931).

30 X'Pert Reflectivity v. 1.1 (PANalytical B. V. , Almelo, The Netherlands, 2004).

31 Binnig, G., Quate, C. F. & Gerber, C. Atomic Force Microscope. *Physical Review Letters* **56**, 930-933 (1986).

32 Technologies, A. 127 (2012).

33 Fleig, J. *et al.* Thin film microelectrodes in SOFC electrode research. *Fuel Cells* **6**, 284-292, doi:10.1002/fuce.200500209 (2006).

34 Pennycook, S. J. *et al.* Transmission Electron Microscopy: Overview and Challenges. *AIP Conference Proceedings* **683**, 627-633, doi:doi:http://dx.doi.org/10.1063/1.1622537 (2003).

35 Kuzmany, H. *Solid-State Spectroscopy: An Introduction*. (Springer, 1998).

36 Irvine, J. T. S., Sinclair, D. C. & West, A. R. Electroceramics: Characterization by Impedance Spectroscopy. *Advanced Materials* **2**, 132-138, doi:10.1002/adma.19900020304 (1990).

37 Duncan, T. in *Advanced Physics* (John Murray, 1995).

38 Evgenij Barsoukov, J. R. M. in *Impedance Spectroscopy Theory, Experiment, and Applications* (Wiley and Sons, 2005).

Chapter 3: Neodymium Barium Cobalt Oxide

3.1 Introduction

Recent experimental and theoretical studies have highlighted the potential of layered oxides, such as those of A-site layered perovskite oxides $LnBaCo_2O_{(5+\delta)}$ (Ln = lanthanide), as candidate materials for intermediate temperature solid oxide fuel cell (IT-SOFC) cathodes. $LnBaCo_2O_{(5+\delta)}$ has been extensively studied in the literature where Ln = Gd, Pr.[1-5] The crystal structure of the $LnBaCo_2O_{(5+\delta)}$ series of oxides is classified as a double perovskite structure $AA'B_2O_{(5+\delta)}$ (where A = Ln, A' = Ba and B = Co). In this structure (see Figure 3.1(b)) the Ba and Ln cations are ordered in alternating BaO, CoO_2, and LnO layers along the *c*-axis, and the oxygen non-stoichiometry is limited to the LnO layers.

The A site cation ordering in these double perovskites $LnBaCo_2O_{(5+\delta)}$ (Ln = lanthanide) (Figure 3.1(b)) creates high ionic mobility for oxide anions within the Ln-containing anion vacancy layers, resulting in highly anisotropic oxide anion conductivity in crystals[1] and thin films.[6-9] The A site ordering strategy thus creates anisotropic materials with properties that would be suitable for enhancement through oriented growth in thin film as opposed to bulk ceramic form.

Neodymium barium cobalt oxide (NBCO) is an example of a double perovskite material and can be found in multiple forms depending on the degree of cationic/oxygen vacancy order. NBCO is a mixed electronic/ionic conductor and is a potential cathode material for solid oxide fuel cells (SOFCs). In Figure 3.1, the structure of the disordered perovskite (a) and the ordered perovskite (b) are

shown. The lattice parameters of the single pseudocubic perovskite unit are simply ($a_p/a_p/a_p$) as is also the case with the disordered bulk structure. The ordered NBCO bulk structure, however, is described as ($a_p/a_p/2a_p$) *i.e.* a doubling of the lattice parameter in the *c* direction.[10]

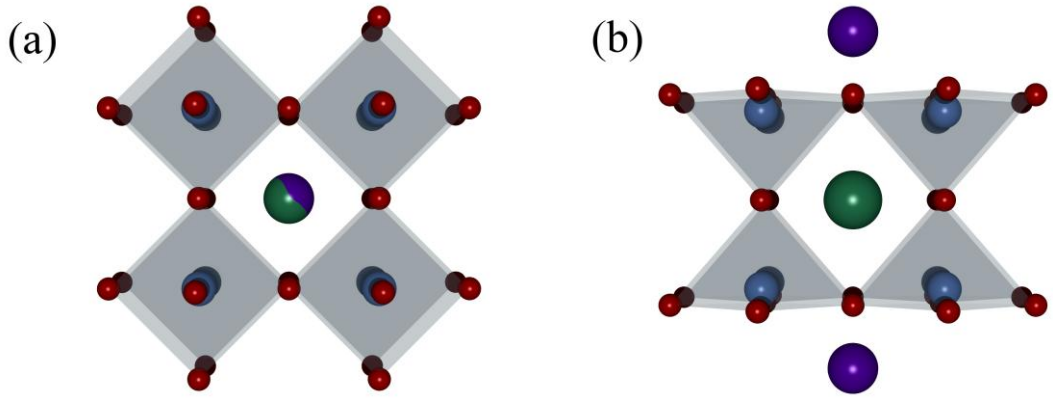

Figure 3.1: Structural depiction of (a) random occupancy of cation site indicated by mixed colour central atom, the disordered perovskite $NdBaCo_2O_5$, (b) the ordered double perovskite $NdBaCo_2O_5$. Nd in purple, Ba in green, Co in blue and O in red.

The NBCO structure can be disordered with respect to the A site cations, neodymium or barium, and with respect to the oxygen vacancies. Ordering of the NBCO structure occurs when the oxygen vacancies order, leaving oxygen in a square pyramidal rather than octahedral coordination around the B site cation, cobalt, as shown in Figure 3.1(b).

The growth of NBCO has been previously reported by Grygiel *et al.*[10] NBCO films were deposited on (001)-STO substrates to favour a low lattice mismatch of less than 1%. Grygiel *et al*. discuss the spiral growth of NBCO, and studied the

differences between conventional PLD and interval deposition. The spiral growth mechanism was investigated by Frank in 1949.[11-13] Spiral growth is caused by the presence of screw dislocations; when one screw dislocation is observed at the centre of the face then the film will grow up as in a spiral staircase. However if two screw dislocations are present then right handed and left handed spirals can occur. 2D growth processes are observable as the film thickness increases and the spirals coalesce. In addition to NBCO observing this spiral growth mechanism,[10] superconductor cuprates such as $YBa_2Cu_3O_{(7-\delta)}$ (YBCO) have been previously reported to exhibit this growth mode.[14]

Conventional deposition can be described as the laser pulsing continuously at the set frequency for a set number of pulses. In interval deposition one monolayer of the film is deposited as rapidly as possible by using a high pulse rate (20Hz), this is followed by a pause in the deposition to allow crystallisation of the monolayer. The process is then repeated to build up the required thickness. Grygiel *et al*. also report that the substrate temperature and the laser energy are critical for the formation of the ordered perovskite.[10] These growth conditions formed the base for this study using the Nano PVD system instead of the Neocera, as used by Grygiel *et al.*[10]

3.2 Growth Optimisation

3.2.1 PLD Target Preparation

The synthesis of neodymium barium cobalt oxide has been previously reported in the literature.[15,16] A pre-existing NBCO target prepared by Dr. Clara Grygiel[10]

was utilized as a comparison point for my synthesis. A new $NdBaCo_2O_{(5+\delta)}$ (NBCO) target was synthesized *via* a conventional solid state reaction from high purity (> 99.99%) precursors of Nd_2O_3,[17] $BaCO_3$ [18] and Co_3O_4 [19] in stoichiometric ratios with the reaction undertaken in a box furnace with re-grinding and sintering. X-ray phase ID was obtained at each step (Figure 3.2) as a check for reaction completion. The reaction was deemed complete when no starting material peaks were present in the pattern. Once the target was phase pure as determined by the X-ray diffraction (XRD) pattern it was pressed into a pellet. The pellet was then isostatically pressed to increase its density before sintering. A density of 85% was achieved as measured by an Archimedean balance.

Figure 3.2 shows XRD patterns from the different synthesis stages for the NBCO powder, leading up to the point where the powder was phase pure and thus able to be pressed into the pellet. The pattern in Figure 3.2 (a) shows the preliminary annealing of the starting materials at 1000°C, pattern (b) is taken after a second sintering at 1000°C, and finally pattern (c) shows that the reaction has gone to completion after heating at 1100°C.

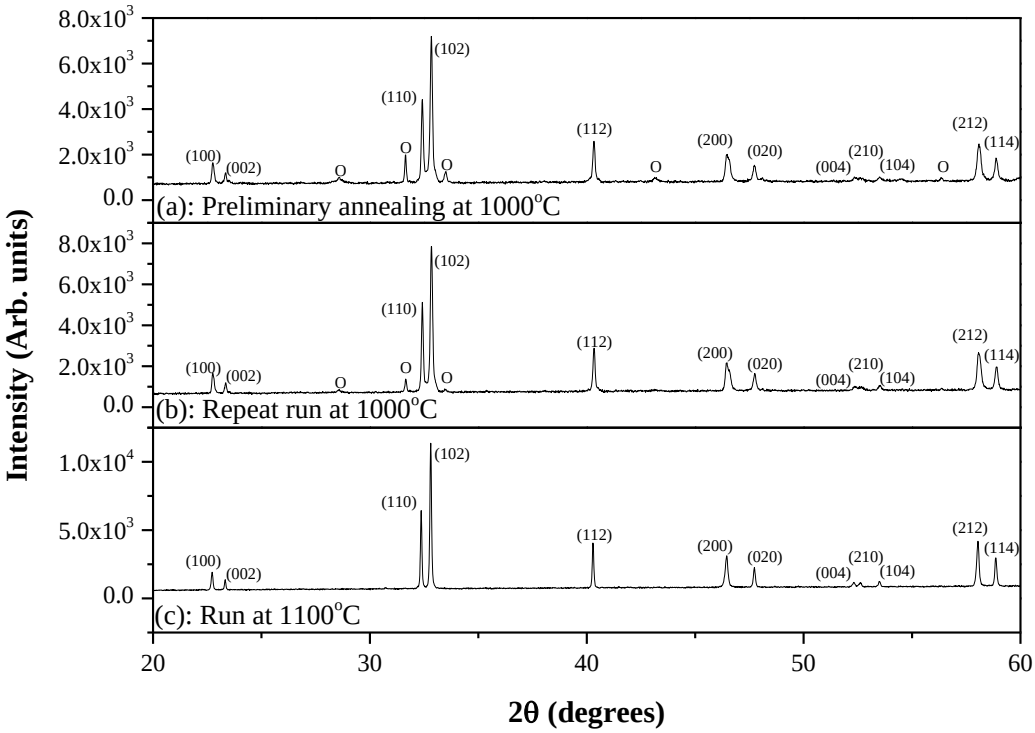

Figure 3.2: Synthesis of the NBCO powder, (a) with a preliminary annealing at 1000°C followed by (b) a repeat run at the same temperature, and (c) a final sintering at 1100°C. The (hkl) NBCO peaks are labeled, and o represents peaks from the starting materials.

Patterns (a) and (b) in Figure 3.2 have additional peaks that are attributed to the starting materials, indicating that the reaction was incomplete. In pattern (c) all of the peaks can be assigned to NBCO indicating that phase pure NBCO was achieved. The material was pressed into a pellet, isostatically pressed and sintered.

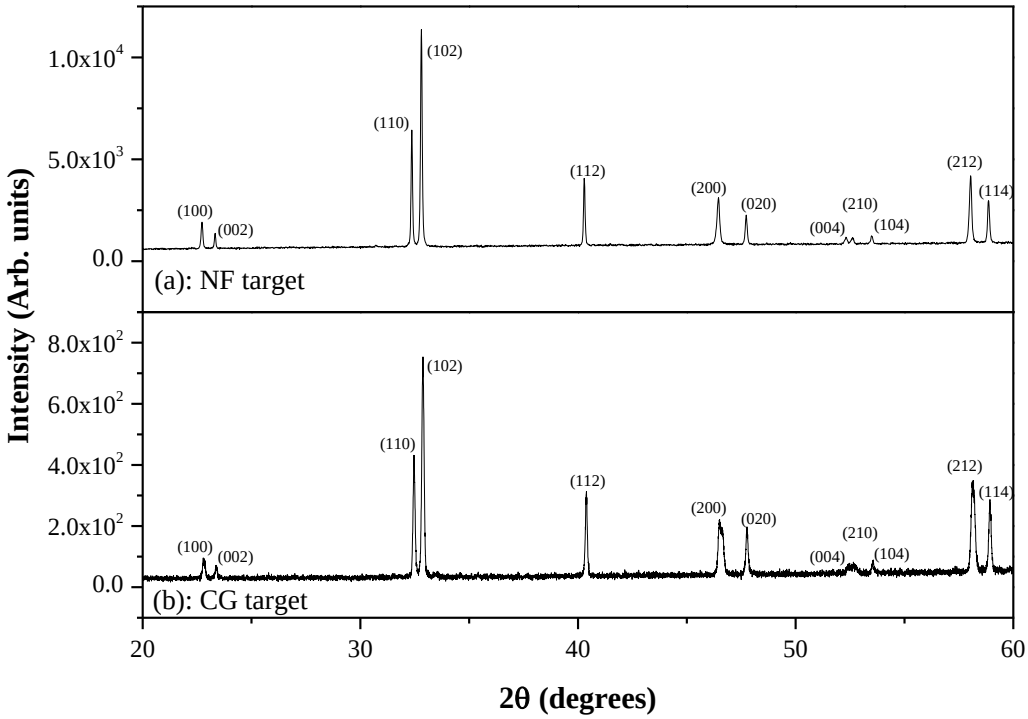

Figure 3.3: XRD comparison of NBCO target materials, (a) synthesised by myself and (b) synthesised by Dr. Clara Grygiel as a reference pattern.

Figure 3.3 shows that the composition of the NBCO powder is comparable to that of a previous target.[10]

Once the phase pure NBCO pellet had been isostatically pressed, it was therefore suitable for film growth. The target was polished prior to starting the initial film growth.

3.2.2 Optimising the Growth Conditions

Single crystal (001)-$SrTiO_3$ (STO) substrates were used for thin film growth of NBCO. Before the substrates were used they were prepared in the manner detailed in section 2.2.2.

Following on from Dr. Clara Grygiel's work,[10] films of NBCO were deposited on the STO substrate under the following conditions. Optimal conditions are shown in Table 3.1, with a substrate temperature of 850°C, a laser energy of 195mJ, a frequency of 4Hz and with an oxygen partial pressure of 1mTorr at a flow rate of 20 standard cubic centimeters per minute (SCCM).

Table 3.1: Optimal NBCO deposition conditions to allow for (00l) oriented NBCO films

Growth conditions	Ordered NBCO	Disordered NBCO
Growth temperature (°C)	850	700
Laser energy (mJ)	195	195
Frequency (Hz)	4	4
pO_2 (mTorr)	1	1

By keeping the deposition conditions the same, except from the temperature, it was possible to change the state of order. By changing the temperature from 850°C to 700°C it was possible to change the NBCO structure from an ordered, to a disordered state. The intention for this work was to achieve an ordered NBCO film. From the XRD pattern in Figure 3.4 (a) the series of 00*l* reflections confirms highly oriented growth of the NBCO film was achieved. For comparison an XRD pattern for disordered NBCO is shown in Figure 3.4 (b). The slight bulge seen at approximately 38° in Figure 3.4 (b) may be attributed to a (003) response from partially ordered areas of the film, or diffuse scattering.

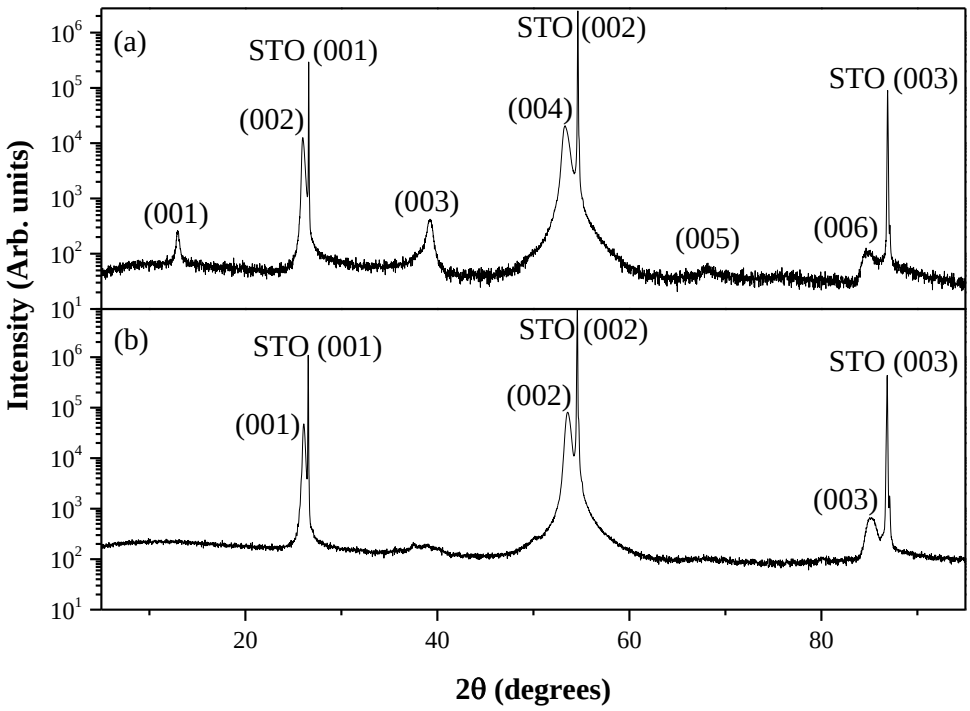

Figure 3.4: Typical XRD patterns of (a) ordered and (b) disordered NBCO films on STO.

3.3 Structural Characterisation

3.3.1 XRR

In addition to the XRD patterns further analysis was carried out on the NBCO films including X-Ray reflectivity (XRR). XRR was utilised to determine the thickness of the films using a Philips X'Pert diffractometer.

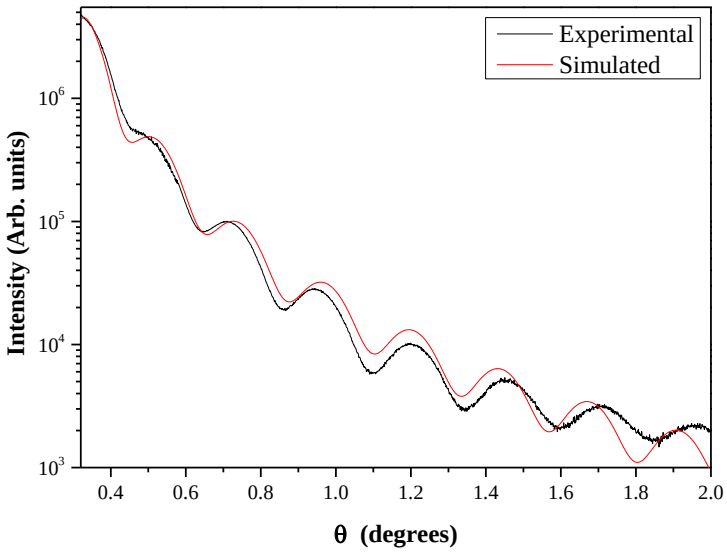

Figure 3.5: XRR of a typical ordered NBCO film on STO, grown at 850°C.

Fitting the oscillations of the XRR shown in Figure 3.5 gives an average thickness of 16.51nm, and therefore a deposition rate of 57.6 pulses per monolayer.

3.3.2 AFM

Atomic force microscopy was used in AC-AFM mode to analyse the topography of the surface of the NBCO films. An Agilent 5600LS Scanning Probe Microscope was used for this. All of the scales on the AFM images in this work are truncated so as to clearly show the surface of the films. There are large artefacts present on the images which are attributed to dirt, and if the images were focused on these, then the surfaces of the films would be obscured.

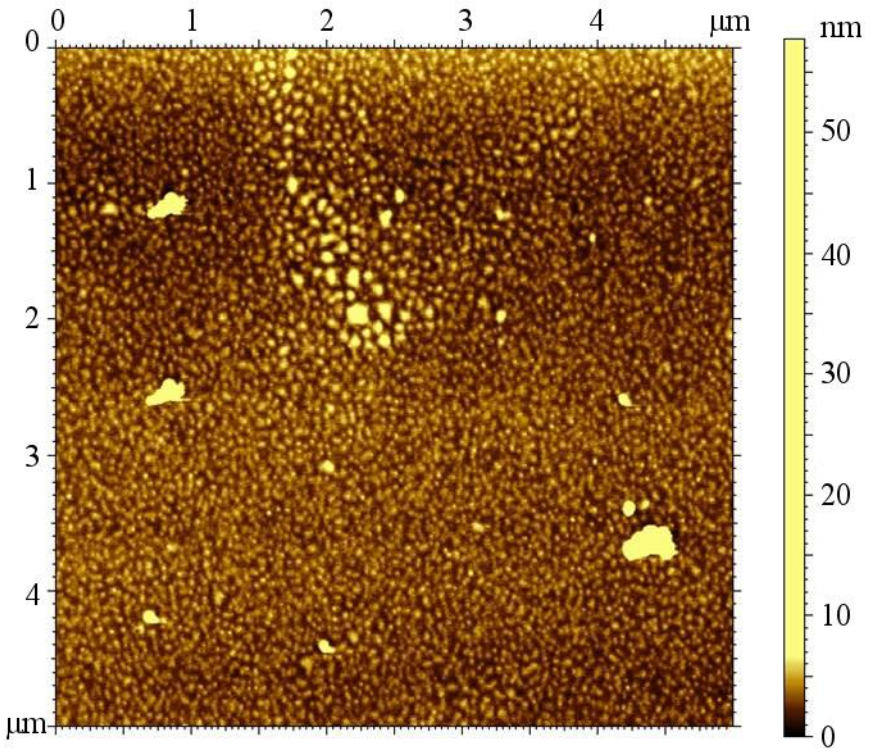

Figure 3.6: AFM topography image of an NBCO film grown at 850°C with a total film thickness of 16.5nm, and a RSM = 2.14nm.

The AFM topography data in Figure 3.6 shows that the NBCO has a root mean squared (RMS) roughness of 2.14nm, which is quite rough considering the film has a total thickness of 16.5nm and a unit cell of 3.8Å.

3.4 Thermal Stability

When performing the alternating current (AC) conductivity measurements, the film composition and morphology was found to change. Thermal stability tests were performed to determine if this change was attributable to the temperature (600°C) used in the AC impedance measurements. The changes in the NBCO film

after AC impedance measurements can be seen both in the SEM images in Figure 3.7 and in the XRD patterns in Figure 3.8. The changes were so drastic they were even evident with the naked eye (Figure 3.7 insets) as the film changed from its characteristic dark colour (a) to a very pale one (b).

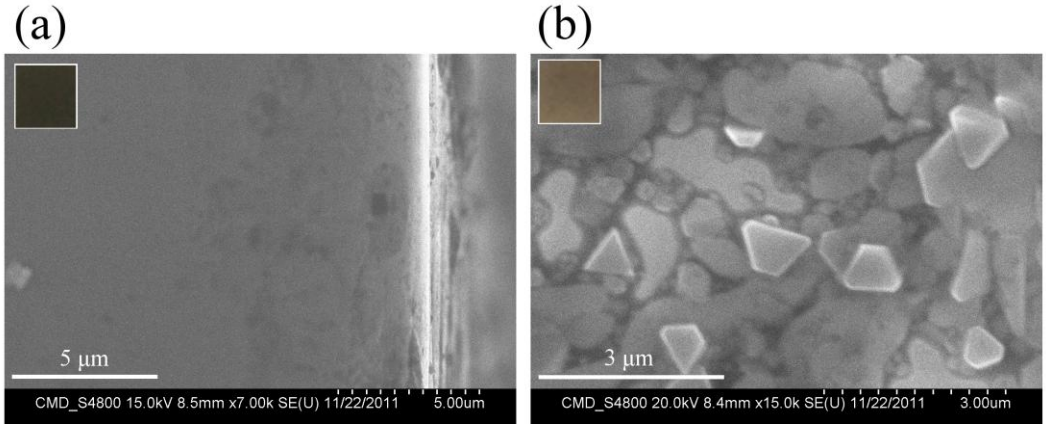

Figure 3.7: SEM images by Dr. Ruth Sayers, at the University of Liverpool, corresponding to (a) the as deposited NBCO film on STO and (b) the film after impedance. Photographs of the respective surfaces are inset in the top left of each SEM image.

From Figure 3.7 the difference between the images is clear, with the film no longer being uniform, and with the formation of separate microstructures after impedance.

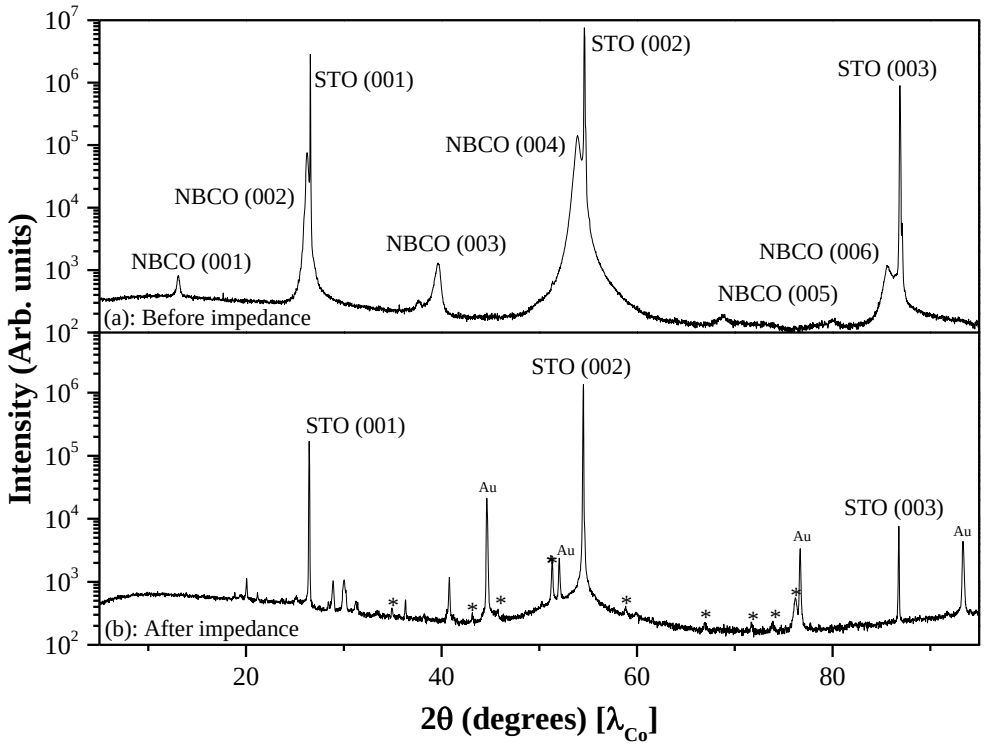

Figure 3.8: XRD pattern of the NBCO film (a) before and (b) after AC impedance analysis. The * represents the holder peaks, Au is from the gold contacts, and the STO and NBCO peaks are also labelled with the relevant *hkl*.

Clearly from Figure 3.8 the stability of the NBCO film needed to be investigated, as the ordered NBCO peaks have been lost. The NBCO film has degraded into Nd_2O_3 [17] (which is ordered on the substrate), $CoNd_2O_4$ [20] (which is a Ruddleson-Popper phase and is also ordered on the substrate) and $BaCO_3$.[18]

Following on from this result further tests were carried out. An NBCO film (film A) was cut into quarters, using a diamond tipped pen, to test the stability of the NBCO film in air at 400°C, 500°C and 600°C. The films were heated and cooled at a rate of 3°Cmin^{-1} and dwelled at temperature for 90 minutes. Figure 3.9 shows

the XRD patterns of these films after annealing at temperature. From this figure it can be seen that NBCO was not stable above 500°C in air, as at 500°C it is possible to observe the shift of the NBCO peak from the left of the STO (002) peak to the right of the STO (002) peak, between (b) and (c).

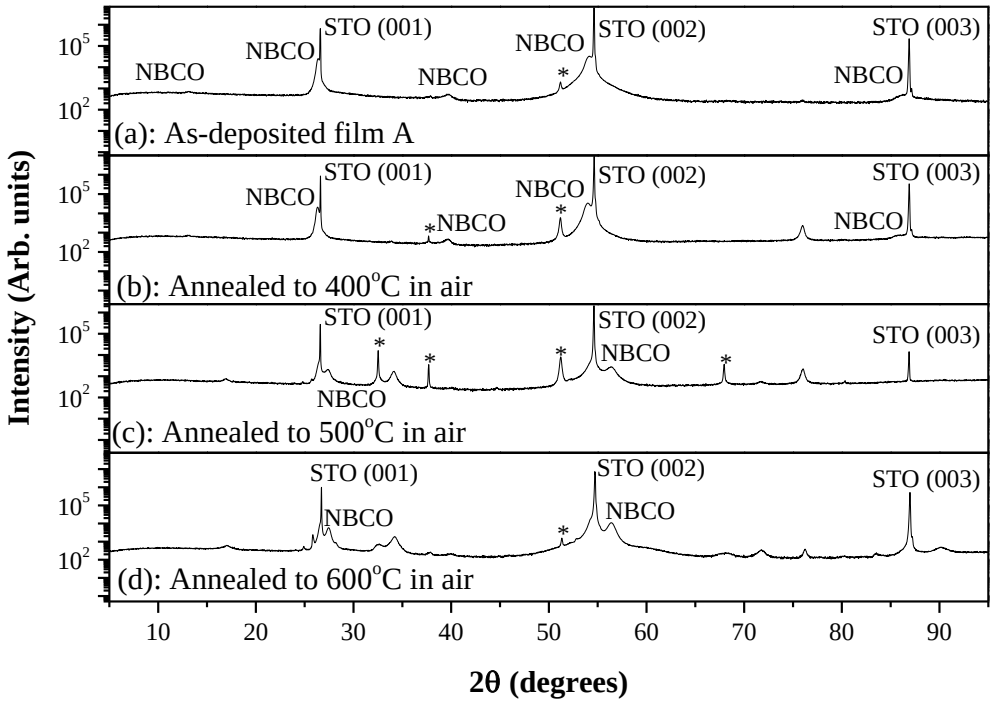

Figure 3.9: XRD pattern of the NBCO film (a) as-deposited, and then annealed in air at (b) 400°C, (c) 500°C and (d) 600°C respectively. The * indicates peaks attributed to the sample holder.

The stability of NBCO was tested in different atmospheres using a second NBCO film (film B). This film was cut into quarters and the films were annealed at 600°C in oxygen, nitrogen, and one was annealed in the PLD chamber with an oxygen pressure of 150Torr. The films were heated and cooled at a rate of

3°Cmin^{-1} and were dwelled at temperature for 90 minutes. XRD patterns following annealing are shown in Figure 3.10.

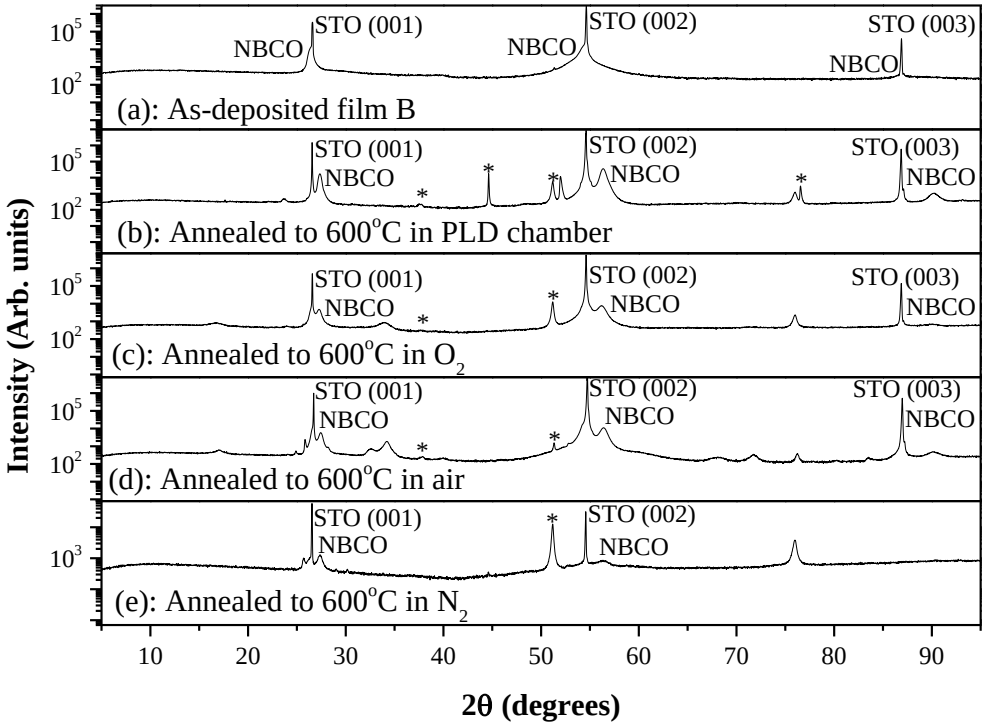

Figure 3.10: XRD pattern of the NBCO film (a) as-deposited, and then annealed at 600°C in (b) the PLD chamber, (c) oxygen, (d) air and (e) nitrogen. The * represents peaks attributed to the sample holder.

From Figure 3.10 (c), (d) and (e) it can be seen that NBCO was not stable in air, nitrogen or oxygen, and so the film was then tested in the PLD chamber. Testing the stability in the PLD chamber allowed the film to be pumped under vacuum, removing the gasses, with oxygen then added to the chamber at a pO_2 of 150Torr, equal the partial pressure of oxygen in the atmosphere. In this environment the

NBCO film was stable, see Figure 3.10 (b), suggesting that carbon dioxide reacting with the Ba was responsible for the decomposition. This highlighted the sensitivity of the NBCO to the carbon dioxide. When the film was found to be unstable under oxygen atmospheres (Figure 3.10(c)) it is supposed that the seal may not have been fitted tightly enough allowing some CO_2 to be present. Alternatively the oxygen may not have been flowing through the furnace sufficiently long enough before the heating began to remove all the air.

3.4.1 Effect of Oxygen Content

Having performed the stability measurements, lattice parameters were calculated for the NBCO films as deposited and after annealing. Table 3.2 shows cell volumes related to the change in oxygen content of the films from the literature, and volumes from two as deposited films and associated stability testing.

Table 3.2: Cell volume calculated for both the literature and experimental data based on the *c* parameters and total strain to the STO substrate for a and b.

Conditions	**Cell volume ($Å^3$)**
Literature ($\delta = 0.18$)[21]	117.4
Literature ($\delta = 0.50$)[21]	116.6
Literature ($\delta = 0.62$)[21]	116.0
Literature ($\delta = 0.92$)[21]	115.7
As deposited (film A)	119.4
600°C air (film A)	115.4
500°C air (film A)	115.2
400°C air (film A)	120.2
As deposited (film B)	119.7
600°C in PLD chamber (film B)	115.5
600°C in nitrogen (film B)	115.4

The cell volume was calculated for both the literature and experimental data based on the *c* parameters and assuming total strain to the STO substrate for *a* and *b*. From Table 3.2 it can be seen that increasing the oxygen content decreases the cell volume. This decrease in overall cell volume occurs due to Co possessing a higher oxidation state, and therefore a smaller volume. Great variance in cell volume is seen in the annealed films.

3.5 SDC/ NBCO Multilayers

3.5.1 Motivation

Garcia-Barriocanal *et al.* reported on the colossal ionic conductivity at the interfaces of epitaxial yttria-stabilised zirconia (YSZ) and strontium titanate (STO) heterostructures. They report a high lateral ionic conductivity, showing up to eight orders of magnitude enhancement near room temperature, in YSZ/STO epitaxial heterostructures.[22] Their reasoning behind the increased conductivity was that the atomic reconstruction at the interface between highly dissimilar structures (such as fluorite and perovskite) provides both a large number of carriers and a high-mobility plane, yielding colossal values of the ionic conductivity. This publication brought about some controversy and a comment was published[23] claiming that the reported ionic conductivity lacks experimental support, and that the observed conductivity enhancement is most probably due to the p-type conductivity of STO. Garcia-Barriocanal *et al.* published a response[24] to this stating that their results show that any electronic contribution to the conductance is at least three orders of magnitude lower than the ionic contribution determined by AC methods. This debate lead to a significant increase in interest in measuring the conductivity of multilayer films. Here we investigate another perovskite fluorite multilayer to see if we can obtain a similar enhancement of our conductivity.

3.5.2 Growth Optimisation

3.5.2.1 SDC Optimisation

Samarium doped ceria, $Sm_{0.2}Ce_{0.8}O_{2-\delta}$, (SDC) has a fluorite structure, as illustrated in Figure 3.11, a bulk lattice parameter of 5.44Å,[25] and is a candidate electrolyte material for SOFCs. This material is ionically conducting due to the presence of oxygen vacancies. To maintain charge neutrality, one oxygen vacancy is created for every two Ce ions replaced with Sm ions.

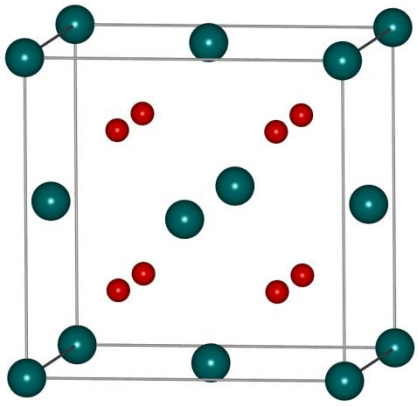

Figure 3.11: Fluorite structure - red spheres are oxygen and turquoise spheres are cations (e.g. Ce or Sm).

A SDC target was made using a commercially available powder (from fuel cell materials (FCM)); the powder was pressed into a pellet, isostatically pressed and then sintered at 1400°C for 10 hours. Isostatic pressing was used to increase the density of the target and the pellet was polished afterwards to provide a good surface for the laser to ablate. A density of 98% was achieved as measured by an Archimedean balance.

The growth of samarium doped ceria (SDC) on a single crystal strontium titanate (001) substrate (from PI-KEM) was optimised. Sanna *et al*. reported[25] the growth of SDC on MgO substrate buffered with a STO layer. Their conditions were used as a starting point for the growth of SDC epitaxially on STO. They found that the optimal growth conditions for achieving high-quality epitaxial SDC thin films on MgO with an STO buffer layer were the following: substrate temperature of 630°C and an oxygen pressure of $4x10^{-3}$mbar (equal to 3mTorr).[25]

The SDC deposition conditions were optimised to be as follows: temperature of 630°C, laser energy of 250mJ, a frequency of 5Hz, oxygen flow rate of 20sccm (standard cubic centimetres), and partial oxygen pressure of 1mTorr. However SDC also grows well at 850°C and as this temperature matches the conditions of the NBCO growth many of the multilayers included SDC grown at 850°C. SDC growth conditions for oriented (00*l*) films are summarised in Table 3.3.

Table 3.3: Optimal SDC deposition conditions to allow for (00l) oriented SDC films.

Growth temperature (°C)	600 - 850
Laser energy (mJ)	195
Frequency (Hz)	4 or 5
pO_2 (mTorr)	1 or 10

XRD spectra of films grown at 630°C and 850°C are shown in Figure 3.12.

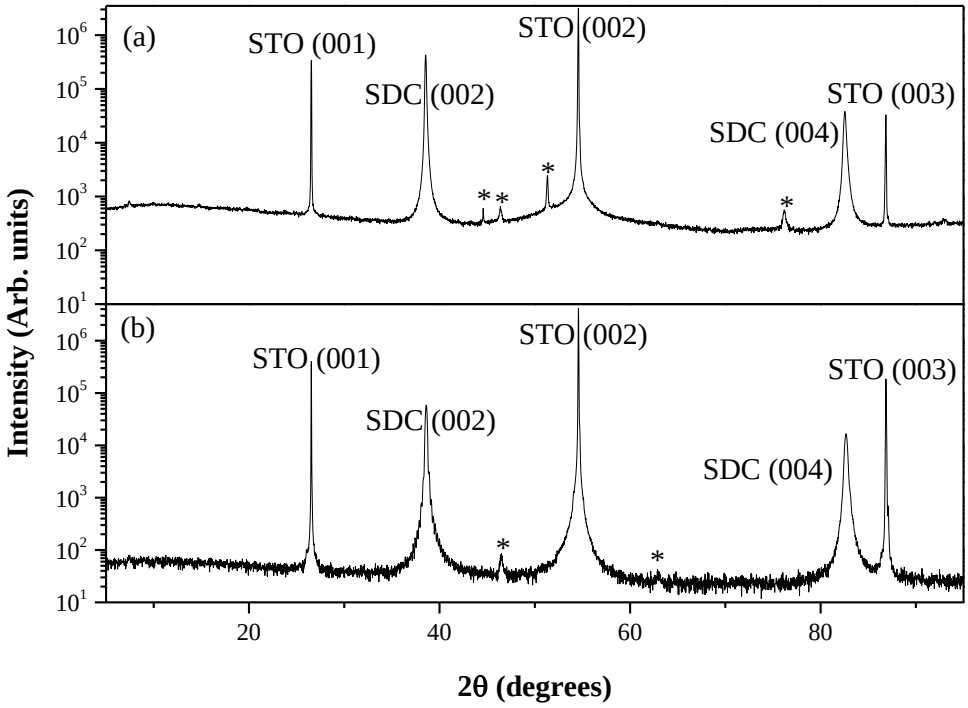

Figure 3.12: XRD of SDC grown in 1mTorr pO_2, at a low temperature of 630°C and at a higher temperature of 850°C. * represent the holder peaks.

From Figure 3.12 it can be seen that high purity SDC films can be grown at both 630°C and 850°C. The base of the STO (002) peak appears broader than that of the (001) and (003) reflections due to constructive and destructive interference. The average thicknesses of these films were obtained by fitting the oscillations from the XRR data, which can be found in Figures 3.13 and 3.14.

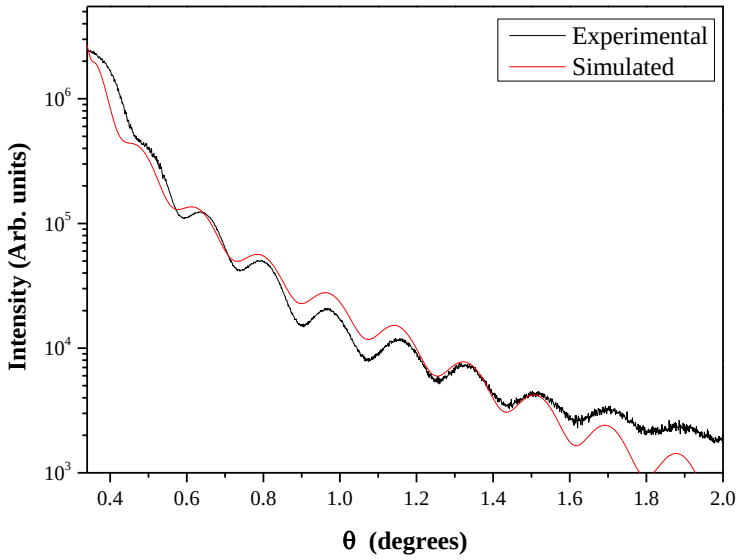

Figure 3.13: XRR of SDC on STO at 630°C grown in 1mTorr pO_2 .

From Figure 3.13 it can be seen that SDC deposited at 630°C has an average total thickness of 23.9nm. Figure 3.14 indicates that SDC deposited at 850°C has an average total thickness of 52.2nm.

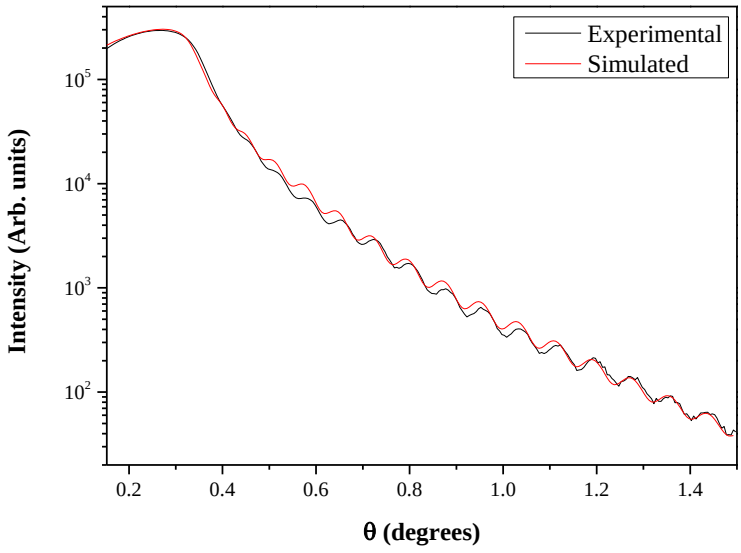

Figure 3.14: XRR of SDC on STO at 850°C grown in 1mTorr pO_2.

Atomic force microscopy images of the SDC films at 630°C and 850°C are shown in Figure 3.15.

(a) (b)

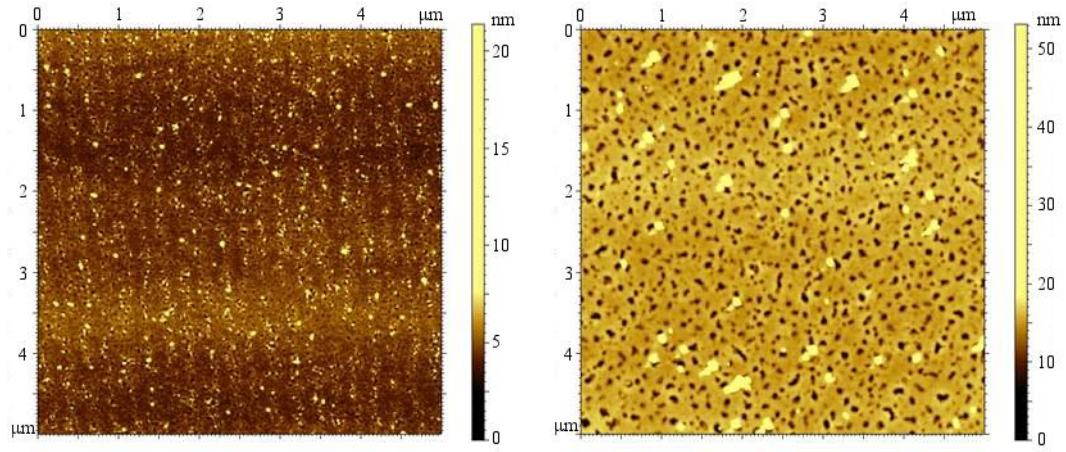

Figure 3.15: Atomic force microscopy topography images of SDC deposited on STO, in (a) at 630°C, and (b) at 850°C.

Figure 3.15 (a) shows the topography of SDC deposited at 630°C. The film has a root mean squared (RMS) value of 0.9nm, and an average total thickness of 23.9nm calculated from the XRR. Figure 3.15 (b) shows the topography of SDC deposited at 850°C. The film has a RMS of 2.8nm and an average total thickness of 28.8nm calculated from the XRR. Both Figure 3.15 (a) and (b) have regular small dark areas are present over the surface of the films, which suggests that pinholes may be present in the SDC films grown at either temperature.

3.5.2.2 Growth Rate Calibration

In order to calculate an accurate deposition rate, SDC was deposited at a temperature of 600°C, pO_2 of 1mTorr, laser energy of 195mJ, with a range of different pulse numbers from 1,000 pulses through to 10,000 pulses. Figure 3.16 shows XRR patterns from four different thicknesses of SDC film.

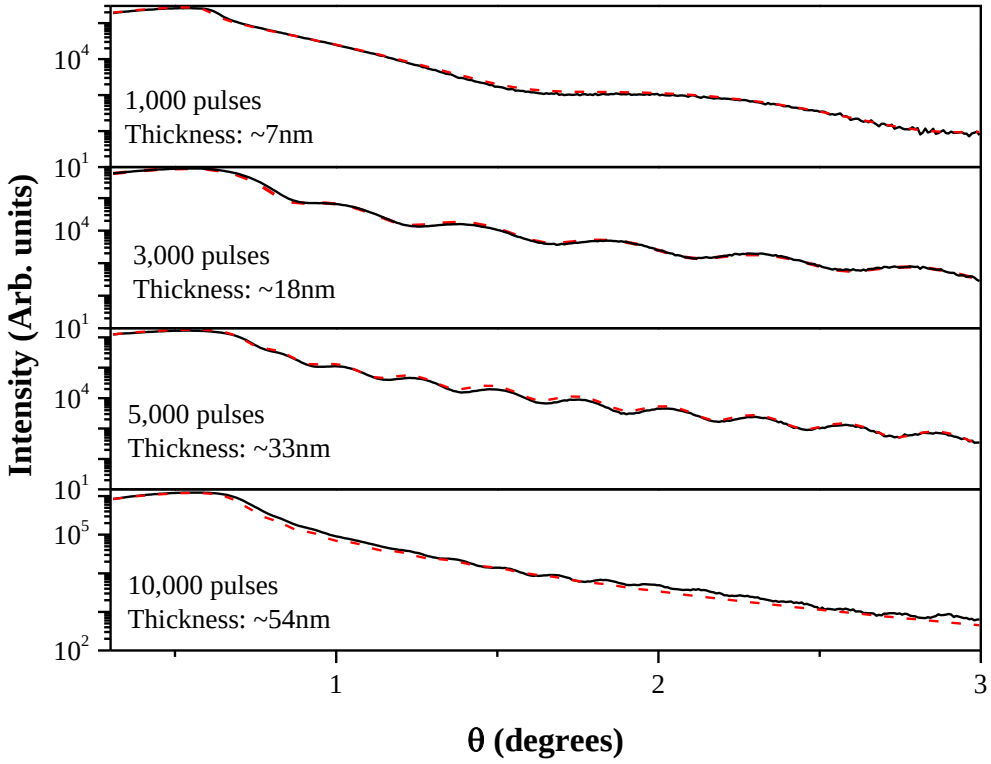

Figure 3.16: XRRs of SDC deposited with different numbers of pulses for a growth rate calibration. The simulated fits are shown in red dotted lines over the experimental data in black.

From the XRR data, one would expect that the number of oscillations increases as the films get thicker, which is observed in Figure 3.16. From this XRR data the film thicknesses are obtained and the thickness is plotted against the pulse number in Figure 3.17 to show if a linear deposition rate has been achieved.

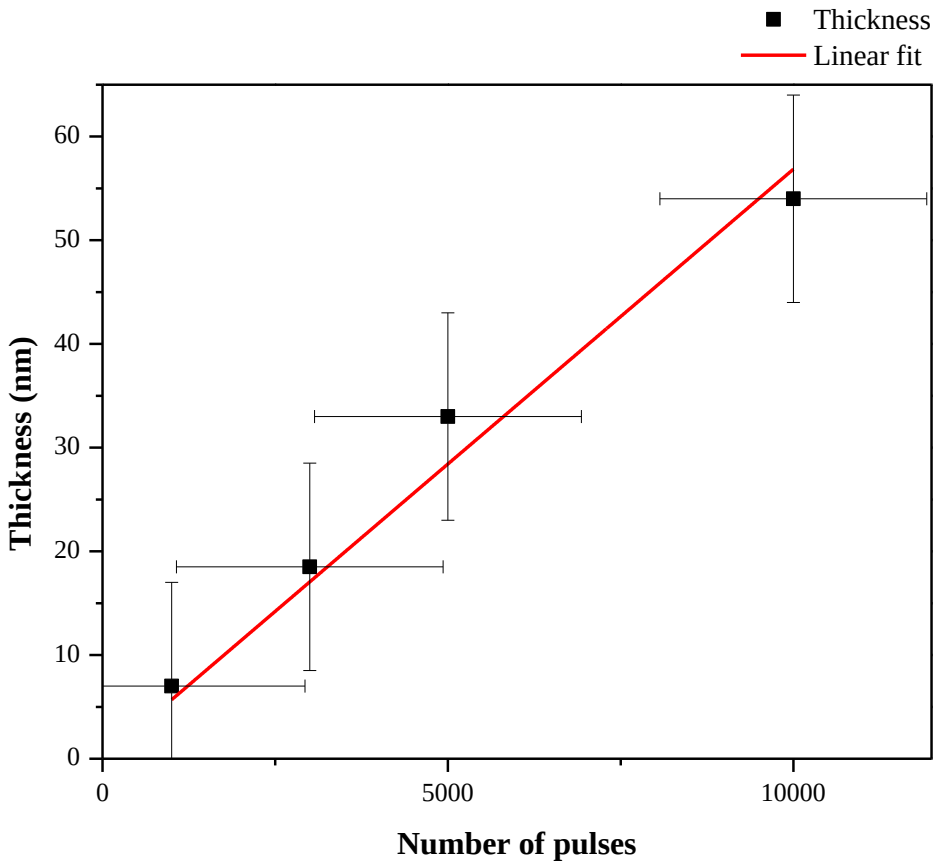

Figure 3.17: Growth rate calibration plot showing a deposition rate of 95 pulses/monolayer for SDC grown at 600°C, 195mJ, 5Hz, pO2 of 1mTorr, 5sccm. Standard error bars are shown

From the gradient of the plot in Figure 3.17 a deposition rate of 95 pulses per monolayer is calculated for the SDC growth.

In addition to optimising the SDC growth rate, the NBCO growth rate was also calibrated. NBCO films were deposited with a substrate temperature of 850°C, a laser energy of 195mJ, a frequency of 4Hz and with an oxygen partial pressure of

1mTorr at a flow rate of 20 standard cubic centimeters per minute (SCCM). Figure 3.18 shows three NBCO films grown to different thicknesses.

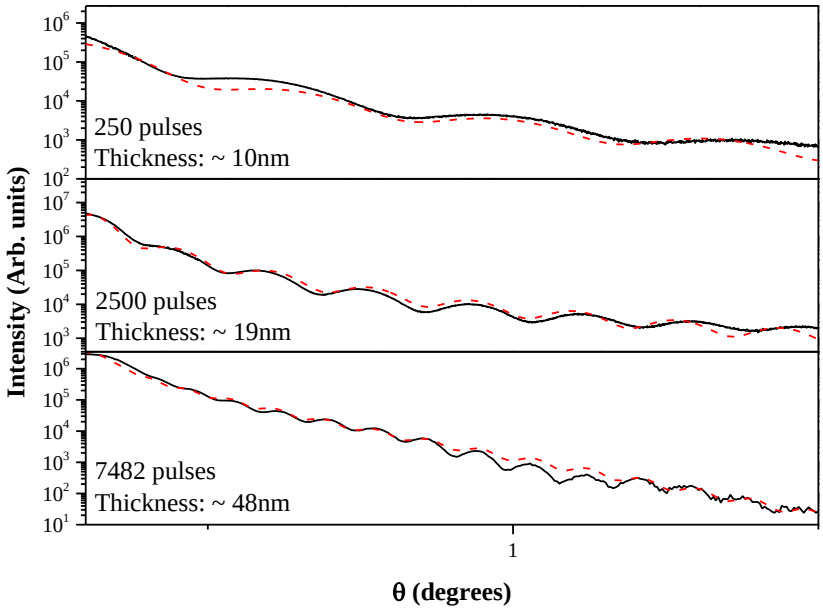

Figure 3.18: XRRs of NBCO deposited with different number of pulses for a growth rate calibration. The experimental data is shown in black with the simulated fits indicated by red dotted lines.

As with the SDC films shown in Figure 3.16, the NBCO films shown in Figure 3.18 also show increasing number of oscillations as the thickness increases. The thicknesses obtained from the simulated fits are plotted against the number of pulses in Figure 3.19 to obtain the deposition rate.

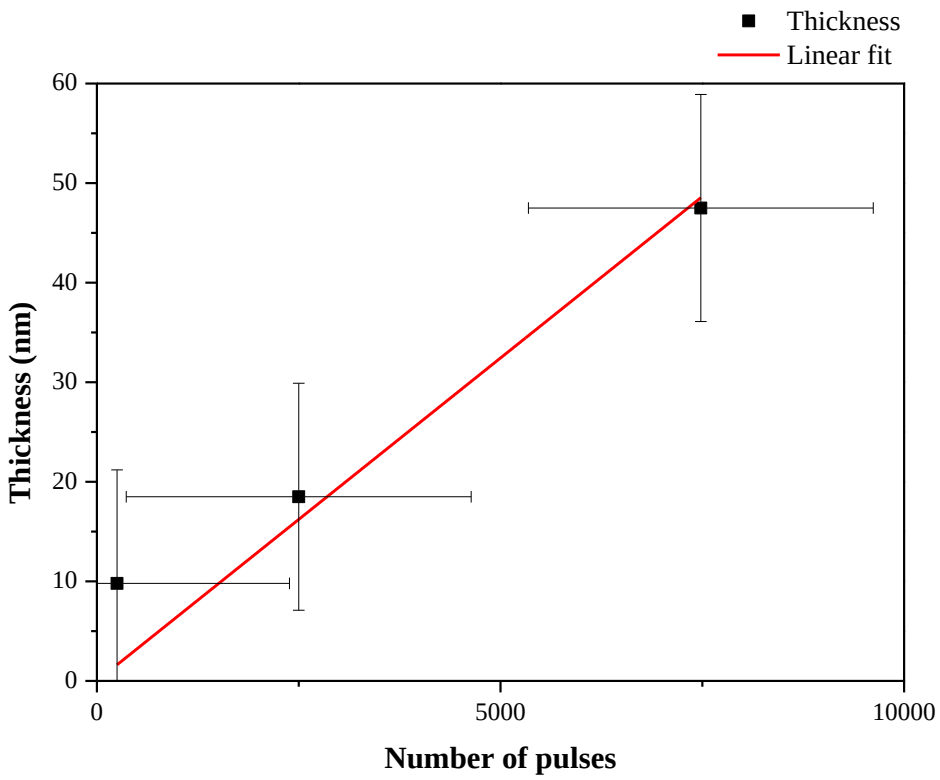

Figure 3.19: Growth rate calibration plot for the NBCO films, showing a deposition rate of 59 pulses per monolayer. Standard error bars are shown.

The deposition rate for the NBCO films was obtained from the gradient of the plot in Figure 3.19 to be 59 pulses per monolayer.

3.5.5 SDC/NBCO Bilayer Films

Having optimized the growth of SDC and NBCO, bilayers were deposited. NBCO was grown on top of an SDC layer which was itself grown on an STO substrate forming the bilayer film. The growths were performed at 630°C for the SDC and

850°C for the NBCO, and with a laser frequency of 5Hz for the SDC and 4Hz for the NBCO. A laser energy of 252mJ was used, and an oxygen partial pressure of 1mTorr and a flow rate of 20sccm were used for both growths. The XRD pattern of a bilayer film is shown in Figure 3.20.

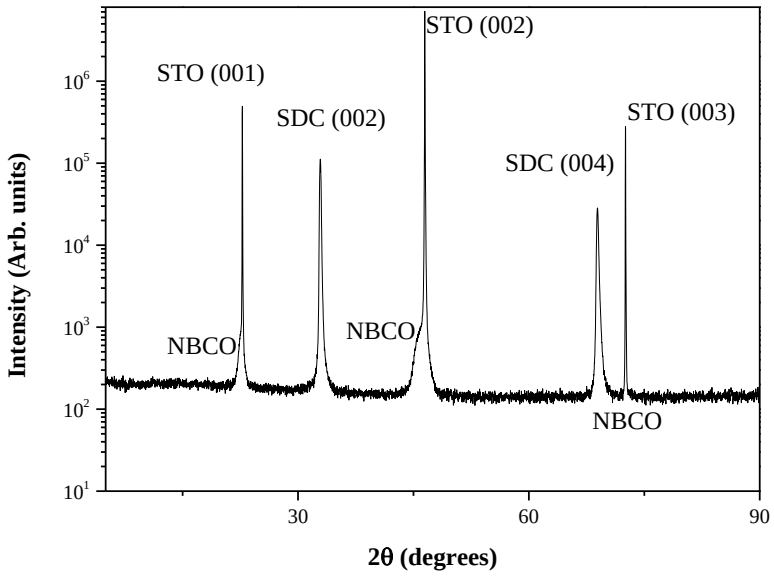

Figure 3.20: XRD pattern of the SDC, NBCO bilayer film.

The NBCO peaks in Figure 3.20 are viewable as shoulder peaks on the STO substrate. The SDC peaks have greater intensity compared to the NBCO peaks, possibly due to constructive interference between even (00*l*) responses, and also due to the NBCO responses being obscured by the substrate peaks. No impurity peaks are observed.

Phi scans were used to analyse a bilayer film, and can be seen in Figure 3.21.

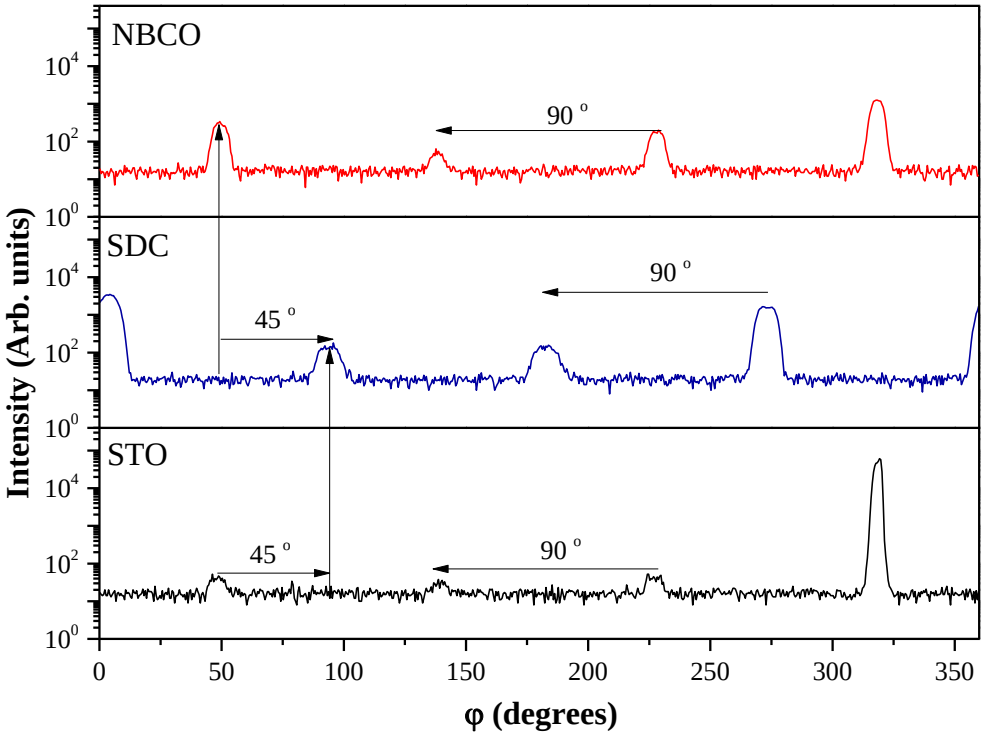

Figure 3.21: XRD phi scans around the (113) peak, indicating the epitaxial relationship of NBCO with respect to SDC and STO substrate.

These scans show that NBCO grows with a cube-on-cube relationship to the STO substrate, and SDC sandwiched between the two is rotated by 45°. The mismatch between the NBCO and SDC is:

$$m_{(SDC/NBCO)} = \frac{3.81 - 3.95}{3.95}$$

$$m_{(SDC/NBCO)} = -0.035$$

$$m_{(SDC/NBCO)} = -3.5\%$$

To further illustrate the structural relationship of how the STO, SDC and NBCO grow on top of each other Figure 3.22 shows a structural representation.

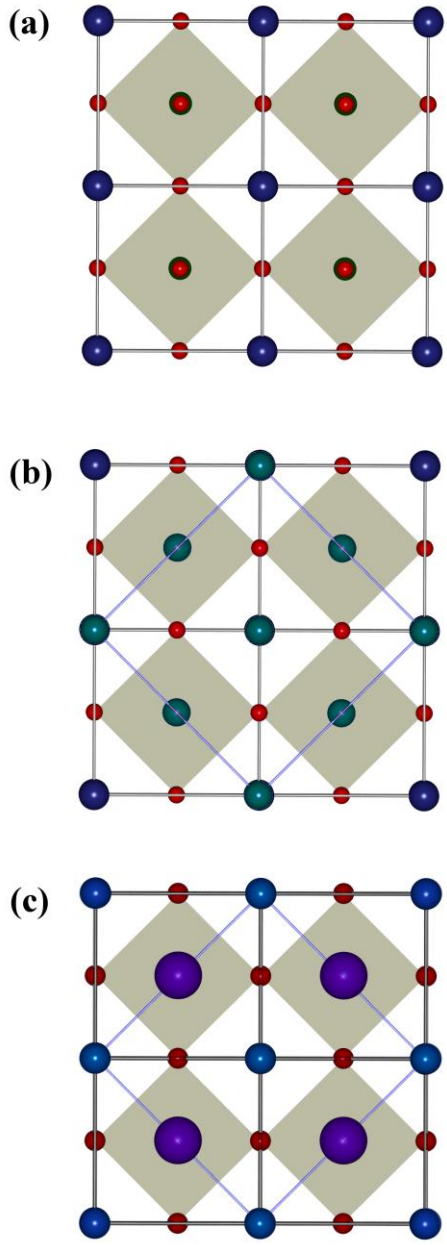

Figure 3.22 : (a) 4 unit cells of STO, (Sr in dark blue, Ti in dark green, O in red) (b) 1 unit cell of SDC over 4 unit cells of STO, grown at a 45° rotation (Sm/Ce in turquoise) (c) 1 unit cell of NBCO cube on cube to the original STO layer with the SDC layer in between. (Nd/Ba in purple, Co in light blue.)

3.5.6 SDC/NBCO Multilayers

A set of SDC/NBCO multilayers were grown with alternating blocks of 2nm, 5nm, 10nm and 15nm layers. These growths were all performed at 850°C, with a laser energy of 195mJ and with an oxygen partial pressure of 1mTorr and a flow rate of 20sccm. The laser had a frequency of 5Hz for the SDC growth and 4Hz for the NBCO growth. The 5nm multilayer was comprised of alternating layers, 5nm of SDC and 5nm of NBCO (on an STO substrate), stopping once the total film thickness reached 50nm. The 2nm multilayer had a total thickness of 48nm; the 10nm had a total thickness of 60nm as did the 15nm film.

A second 2nm multilayer system was also grown using different temperatures for the SDC and NBCO layers, with the SDC layer grown at 630°C while the NBCO was deposited at 850°C.

2nm multilayer films were grown at both 630°C and 850°C because the atomic force microscopy (AFM) images of the monolayer films indicated that SDC grew with a better surface roughness at 630°C, whereas it was only possible to grow the NBCO at 850°C. These AFM images were shown previously in sections 3.3.2 and 3.5.2.1, Figures 3.6 and 3.15 respectively.

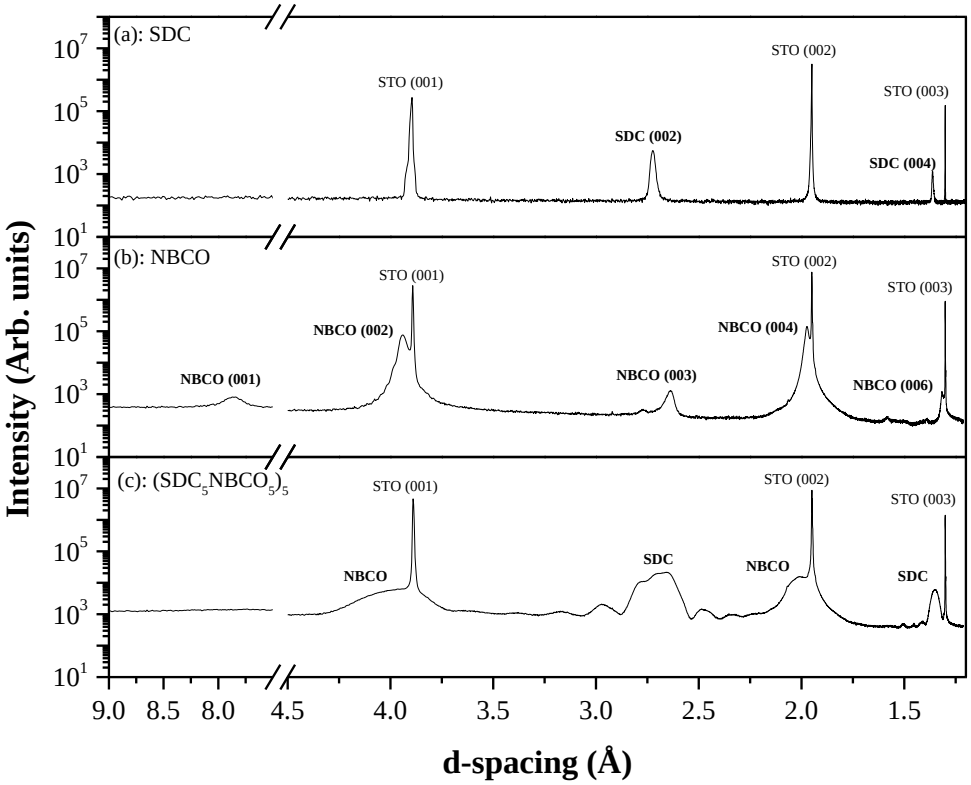

Figure 3.23: XRD patterns of (a) a single layer of SDC on STO, (b) a single layer of NBCO on STO, and (c) the 5nm multilayer of SDC and NBCO on STO.

From Figure 3.23 we can see that the multilayer film is of high quality as shown by the presence of Pendellosung fringes/satellite peaks around the SDC.

Dr. Robert Palgrave at the University of Liverpool simulated the 5nm multilayer film using DIFFaX,[26] and his results are plotted in Figure 3.24.

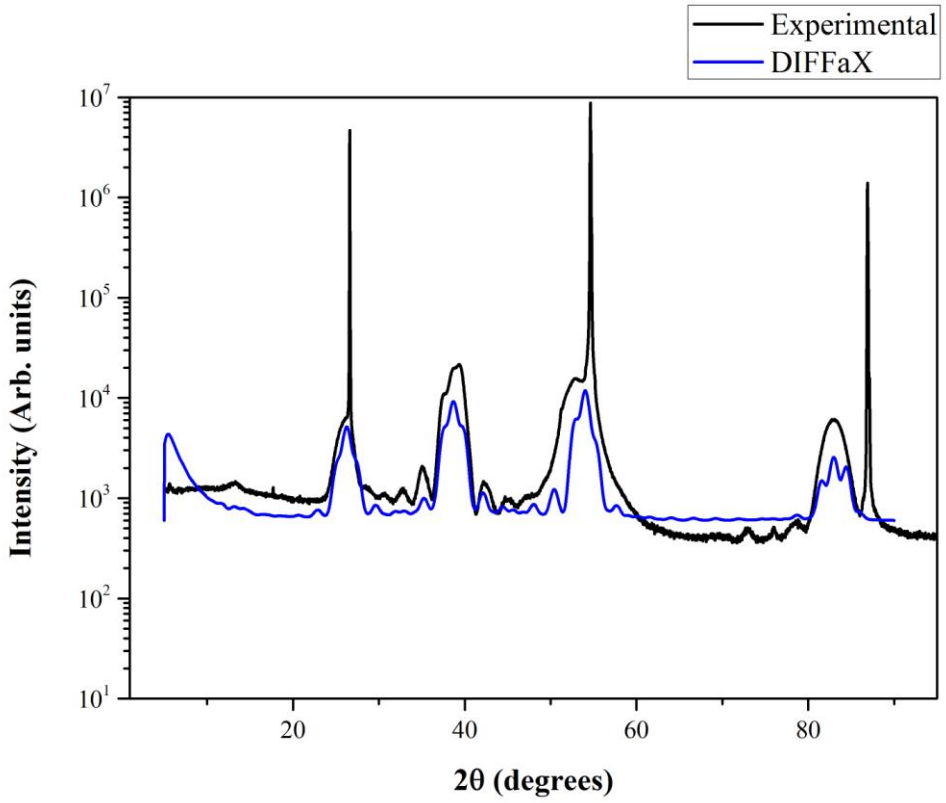

Figure 3.24: XRD pattern of the experimental data from the 5nm multilayer in black compared to Dr. Robert Palgrave's DIFFaX simulation in blue.

The DIFFaX simulation comprises SDC and NBCO multilayers, but does not take into account the STO peaks. The model used has 8 unit cells of SDC and 6.5 unit cells of ordered NBCO.

The complex shape of the diffraction peaks in a multilattice is due to the interference between X-rays diffracted from one SDC layer with those diffracted from the neighbouring layers. If the SDC layers were a constant distance apart, then they will always produce the same type of interference, leading to the same peak shape. However, if the SDC layers are not always the same distance apart,

they will produce lots of different interference patterns leading to a less well defined peak shape.

SDC layers being at constant distance apart implies that the NBCO layers are of constant thickness. Since the SDC peaks are well defined and the NBCO peaks much less so, this suggests that the NBCO layers are of constant thickness and the SDC layers are not. The uniformity of the layers has also been explored by transmission electron microscopy (TEM), and the results of this are discussed later in Section 3.5.9.

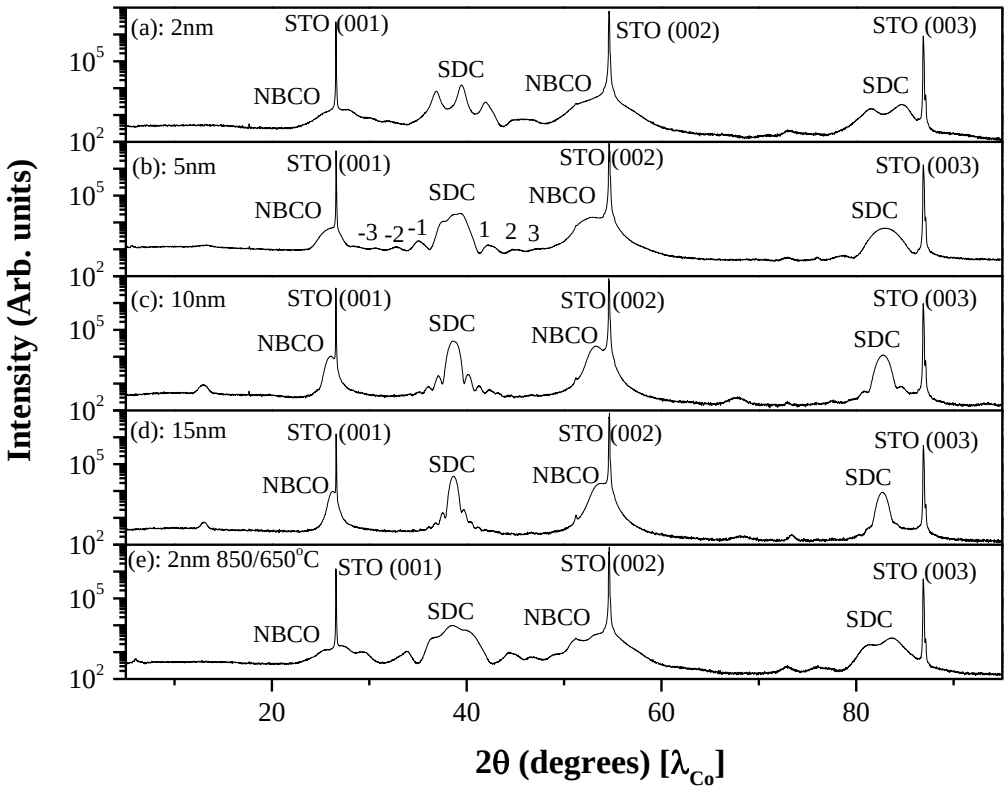

Figure 3.25: XRD of the set of multilayer films, (a) 2nm, (b) 5nm, (c) 10nm, (d) 15nm and (e) 2nm with NBCO deposited at 850°C and SDC deposited at 650°C.

The XRD patterns in Figure 3.25 show that as the periodicity of the multilayers changes, the position of the satellite peaks change as indicated in Figure 3.25 by -3,-2,-1 etc. The films with the smallest periodicity have broader peaks than those with higher periodicity. Also when comparing the 2nm films (a) and (e) the film deposited with the SDC at the lower temperature has broader SDC peaks. One might think that decreasing the temperature would result in a lower crystallinity, however from Dr. Robert Palgrave's work it was observed that the shape of the SDC peak was affected by the NBCO film quality and vice versa. We

might therefore conclude that depositing the SDC at the lower temperature has had an adverse affect on the growth of the NBCO films.

The multilayer films were analysed with atomic force microscopy (AFM), and representative topography images are shown in Figure 3.26.

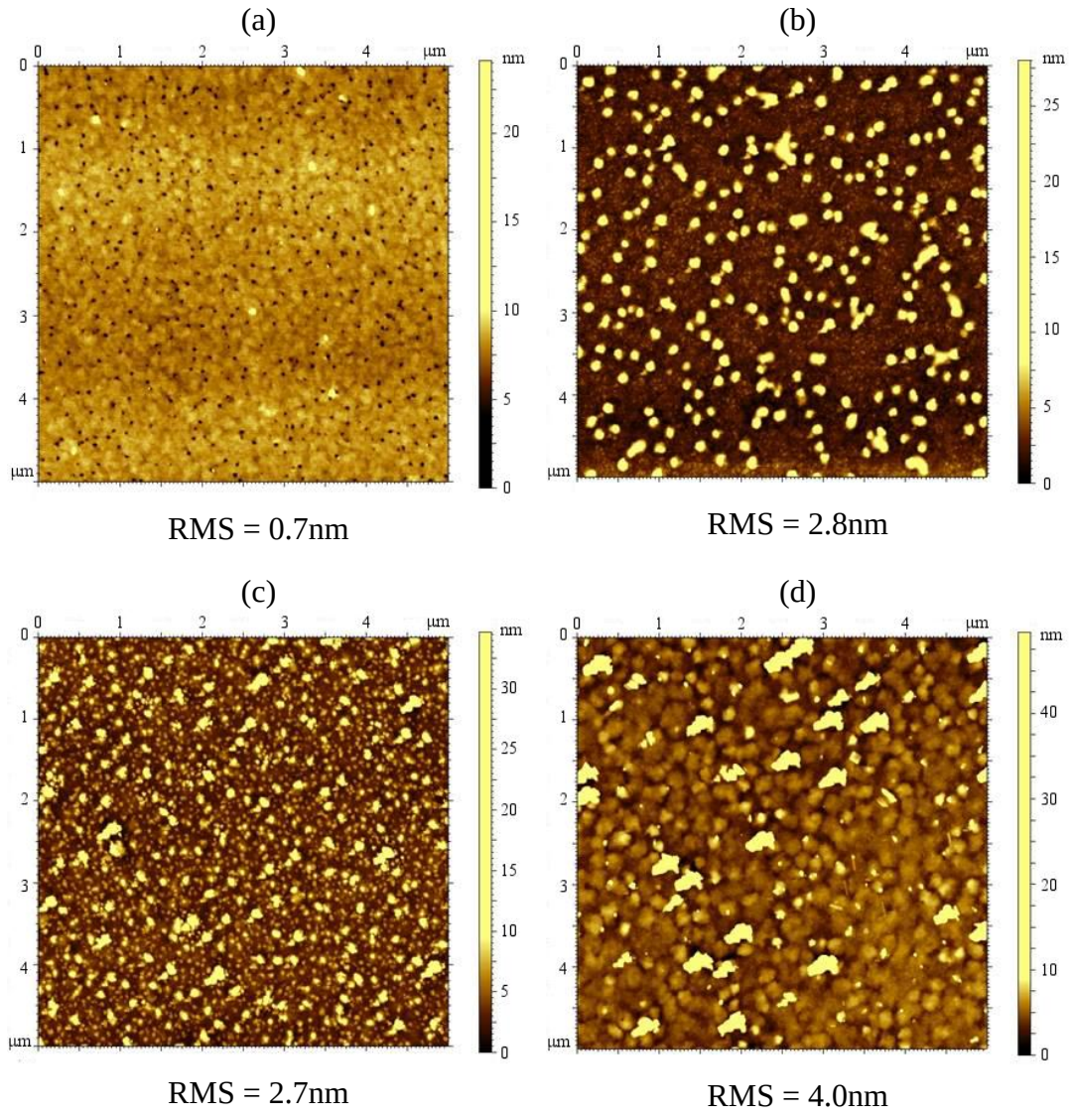

Figure 3.26: 5 x 5μm AFM scans of the multilayer films grown at 850°C, (a) 2nm layer thickness, (b) 5nm, (c) 10nm and (d) 15nm films.

From the AFM images and their associated root mean squared (RMS) values it can be seen in Figure 3.26 that the surface roughness increases as each film layer

increases from 2nm to 15nm, and therefore the periodicity of the multilayer films increases from 4nm to 30nm.

3.5.7 Structural Characterisation

X-ray reflectivity (XRR) was used to analyse the thickness of the multilayer films. The oscillations from the XRR can be attributed to both the total thickness of the multilayer film, and the periodicity of the film. The periodicity of the film is the total thickness of the repeating unit, so in the 2nm film where the SDC is 2nm and the NBCO is 2nm the periodicity would be 4nm. Theoretical XRR simulations were carried out to compare to the experimental data, and these are shown in Figure 3.27.[27]

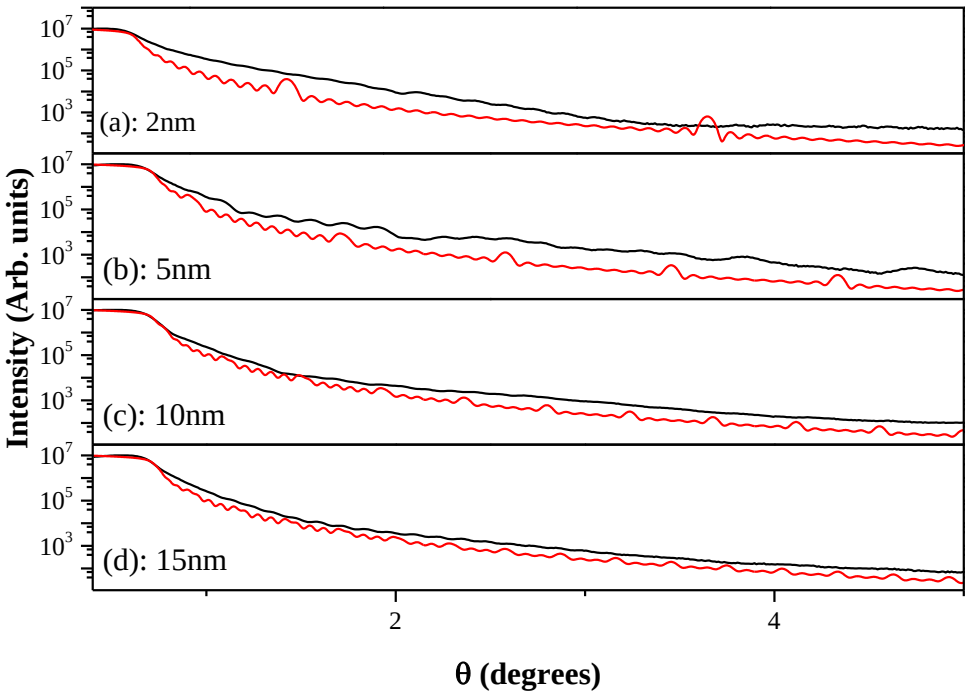

Figure 3.27: Experimental XRR patterns for multilayers of differing thickness shown in black and theoretical simulation in red of the XRR for multilayers of differing thickness; (a) 2nm layer thickness to give a total thickness of 48nm, (b) 5nm layer thickness to give a total thickness of 50nm, (c) 10nm layer thickness to give a total thickness of 60nm and (d) 15nm layer thickness to give a total thickness of 60nm.

The oscillations corresponding to the periodicity of the film are much more pronounced in the theoretical XRR data than the experimental data in Figure 3.27. It can be concluded that the simulations for the 2nm and 5nm multilayers fit better than the 10nm and 15nm multilayers and more detail for the 2nm and 5nm comparisons is shown in Figure 3.28.

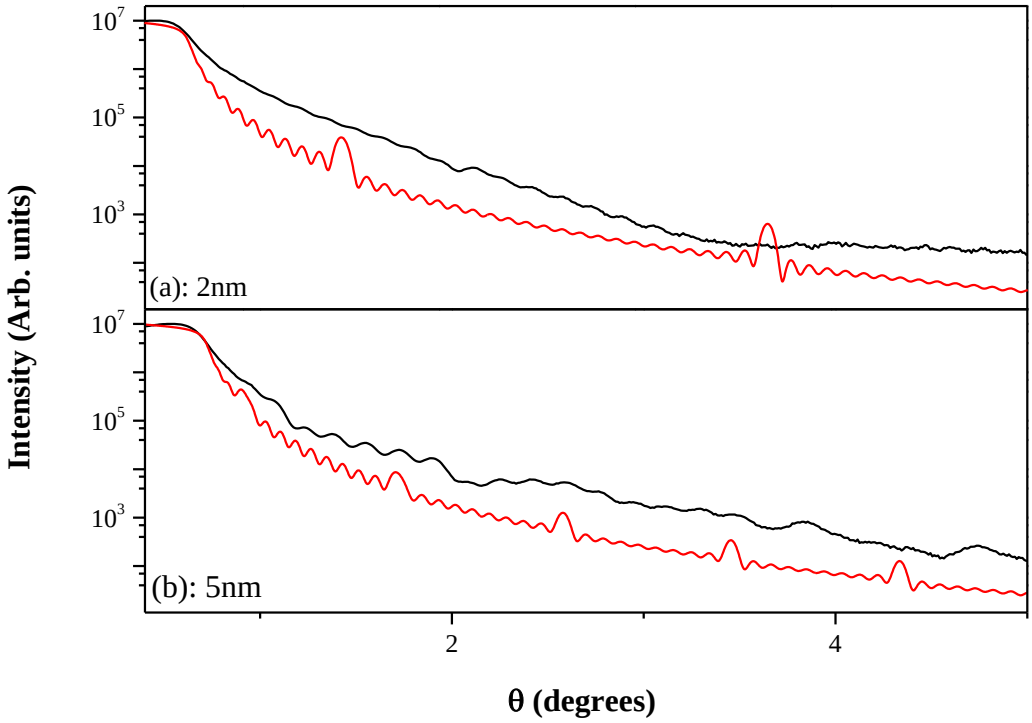

Figure 3.28: Experimental XRR patterns for multilayers of differing thickness shown in black and theoretical simulation in red of the XRR for multilayers of differing thickness; (a) 2nm layer thickness to give a total thickness of 48nm, (b) 5nm layer thickness to give a total thickness of 50nm.

From the detailed view in Figure 3.28, it can be seen that the 5nm experimental XRR has a greater number of the large oscillation peaks that are required for calculating the superlattice periodicity (Λ): [28,29]

$$\Lambda = l\lambda \left[2\left(\sqrt{\theta_l^2 - \theta_c^2}\right)\right] \qquad \text{Eqn. (3.1)}$$

Where: l is reflectivity peak of order, λ is wavelength of X-rays, θ_l is angle and θ_c is critical angle for total reflection.

The superlattice periodicity of the 5nm multilayer film was calculated from the oscillations in the XRR pattern, which are numbered in Figure 3.29, and reported in Table 3.4.

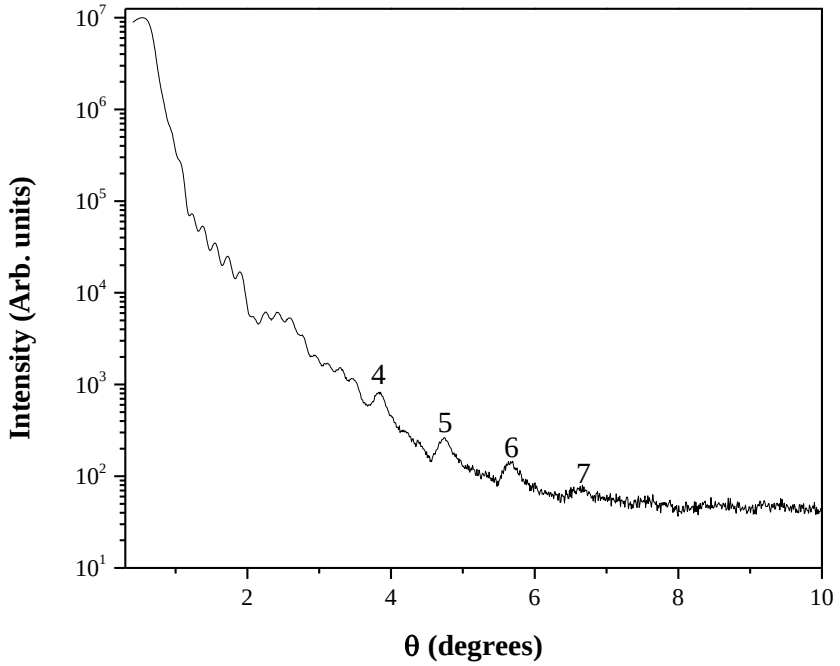

Figure 3.29: XRR data from the 5nm film with peak numbers relating to the calculation for periodicity.

Table 3.4: Linking the labelled peaks in Figure 3.29 on the XRR data to the calculated superlattice periodicity for the 5 nm multilayered structure.

Peak number on the XRR	Superlattice periodicity (Å)
4	92.9
5	93.7
6	94.2
7	93.4

Our expected superlattice periodicity would be 100Å for the 5nm multilayer film as each multilayer consists of 5nm of SDC and 5nm of NBCO making a repeating unit of thickness 10nm, or 100Å. Therefore with the calculated superlattice periodicity from the XRRs equal to ~93.5Å, it can be concluded that these multilayer systems can be grown consistently, with an average layer thickness of 5nm ± 0.3nm.

3.5.8 Thermal Stability of the Multilayers

Due to the problems with the NBCO stability, (see section 3.4) the stability of the multilayer film also needed to be investigated given our intention to perform AC impedance measurements on the films.

Firstly a 2nm multilayer, (STO|SDC|NBCO|SDC) was grown with an SDC terminated layer to protect the NBCO. This film was annealed in air at 600°C for 90 minutes, with a heating and cooling rate of 3°Cmin^{-1}. The film was tested before and after annealing *via* XRD, and the film was stable as can be seen in Figure 3.30 (b).

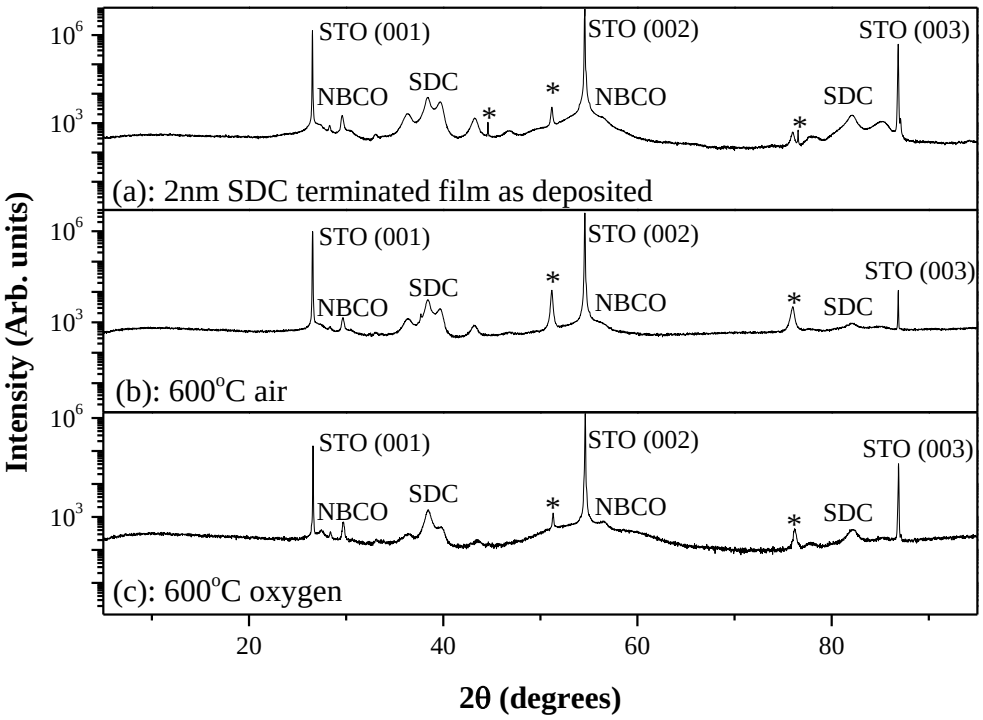

Figure 3.30: XRD pattern of the SDC terminated 2nm multilayer (a) as-deposited, after annealing in (b) air and (c) oxygen. * indicates peaks from the sample holder.

A 10 nm multilayer SDC terminated film was grown and the stability again tested by annealing at 600°C in air for 90min, with a heating and cooling rate of 3°Cmin^{-1} as before, however this time the film degraded, as can be seen from Figure 3.31(b).

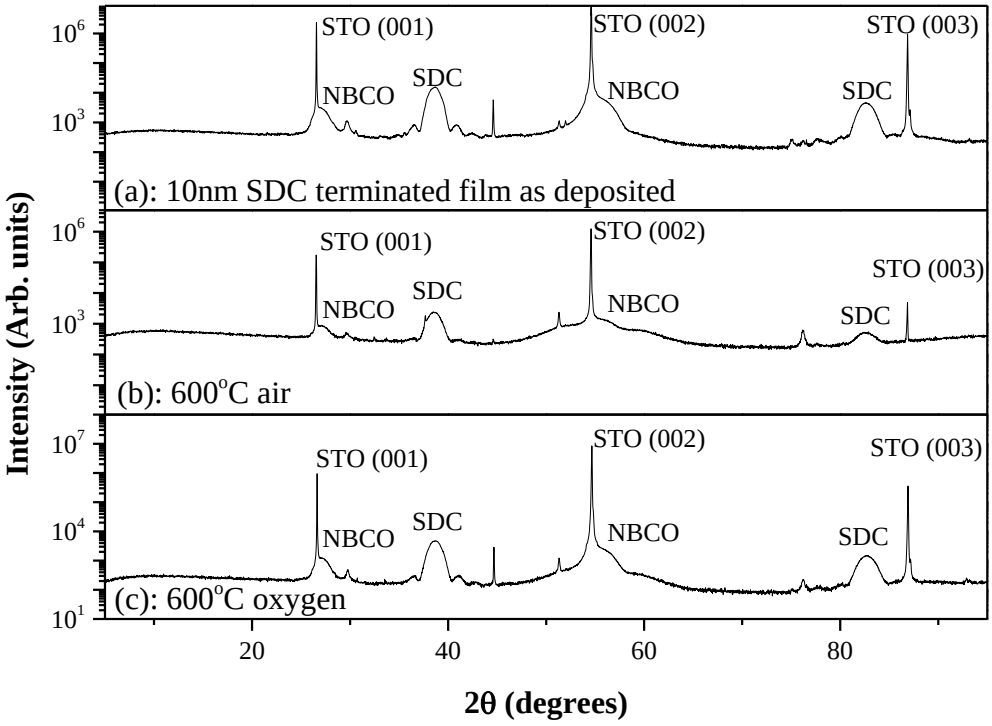

Figure 3.31: XRD pattern of the SDC terminated 10nm multilayer (a) as-deposited, after annealing in (b) air and (c) oxygen.

Separate quarters of these films were also annealed in oxygen at the same temperature and duration as before, to test their stability and the resultant XRD patterns can be seen in Figures 3.30 (c) and 3.31 (c). The thickness of the multilayer films appears to have an effect on the stability, as the 10nm SDC terminated film is more stable than the 2nm SDC terminated film at 600°C in oxygen.

The stability of a 2nm NBCO terminated multilayer was also tested in air and oxygen, in the same manner as before and the XRD patterns are shown in Figure 3.32.

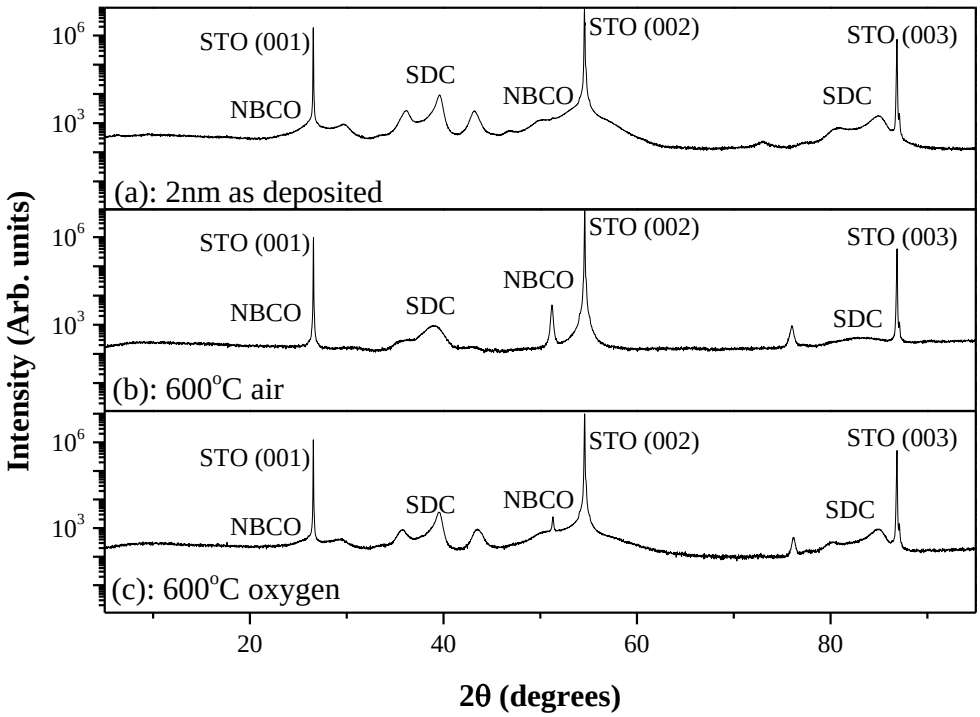

Figure 3.32: XRD pattern of the NBCO terminated 2nm multilayer (a) as-deposited, after annealing in (b) air and (c) oxygen.

From Figure 3.32 it can be seen that pattern (c) in oxygen is comparable to the as deposited film in pattern (a), however pattern (b) shows more broadening of the SDC peak in particular, which could indicate that the film is being affected by the heating in air.

Finally the stability of a 10nm NBCO terminated multilayer was annealed in air and oxygen before XRD analysis to determine the stability, shown in Figure 3.33.

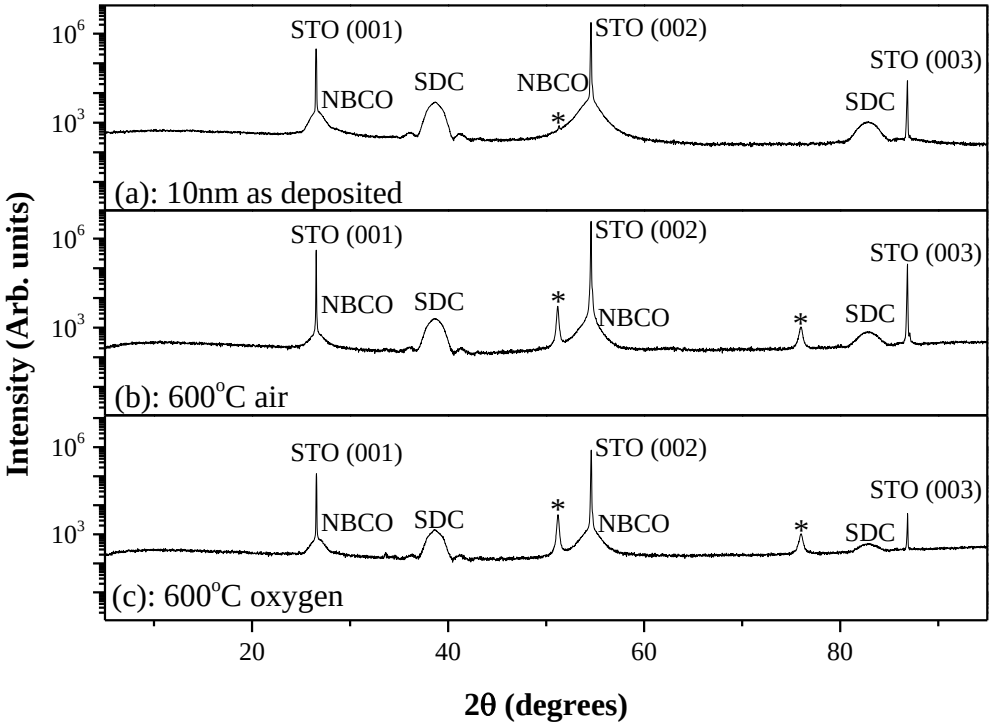

Figure 3.33: XRD pattern of the NBCO terminated 10nm multilayer (a) as-deposited, after annealing in (b) air and (c) oxygen. The * indicate the holder peaks.

The NBCO terminated 10nm multilayer shown in Figure 3.33 has little change after annealing in either air or oxygen. The intensity of the peaks do decrease in pattern (c) particularly, however this is also the case for the STO (003) peak and therefore caused by sample alignment.

The stability tests from the multilayers show that the thickness and termination of the layers is important for the stability of the films. The 2nm NBCO terminated multilayer (shown in Figure 3.32) showed broadening of the SDC peaks having been annealed in air at 600°C. The thicker 10nm NBCO terminated film (shown

in Figure 3.33) showed little change in the XRD pattern after annealing in air at 600°C suggesting that the thicker layer was more stable. With regard to the SDC termination the 2nm film was stable, whereas the 10nm film showed broadening of the peaks after annealing in air at 600°C. In conclusion a thinner multilayer film is more stable with the SDC termination, whereas with the thicker multilayer films the NBCO termination is stable.

3.5.9 TEM

A selection of NBCO/SDC multilayer films were analysed by TEM. A summary of these films is shown in Table 3.5.

Table 3.5: Summary of the multilayers sent for analysis.

Film number	Layer thickness (nm)	Total film thickness (nm)	Growth temperature (°C)
1	2	48	850
2	5	50	850
3	2	48	NBCO 850 / SDC 650

A schematic of a 2nm multilayer film, with a representative TEM image by Prof. Joke Hadermann at Electron Microscopy for Materials Science (EMAT), University of Antwerp is shown in Figure 3.34 (a) and (b) respectively. The 2nm multilayer images will be discussed in more detail later in the chapter, however as much of the analysis to this point has been focused on the 5nm multilayer film this will be discussed initially.

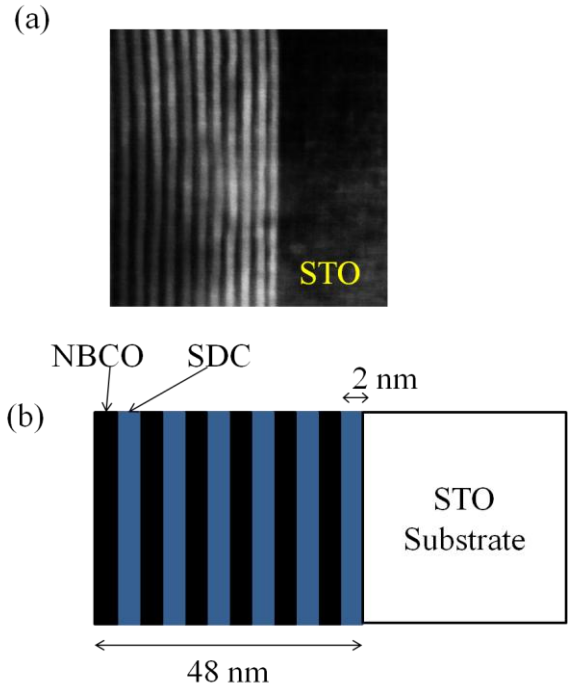

Figure 3.34: (a) TEM image by Prof. Joke Hadermann from a 2nm multilayer film and (b) a schematic describing the multilayer film.

3.5.9.1 5nm SDC/NBCO

Film 2 from Table 3.5, (the SDC NBCO 5 nm multilayer) was analysed *via* transmission electron microscopy (TEM) by Dr. Simon Romani at Nanoinvestigation Centre at Liverpool (NiCaL).

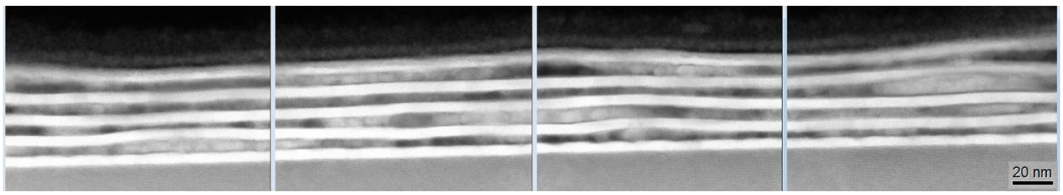

Figure 3.35: TEM across the multilayer film. SDC layers are brighter, NBCO layers are darker.

From the TEM images in Figure 3.35 it is possible to see that the darker NBCO layers have an irregular structure, whereas the brighter SDC layering appears to be better defined.

The TEM and elemental analysis results in Figure 3.36 showed that there were regions of Co metal in the NBCO layers of the multilayer film, and there were many regions where the layers were intermixed.

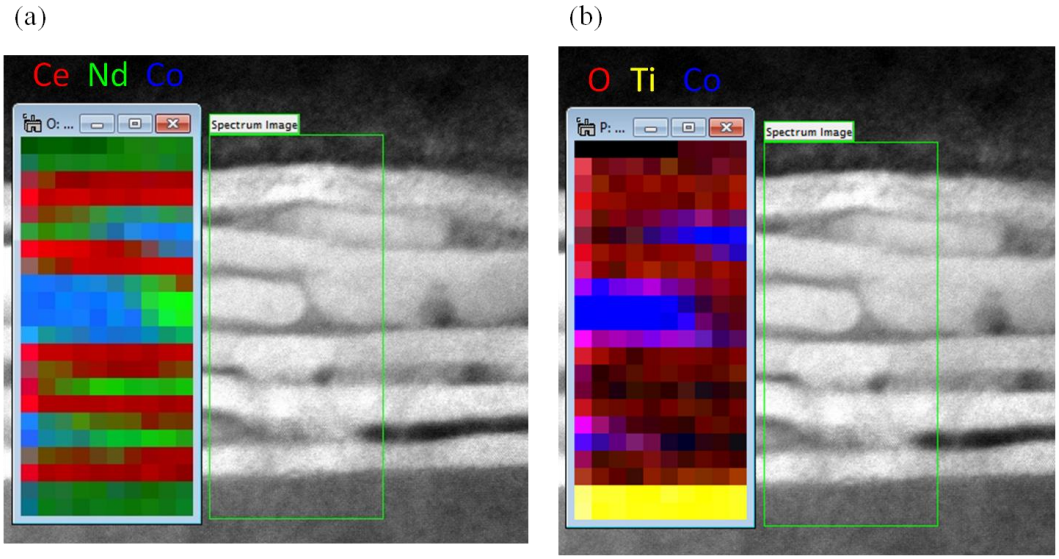

Figure 3.36: Elemental analysis of the TEM (a) showing analysis of Ce, Nd and Co and (b) showing analysis of O, Ti and Co.

From Figure 3.36 (a) the Ce (in red) from the SDC is generally in separate layers to the Nd and Co (in green and blue respectively) from the NBCO. The Ti layers in yellow in Figure 3.36 (b) are from the STO substrate. Interestingly in Figure 3.36 (b), the O (red) is generally distributed over the entire film as expected, however there are some deep blue Co regions which stand out. Further analysis

was carried out as can be seen in Figure 3.37 (a) through (d), where in (d) regions of Co metal have been identified in addition to the Co-O_x and the Ce layers.

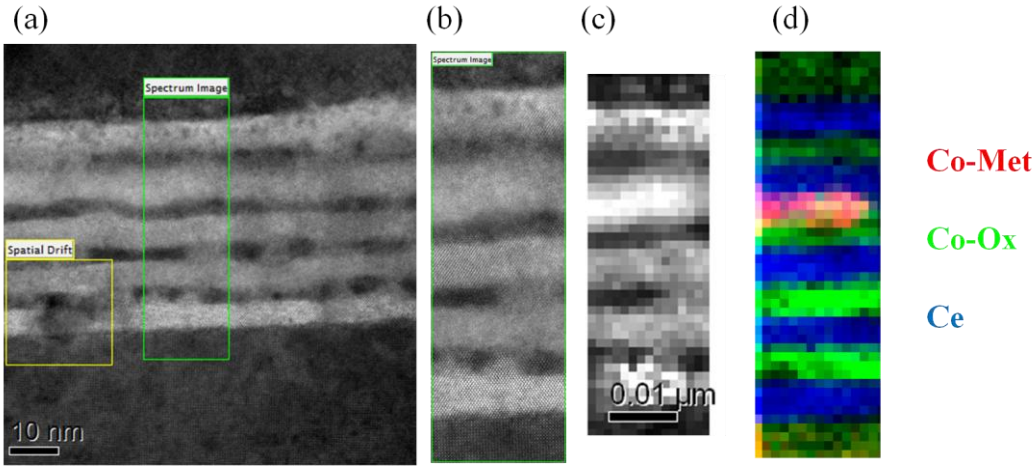

Figure 3.37: (a) Cross-Sectional STEM of 5nm alternating SDC/NBCO, (b) area sampled for elemental analysis, (c) effective resolution of sample area, (d) elemental analysis with cobalt metal in red, cobalt oxide in green and cerium in blue.

It is difficult to understand how the regions of Co metal were deposited in the film. A paper by Laureti and Kaciulis *et al.*[30] discusses the effect of oxygen partial pressure on cobalt oxide films grown *via* PLD. They grow CoO_x layers in a range of pO_2 from 10^{-4} up to 10^{-2}mbar, and do not mention any cobalt metal formation. Our NBCO films were deposited at 1mTorr (~10^{-3}mbar), and the film is cooled in a pO_2 of 1.0 x 10^{-1}Torr, and so it is surprising that Figure 3.37 (d) indicates the presence of Co metal.

3.5.9.2 Film 3 - 2nm SDC/NBCO

Dr. Simon Romani also analysed the 2nm SDC NBCO film where the SDC was deposited at a lower temperature to the NBCO (film 3 in Table 3.5). For this analysis he used the focused ion beam (FIB) technique.

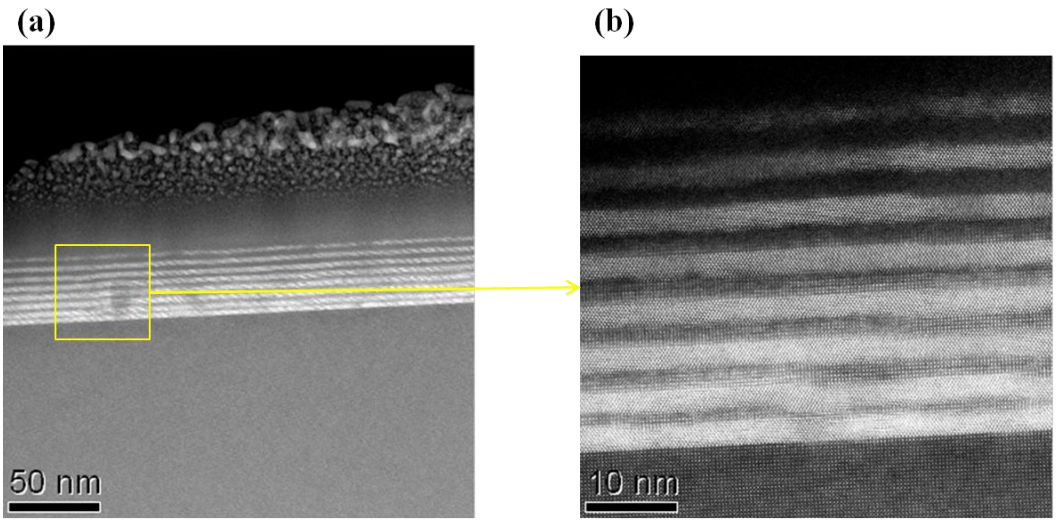

Figure 3.38: (a) Large scale FIB image of the 2 nm multilayer film deposited with SDC at the lower temperature with a more zoomed in section in the yellow box shown in (b).

The STO substrate is shown at the bottom of Figures 3.38 (a) and (b). Figure 3.38 (b) is a zoomed in section of (a). The SDC layers are again much brighter than the NBCO layers, and the SDC layers appear to be of a more consistent thickness throughout the film.

Figures 3.39 and 3.40 show high angle annular dark field (HAADF) and inverse fast Fourier transform (IFFT) images on increasing magnification.

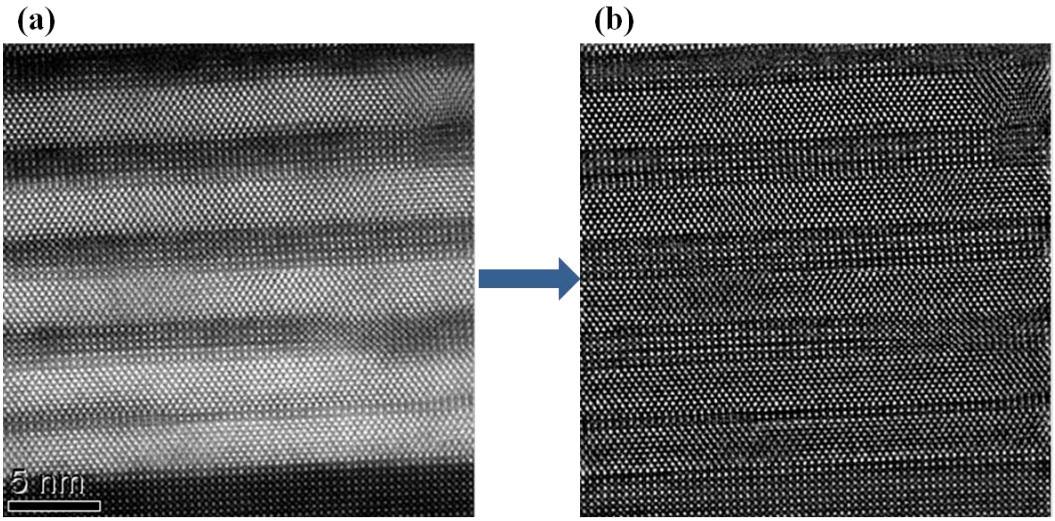

Figure 3.39: (a) Original HAADF Image and (b) IFFT Filtered (Annular Mask) on a 5nm scale.

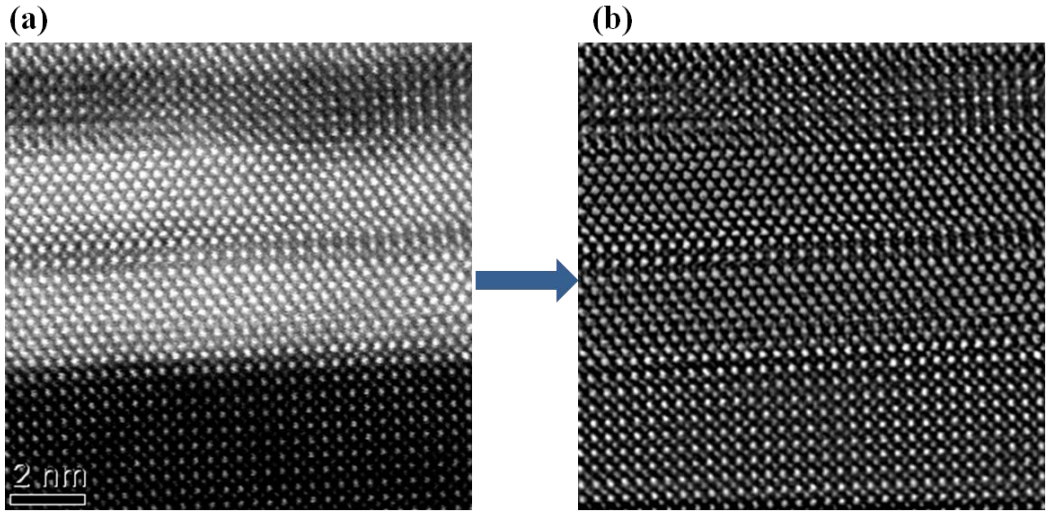

Figure 3.40: (a) Original HAADF Image and (b) IFFT Filtered (Annular Mask) on a 2nm scale.

Figures 3.39 and 3.40 show the interfaces between the film and substrate as well as the SDC film and NBCO film layers. In part (a) of Figures 3.39 and 3.40 the darker perovskite layer shows varying thickness throughout the film. The IFFT filtering (b) gives a clearer image of the interfaces, and the perovskite → fluorite interfaces are observed to be not as sharp as the fluorite → perovskite interfaces.

Films 1 and 3 from Table 3.5 were also analysed by Prof. Joke Hadermann at Electron Microscopy for Materials Science (EMAT), University of Antwerp. Films 1 and 3 were both 2nm SDC NBCO films, with differing SDC growth temperatures (film 1 NBCO/SDC both at 850°C and film 3 is with SDC at 650°C).

Initially film 3 was analysed (for which Dr. Simon Romani performed the FIB analysis). Figure 3.41 indicates that the layers are of unequal thickness, in particular the darker perovskite layers, in agreement with the FIB analysis.

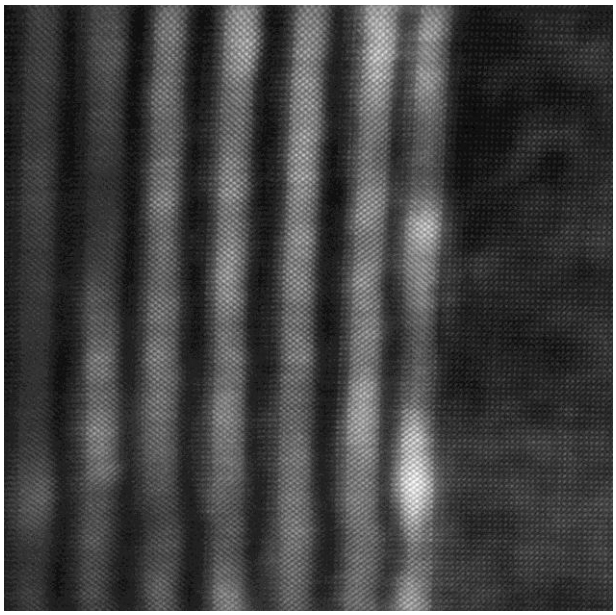

Figure 3.41: TEM of film 3 by Prof. Joke Hadermann to see if the thickness of the layers are equal throughout the film.

A magnified TEM image is shown in Figure 3.42 where the quality of the interfaces can be observed.

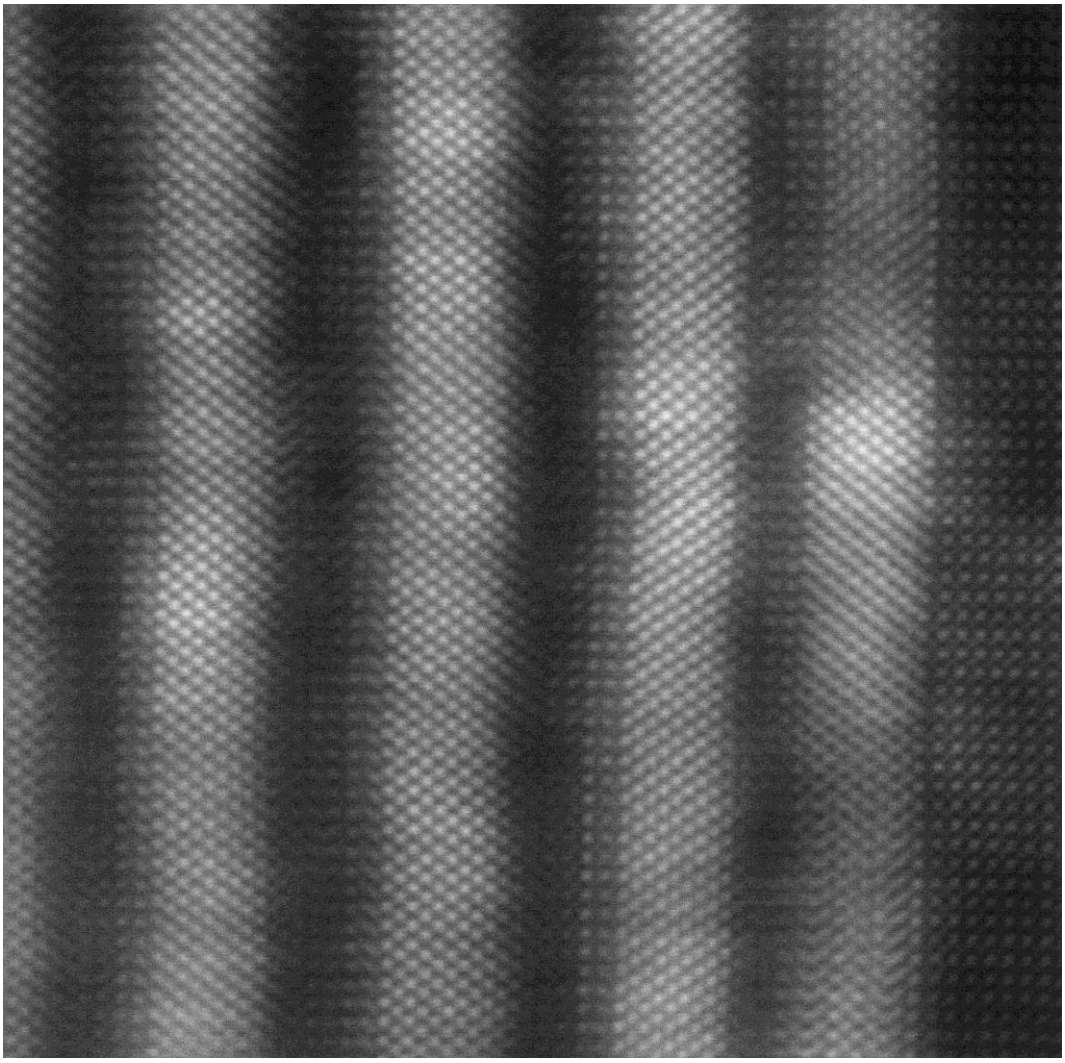

Figure 3.42: TEM of film 3 by Prof. Joke Hadermann to see the quality of the interfaces of the multilayer film.

The start of the first fluorite block is sharp throughout large parts of the film. Also, the first fluorite → perovskite interface is clear, although there occur steps where a layer has fluorite structure on one side of the film, and perovskite structure on the other side. For example in the yellow box in Figure 3.43, at the first fluorite → perovskite interface there is a layer that is definitely fluorite at the bottom of the image and turns to perovskite halfway up the image.

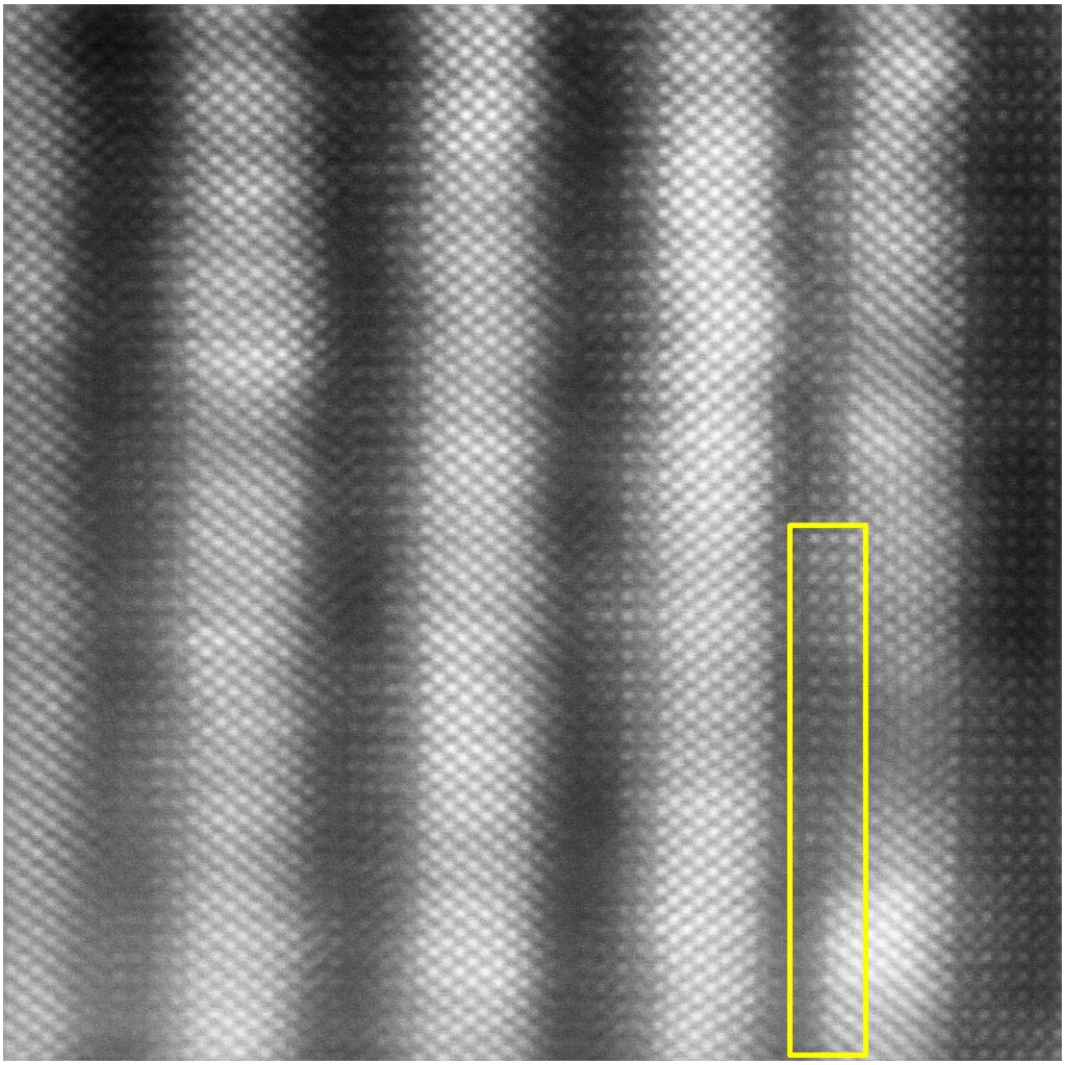

Figure 3.43: TEM of film 3 by Prof. Joke Hadermann to see the quality of the interfaces of the multilayer film.

In general throughout the rest of the film, the fluorite → perovskite interfaces look abrupt and the perovskite → fluorite interfaces do not, in agreement with the FIB analysis. The brightness gradient which is present in each perovskite block, going from bright dots at the A site positions to almost invisible ones may be caused by strain, as the difference between the four A site elements (Sm-62, Ce-58, Nd-60, Ba-56) is not that large that it could explain such large difference in the colour of the A site cation column.

The perovskite layer can be terminated with an AO or BO_2 layer and from Figure 3.44 it can be seen that there is a mixture of both. The first two transitions from fluorite to perovskite (starting from the substrate at the right) occur with a CoO_2 layer first, numbered 1 and 2 in Figure 3.44, while the third fluorite to perovskite transition starts with an AO layer numbered 3. The perovskite to fluorite interfaces are not clear enough to determine their termination.

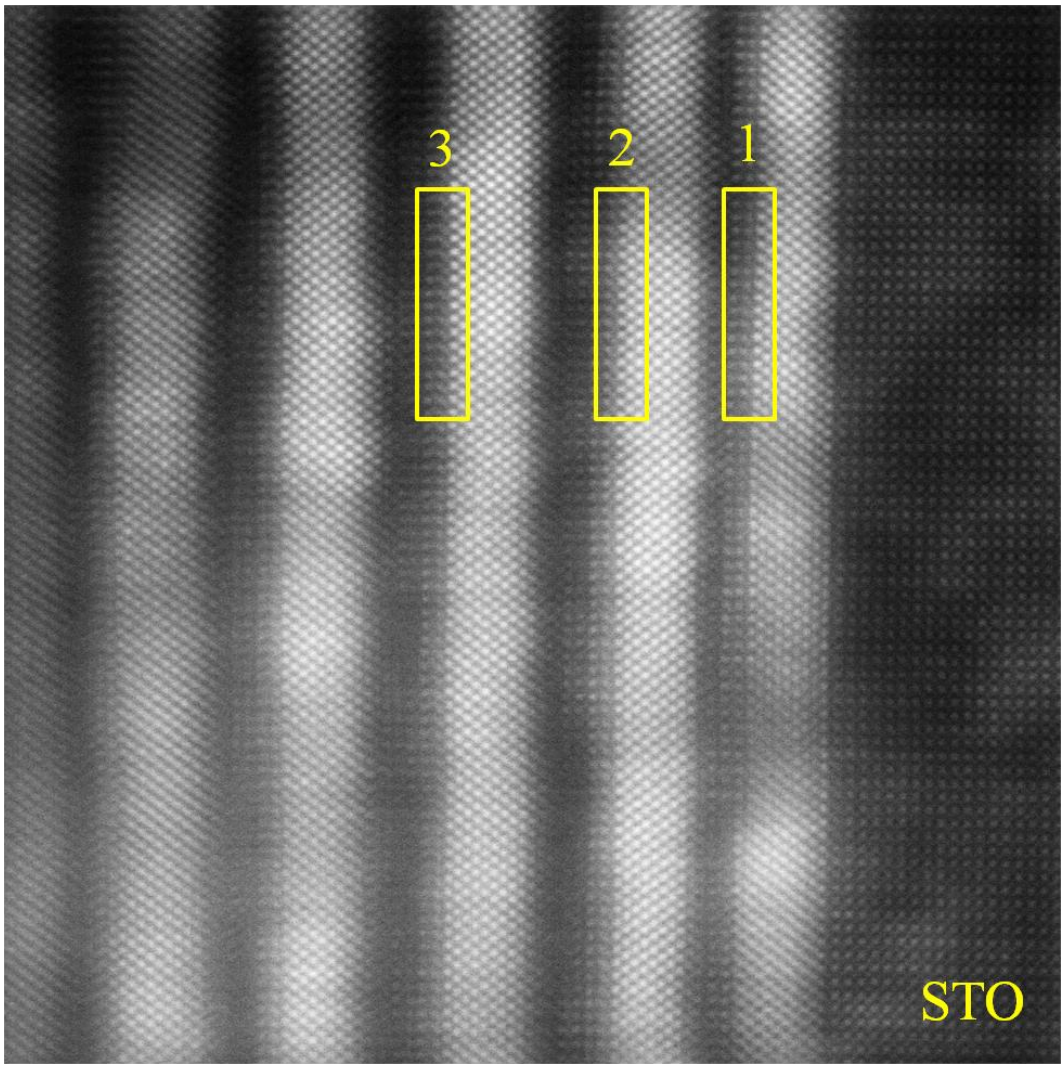

Figure 3.44: TEM by Prof. Joke Hadermann to see the interfacial termination of the perovskite layer in the multilayer film. The initial fluorite to perovskite transitions are numbered from the STO substrate.

EDX analysis was performed to determine the elemental composition of each layer and to see if there was any chemical diffusion across the interfaces. The vague borders in the TEM (as shown in Figure 3.45 (a)) when going from perovskite → fluorite suggests that there is diffusion occurring.

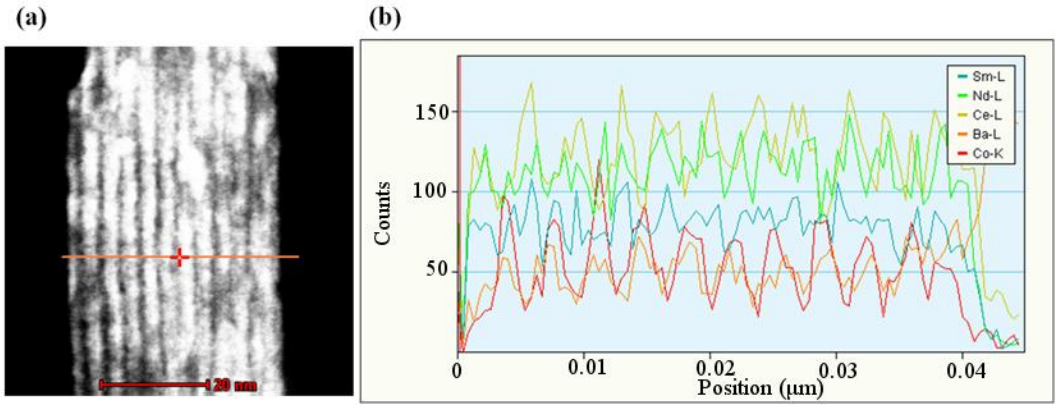

Figure 3.45: EDX analysis by Prof. Joke Hadermann of the multilayer film (a) HAADF-STEM image of the area across which the EDX was performed (b) EDX profile across the film.

The EDX measurements are shown in Figure 3.45 (b). Figure 3.45 (a) shows a line of the intended area, over a HAADF-STEM image. Figure 3.45 (b) shows EDX spectra for the elements Co, Ba, Nd, Ce, and Sm. The HAADF-STEM image is of poorer quality due to the spot size being larger, to obtain sufficient counts for the EDX. The spectra do not precisely correspond to the line drawn on the image in Figure 3.45 (a), because during the measurement, which takes 15-30 minutes, a continuous shift of the sample occurs.

From Figure 3.45 (b) it can be seen that Ce-L has the opposite profile of Co-K, and has peaks where the HAADF-STEM profile has bright areas, indicating that Ce and Co are indeed in separate layers. Sm-L is not so clear, but this is not

unexpected since there is only 20% Sm mixed with the Ce, so the counts are low and noisy.

Comparing the HAADF-STEM profile to the Co-K profile it can be seen that they agree with the supposition that bright layers are SDC and the dark ones NBCO. Each bright region in the HAADF-STEM profile corresponds to a trough in the Co-K profile. The peaks in the Ba-L profile correspond to the peaks in the Co-K profile, although they are less clear because there is less Ba than Co in these layers. The high plateau of Ba at the end of the EDX is an artifact due to the exact overlap of the Ti curve with the Ba curve. In the film it is assumed that this curve is due to Ba and at the end where the substrate is encountered, it is assumed that this curve is Ti.

The Nd-L profile should also follow the Co-K profile if there are well defined $NdBaCo_2O_5$ perovskite blocks alternating with $Sm_{0.2}Ce_{0.8}O_2$ fluorite blocks. However, the Nd does not show the same alternation as Co, and occasionally there is a Nd peak where there is a Co trough. This suggests that diffusion of Nd is occurring to the fluorite blocks. This is also observed with the second 2nm multilayer film (film 1 in Table 3.5) where SDC is deposited at 850°C.

3.5.9.3 Film 1 - 2nm SDC/NBCO

As with the previously analysed 2nm multilayer, film 3, the layers are of inconsistent thickness, particularly for the perovskite layers. Even within a layer there is greater variance in width, as can be seen in Figure 3.46.

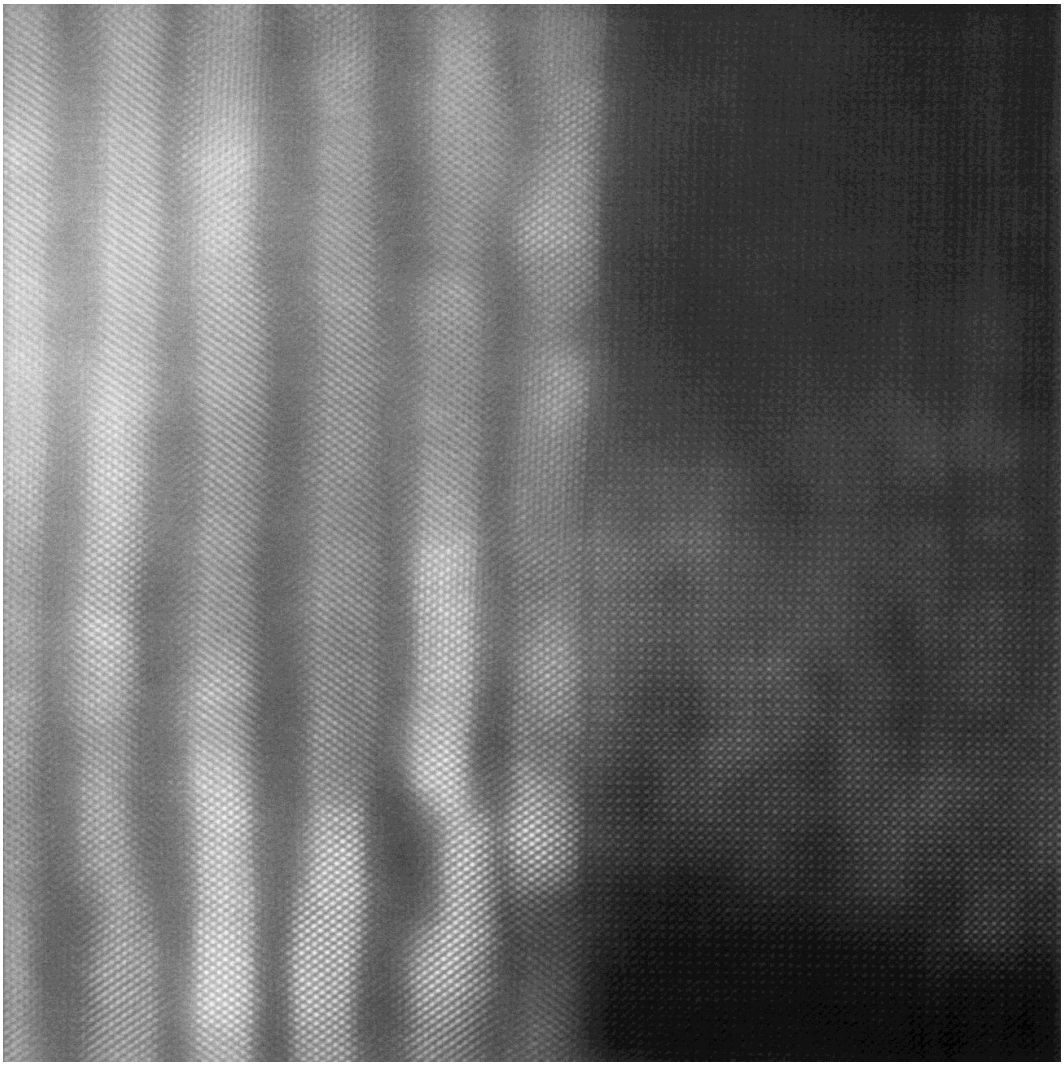

Figure 3.46: TEM by Prof. Joke Hadermann to see if the thicknesses of the layers are equal throughout the film.

The layers appear less abrupt than they were in film 3, as can be seen in Figure 3.47. This is not entirely unexpected as the lower growth temperature for the SDC film used for film 3 produced a better surface topography in the AFM data previously discussed in Section 3.5.2.1 and shown in Figure 3.15.

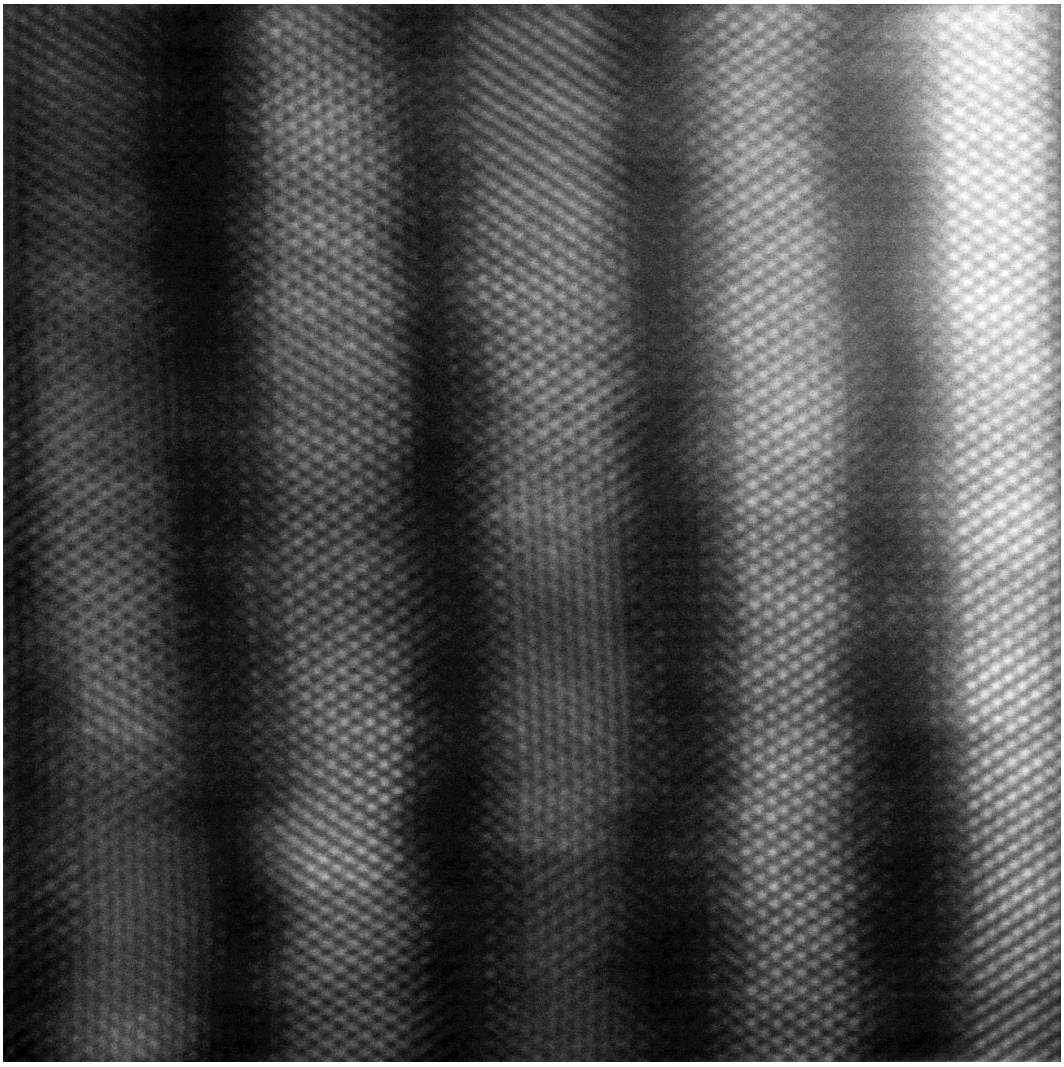

Figure 3.47: TEM by Prof. Joke Hadermann, showing the layers are less abrupt than in the 2nm multilayer film with the SDC grown at the lower temperature.

3.5.9.4 2 nm SDC/NBCO Film Comparison

The layers in film 1 are less uniform compared to film 3. However, in film 3 there are darker areas between the perovskite and fluorite layer (on the transition from perovskite → fluorite, not fluorite → perovskite which was sharp), and this is not present in film 1. A possible explanation for the darker regions observed in film 3 could be that the fluorite structure has been taken on by Co and oxygen. It is

difficult to explain how with the same elements, areas can be made darker than the CoO_2 layers of the perovskite block. However, if they are layers of fluorite CoO_2, the Z per unit of length would indeed be smaller than in the CoO_2 layers of the perovskite block, which could explain why it appears darker. Again it is possible to see that the darker area has a distance between the columns that agrees with fluorite rather than perovskite. This could also be further supported by the diffusion of Nd to the fluorite layer, which could leave a Nd deficiency in the areas where there should have been perovskite.

In film 1 there are also areas where the perovskite structure is not reached but these are less numerous than in film 3. For example the 2nd and 3rd fluorite type layers (from the left) in Figure 3.48 show a layer that is darker between them, but does not have perovskite periodicity and appears as fluorite which may be CoO_2 with a fluorite-type structure.

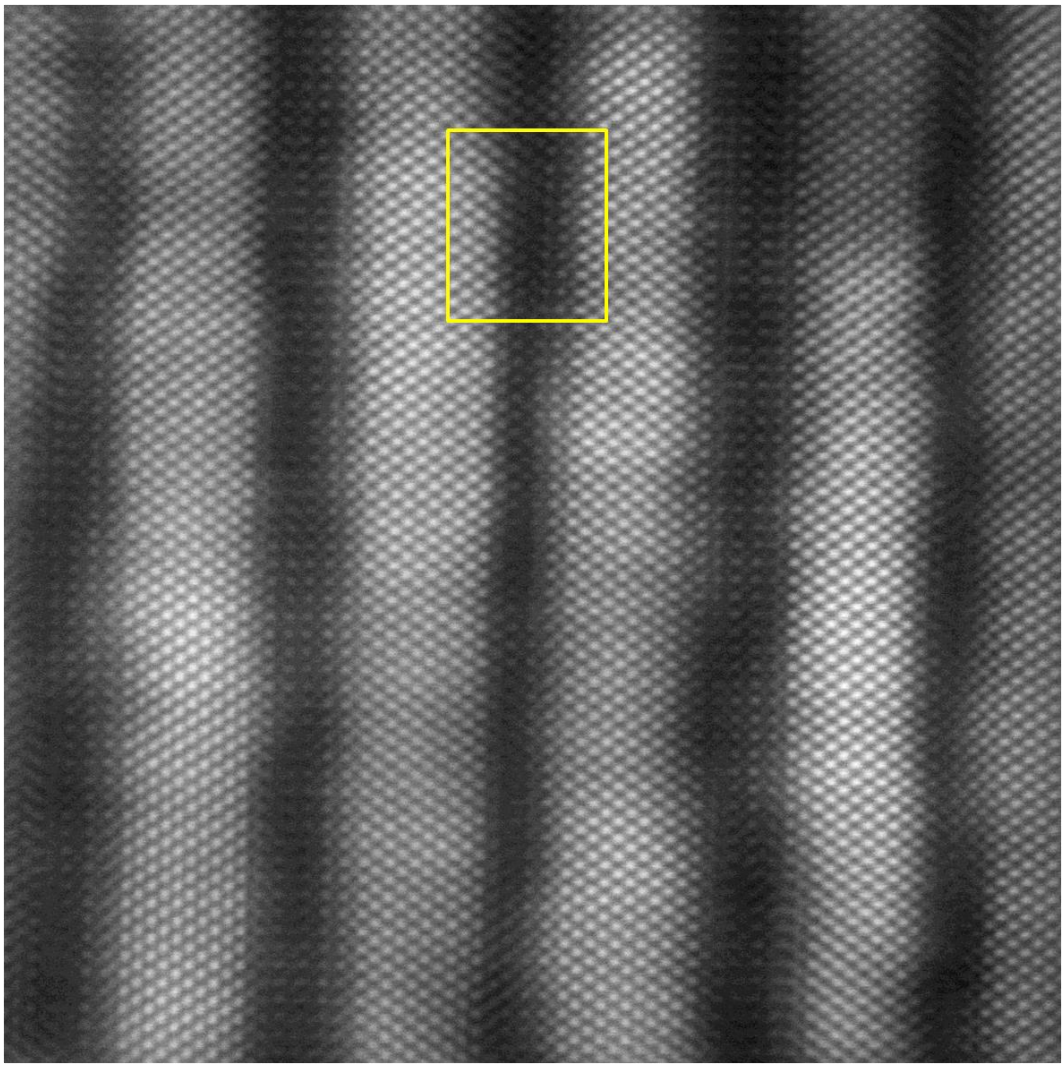

Figure 3.48: TEM by Prof. Joke Hadermann showing the regions between fluorite layers where the perovskite structure is not reached.

From the TEM analysis of all of the films in Table 3.5, it is found that the SDC regions of the film are more consistent in thickness than the NBCO regions. The model from Dr. Robert Palgrave's DIFFaX analysis of the 5nm multilayer film discussed previously in Section 3.5.6 used 8 unit cells of SDC and 6.5 unit cells of ordered NBCO. The TEM data also shows that the perovskite regions are thinner than the fluorite regions.

Some of the problems with the NBCO film can be attributed to the quality of the NBCO target that was used to grow the films. NBCO is a very soft material and it was particularly challenging to press and isostatically press into a pellet. It is therefore possible that the target has regions of varying density. This may have contributed to the observation of the regions of cobalt metal in the TEM from the 5nm multilayer film, and could also contribute to the inhomogeneity of the layers. A further possibility is that the Co-M may be an artefact of the TEM sample preparation rather than direct incorporation of the metal during the PLD process.

3.6 Conclusions

Both oriented ordered NBCO films and oriented SDC films were successfully deposited on STO (001) substrates.

The initial aim when depositing the single layer films was also to compare the AC impedance of the single layer with the multilayer films, however instability in the NBCO material prevented this. As the NBCO was designed to be used as a cathode for IT-SOFCs, its instability in air and oxygen at 600°C shows that it is not fit for purpose. One of the hopes was that growing multilayers with SDC capping layers would improve the stability, however this was also unsuccessful.

Following on from this work multilayers of the SDC and NBCO films were also grown. A set of multilayer films were deposited with 2nm, 5nm, 10nm and 15nm of each layer.

One of the challenges of these multilayer films was that the NBCO required deposition at 850°C, whereas it was found that the SDC grew with a lower surface roughness at lower temperatures of around 650°C. Combining these films into the multilayer introduced the challenge of whether it was better to sacrifice some of the surface roughness of the SDC and use the higher temperature or not. From the TEM and EDX data there is likely migration of Nd into the SDC layers. The interfaces are also less sharp for the multilayer films deposited at the higher temperature for the SDC growth. However, in all cases the SDC growth appears more favourable in the TEM when compared to the NBCO, with some regions even showing Co-metal and fluorite structures potentially attributed to Co-O_x where we would expect to see the perovskite block.

As the NBCO was not stable enough to carry out reliable impedance measurements a second cathode material was chosen for further study and more information on this is discussed in Chapter 4. Further experiments could include replacing the NBCO in the multilayer film with another more stable perovskite structure to continue to investigate the relationship between the perovskite and fluorite interfaces.

3.7 References

1 Taskin, A. A., Lavrov, A. N. & Ando, Y. Transport and magnetic properties of $GdBaCo_2O_5$ single crystals: A cobalt oxide with square-lattice CoO_2 planes over a wide range of electron and hole doping. *Physical Review B* **71**, 134414 (2005).

2 Burriel, M. *et al.* Anisotropic Oxygen Ion Diffusion in Layered $PrBaCo_2O_{5+\delta}$. *Chemistry of Materials* **24**, 613-621, doi:10.1021/cm203502s (2012).

3 Tarancon, A., Burriel, M., Santiso, J., Skinner, S. J. & Kilner, J. A. Advances in layered oxide cathodes for intermediate temperature solid oxide fuel cells. *Journal of Materials Chemistry* **20**, 3799-3813, doi:10.1039/b922430k (2010).

4 Parfitt, D., Chroneos, A., Tarancon, A. & Kilner, J. A. Oxygen ion diffusion in cation ordered/disordered $GdBaCo_2O_{5+[delta]}$. *Journal of Materials Chemistry* **21**, 2183-2186, doi:10.1039/c0jm02924f (2011).

5 Taskin, A. A., Lavrov, A. N. & Ando, Y. Achieving fast oxygen diffusion in perovskites by cation ordering. *Applied Physics Letters* **86**, -, doi:doi:http://dx.doi.org/10.1063/1.1864244 (2005).

6 Kim, G. *et al.* Rapid oxygen ion diffusion and surface exchange kinetics in $PrBaCo_2O_{5+x}$ with a perovskite related structure and ordered A cations. *Journal of Materials Chemistry* **17**, 2500-2505, doi:10.1039/b618345j (2007).

7 Yuan, Z. *et al.* Epitaxial behavior and transport properties of $PrBaCo_2O_5$ thin films on (001) $SrTiO_3$. *Applied Physics Letters* **90**, -, doi:doi:http://dx.doi.org/10.1063/1.2741407 (2007).

8 Burriel, M. *et al.* Influence of the Microstructure on the High-Temperature Transport Properties of $GdBaCo_2O_{5.5+\delta}$ Epitaxial Films. *Chemistry of Materials* **22**, 5512-5520, doi:10.1021/cm101423z (2010).

9 Kim, G. *et al.* Oxygen exchange kinetics of epitaxial $PrBaCo_2O_{5+\delta}$ thin films. *Applied Physics Letters* **88**, -, doi:doi:http://dx.doi.org/10.1063/1.2163257 (2006).

10 Grygiel, C. *et al.* A-Site Order Control in Mixed Conductor $NdBaCo_2O_{5+\delta}$ Films through Manipulation of Growth Kinetics. *Chemistry of Materials* **22**, 1955-1957, doi:10.1021/cm9037022 (2010).

11 Frank, F. C. The influence of dislocations on crystal growth. *Discussions of the Faraday Society* **5**, 48-54, doi:10.1039/df9490500048 (1949).

12 Burton, W. K., Cabrera, N. & Frank, F. C. The Growth of Crystals and the Equilibrium Structure of their Surfaces. *Philosophical Transactions of the Royal Society of London. Series A, Mathematical and Physical Sciences* **243**, 299-358, doi:10.1098/rsta.1951.0006 (1951).

13 Bennema, P. Spiral growth and surface roughening: Developments since Burton, Cabrera and Frank. *Journal of Crystal Growth* **69**, 182-197, doi:http://dx.doi.org/10.1016/0022-0248(84)90027-7 (1984).

14 Scheel, H. J. Materials Engineering Problems in Crystal Growth and Epitaxy of Cuprate Superconductors. *MRS Bulletin* **19**, 26-32, doi:doi:10.1557/S0883769400047953 (1994).

15 Lobanovsky, L. S., Troyanchuk, I. O., Szymczak, H. & Prokhnenko, O. Structure and physical properties of layered double perovskite $NdBaCo_2O_{5.50+\delta}$ ($\delta \approx 0.25$). *J. Exp. Theor. Phys.* **103**, 740-746, doi:10.1134/s1063776106110094 (2006).

16 Pralong, V., Caignaert, V., Hebert, S., Maignan, A. & Raveau, B. Soft chemistry synthesis and characterizations of fully oxidized and reduced $NdBaCo_2O_{5+\delta}$ phases δ=0,1. *Solid State Ionics* **177**, 1879-1881, doi:http://dx.doi.org/10.1016/j.ssi.2006.06.013 (2006).

17 Zachariasen, W. H. *Zeitschrift fuer Physikalische Chemie* **123**, 134 (1926).

18 B. E. Gushee, L. K., R. Ward. The preparation of a barium cobalt oxide and other phases with similar structures. *Journal of the American Chemical Society* **79**, 5601 (1957).

19 Roth, W. L. The magnetic structure of Co_3O_4. *Journal of Physics and Chemistry of Solids* **25**, 1 (1964).

20 Kniga, M. *Russ. J. Inorg. Chem.* **24**, 652 (1979).

21 Troyanchuk, I. O. *et al.* Magnetic and crystal structure phase transitions in $R_{1-x}Ba_xCoO_{3-y}$ (R = Nd, Gd). *Journal of Physics: Condensed Matter* **12**, 2485 (2000).

22 Garcia-Barriocanal, J. *et al.* Colossal Ionic Conductivity at Interfaces of Epitaxial ZrO_2:Y_2O_3/$SrTiO_3$ Heterostructures. *Science* **321**, 676-680 (2008).

23 Guo, X. Comment on "Colossal Ionic Conductivity at Interfaces of Epitaxial ZrO_2:Y_2O_3/$SrTiO_3$ Heterostructures". *Science* **324**, 465, doi:10.1126/science.1168940 (2009).

24 García-Barriocanal, J. *et al.* Response to Comment on "Colossal Ionic Conductivity at Interfaces of Epitaxial ZrO_2:Y_2O_3/$SrTiO_3$ Heterostructures". *Science* **324**, 465, doi:10.1126/science.1169018 (2009).

25 Sanna, S. *et al.* Fabrication and Electrochemical Properties of Epitaxial Samarium-Doped Ceria Films on $SrTiO_3$-Buffered MgO Substrates. *Advanced Functional Materials* **19**, 1713-1719, doi:10.1002/adfm.200801768 (2009).

26 M.M.J. Treacy, M.W. Deem & Newsam, J. M. *DIFFaX*. (http://www.public.asu.edu/~mtreacy/DIFFaX.html).

27 Windt, D. L. IMD—Software for modeling the optical properties of multilayer films. *Computers in Physics* **12**, 360-370, doi:doi:http://dx.doi.org/10.1063/1.168689 (1998).

28 Geiersbach, U., Bergmann, A. & Westerholt, K. Preparation and structural properties of thin films and multilayers of the Heusler compounds Cu_2MnAl, Co_2MnSn, Co_2MnSi and Co_2MnGe. *Thin Solid Films* **425**, 225-232, doi:http://dx.doi.org/10.1016/S0040-6090(02)01091-X (2003).

29 Zabel, H. *Festkörperprobleme 30, Advanced solid state physics, X-ray and Neutron Scattering at Thin Films*. (1990).

30 Laureti, S. *et al.* Effect of oxygen partial pressure on PLD cobalt oxide films. *Applied Surface Science* **254**, 5111-5115, doi:http://dx.doi.org/10.1016/j.apsusc.2008.02.055 (2008).

Chapter 4: Barium Calcium Yttrium Iron Oxide

4.1 Introduction

$Ba_{1.7}Ca_{2.4}Y_{0.9}Fe_5O_{13}$ is a potential cathode material for solid oxide fuel cells (SOFC). In the bulk it has been reported to have a perovskite-based, cation ordered, layered structure.[1] Some of the work in this chapter is published,[2] and discusses the advantages of the thin film form over the bulk material. The $Ba_{1.7}Ca_{2.4}Y_{0.9}Fe_5O_{13}$ material is related to an intergrowth between $Ca_2Fe_2O_5$ [3] and $YBa_2Fe_3O_8$ [4,5] building blocks leading to a complex superstructure displaying 20 times the unit-cell volume of a classic cubic perovskite (Figure 4.1).

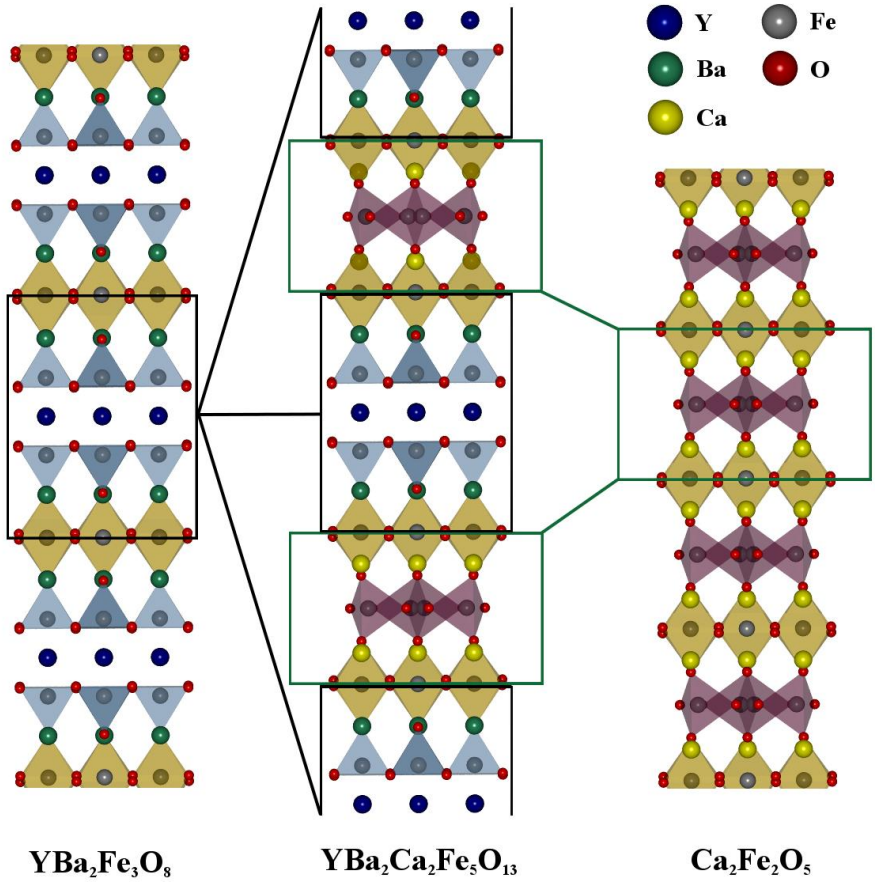

Figure 4.1: Crystal structure showing the intergrowth between $Ca_2Fe_2O_5$ and $YBa_2Fe_3O_8$ building blocks. The iron sites in the purple polyhedra are disordered.

$Ba_{1.7}Ca_{2.4}Y_{0.9}Fe_5O_{13}$ belongs to the orthorhombic space group *Imam*, and has bulk lattice parameters a = 5.50Å, b = 5.54Å, and c = 38.20Å, with the c axis corresponding to a 10 layer ($10a_p$) repeat of the basic cubic perovskite cell. Hereafter $Ba_{1.7}Ca_{2.4}Y_{0.9}Fe_5O_{13}$ shall be referred to as the 10 layer material. The c axis corresponds to the long axis and points out-of-plane as is conventional for describing thin films of layered materials.

Comparing the disordered structure of $NdBaCo_2O_5$ from Chapter 3 with the 10 layer structure of $Ba_{1.7}Ca_{2.4}Y_{0.9}Fe_5O_{13}$ in Figure 4.2 it is clearly evident how the 10 layer is 20 times the unit-cell volume of a classic cubic perovskite.

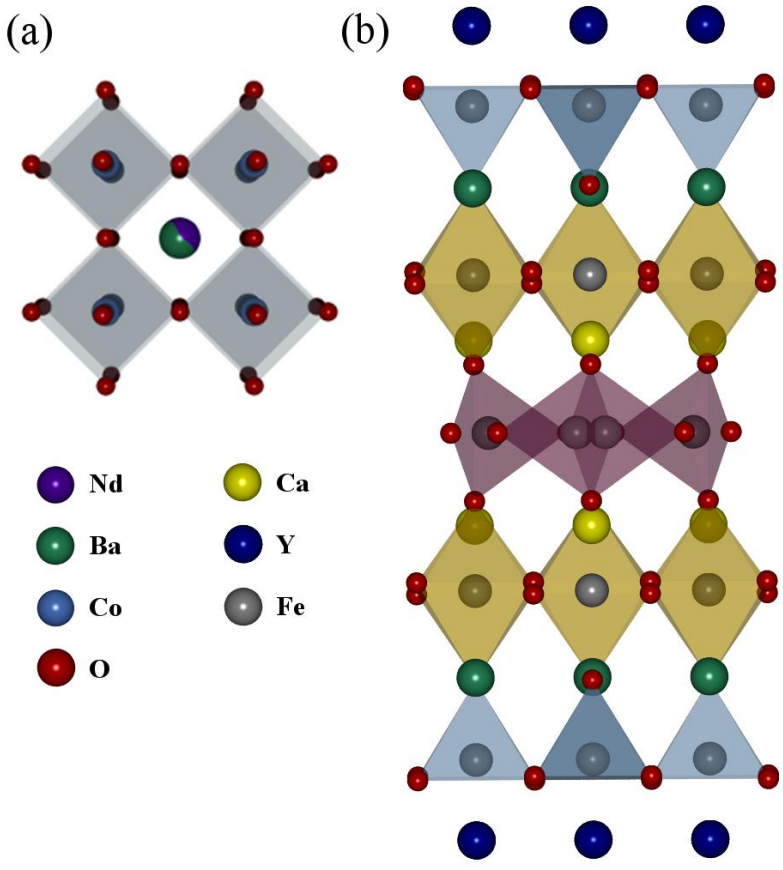

Figure 4.2: Crystal structures of (a) disordered $NdBaCo_2O_5$ with random occupancy of the cation site indicated by mixed colour central atom, and (b) $Ba_{1.7}Ca_{2.4}Y_{0.9}Fe_5O_{13}$. The iron sites in the purple polyhedra are disordered.

There are six distinct cation sites (3 perovskite A sites and 3 B sites) describing this complex material. The eight-coordinated A site is predominantly occupied by Y^{3+}, the nine-coordinated site by Ca^{2+} and the 12-coordinated site by Ba^{2+} and Fe is present in three unique B site co-ordination environments, namely tetrahedral, square based pyramidal and octahedral; the ordering of these cations leads to a layered structure in which partially oxygen deficient layers allow oxygen ion transport. The composition of the films deposited are described using the nominal stoichiometry of the target ($Ba_{1.7}Ca_{2.4}Y_{0.9}Fe_5O_{13}$). A study on the experimentally determined cation ratios to obtain this layered and ordered structure free from impurities has been previously conducted by Demont *et al.*,[1] where a nominal cation stoichiometry of $Ba_{1.7}Ca_{2.4}Y_{0.9}Fe_5O_{13}$ was found to give a phase pure material. Bulk cathodes of $Ba_{1.7}Ca_{2.4}Y_{0.9}Fe_5O_{13}$ have an area specific resistance (ASR) of $0.87\Omega cm^2$ at 700°C,[1] and with optimisation of the microstructure this has been lowered to $0.25\Omega cm^2$ suggesting that they are candidates for intermediate temperature (IT) SOFC applications.[6] This electrochemical behaviour is combined with excellent thermal stability in air and under a CO_2 atmosphere, as well as chemical stability and a good thermal expansion match with the $Ce_{0.8}Sm_{0.2}O_{(2-\delta)}$ (SDC) electrolyte. The electronic conductivity of the bulk ceramic is notably low compared with Co-containing materials such as $La_{0.6}Sr_{0.4}Co_{0.2}Fe_{0.8}O_{(3-\delta)}$ (LSCF), $La_{0.8}Sr_{0.2}CoO_{(3-\delta)}$ (LSC) and the $LnBaCo_2O_5$ systems.[7] Density functional theory (DFT) calculations on the $10a_p$ Fe-based material show that it is expected to have highly anisotropic conductivity behaviour as the 3d bandwidth and thus the electronic conductivity should be strongly enhanced in the *ab* plane.[1] This suggests the growth of this SOFC

cathode in thin film form would be advantageous, in order to exploit the complex A cation ordering-based superstructure to enhance the properties over the bulk ceramic material. An epitaxial thin film would have a single crystallographic orientation enhancing anisotropic conductivity over a ceramic sample with randomly oriented crystallites.

There are several possible oxygen diffusion pathways, with different calculated activation energies[6] in $Ba_{1.7}Ca_{2.4}Y_{0.9}Fe_5O_{13}$ which arise as a consequence of having multiple iron environments and general structural anisotropy. The pathway with the lowest activation energy (0.45eV) was found to be for longitudinal oxygen diffusion, and this compares favorably with activation energies found for another commonly used perovskite-based IT-SOFC cathode, $GdBaCo_2O_5$. The rationale behind the low energy diffusion pathway is that the system is subject to an internal activation strain, which assists in the ionic bond breaking required as part of the diffusion process. This internal activation strain itself arises from the two sub-blocks of the structure inherently having different lattice parameters, and an intergrowth of the two generates an intrinsic lattice parameter compromise, and therefore strain. Surfaces that terminate in planes perpendicular to the layers, such as the (001) and (100) planes, form reactive surfaces from cleaving strong bonds across the layer. These reactive surfaces allow fast longitudinal oxygen ion transport away from the surface.[6]

4.2 Growth Optimisation

10 layer thin films were deposited on (001) $SrTiO_3$ (STO) substrates by pulsed laser deposition (PLD) utilising a Nano PVD chamber, with a KrF COMPeX Pro Lambda Physik excimer laser with λ = 248nm. A dense pellet (90% of the theoretical density) of the 10a_p compound was prepared by Dr. Ruth Sayers at the University of Liverpool, following the procedure described by Demont *et al*.[1]

The growth conditions were optimised by investigating several parameters; growth temperature (varying the growth temperature from 750-950°C), partial pressure of oxygen (1mTorr and 10mTorr), laser energy (240-300mJ)/ fluence (0.30-0.24Jcm^{-2}) and finally the cooling procedure.

Standard $\theta/2\theta$ XRD patterns were collected on the films prepared under the different growth conditions to determine the most favourable for the formation of the 10a_p phase, with details on the two diffractometers in Chapter 2.

Dr. Ruth Sayers initially investigated the effect of growth temperature on the formation of the 10 layer film, at 1mTorr pO_2. XRD patterns of films grown at 750°C, 850°C and 950°C are shown in Figure 4.3. From this Figure it can be seen that the temperature played a crucial role in the formation of impurities, namely $BaCaFe_4O_8$ and a 3a_p phase. The 3a_p phase is based upon the ABO_3 perovskite structure from $YBa_2Fe_3O_8$,[5] that is extended to form a three-fold super structure.

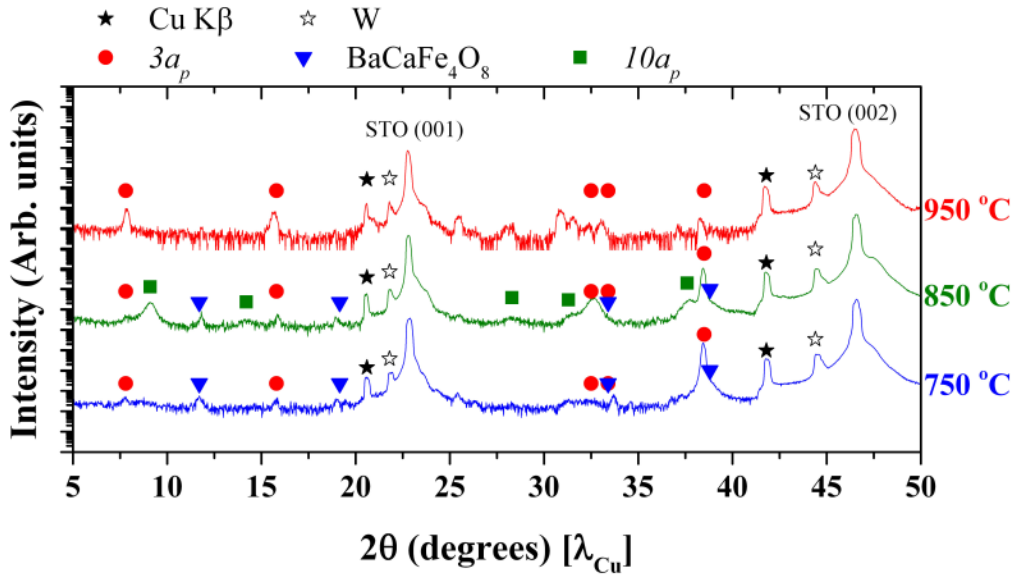

Figure 4.3: XRD patterns of the optimization of the $10a_p$ growth showing the effect the growth temperature has on the film. The film deposited at 750°C is shown in blue, 850°C in green and 950°C in red. The radiation used to collect the patterns was contaminated by Cu K_β and W components marked with asterisks. Impurities from $BaCaFe_4O_8$ are highlighted with blue triangles and peaks attributed to the $3a_p$ phase are shown by red circles. The desired $10a_p$ phase is indicated by green squares.[2]

From the temperature study performed by Dr. Sayers at 1mTorr pO_2, it was found that the 10 layer phase only formed at 850°C, and so this temperature was used as the basis for this work. Here, the temperature was also varied at 10mTorr from 850°C to 900°C to attempt to grow an impurity-free 10 layer film. Table 4.1 summarises the growth conditions used in this study.

Table 4.1 : Summary of the growth parameters varied.

Film	Substrate Temperature (°C)	pO_2 (mTorr)	Laser Fluence (Jcm^{-2})
1	850	10	0.27
2	900	10	0.27
3	850	1	0.27
4	850	1	0.30
5	850	1	0.27
6	850	1	0.24

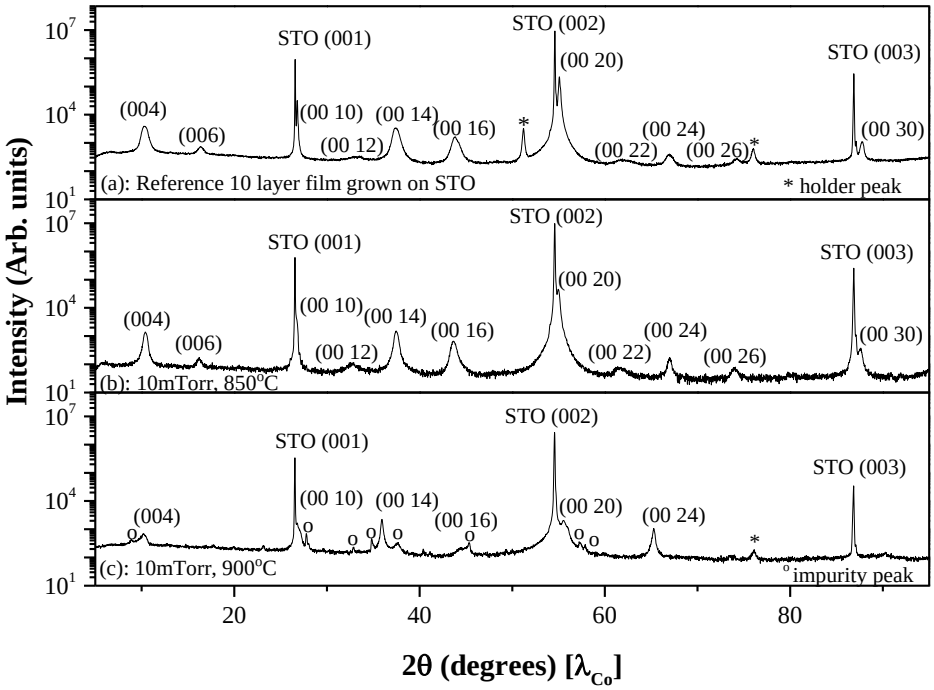

Figure 4.4: XRD patterns of the optimization of the $10a_p$ growth showing the effect the growth temperature has on the film at 10mTorr. (a) shows the optimised pattern of the 10 layer film for reference. (b) shows the film grown at 850°C and 10mTorr. (c) shows the film grown at 900°C and 10mTorr. The radiation used to collect the patterns was Co. The * represents peaks from the sample holder, and ° represents impurity phases.

From Figure 4.4 it can be seen that the film deposited at 900°C and 10mTorr shows additional peaks caused by impurities, such as the $3a_p$ phase. As a result of

this temperature study it can be concluded that the growth temperature is important to ensure the $3a_p$ phase does not form. The optimal growth temperature is 850°C (as at this temperature there were no observable peaks attributable to the $3a_p$ phase) and was used in further depositions.

Secondly, the growth of films at 1mTorr and 10mTorr was used to investigate the influence of the partial pressure of oxygen on film quality.

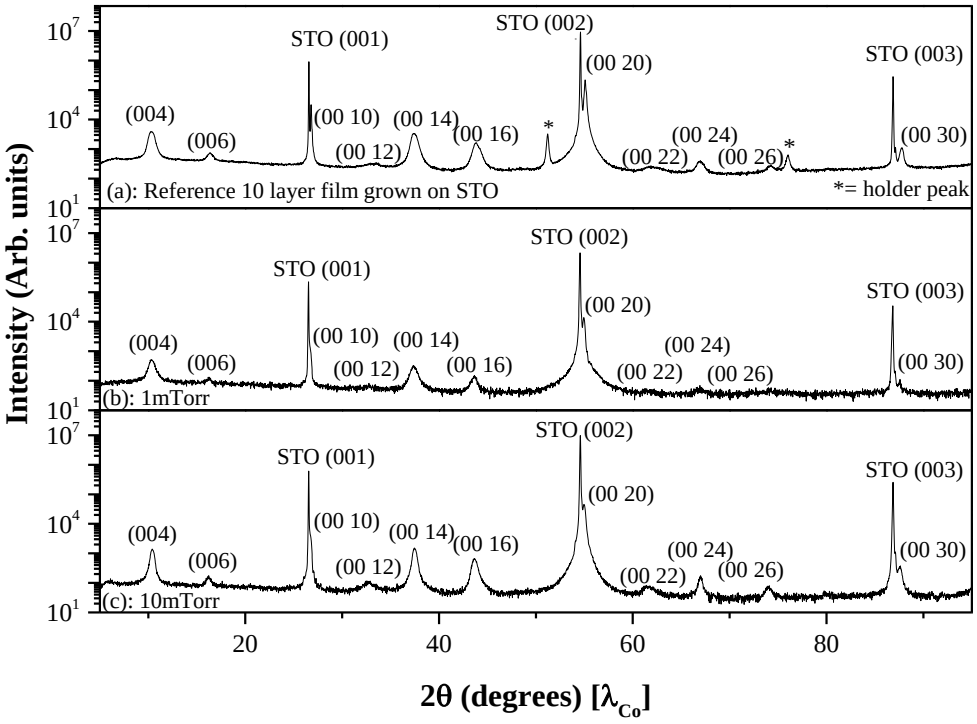

Figure 4.5: XRD patterns of the optimisation of the $10a_p$ growth showing the effect the partial pressure of oxygen has on the film. (a) shows the optimised pattern of the 10 layer film for reference. (b) shows the film grown at 1mTorr. (c) shows the film grown at 10mTorr. The radiation used to collect the patterns was Co. The * represents peaks from the sample holder.

The $3a_p$ phase formation is not affected by an oxygen partial pressure of either 1mTorr or 10mTorr, as no additional peaks are present in the patterns seen in

Figure 4.5. An oxygen partial pressure of 1mTorr was used for the remaining study to enable the cathode material deposition to be consistent with the electrolyte growth conditions discussed in Chapter 5.

The laser fluence was varied to determine the optimum value for phase pure 10 layer growth. Providing that the laser energy and the laser spot size are known the growth fluence, or energy density on the target, can be calculated using the following equation:

$$\Phi = \frac{E}{A} \qquad \text{Eqn. (4.1)}$$

Where Φ is the laser fluence in Jcm^{-2}, E the energy inside the chamber in J and A the area of laser spot in cm^2.

The area of the laser spot was measured by placing fax paper in the laser path at the target position, which is then marked by one laser pulse. This then gives the area of the laser spot size, in this case the spot area is $0.05 \pm 0.01 cm^2$, based on a rectangular beam profile formed by passing the beam through optical components such as lenses and apertures. To determine the laser energy a Coherent laser energy meter was placed in the laser path. When the laser was set to 270mJ the energy inside the chamber was measured to be 13.5mJ, the difference in energy between source and chamber is expected due to losses incurred through the laser optics. The laser passes through mirrors, windows, lens and apertures all of which reduce the laser energy.

Set energies of between 240 and 300mJ were used to grow 10 layer films, giving a fluence range of 0.24 - 0.30Jcm^{-2} , with resultant XRD patterns shown in Figure 4.6.

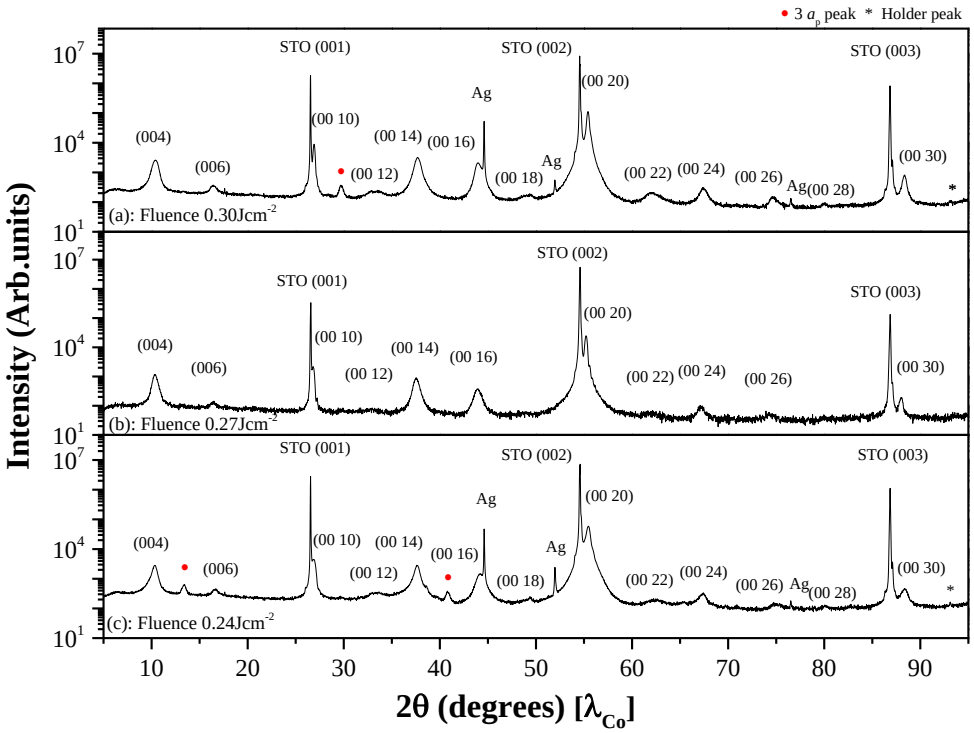

Figure 4.6: XRD patterns of the optimization of the 10a_p growth showing the effect the change in fluence has on the growth. (a) Fluence of 0.30Jcm^{-2}, (b) fluence of 0.27Jcm^{-2} and (c) fluence of 0.24Jcm^{-2}. The * represents peaks from the sample holder, red circles indicate peaks from the 3a_p phase, Ag represents peaks from the silver DAG used to adhere the substrate to the heater block.

When the laser energy was set to 300mJ additional peaks formed (Figure 4.6 (a)), these peaks were attributed to the 3a_p phase. Equally when the laser energy was too low, at 240mJ, the 3a_p phase also forms. The laser energy proved critical to the formation of the 10a_p film and 267mJ was found to be the optimal laser

energy, and was used for all further growths. The silver peaks that are present in the film scans (Figure 4.6) are a result of the silver DAG (from Agar Scientific) that was used to adhere the substrates to the heater block.

A thorough investigation into the cooling procedure was undertaken. Three variables were considered in the cooling procedure; oxygen pressure (1×10^{-3}Torr - $1.5 \times 10^{+2}$Torr); timing (setting the pO_2 or starting the cooling first); rate of cooling (manually switching off the heater, or using a controlled cooling rate of 30°Cmin^{-1}). The cooling procedure was split into three different methods, the cooling conditions are summarized in Table 4.2 with Figure 4.7 showing an overview of all the XRD patterns to make comparison across the changing conditions clearer.

Table 4.2: Summary of cooling procedure conditions.

Film	Oxygen Pressure /Torr	Procedure order
A	1×10^{-3}	At growth pressure, cooling started by manually switching off heater
B	1×10^{-3}	At growth pressure, cooling started at 30°Cmin^{-1}
C	$1.5 \times 10^{+2}$	Pressure set then cooling started by manually switching off heater
D	$1.5 \times 10^{+2}$	Pressure set then cooling started at 30°Cmin^{-1}
E	$1.5 \times 10^{+2}$	Cooling started at 30°Cmin^{-1} then pressure set and cooling rate changed by manually switching off heater
F	$1.5 \times 10^{+2}$	Cooling started at 30°Cmin^{-1} then pressure set and cooling rate remains at 30°Cmin^{-1}

Films A and B were cooled in the growth oxygen pressure (1mTorr) at either 30°Cmin^{-1} (slow rate) or by manually turning off the heater (fast rate). Films C

and D were exposed to an increased oxygen pressure (1.5 x 10^{+2}Torr) after growth and then cooled at the fast and slow rate, respectively. It was observed that by increasing the oxygen pressure the chamber was cooled to around 420°C before the set pressure was obtained. As a result, a further cooling procedure was investigated for films E and F where the films had controlled cooling at 30°Cmin^{-1} while the oxygen pressure was set to 1.5 x 10^{+2}Torr. Having reached this pressure the films were then cooled to room temperature at either the fast or slow rate.

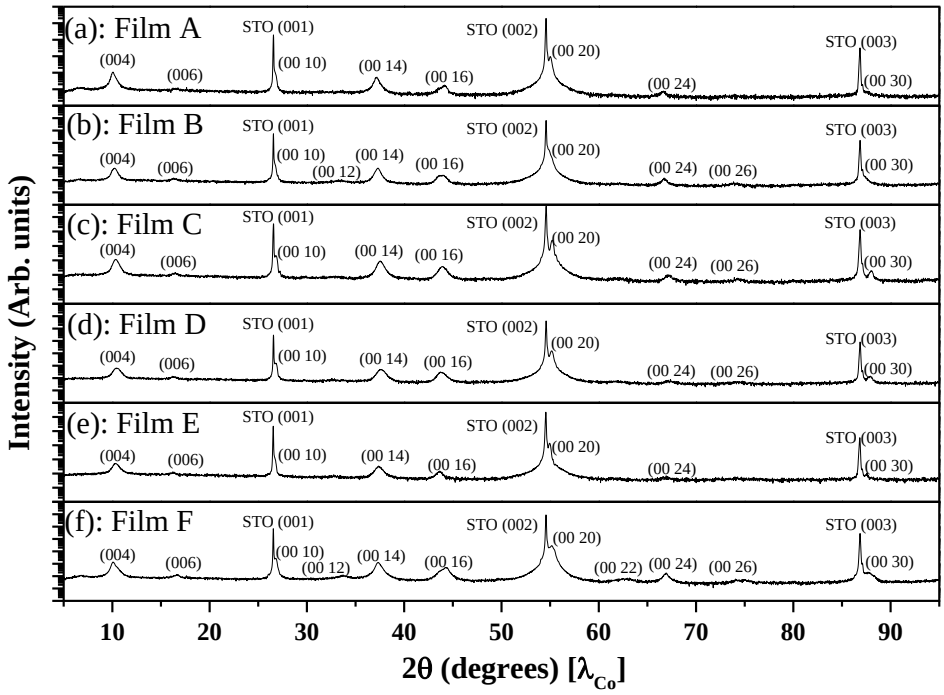

Figure 4.7: (a) - (f) XRD patterns of the films described in Table 4.2. The y-axis is logarithmic.

From Figure 4.7 the XRD patterns A through F clearly show that no $3a_p$ phase is formed in any of the films. The cooling procedure is not thought to be critical to

the formation of this $3a_p$ phase. This hypothesis is further supported by the results of the thermal stability test as reported in Section 4.4.1.

The optimised growth conditions were found to be a deposition temperature of 850°C with a laser energy of 267mJ which gives a fluence of $0.27Jcm^{-2}$, a frequency of 5Hz and pO_2 of 1mTorr. The cooling procedure could be varied and still obtain a pure $10a_p$ film. These optimised growth conditions were then used to grow a set of films for further structural analysis, which is discussed in Section 4.3, and for physical measurements in Section 4.4.

4.3 Structural Characterisation

4.3.1 XRD

In addition to the θ/2θ XRD patterns further analysis was carried out including rocking curves (RCs), reciprocal space maps (RSMs), and X-ray reflectivity (XRR). The out-of-plane and in-plane lattice parameters were determined by measuring appropriate diffraction peaks using either coupled symmetrical θ/2θ scans or by measuring RSMs. The RSMs in this section were carried out by Dr. Jonathan Alaria. The deposition rate of the $10a_p$ films was obtained by measuring XRR on a series of thin films grown with various numbers of pulses.

XRR was utilized to determine the thickness of the 10 layer films, for this technique the films need to be thinner than about 80nm in order to achieve clear oscillations that can be fitted to simulation. Thicknesses greater than 100nm typically do not give strong enough oscillations for fitting.[8]

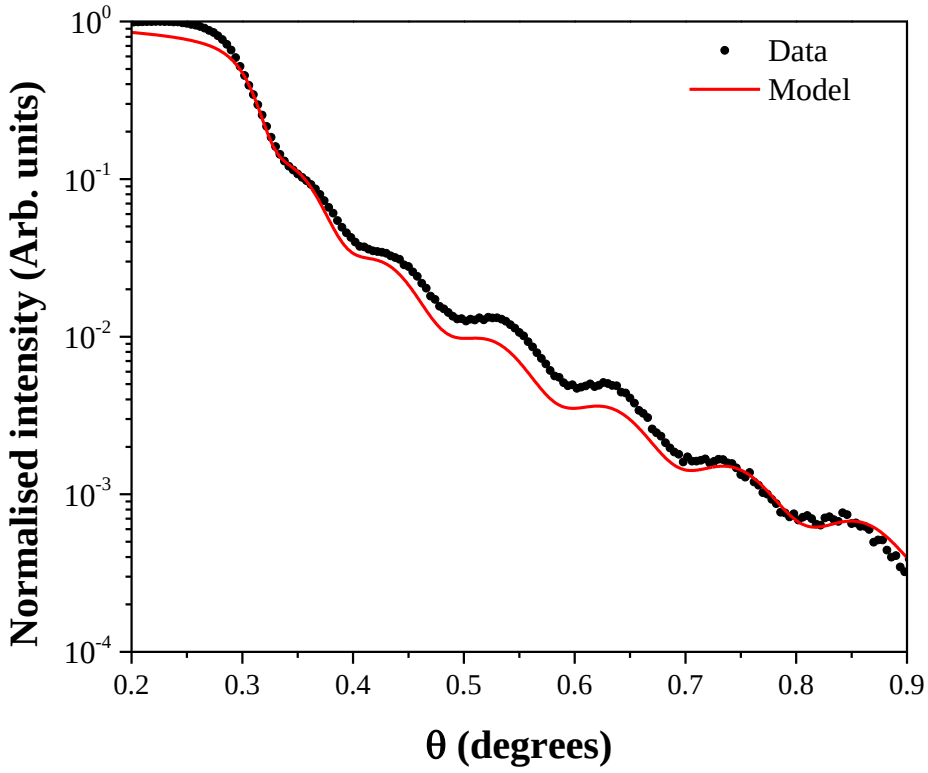

Figure 4.8: XRR of a typical 10 layer film with the measured data in black and the simulated model in red.[2] IMD software[9] was used to model the data by Dr. Jonathan Alaria.

The thickness of the 10 layer film shown in Figure 4.8 was found to be 35.7nm. The observation of Kiessig fringes is an indication of a film with sharp interfaces. IMD software[9] was used to model the data by Dr. Jonathan Alaria at the University of Liverpool.

High Resolution X-ray Diffraction (HRXRD) was conducted by Dr. Jonathan Alaria around the (00 20) peak of the 10 layer film show Pendellosung fringes, see Figure 4.9, which can be fitted using the sinc function to determine the

thickness of the film. The film shown in Figure 4.9 is 25 monolayers thick, which equates to approximately 95 ±5nm .

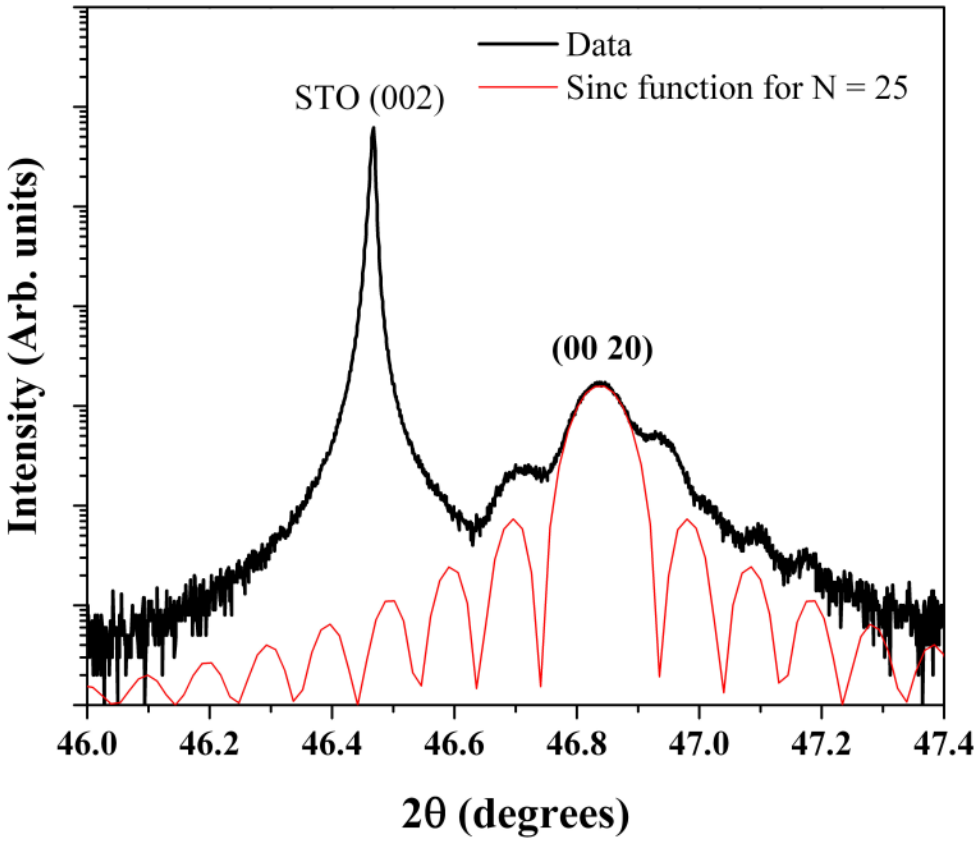

Figure 4.9: HRXRD around the (00 20) 10 layer peak and the STO (002).[2]

In addition to this SEM, performed by Dr. Ruth Sayers, was used to confirm the thickness of a thicker film to establish if the growth rate was linear ensuring accuracy on the thicker films used for AC impedance, as reported in Section 4.4.2.

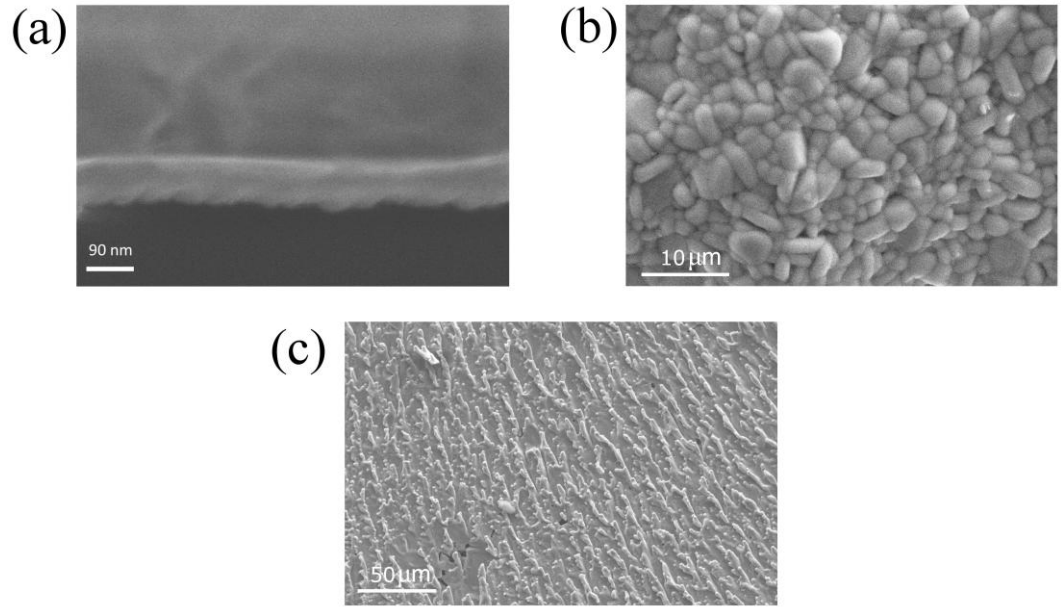

Figure 4.10: (a) SEM, performed by Dr. Ruth Sayers, of the 10 layer film with a thickness of ~ 90nm, and STO substrate, (b) and (c) are SEM images of the 10 layer PLD target.

The SEM image shown in Figure 4.10 (a) shows the 10 layer film is around 90nm thick, it is also clear that the surface of the film is not perfectly smooth. The main focus of the SEM image is to support the HRXRD results taken around the (00 20) 10 layer Bragg peak. The fitted Pendellosung fringes from the HRXRD pattern in Figure 4.9 gave a thickness of 95nm. This is in good agreement with the thickness of 90 ±5nm determined from the cross-sectional SEM image in Figure 4.10 (a).

SEM images were also taken from the 10 layer PLD target and two of these images can been seen in Figure 4.10 (b) and (c). The images show the grain microstructure of the surface of the PLD target, indicating grain sizes of between 1-5µm and typically round / oblong shape grains. The target is also dense, being

90% of the theoretical density, and the target significantly reduced in size upon sintering, although there were some cracks present.

Omega scans were carried out on the STO substrate and the 10 layer film to determine the crystalline quality of the film.

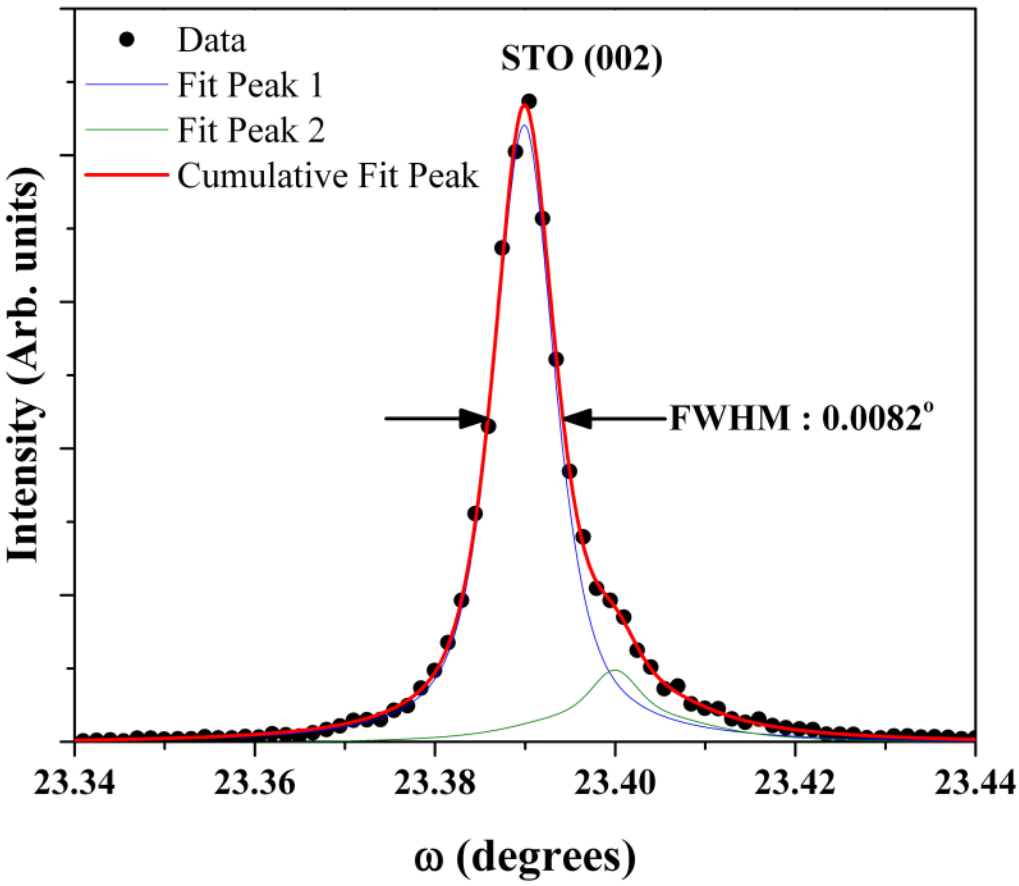

Figure 4.11: Rocking curve of the STO (002) peak showing a full width half maximum of 0.0082°.[2]

The observed shoulder on the STO rocking curve (RC) (Figure 4.11) is due to the presence of slightly misoriented twin crystals and is commonly observed in STO substrates.[10]

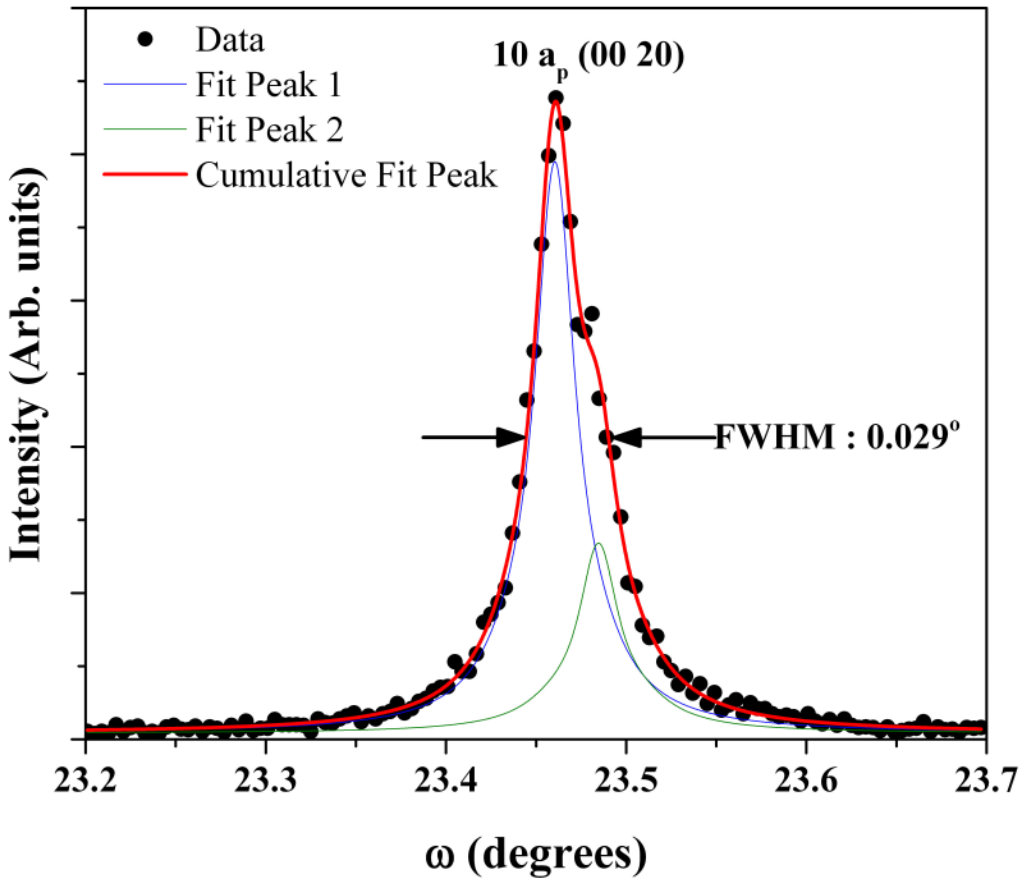

Figure 4.12: Rocking curve of the 10 layer (00 20) peak showing a full width half maximum of 0.029°.[2]

The omega scan from the 10 layer (00 20) peak (Figure 4.12) displays a similar shoulder to that of the STO (002) indicating that the film grows oriented onto each twin. The narrowness of the FWHM emphasizes the high degree of crystalline quality.

Texture studies including pole figures and reciprocal space maps, have also been carried out on the 10 layer film.

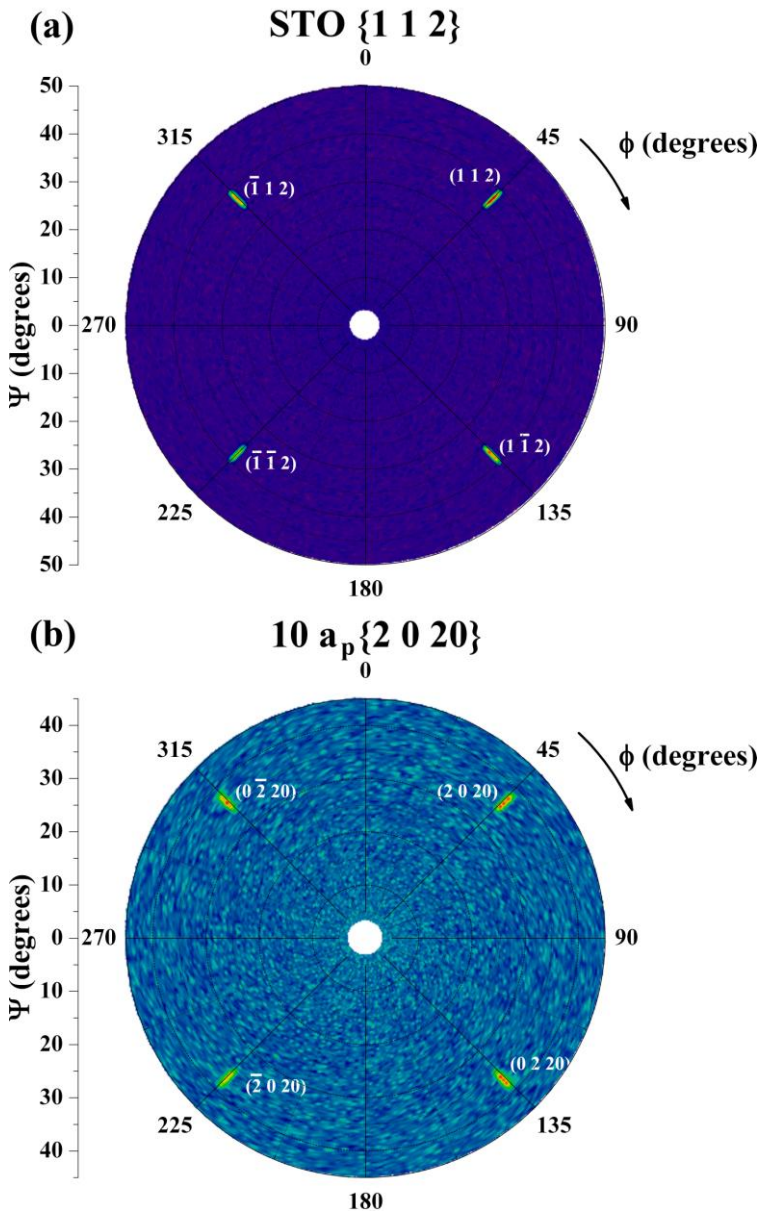

Figure 4.13: (a) Pole figure of STO (112) reflection and the (b) 10 layer film (2 0 20) reflection.[2]

The pole figures shown in Figure 4.13 could be interpreted in three different ways. Firstly, the film could be considered to be orthorhombic and not twinned. If this were the case then we would expect to see 4 peaks on Figure 4.14, 2 peaks corresponding to (2 0 20) and 2 peaks to (0 2 20).

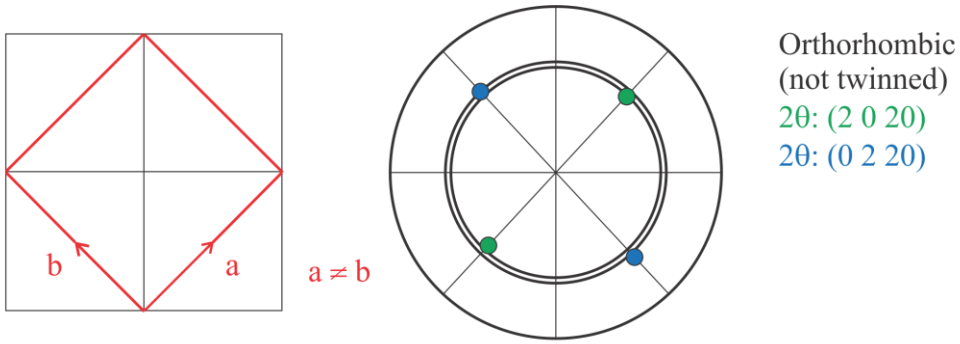

Figure 4.14: Expected pole figure for an orthorhombic and not twinned system.

Secondly if the film were orthorhombic and twinned then as is displayed in Figure 4.15 we would expect to see 8 peaks from both the (2 0 20) and the (0 2 20). However due to the resolution of the scan we would be unable to distinguish the 8 peaks from the 4 peaks, and it would therefore appear as in Figure 4.14.

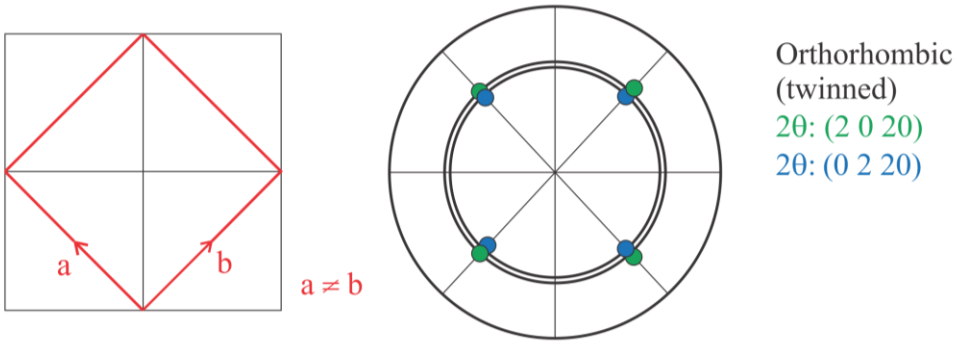

Figure 4.15: Expected pole figure for an orthorhombic and twinned system.

Thirdly we could expect the film to be tetragonal where d(2 0 20) == d(0 2 20), as shown in Figure 4.16.

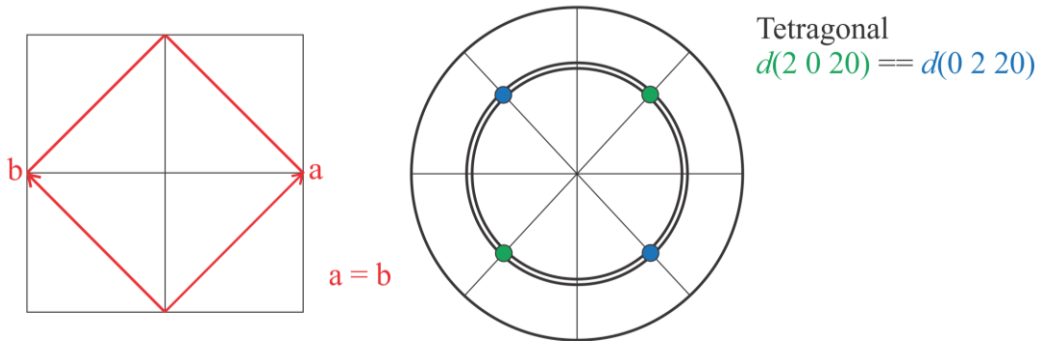

Figure 4.16: Expected pole figure for a tetragonal system.

From these three scenarios we are unable to conclude between them from the experimental pole figures shown in Figure 4.13. To solve the pole figure interpretation puzzle further analysis was required, and reciprocal space maps were utilized for this.

A further thought experiment is utilised here to explain how the RSMs will help to decide which scenario from the pole figure explanation is correct. If the film is tetragonal then $a = b$, as a result in the RSM we would expect the (20 20) and the (02 20) to be equidistant as shown in Figure 4.17.

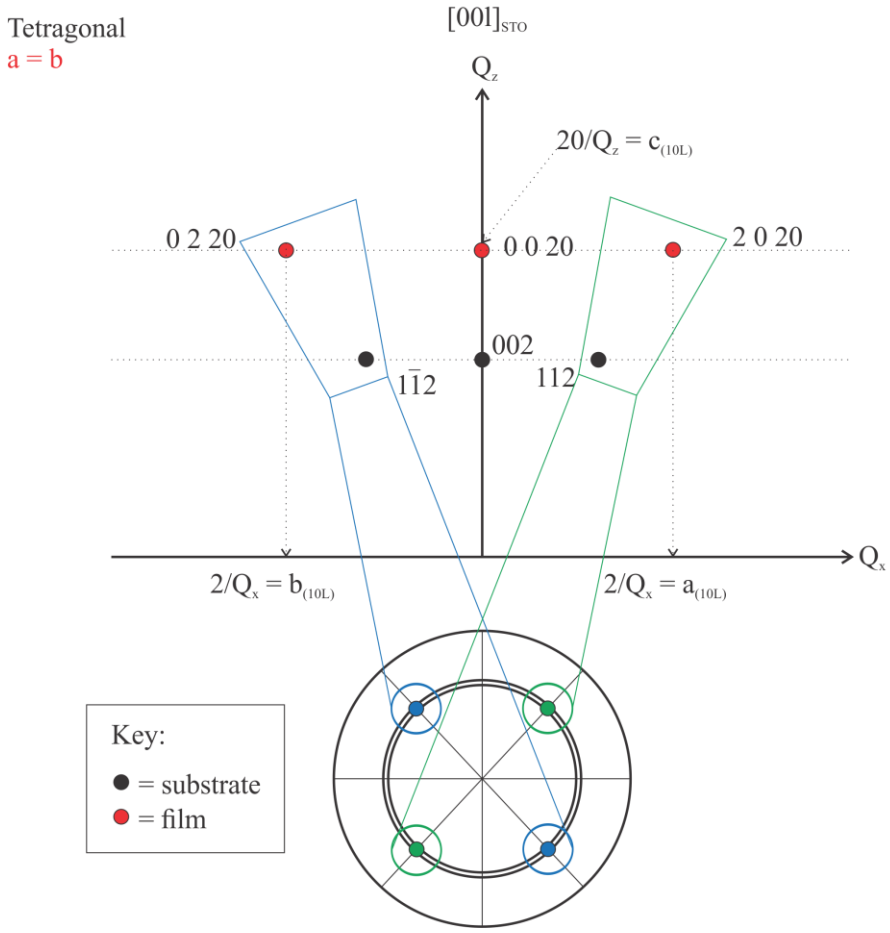

Figure 4.17: Expected RSM for a tetragonal system.

However if the film is orthorhombic and not twinned we would expect $a \neq b$, but for there also to be one peak for the (20 20) and one for the (02 20), depicted in Figure 4.18.

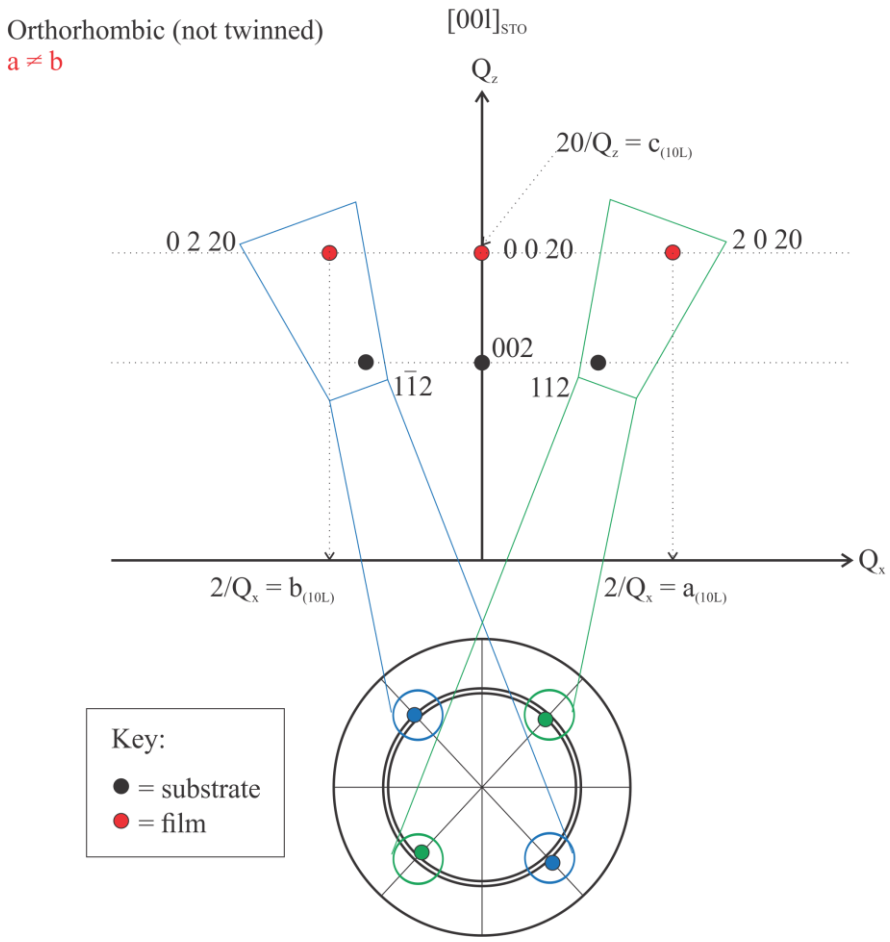

Figure 4.18: Expected RSM for an orthorhombic and not twinned system.

If the film was twinned and orthorhombic then we would expect to see two additional peaks coming from the twinning as can be seen in Figure 4.19.

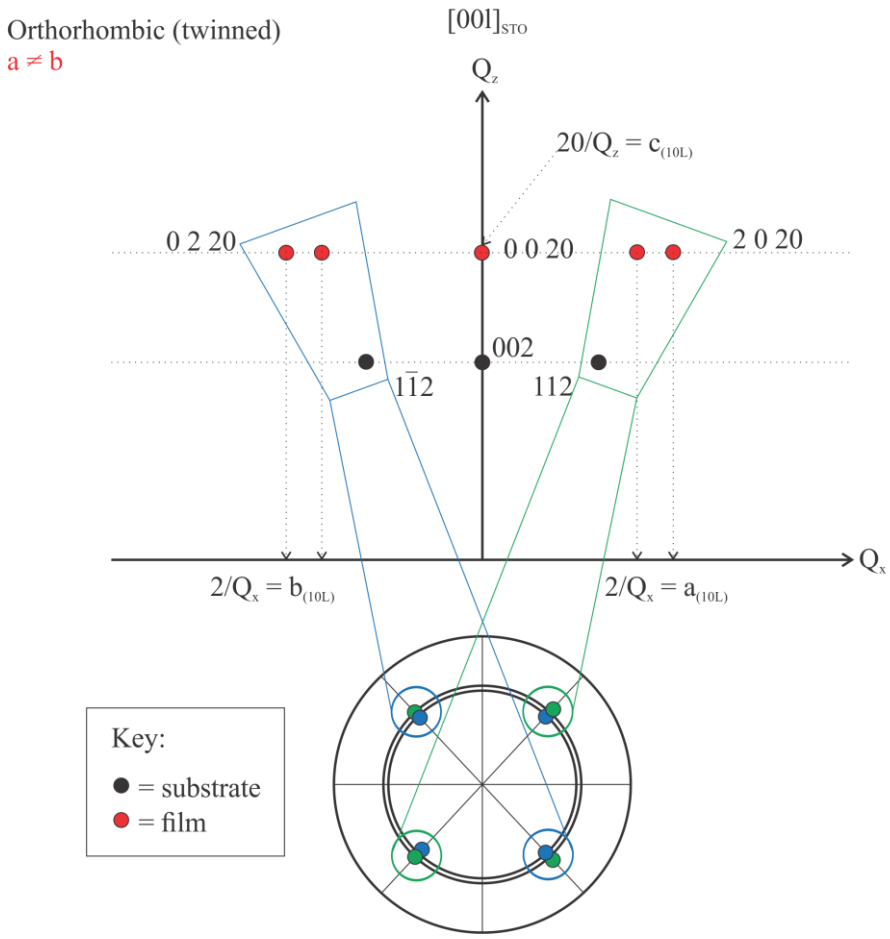

Figure 4.19: Expected RSM for an orthorhombic and twinned system.

To confirm the potential epitaxial relationship between the substrate and the film, and the in-plane symmetry of the film, high-resolution X-ray diffraction measurements were performed. Figure 4.20 shows a RSM of the STO (0 0 2) and the 10 layer (0 0 20) reflections. It can be seen that the substrate and film peaks are vertically aligned, confirming the growth direction as the long axis of the 10 a_p unit cell as well as the low mosaicity of the film. To obtain information on the in-plane lattice parameter asymmetric RSMs were measured around the STO (1 1 2) and the (1 $\bar{1}$ 2) reflections as presented in Figure 4.20 (a) and (c).

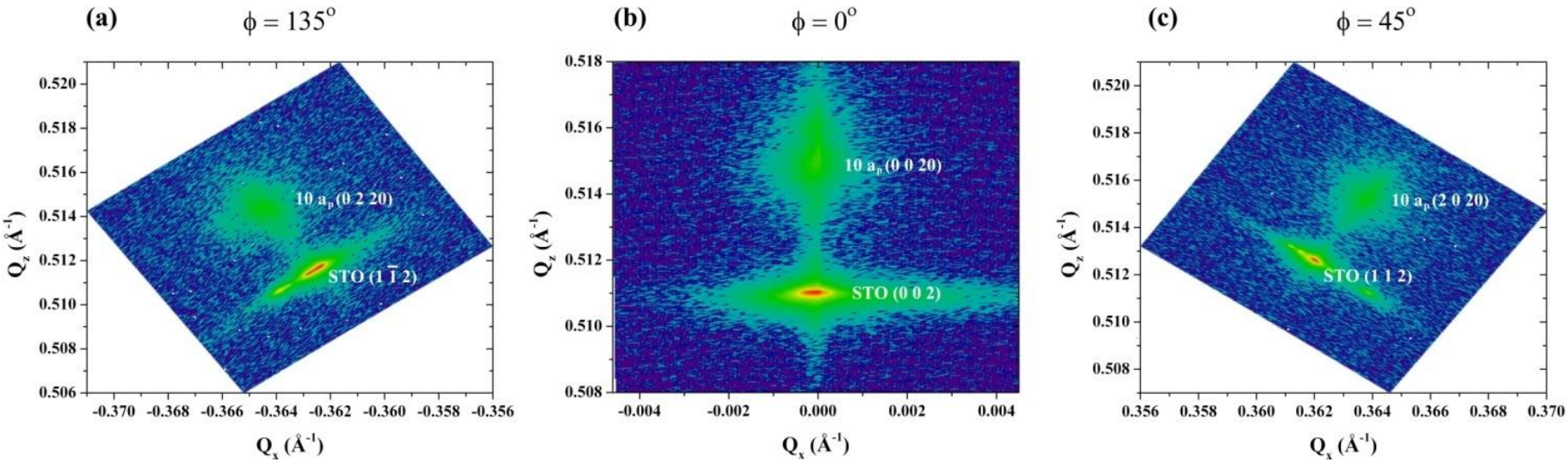

Figure 4.20: RSM of the STO substrate and the 10 a_p film. (a) around the (0 2 20) reflection (b) around the (0 0 20) reflection, (c) around the (2 0 20) reflection.[2]

This RSM data for the film would be expected to be non-equivalent if the symmetry was orthorhombically distorted like the bulk phase, with slightly different Q_x values for the film peaks (0.364Å^{-1} and 0.361Å^{-1} for the (2 0 20) and (0 2 20) reflections respectively). However, both in-plane lattice parameters are found to be equivalent with a value of a_T = 5.48(3)Å, leading to the assignment of tetragonal symmetry within the resolution of the measurement, explaining the apparent 4-fold symmetry observed in the Pole Figure (Figure 4.13). The epitaxial relationship shows the film grows with a 45° rotation in-plane to align the perovskite subcell parameters of the film with the STO perovskite unit cell. The small orthorhombic distortion observed in the bulk (c/a = 1.009) is not observed within the error of the measurements employed for the thin film grown on a cubic substrate.

4.3.2 TEM

The transmission electron microscopy (TEM) work was conducted by Dr. Simon Romani at the Nanoinvestigation Centre at Liverpool, Dr. Q. M. Ramasse at SuperSTEM Laboratory, STFC Daresbury Campus, and Dr. T. J. Pennycook at SuperSTEM Laboratory, STFC Daresbury Campus and at the University of Oxford. The epitaxial nature of the thin film can be seen in the High Angle Annular Dark Field (HAADF) Scanning Tunnelling Electron Microscopy (STEM) image shown in Figure 4.21. The STO substrate appears in the top right corner of this Z-contrast image, and can be identified by the interpenetrating cubic sublattices of the brighter Sr and darker TiO columns. Tracing rows of atomic columns diagonally from the top right perpendicularly across the interface in this

image, one can see the interface is coherent. Every one of these rows of columns continues from inside the STO, straight across the interface and all the way through the film visible in the image. The Fast Fourier transform (FFTs) of both the substrate and film, shown in (b) and (c) respectively, can be used to determine the zone axis, which is found to be (1 $\bar{1}$ 0) for the $10a_p$ film, and (0 1 0) for the STO substrate, confirming the 45° rotation of the film in-plane and the growth direction. The 10 layer periodicity can be seen in Figure 4.21 (c) with the five expected superstructure reflections from the body-centred ten layer superstructure observed along the (0 0 1) axis.

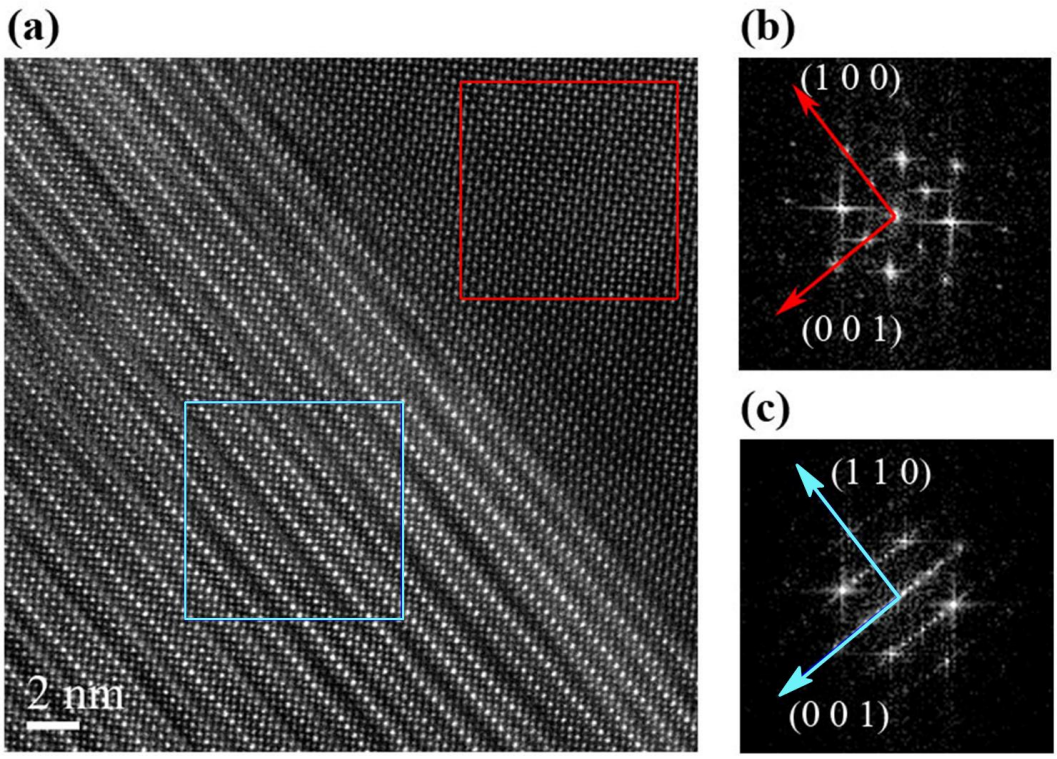

Figure 4.21: (a) HAADF STEM image (8cm camera length) showing the interface between the $10a_p$ film and the STO substrate. Fast Fourier transform (FFT) images of the substrate (b) and film (c).[2]

The complex layered structure of the material is shown in detail in Figure 4.21. The HAADF STEM image in Figure 4.21 (a) was filtered using an annular mask in the FFT of the raw image to remove environmental noise sources. The qualitative information remains intact, with the higher localized intensities indicative of higher average atomic number in the associated atom column along the beam direction. The registration of higher and lower Z atom rows with the structural model, shown alongside Figure 4.22 (a), provides a clear match to the entire unit cell.

Five types of atomic columns are expected: $Ba_{0.90}Ca_{0.08}Y_{0.02}$, $Ca_{0.34}Y_{0.66}$, $Ba_{0.05}Ca_{0.80}Y_{0.15}$, FeO and pure O columns with average atomic numbers of 52.8, 32.5, 24.7, 17.0 and 8.0 respectively. As the intensity in the HAADF images varies roughly as the square of the atomic number, there should be significant contrast between the different layers. Figure 4.22 (a) shows, horizontal rows of the brightest atomic columns bounding layers containing either 3 or 5 rows of less intense columns, creating 4 row building blocks ($Ca_2Fe_2O_5$) and 6 row ($YBa_2Fe_3O_8$-like) building blocks respectively. The 10 layer unit cell is highlighted in blue. Blurring of two sets of atom columns within the experimental image in Figure 4.22 (a) is due to disorder associated with the Fe^{3+} tetrahedral layer, as depicted in the structural schematic (purple polyhedra) and confirmed in Figure 4.22 (b), which shows a simulated HAADF-STEM image using the computer program QSTEM.[11]

Defects can be seen in the HAADF image shown in Figure 4.22 (c). On the left side of this image the intensities of the columns are consistent with the expected 10 layer stacking continuing for at least 5 unit cells starting from the top of the image. However, the majority of the rows in this image starting with very high intensity on the left do not maintain that intensity much more than halfway across the image to the right. Most often, the row becomes less intense on the right side, and the row below it takes on the high intensity corresponding to the Ba rich columns. Using the width between successive rows of the brightest columns as a guide, it appears the steps often correspond to a change from the one kind of building block on the left to the other. The layering on the right side of the image is harder to determine in general though, perhaps due to the propagation of the stacking fault through the thickness of the sample. The perovskite structure is maintained over long distances however, with the defects appearing to affect the occupation of the sites in the crystal rather than their general arrangement. These step-like defects can be assigned to steps in the substrate and also the presence of mixed surface SrO and TiO_2 surface terminations, which will change the initial layer in the perovskite superstructure from BO_2 to AO respectively.

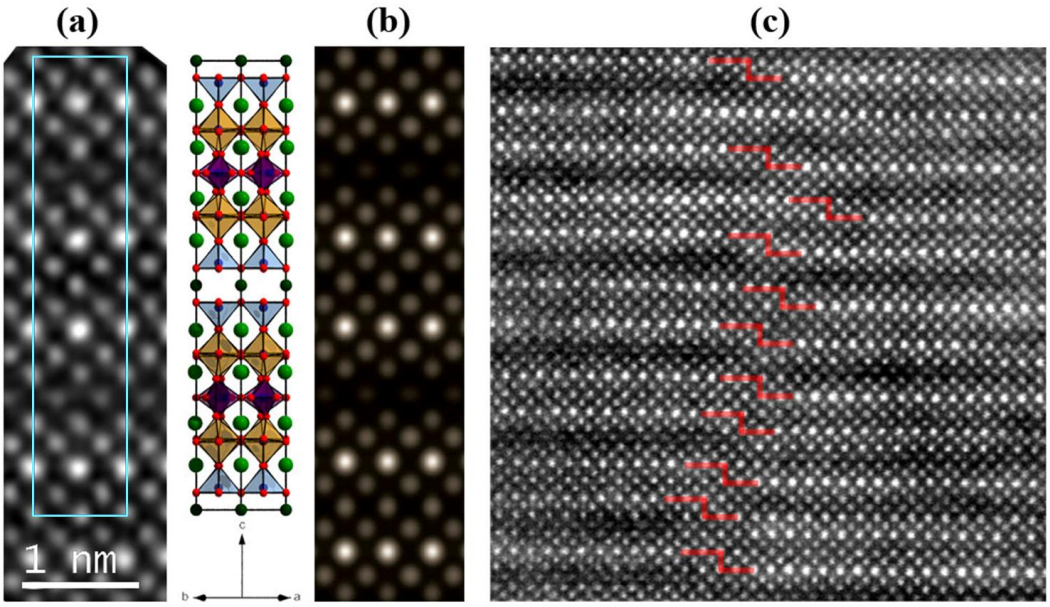

Figure 4.22: (a) FFT filtered HAADF STEM image (12cm CL, JEOL 2100 FCs), with a scaled structural schematic of the $10a_p$ unit cell alongside where dark green atoms are yttrium, red atoms are oxygen, blue atoms are iron and light green atoms are disordered calcium and barium. An unfiltered version of this image is shown in Figure 4.23 (a) and (b) simulated HAADF-STEM image viewed down the (0 1 0) direction of the $10a_p$ unit cell, (c) wider view showing stacking fault of one atomic step in the 10 layer sequence (indicated by red lines) – this image was collected on the Nion UltraSTEM.[2]

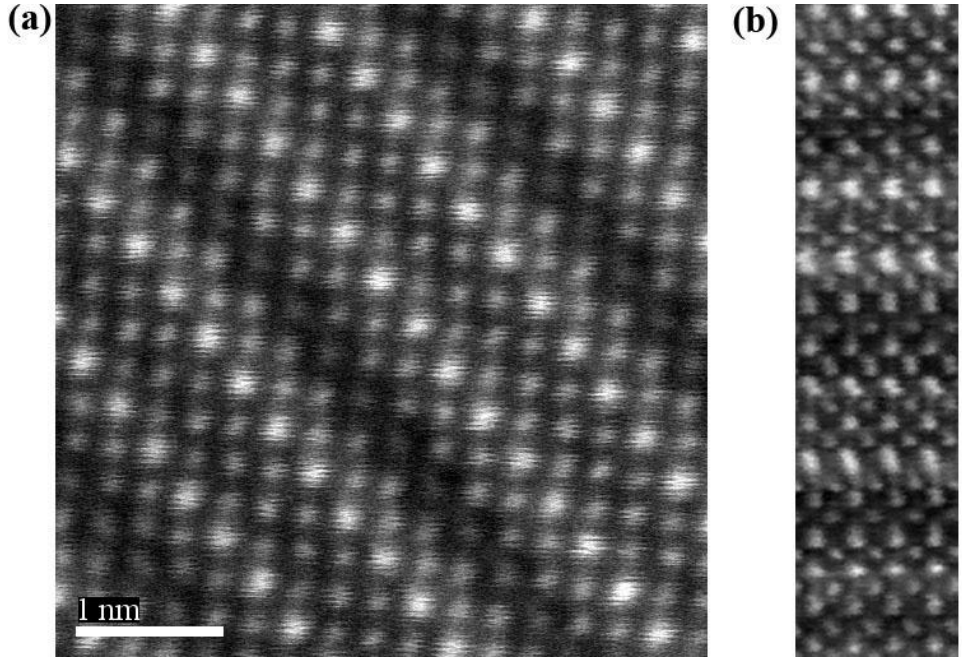

Figure 4.23: (a) and (b) Unfiltered HAADF STEM image used in Figure 4.22 (a), (b) HAADF signal recorded simultaneously with EELS spectra presented in Figure 4.24 (b)-(e).[2]

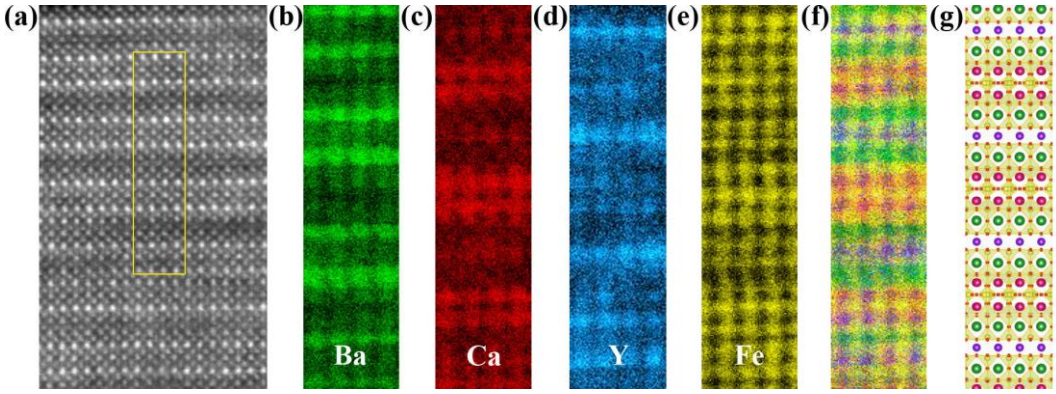

Figure 4.24: Atomic resolution Z-contrast STEM images and elemental maps. Spectra were acquired in a 70 by 280 pixel grid in the region indicated by the yellow box in survey image (a), with an acquisition time of 0.01 seconds per spectrum. (b)–(e) represent the EELS maps of Ba M_{45}, Ca L_{23}, Y M_{45} and Fe L_{23}, respectively. (f) Colour overlay of the individual maps, with green, red, blue and yellow channels representing Ba, Ca, Y and Fe, respectively. (g) Scaled structural model of the $10a_p$ unit cell. The colours were chosen to match that which one would expect to see in the composite Electron Energy Loss Spectroscopy (EELS) map for a given type of cation column according to the refined cation site occupancies.[2]

Electron Energy Loss Spectroscopy (EELS) spectrum imaging was performed to determine the chemical identities of the columns forming the 10 layer structure. Spectra were acquired in a 70 by 280 pixel grid across the region indicated by the yellow box in Figure 4.24 (a) with an acquisition time of 0.01 seconds per pixel. The HAADF signal was recorded simultaneously with each spectrum, forming the Z-contrast image shown in Figure 4.23 (b). The image facilitates an accurate spatial registration of the elemental maps. Some elongations and distortions can be seen in the image due to sample drift, but the individual atomic columns are clearly resolved. Figure 4.24 (b) through (e) map the intensities of the Ba M_{45}, Ca L_{23}, Y M_{45} and Fe L_{23} EELS edges respectively. The final map shown in Figure 4.24 (f) is a colour overlay of the individual maps, with the green, red, blue and yellow channels representing the respective Ba, Ca, Y and Fe intensities. The spectra were acquired by scanning from left to right in rows starting from the top of the yellow box in Figure 4.24 (a) and progressing down one pixel at a time. As can be seen by the presence of elongated atoms in the HAADF image acquired during the acquisition of the spectrum image, the sample drifted downwards in the plane of the image during the acquisition. Because of the drift, the lattice seen in the spectrum image is stretched in this direction.

Figure 4.24 (g) displays a model of the structure based on refined structure of the bulk material, scaled to match the magnification of the EELS map. The atoms in the model have been coloured to indicate the overall occupation of each type of site throughout the material rather than to indicate the precise locations of any dopant atoms.

The correct proportions have been used in the model, so the model and the maps do not align perfectly along the whole length from top to bottom due to the spatial drift of the microscope during acquisition. It is, however, clear from the side-by-side comparison of the model and the composite map that the expected 10 layer ordering is present in the thin film. The first row of atomic columns at the top of the spectrum image appear among the brightest in the HAADF image, and EELS indicates they are indeed Ba rich, showing strongly green in the composite map, consistent with their identification as $Ba_{0.90}Ca_{0.08}Y_{0.02}$ columns. Following these are a row of Fe rich columns, then a row of columns rich in both Ca and Y, then another row of Fe rich columns completing the first 4 layer building block of the ten layer structure. As Ca shows in the red channel and Y in the blue channel in the composite map, the fact that the columns containing both in this first 4 layer building block appear dark purple is consistent with the expectation that these columns are $Ca_{0.34}Y_{0.66}$. The second 6 row building block of the 10 layer structure can be seen to follow the first building block as expected with a bright green Ba rich row followed by three rows of yellow Fe rich columns interspersed by 2 rows of columns appearing mostly red, but with some areas of light purple, consistent with what one would expect for $Ba_{0.05}Ca_{0.80}Y_{0.15}$.

4.4 Physical Properties

4.4.1 Thermal Stability

The stability of the 10 layer film was analysed by heating the film to 600°C with a heating rate of $3°Cmin^{-1}$. Once the film reached 600°C it dwelled at temperature

for 200 hours. The 10 layer stability test was designed to test the film at SOFC operating temperature, 600°C, for a reasonable duration of 200 hours.

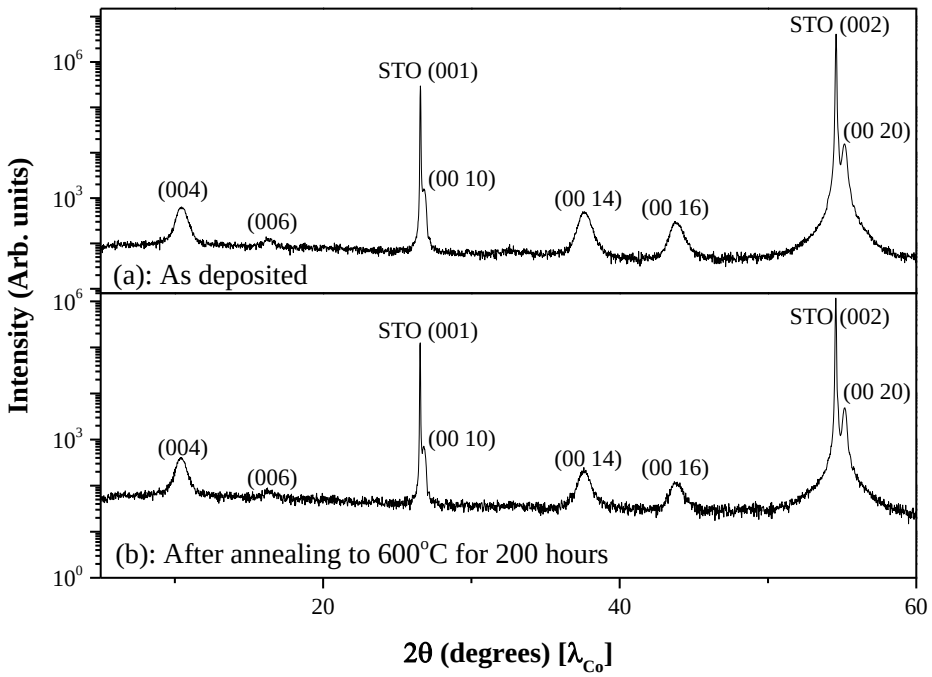

Figure 4.25: XRD patterns of the 10a_p film before and after annealing to 600°C for 200 hrs.

The film was annealed for 200 hours at 600°C in air also shows no additional peaks after the thermal stability measurement. Therefore it can be concluded that the 10 layer films are stable at 600°C in flowing oxygen.

4.4.2 AC Impedance

AC impedance spectroscopy was conducted in a 2-probe in-plane geometry; sputtered gold electrodes were used for the contacts, with gold wires attached using a small spot of gold paste. The gold paste was dried at 200°C for 2 hours in air, with a heating and cooling rate of 3°Cmin^{-1}. The film was then heated slowly

at 3°Cmin^{-1} to 600°C in oxygen and AC impedance measurements were made on cooling to 200°C. The conductivity was measured over the frequency range 0.01Hz to 1MHz, and in the temperature range 200°C to 600°C in flowing oxygen (1 atm O_2). The thin film was left to equilibrate at each temperature for 90 minutes prior to each conductivity measurement, which was found to be sufficient to stabilise the conductivity. A Solatron 1255B Frequency Response Analyser (FRA) in conjunction with a Solartron 1296 Dielectric interface and SMaRT software was used to carry out the measurements. The collected data was analysed using the Z-view software (Scribner Associates). The Nyquist plots of the 10 layer AC impedance cooling data and equivalent circuit model (ECM) are shown in Figure 4.26.

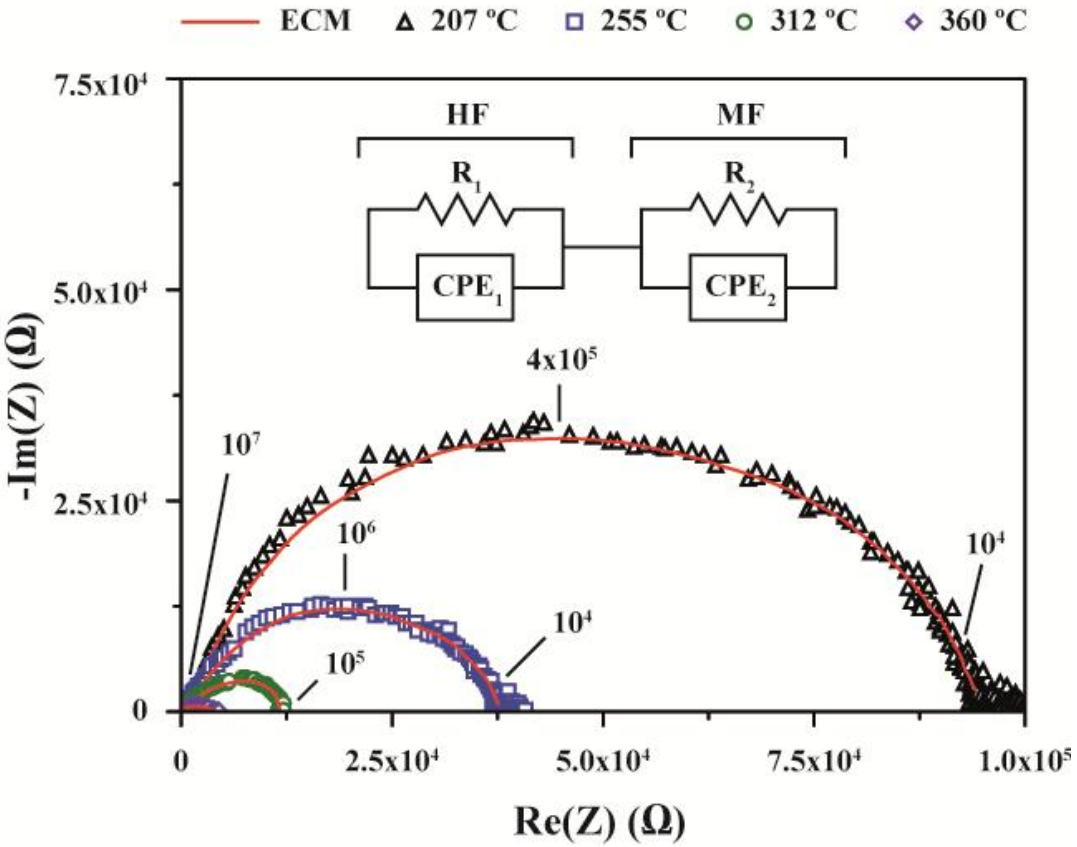

Figure 4.26: Experimental arcs, and fits to the equivalent circuit model (ECM) measured at a range of different temperatures, with an inset which shows the ECM for the high frequency (HF) and mid-frequency (MF) arcs. Measured frequency is shown on the Nyquist plot in Hz.[2]

The conductivities are calculated from the low frequency intercept of the x-axis and on increasing temperature the resistance (intercept) decreased, showing thermally activated conductivity in films of the 10 layer material. In an effort to elucidate the conductivity processes present in the thin film, attempts were made to fit the impedance arcs using an equivalent circuit model (ECM); typical Nyquist plots and fitting of the AC impedance data at a selection of temperatures are shown in Figure 4.26.

The impedance response could be separated into three distinct regions; high, medium and low frequency. From consideration of the observed low polarisation and the scattering phenomena at low frequency (LF) below 1 x 10^4Hz, this response is assigned to the gold contact electrodes.[12] A response of this nature is also observed at low frequencies for Au contacts deposited in the same orientation as that used here when measuring thin films of $Ce_{0.8}Sm_{0.2}O_{2-\delta}$.[13] The remaining parts of the Nyquist plot are composed of two overlapping depressed arcs in the high to mid frequency region (10^7 to 10^4Hz). The arc observed at high frequency (HF) (10^7 to 10^6Hz) displayed a characteristic capacitance of the order of 10^{-11}F and the best fit to this arc was achieved by a resistor (R_1) and constant phase element (CPE_1) in parallel with one another. The CPE is used to model the capacitance of an arc with a depressed angle i.e. when the impedance response does not belong to a perfect capacitor. The arc fitted to the mid-frequency (MF) range (10^6 to 10^4Hz) was also modelled by a resistor (R_2) and constant phase element (CPE_2) in parallel with one another and the fitted capacitance of this arc is 10^{-12}F.

The resistance associated with the high frequency arc was consistently smaller than that of the arc in the mid-frequency range, indicating that the conductivity process associated with the mid-frequency contributes the larger resistance to the total conductivity. In polycrystalline materials, the high frequency arc is associated with conductivity in the bulk (capacitance of 10^{-12}F), whilst the lower frequency arc is assigned to grain boundary conductivity (capacitance of 10^{-11} to 10^{-8}F), whereas in single crystals or thin films without grain boundaries, the AC impedance response is typically a single arc belonging to the bulk material. In thin

films of $Ba_{1.7}Ca_{2.4}Y_{0.9}Fe_5O_{13}$, we observe two overlapping arcs, indicating that there are multiple conduction processes occurring. Given the presence of twinning in the STO substrate, there exists the likelihood of the presence of a small number of grain boundaries in the film, which could contribute to the observed film resistance. This would explain the presence of two overlapping arcs in the high to mid-frequency region, with the HF arc assigned to the bulk response and the MF to the grain boundary response. The HF arc displays a slightly lower capacitance than that of the MF region (10^{-11}F, compared with 10^{-12}F), which is the inverse of what would be expected for a bulk response in the HF region. The reason for this disparity is unknown, however given the relatively small difference in the capacitances as well as the overlapping nature of the HF and MF arcs, separation of the processes is made more complex, and may result in small errors on these values.

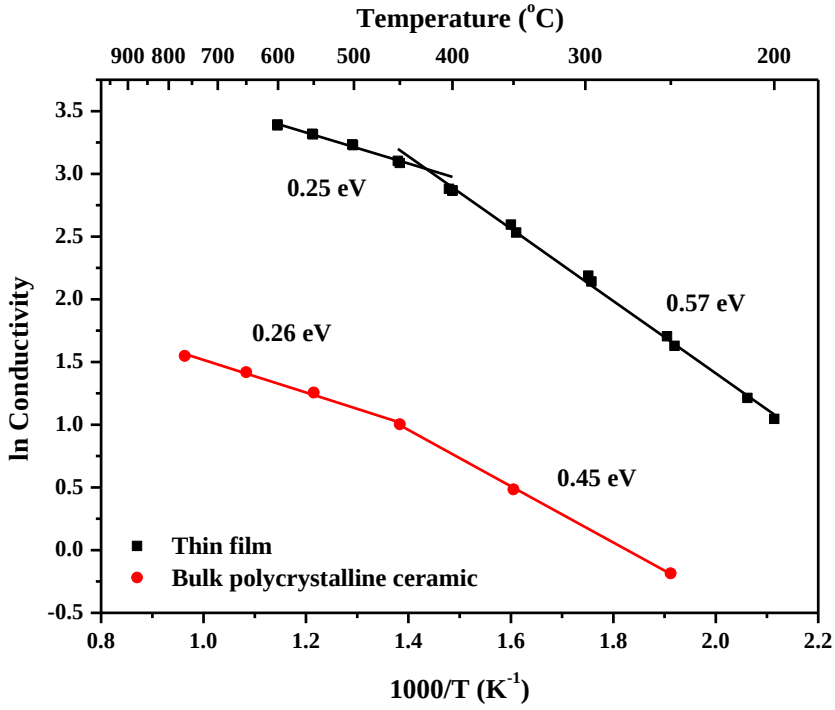

Figure 4.27: Arrhenius plot for conductivity of $10a_p$ bulk and thin film as a function of temperature in flowing oxygen. All data shown are on cooling.[2]

The conductivity as a function of the temperature in an oxygen atmosphere is shown in Figure 4.27 and reaches 30.0Scm^{-1} at 600°C for thin films of $Ba_{1.7}Ca_{2.4}Y_{0.9}Fe_5O_{13}$. Any contribution to the total film conductivity from the STO substrate was taken into account by directly measuring a substrate from the same batch in the same electrode configuration. The STO substrate was found to have a conductivity of the order of 10^{-7}Scm^{-1} at 300°C and 10^{-3}Scm^{-1} at 600°C in agreement with the expected values from the literature,[14] and its contribution to the overall measured conductivity is considered negligible. The conductivity of the bulk ceramic in oxygen is 3.5Scm^{-1} (Figure 4.27).

The activation energies for the thin film and polycrystalline sample measured in an O_2 atmosphere are shown on Figure 4.27, with both samples showing a change in activation energy and displaying low and high temperature regimes. In the thin film, the activation energies are 0.57 and 0.25eV, for the low (200°C to 420°C) and high temperature (420°C to 600°C) regimes respectively, with the change in slope occurring in the region of 420°C. The conductivity of the bulk material displays a transition between the two regimes observed at 450°C and different activation energies of 0.45eV (250°C to 450°C) and 0.26eV (450°C to 765°C). This clearly shows that the high temperature conductivity is associated with process(es) which display lower activation energy than those at low temperature in both the thin film and the bulk. It also appears that the activated processes in the high temperature regime are the same in the bulk and thin film given the similarity in the activation energies; however the absolute values of conductivity in the thin film are much higher.

In the 10 layer material the total measured conductivity is composed of electronic and ionic components, and the magnitude is dominated by the electronic component (as typical for MIEC materials with ionic conductivity several orders of magnitude lower than the electronic conductivity). The activation energy for conductivity also represents a combination of ionic and electronic components and separation of the contribution from each component to the overall activation energy is complex. The ionic transport as a function of anisotropy of $Ba_{1.7}Ca_{2.4}Y_{0.9}Fe_5O_{13}$ is currently the subject of further detailed study. Demont *et al.*[1] measured the conductivity of dense polycrystalline $Ba_{1.7}Ca_{2.4}Y_{0.9}Fe_5O_{13}$

(nominal stoichiometry) in air and observed two conductivity regimes with the transition in behaviour occurring at approximately 480°C, at the Néel temperature, coinciding with realignment of Fe^{2+}/Fe^{3+} magnetic spin states. The activation energies were 0.20eV and 0.11eV below and above this temperature respectively. We observe a similar transition when measuring in oxygen suggesting a realignment of Fe^{2+}/Fe^{3+} magnetic spin states also occurs when in an oxygen atmosphere. The band structure indicates that the electronic conduction of ideal composition $Ba_2Ca_2YFe_5O_{13}$ would be dominated by transport along the *a–b* plane and is essentially 2-dimensional in nature.[1] This would explain the enhanced conductivity measured in the oriented thin film of $Ba_{1.7}Ca_{2.4}Y_{0.9}Fe_5O_{13}$, where the electrode configuration leads to measurement along the *a–b* plane compared with the conductivity of a polycrystalline ceramic where the total conductivity is an average over all the randomly oriented grains, that is an average of high transport in the *a–b* plane and reduced transport along the *c*-axis. As $Ba_{1.7}Ca_{2.4}Y_{0.9}Fe_5O_{13}$ is a mixed ionic–electronic conductor, the total conductivity will also have an ionic contribution, however this will be significantly smaller than the electronic contribution; it is therefore not possible to confirm whether oxygen ion conductivity is also enhanced in the oriented thin film and this is the subject of further work. It would, however, be expected that the ionic conductivity would also be enhanced in the direction of the *a–b* plane as there are oxygen deficient layers which will favour oxygen ion transport in this direction. In addition to the differences in measured directions between the thin film and the bulk materials, there are also microstructural differences which may contribute to the differences in the measured conductivities. The polycrystalline bulk ceramic

contains many grain boundaries, whereas the thin film is essentially a single crystal and is almost grain boundary free (the substrate was twinned so a limited number of grain boundaries may be present within the film); assuming that the grain boundaries are to some extent blocking for carrier migration then the greatly reduced number in the thin film would also lead to the observed improvements in conductivity.

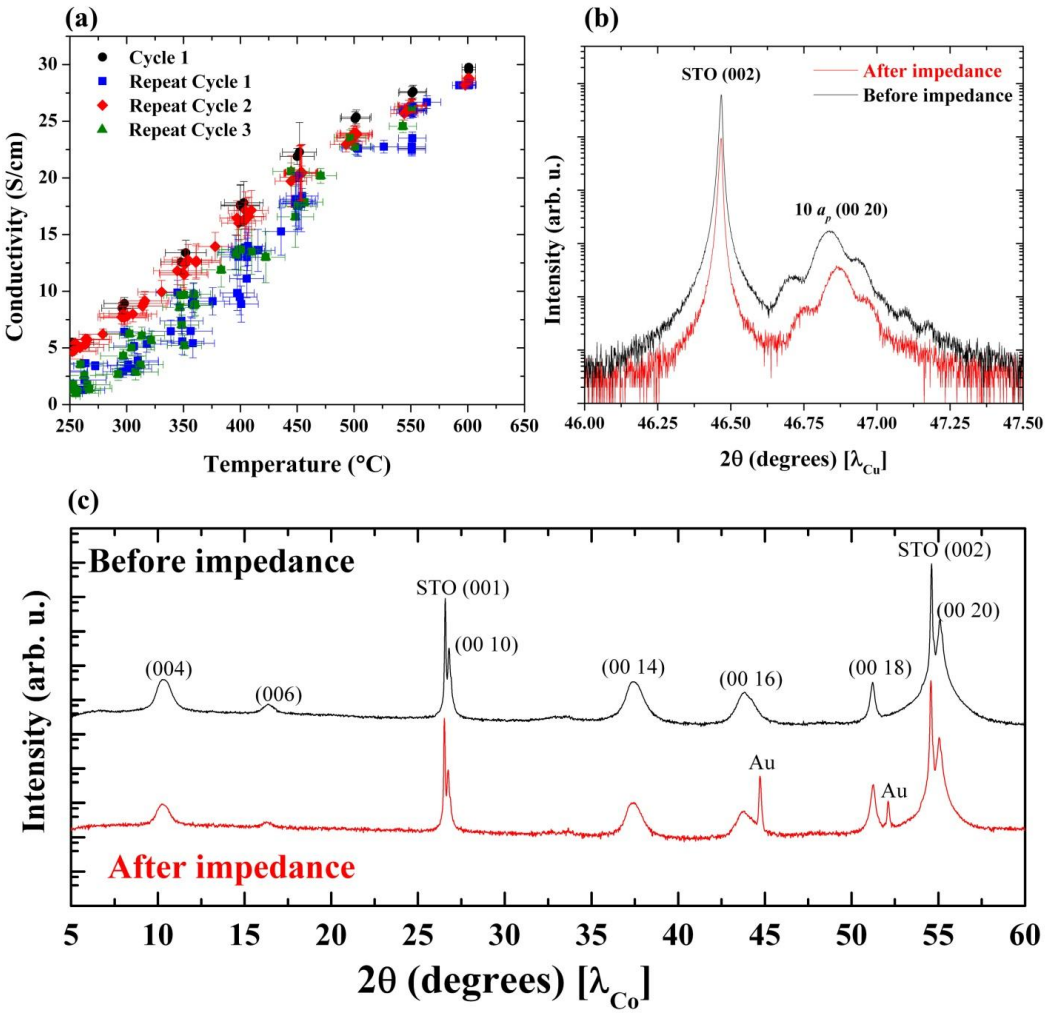

Figure 4.28: (a) AC impedance cooling cycles measured on the 10a_p film, showing the reproducibility and the durability of the film. (b) HRXRD around the (00 20) peak (c) XRD patterns before and after AC impedance measurements to 600°C.[2]

The reproducibility and stability of the thin film conductivity was verified by cycling of the film over three cooling–heating cycles in oxygen, and is shown in Figure 4.28 (a). The errors in temperature are reduced at higher temperature because the Eurotherm controlled thermostat was more accurate at higher temperatures. The stability of these films under the measurement conditions is verified by the observation that there are no changes to the XRD patterns before and after electrical measurement, shown in Figure 4.28 (b) and (c), confirming that the lattice parameters remain unchanged and therefore the structure and oxygen stoichiometry are retained. To study the thermal stability of the film, a sample was heated to 600°C in oxygen, at a heating rate of 3°Cmin^{-1}; once the film reached 600°C it dwelled at temperature for 200 hours. No change in the diffraction pattern (Figure 4.25) was observed before and after heating showing that the film is stable for a long period of time at the operating temperature.

4.5 Conclusions

The growth of a strongly cation ordered 10 layer perovskite film, with a more complex structure than previous SOFC cathode materials, grown in thin film form, has been achieved via pulsed laser deposition (PLD). The A site cation composition which produces the six cation site, 39Å repeat structure in the bulk ceramic also drives the assembly of this complex superstructure when grown as an epitaxial thin film. The symmetry of the film appears to be tetragonal within the resolution of the measurements employed, as opposed to the orthorhombic symmetry of the bulk phase, which may be attributed to the in-plane structural match between the cubic STO substrate and the grown layer. This complex

structure was confirmed by HRTEM data, which shows the faithful reproduction of the cation site ordering from the bulk material, is associated with retention of the A site layering, and the presence of defects associated with faulting in the ordering of the component structural units. The high degree of uniformity and structural perfection of the grown films averaged over larger areas than those probed by TEM was clear from XRD data, with the narrowest rocking curve peak widths thus far reported for ordered layered SOFC cathode candidate materials.

The self-assembly of the six-site 39Å repeat structure derived from the essentially isotropic perovskite subcell in single-target pulsed laser deposition growth reflects the favourable nature of the A site cation ordering which drives the formation of the structure. The perovskite-based nature of the superstructure makes it distinct from large repeat Aurivillius and Ruddlesden-Popper phases, which are intrinsically layered due to the insertion of fluorite and rock-salt type layers respectively.

The conductivity of these $10a_p$ films is significantly higher than that of the bulk polycrystalline ceramic. The conductivity attained by the film is $30.0 Scm^{-1}$ at 600°C, greater than that of the bulk $3.5 Scm^{-1}$, which is a key temperature for IT-SOFCs.

The enhanced conductivity is assigned to the reduction in the density of grain boundaries and the *a*-*b* orientation of the film in-plane. This shows that the electronic conductivity can be increased by oriented growth related to the cation

stacking sequence. The film growth has thus revealed good intrinsic transport properties of the complex superstructure $Ba_{1.7}Ca_{2.4}Y_{0.9}Fe_5O_{13}$, as the measured conductivity shows that Fe^{3+}-based oxides can have acceptable conductivities for application as IT-SOFC cathodes.

The 10 layer film project could be further studied by measuring the area specific resistance of this cathode material as is commonly done for bulk SOFC cathode materials.

4.6 References

1 Demont, A. *et al.* Stabilization of a Complex Perovskite Superstructure under Ambient Conditions: Influence of Cation Composition and Ordering, and Evaluation as an SOFC Cathode. *Chemistry of Materials* **22**, 6598-6615, doi:10.1021/cm102475n (2010).

2 Sayers, R. *et al.* Epitaxial growth and enhanced conductivity of an IT-SOFC cathode based on a complex perovskite superstructure with six distinct cation sites. *Chemical Science* **4**, 2403-2412, doi:10.1039/c3sc21931c (2013).

3 Bertaut, E. F., Blum, P. & Sagnieres, A. Structure du ferrite bicalcique et de la brownmillerite. *Acta Crystallographica* **12**, 149-159, doi:doi:10.1107/S0365110X59000433 (1959).

4 Huang, Q. *et al.* Neutron-powder-diffraction study of the nuclear and magnetic structures of $YBa_2Fe_3O_8$ at room temperature. *Physical Review B* **45**, 9611-9619 (1992).

5 Karen, P., Suard, E. & Fauth, F. Crystal Structure of Stoichiometric $YBa_2Fe_3O_8$. *Inorganic Chemistry* **44**, 8170-8172, doi:10.1021/ic048746b (2005).

6 Sayers, R. *et al.* Internal Activation Strain and Oxygen Mobility in a Thermally Stable Layered Fe^{3+} Oxide. *Chemistry of Materials* **25**, 3441-3457, doi:10.1021/cm4013359 (2013).

7 Tarancon, A., Burriel, M., Santiso, J., Skinner, S. J. & Kilner, J. A. Advances in layered oxide cathodes for intermediate temperature solid oxide fuel cells. *Journal of Materials Chemistry* **20**, 3799-3813, doi:10.1039/b922430k (2010).

8 Birkholz, M. in *Thin film analysis by X-ray scattering* (Wiley-VCH Verlag GmbH & Co. KGaA, Weinheim, 2005).

9 Windt, D. L. IMD—Software for modeling the optical properties of multilayer films. *Computers in Physics* **12**, 360-370, doi:doi:http://dx.doi.org/10.1063/1.168689 (1998).

10 Biegalski, M. D. *et al.* Critical thickness of high structural quality $SrTiO_3$ films grown on orthorhombic (101) $DyScO_3$. *Journal of Applied Physics* **104**, -, doi:doi:http://dx.doi.org/10.1063/1.3037216 (2008).

11 Koch, C. T. Ph.D. thesis, Arizona State University, (2002).

12 Irvine, J. T. S., Sinclair, D. C. & West, A. R. Electroceramics: Characterization by Impedance Spectroscopy. *Advanced Materials* **2**, 132-138, doi:10.1002/adma.19900020304 (1990).

13 Sanna, S. *et al.* Fabrication and Electrochemical Properties of Epitaxial Samarium-Doped Ceria Films on $SrTiO_3$-Buffered MgO Substrates. *Advanced Functional Materials* **19**, 1713-1719, doi:10.1002/adfm.200801768 (2009).

14 Guo, X. Comment on "Colossal Ionic Conductivity at Interfaces of Epitaxial ZrO_2:Y_2O_3/$SrTiO_3$ Heterostructures". *Science* **324**, 465, doi:10.1126/science.1168940 (2009).

Chapter 5: Area Specific Resistance Measurements for Thin Film Cathodes

5.1 $Ba_{1.7}Ca_{2.4}Y_{0.9}Fe_5O_{13}$ ASR Motivation

Having concluded at the end of Chapter 4 that the conductivity of the $Ba_{1.7}Ca_{2.4}Y_{0.9}Fe_5O_{13}$ (10 layer) film has been improved with respect to the bulk, the subsequent task is to determine the area specific resistance (ASR) of the film which is typically used to evaluate the performance of cathodes. ASR takes into account all the processes that are occurring (e.g. electrical and ionic resistance, catalytic activity, cathode morphology/microstructure, interface exchange/reactions), and not just electrical resistance. The ASR is the resistance of the film normalised by its area and calculated from the resistance obtained from impedance measurements, multiplied by the electrode area. The combined ASR of cathode, anode and electrolyte should be less than $0.5\Omega cm^2$ and ideally approach $0.1\Omega cm^2$ to ensure high power densities.[1] Values for the ASR are strongly dependent on the microstructure of the material, with up to two orders of magnitude difference reported for $La_{0.4}Sr_{0.6}Co_{0.8}Fe_{0.2}O_{3-\delta}$ (LSCF) cathodes with identical composition, but with different morphologies.[2] The rate of change of the overall ASR is called degradation and gives an indication of the lifetime of the fuel cell.[3] From the literature it is known that μ-solid oxide fuel cells (μ-SOFCs) have geometrical constraints, as outlined by Fleig *et al*.[4] In this report they discuss an electrode geometry with the cathode on the same side of the electrode as the anode, by making use of interdigital electrodes, as can be seen in Figure 5.1.

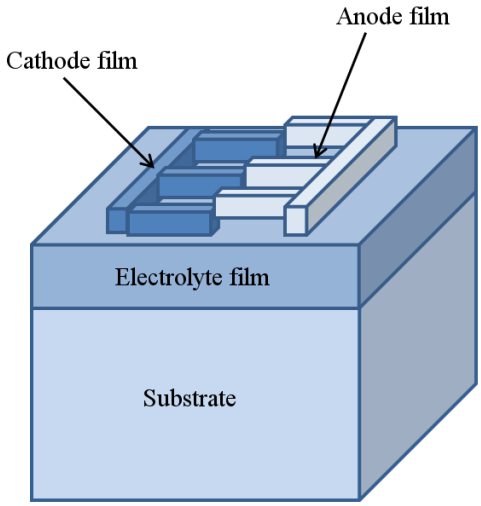

Figure 5.1: μ-SOFC geometry with the anode and cathode on the same side of the electrolyte film.

The geometry shown in Figure 5.1 could be modified by replacing the anode with a secondary cathode film to measure the ASR. This would enable the measurement of ASR without having to grow on both sides of the electrolyte. Few groups measure the ASR of films, and some of their geometries are discussed in the following section.

5.2 Literature of ASR geometries

Pulsed laser deposition (PLD) has been used to grow thin films of cathode materials to measure the ASR in the literature. Hendriksen *et al.* utilized the symmetrical cell geometry as depicted in the schematic in Figure 5.2.[5]

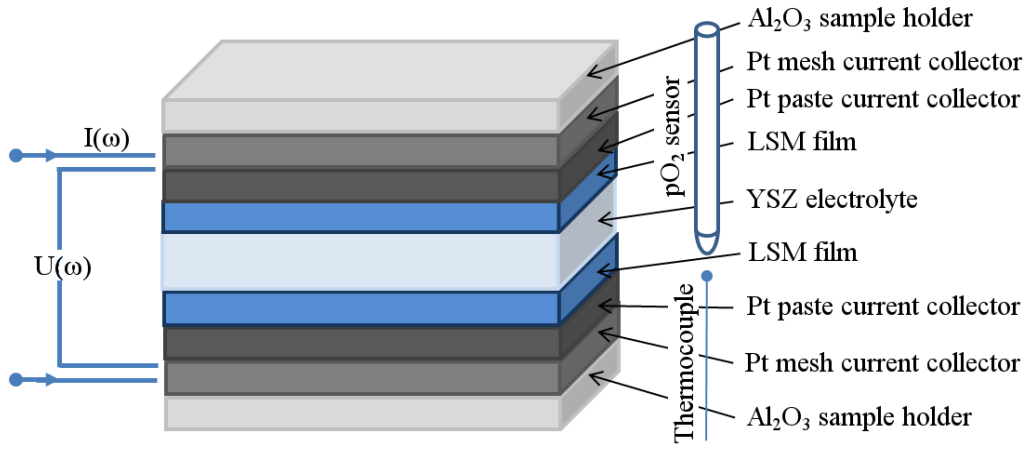

Figure 5.2: Schematic showing the geometry that Hendriksen *et al.* used.[5]

This symmetrical cell geometry is also commonly used for measuring the ASR of bulk pellets.[6] This geometry poses several challenges due to our current deposition method of adhering the substrate to the sample holder with silver DAG (from Agar Scientific), thus contaminating the surfaces with an electrically conducting material.

Rupp *et al.* used the geometry in Figure 5.3 to calculate the ASR,[7] and used the procedure for patterning the electrodes as reported by Gauckler *et al.*[8]

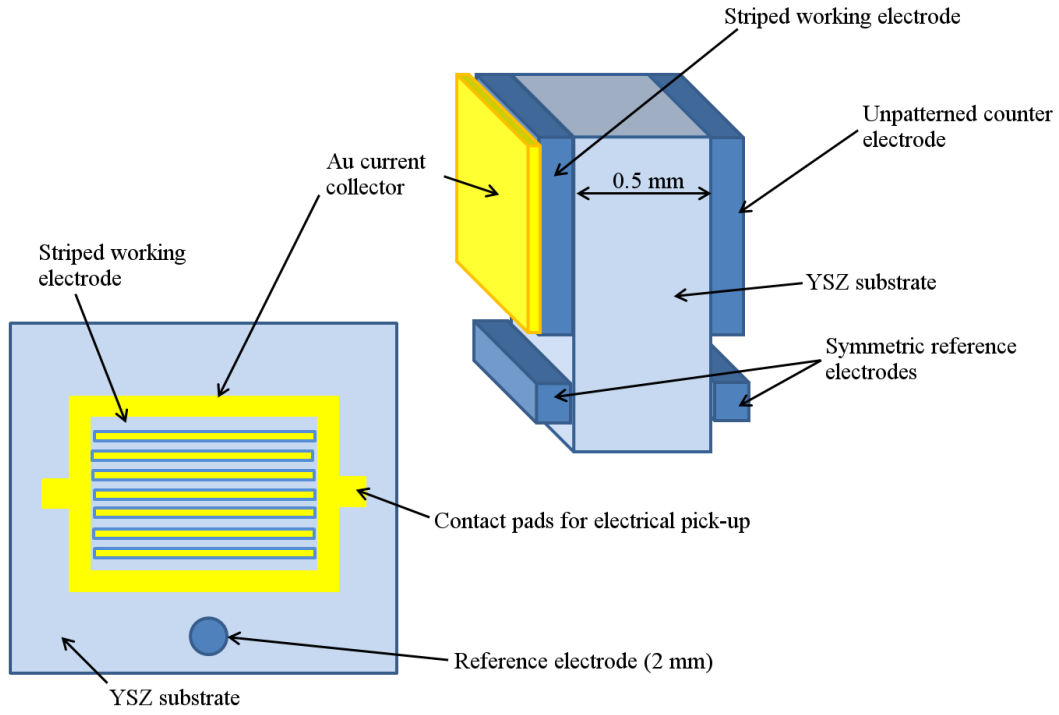

Figure 5.3: Schematic showing the geometry that Rupp *et al.* used.[7]

Both Rupp *et al*. and Hendriksen *et al*. used geometries that require film growth on both sides of the substrate.

The combination of ideas led us to investigate and develop several different geometries for measuring the ASR of the films, which are outlined in this chapter.

5.3 ASR geometries

Three potential geometries were considered for measuring the ASR of the $Ba_{1.7}Ca_{2.4}Y_{0.9}Fe_5O_{13}$ (10 layer) cathode films.

5.3.1 Geometry One

Initially a geometry inspired by the work of Yang Shao-Horn *et al.* was attempted. In their paper, they measured the oxygen reduction reaction (ORR) of lanthanum strontium cobalt oxide ($La_{0.8}Sr_{0.2}CoO_{(3-\delta)}$) (LSC) grown by PLD on yttrium stabilized zirconia (YSZ) substrates.[9] The schematic below (Figure 5.4) shows the geometry which was used for their ORR measurements.

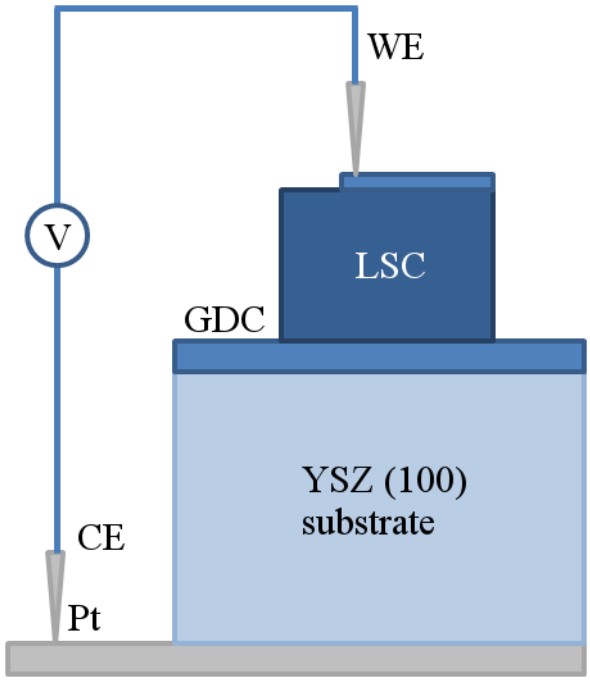

Figure 5.4: Schematic of the geometry used by Yang Shao-Horn *et al.*[9], where WE is the working electrode, CE the counter electrode, LSC is lanthanum strontium cobalt oxide, GDC is gadolinium doped ceria and YSZ is yttrium stabilized zirconia.

In an analogous fashion, a $Ba_{1.7}Ca_{2.4}Y_{0.9}Fe_5O_{13}$ cathode film can be deposited on YSZ with a layer of Pt on the underside, to measure the ASR rather than the ORR, as in the schematic shown in Figure 5.5. From previous studies of bulk $Ba_{1.7}Ca_{2.4}Y_{0.9}Fe_5O_{13}$ cathodes it is known that it reacts with YSZ at high temperature.[6,10] Typically, a buffer layer of SDC is used to prevent this.[11-13]

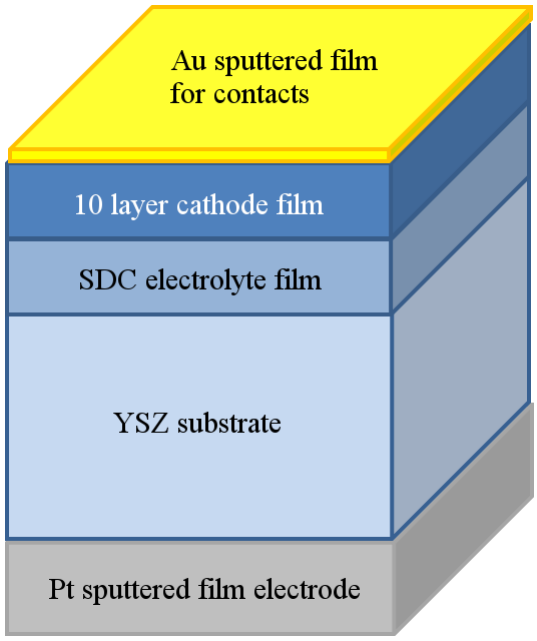

Figure 5.5: Schematic showing geometry one.

From our previous work growing both $Sm_{0.2}Ce_{0.8}O_2$ (SDC) and the $Ba_{1.7}Ca_{2.4}Y_{0.9}Fe_5O_{13}$ cathode, the growth conditions have already been optimised in Chapters 3 and 4. Both layers were deposited at 850°C, 5Hz and in a pO_2 of 10mTorr, with a flow rate of 12.8 standard cubic centimeters (sccm). The SDC film was deposited using 866 pulses with a laser energy of 195mJ to give a target thickness of 10nm. The $Ba_{1.7}Ca_{2.4}Y_{0.9}Fe_5O_{13}$ cathode layer was deposited at 300mJ using 43,947 pulses to give a target thickness of 95nm.

X-ray diffraction (XRD) was performed on the films, initially grown as individual layers to confirm the optimised growth conditions and the patterns are shown in Figure 5.6. The 10 layer film (Figure 5.6 (b)) was deposited on STO due to its reactivity with YSZ. The bilayer SDC|10 layer film XRD patterns are shown in Figure 5.6 (c).

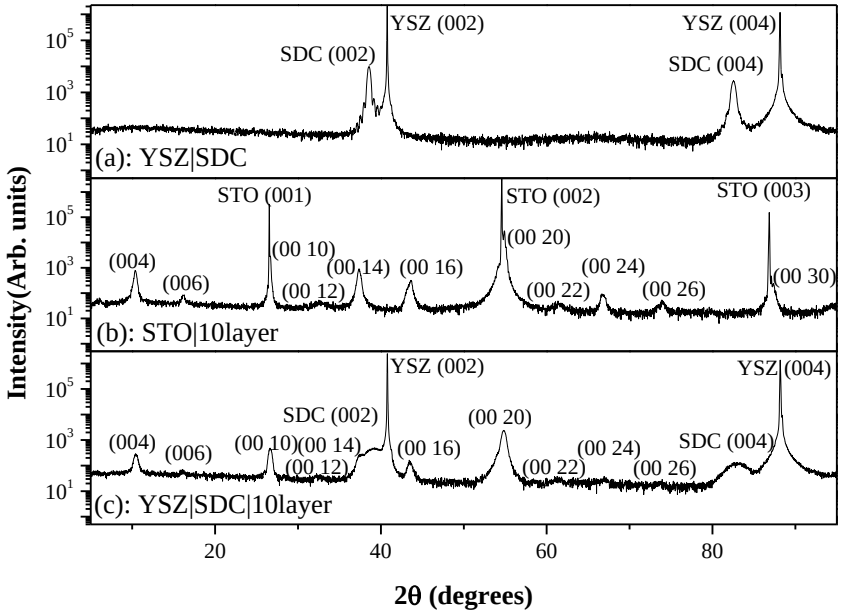

Figure 5.6: XRD patterns showing (a) the single layer of SDC grown on YSZ, (b) 10 layer grown on STO, and (c) the bilayer of the 10 layer grown on SDC on YSZ.

In the bilayer film XRD pattern (Figure 5.6 (c)) both the SDC and 10 layer peaks are clearly visible. It is therefore possible to deposit an oriented 10 layer film on the SDC electrolyte layer.

To determine if the target thickness of 10nm SDC and 95nm 10 layer was achieved for the bilayer, X-ray reflectivity (XRR) and subsequent modelling (using X'Pert Reflectivity)[14] was used.

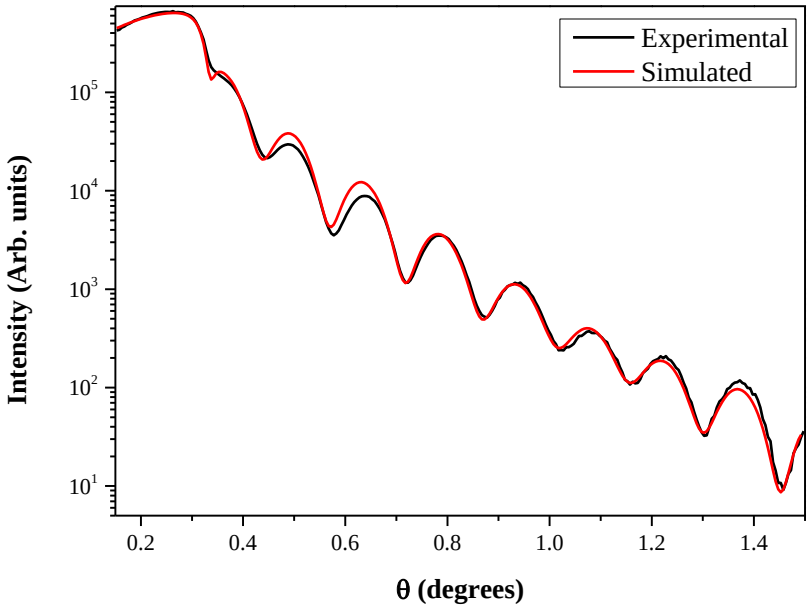

Figure 5.7: XRR of the bilayer film of 10 layer grown on SDC on YSZ, with the experimental data in black and the simulated data in red.

The model shown in red in Figure 5.7, gave an SDC thickness of 4.3nm, and a roughness of 1.2nm. For the 10 layer the model gave a thickness of 24.1nm and a roughness of 0.7nm. The thickness values were greatly reduced compared to the expected thicknesses (43% of SDC target thickness and 25% of 10 layer target) and, this deposition rate reduction may be due to the laser optics requiring re-alignment at the time.

The ASR of the bilayer film was then measured with a Solartron 1260 with SMaRT software, and compared to a Pt|YSZ|Pt sample as shown in the schematic in Figure 5.8.

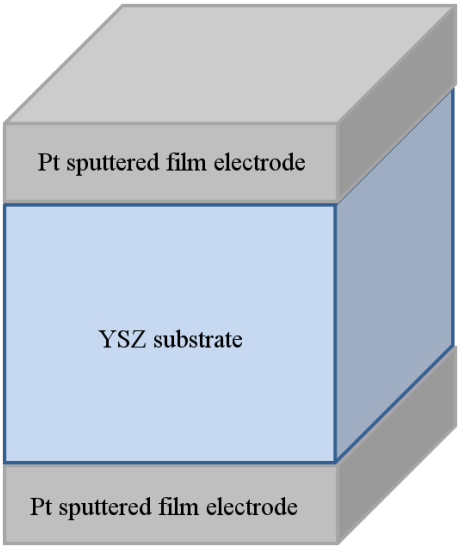

Figure 5.8: Schematic showing the Pt|YSZ|Pt geometry.

Both the Pt|YSZ|Pt sample and the Pt|YSZ|SDC|10 layer sample were analysed by AC impedance over 650°C – 800°C. The film was analysed by XRD after the impedance measurement, and the patterns are in Figure 5.9.

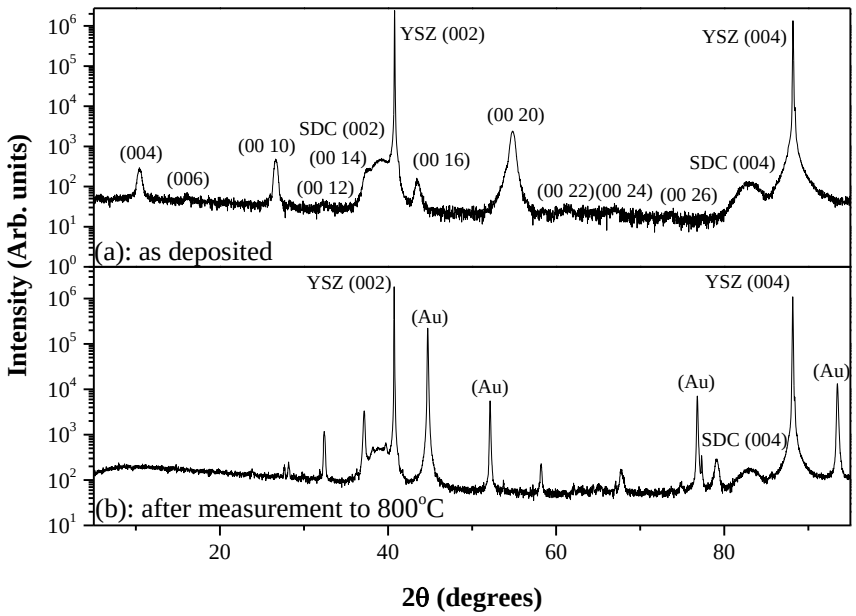

Figure 5.9: XRD pattern of the bilayer film (a) before and (b) after the impedance measurement to 800°C.

From Figure 5.9 (b) it is clear that the 10 layer peaks are no longer visible. This has prompted further stability measurements of the 10 layer film, which are discussed in Section 5.3.2 (Geometry 2). Additionally the AFM results of the SDC films shown in Chapter 3 Figure 3.15 suggest that pinholes may be present in the SDC films. It is therefore possible that the 10 layer film is reacting with the YSZ through holes in the SDC layer.

5.3.2 Geometry Two

The second geometry, as pictured in Figure 5.10, is based on the way ASR is measured in the bulk, using symmetrical cells.

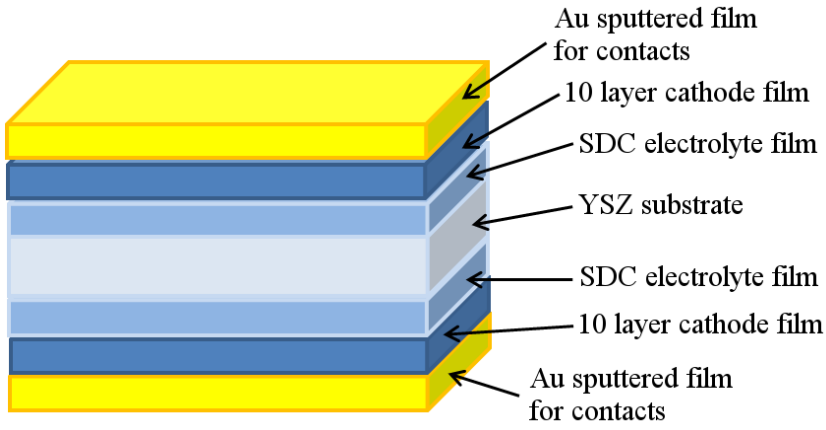

Figure 5.10: Schematic showing geometry two.

A new holder is required for the double sided growth. This was made for the Nano PVD chamber, and incorporates a ledge for resting the substrate on, leaving the back of the substrate open to the heater. The previous setup required the substrate to be adhered to the heater block using silverDAG (Agar Scientific). The holders

each supported the substrate differently, requiring the growth conditions of the films to be re-optimised.

Previously it was found that the 10 layer material reacts with YSZ at high temperatures,[6] and so initial optimisation of the 10 layer was performed on STO. XRD patterns showing the effect of changing the growth temperature using the new holder can be found in Figure 5.11.

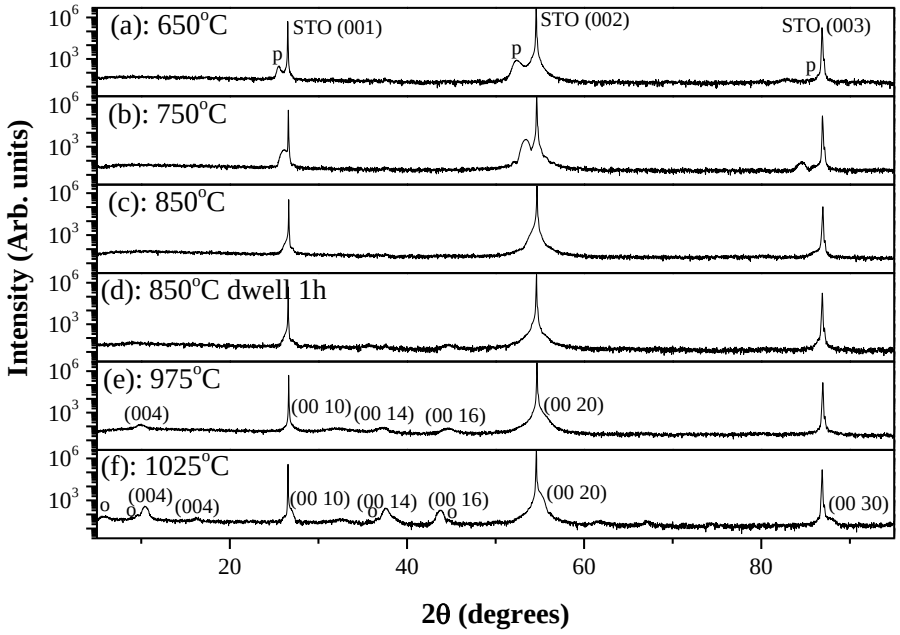

Figure 5.11: XRD patterns of growing 10 layer films on STO at various temperatures. (a) at 650°C, (b) at 750°C, (c) 850°C, (d) 850°C, dwelling at temperature for 1 hour, (e) 975°C and (f) 1025°C. The 'o' represents the $3a_p$ phase, and 'p' represents a simple perovskite peak.

Varying the temperature showed that higher temperatures were required for growth on the new holder. Previously on the old holder the films were optimised at 850°C, whereas on the new holder the peaks in Figure 5.11 for the 850°C run

are very broad and not very intense. Increasing the temperature to 975°C provides better 10 layer peaks, but increasing the temperature further to 1025°C produces additional unwanted peaks from the $3a_p$ phase.

Due to the emissivity difference between STO and YSZ, the 10 layer film also needed to be optimised on YSZ. Emissivity is the ratio between the energy radiated from a materials surface compared to the energy emitted from a perfect emitter for a given temperature and wavelength under the same conditions. XRD patterns of growths at 925°C, 975°C and 1025°C are shown in Figure 5.12 (a) - (c) respectively.

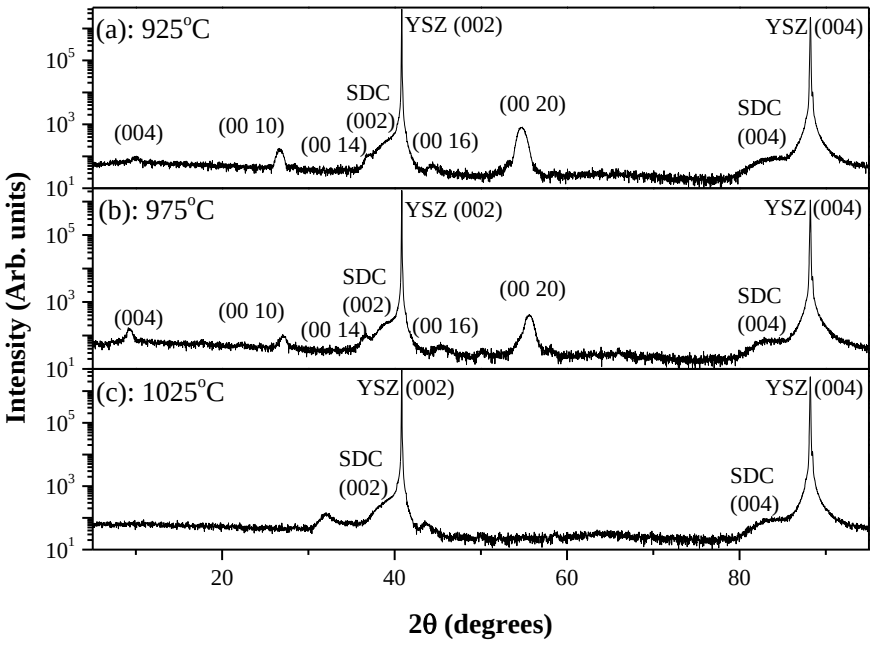

Figure 5.12: XRD patterns showing the effect of changing growth temperature of the 10 layer film on SDC on YSZ, (a) at 925°C, (b) at 975°C and (c) at 1025°C.

When comparing the different temperatures on the new holder (growing on YSZ substrates) to the old holder, increasing the temperature from 850°C (as in Geometry one, Figure 5.6 (c)) to 925°C (Figure 5.12 (a)) and 975°C (Figure 5.12 (b)) is required for the deposition of the 10 layer. Depositing at the higher temperature of 1025°C (Figure 5.12 (c)) inhibits the growth as many of the 10 layer peaks are missing from the XRD pattern, such as the (004) and the (00 20). It was concluded that 975°C was the optimum deposition temperature for the 10 layer film using the new holder.

The growth conditions to deposit films on one side of the substrate are optimised, however for this geometry it is necessary that deposition can occur on both sides of the substrate. After an initial film was grown on one side of the substrate, the substrate was flipped to allow growth on the other side. The previously deposited film was then effectively annealed as a consequence of heating the chamber for a second time for the second deposition. Double-sided growth of SDC was used to test the viability of this process.

The first film of SDC was deposited on one side of the substrate at 975°C, 10mTorr, 12.8sccm, 5Hz, 195mJ for 8433 pulses. Immediately after the film had cooled in the chamber the substrate was removed, flipped and replaced into the chamber for deposition onto the other side of the substrate. The same deposition conditions were then repeated for the film on the second side of the substrate as used for side one. The resultant XRD patterns from both sides of the substrate are shown in Figure 5.13.

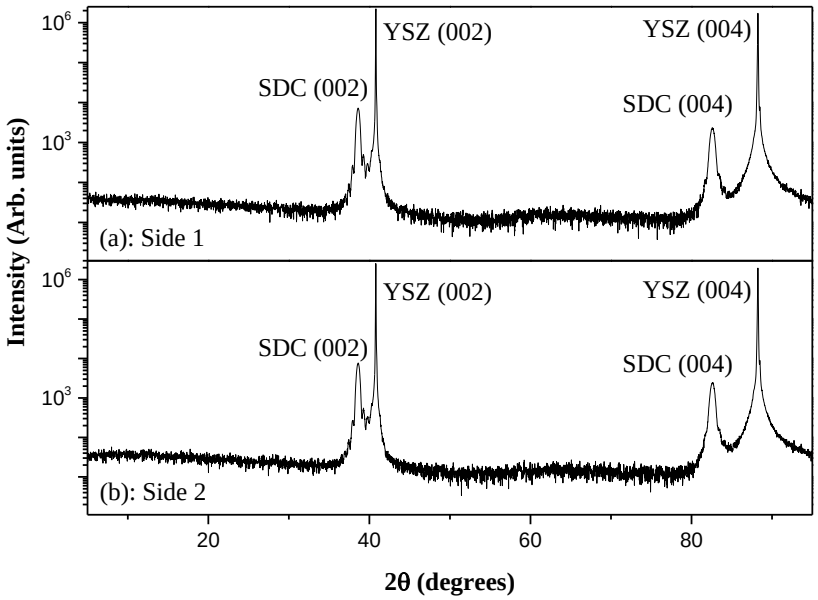

Figure 5.13: XRD patterns from both sides of the SDC|YSZ|SDC film growth, (a) side 1 and (b) side 2.

From Figure 5.13 it is clear that SDC can be deposited on both sides of the double side polished YSZ substrates. The precise thickness of SDC required to serve as an effective buffer layer between the 10 layer and the YSZ substrate was then investigated.

Due to the heavy Pt influence on the ASR found from the measurements in Geometry 1, a 10 layer ink formulated by Darren Hodgeman at the University of Liverpool was considered for use as the secondary cathode instead of Pt.[6] Both the stability of the 10 layer film and the 10 layer ink are therefore discussed in the following section.

5.3.2.1 Stability of the 10 layer Ink and Film

The stability of the 10 layer material was thoroughly investigated both as a thin film and as the 10 layer ink.[6] The 10 layer ink was painted onto a glass slide and dried in a furnace at 100°C for 1 hour, before an X-ray diffraction pattern was collected, which is shown in Figure 5.14.

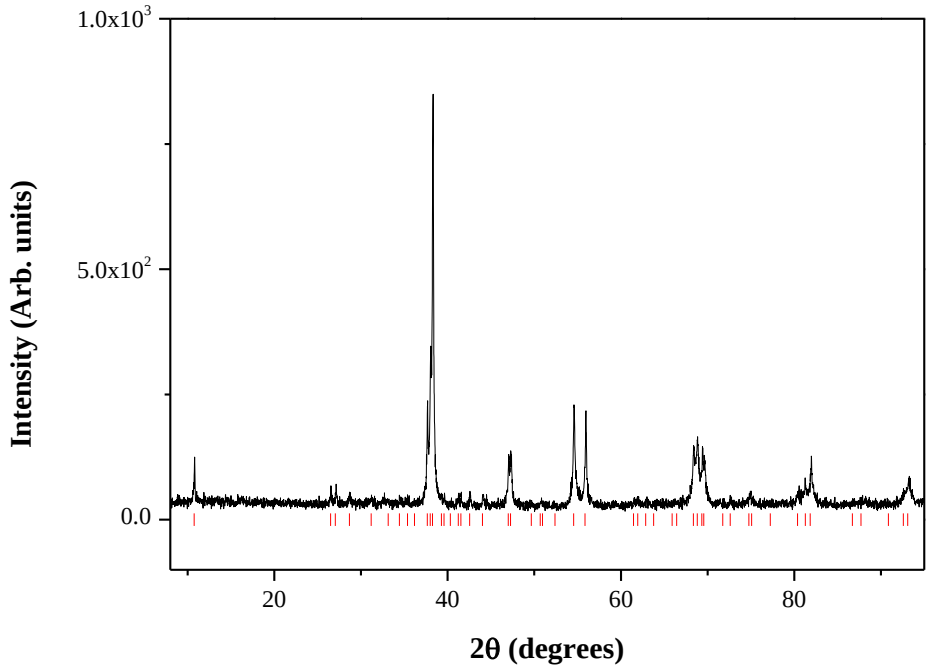

Figure 5.14: XRD pattern of the 10 layer ink dried onto a glass slide. Red lines indicate 10 layer peak positions.

SDC was deposited on YSZ utilising the new holder, at 975°C with a pO_2 of 10mTorr, as was found to be the optimum temperature for the 10 layer deposition. Firstly a 22nm SDC film was grown to test the sintering conditions required by the 10 layer ink. The film was cut into quarters using a diamond tipped pen. Each quarter of the YSZ|SDC had the 10 layer ink applied to it, before drying in a

furnace at 100°C for 1 hour. Once the films were dry they were split into separate furnaces to test the sintering temperatures at 600°C, 700°C, 800°C and 950°C. 600°C was chosen as the lowest temperature as it is the operating temperature for the ASR measurement, and 950°C was chosen as the upper limit because that is the sintering temperature used for the bulk 10 layer ink on SDC pellets. X-ray diffraction was subsequently carried out on the samples, and the patterns can be seen in Figure 5.15.

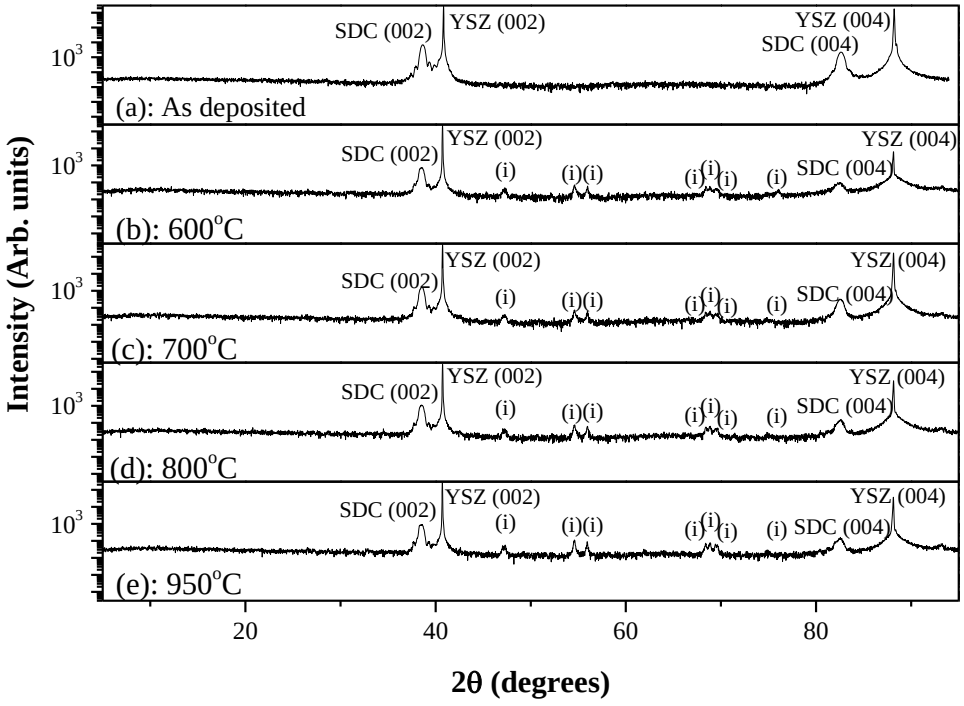

Figure 5.15: XRD patterns of the SDC film on YSZ with the applied 10 layer inks at various sintering temperatures. (a) as deposited film, (b) film with the ink sintered at (b) 600°C, (c) 700°C, (d) 800°C and (e) 950°C. The (i) represents the peaks from the 10 layer ink.

In addition to the XRD results, pressure was applied using a spatula to the inks to establish if the inks were in good contact with the SDC film. At 600°C a small amount of pressure was applied, which made the ink come off, and therefore the

sintering temperature was too low. The 10 layer was broken into small pieces (powder-like). At 700°C the response was very similar to 600°C in terms of the pressure required to remove the ink, and the powdery nature of the ink when removed. After sintering at 800°C more pressure was required than for 700°C to remove the ink, and when removed the ink was more crumbly than at 950°C. At 950°C even greater pressure was needed to remove the ink, and the ink came off in one chunk. The 10 layer patch is darkest having removed the top layer of ink. After these observations were taken, and the underside of the ink had become exposed the samples were X-rayed again.

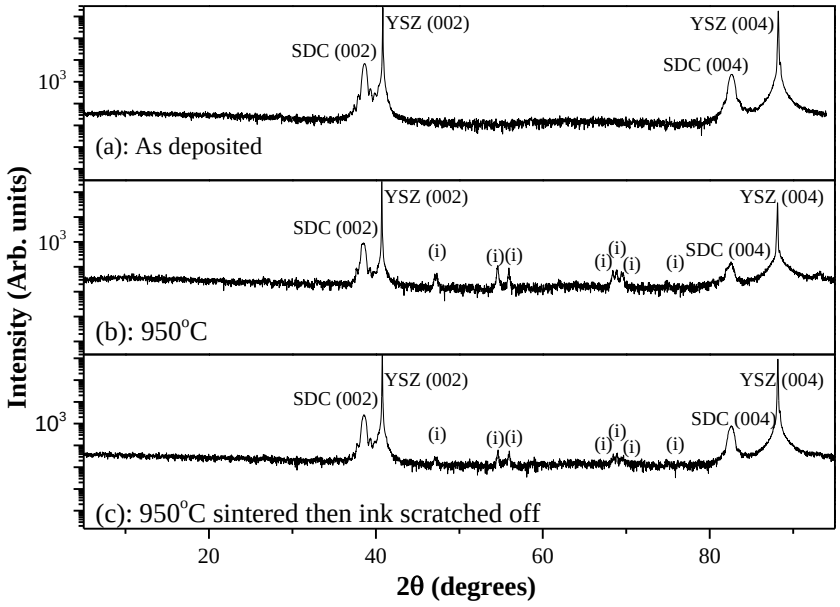

Figure 5.16: XRD patterns from (a) the as deposited film, (b) the film and ink after sintering at 950°C and (c) after having the ink scratched away. The (i) represents the peaks from the 10 layer ink.

As can be seen from Figure 5.16 the SDC film remains intact having been sintered at 950°C, and thus the following experiments used 950°C as the sintering temperature.

Thin films of YSZ|SDC were deposited with varying thickness of SDC. Three films were grown with target thicknesses of 10, 55 and 100nm. XRR was used to determine the actual thicknesses of the films prior to any further stability measurements.

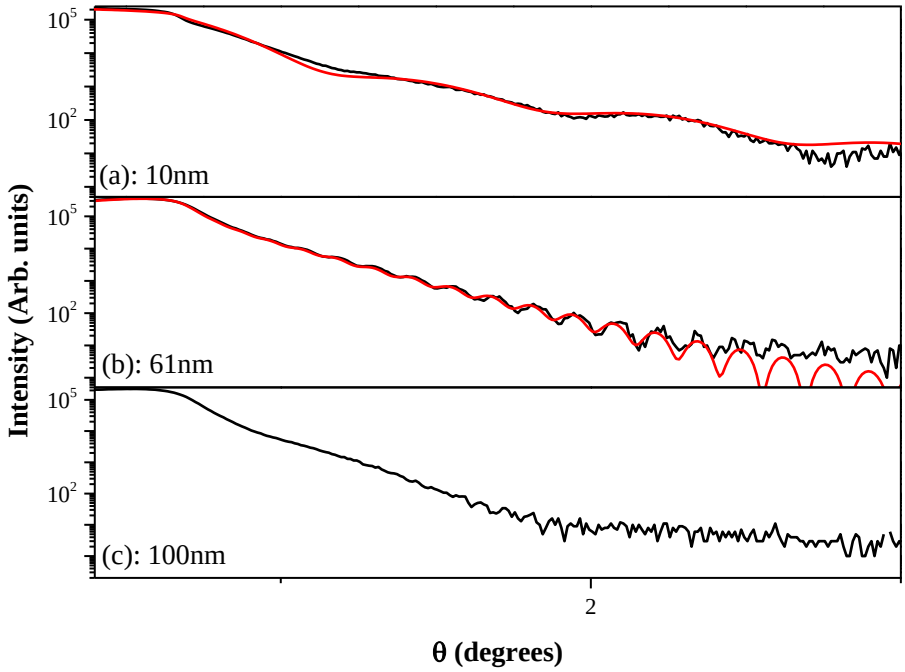

Figure 5.17: Experimental XRR patterns from the SDC films of varying thickness, (a) 10nm, (b) 61nm and (c) 100nm. XRR simulations are in red for the 10nm and 61nm films. The 100nm film was not fitted due to the lack of oscillations.

The XRR plots are shown in Figure 5.17. Only the two thinnest films had sufficient oscillations observed in the XRR for them to be fitted. The fits can be observed in red in Figure 5.17 (a) and (b) respectively, where thicknesses of 10nm

and 61nm were simulated[14], with experimental target thicknesses of 10nm and 55nm respectively.

Rocking curves for the 100nm film were also carried out, and can be seen in Figure 5.18 for both the YSZ substrate around the (002) peak and the SDC thin film (002) peak.

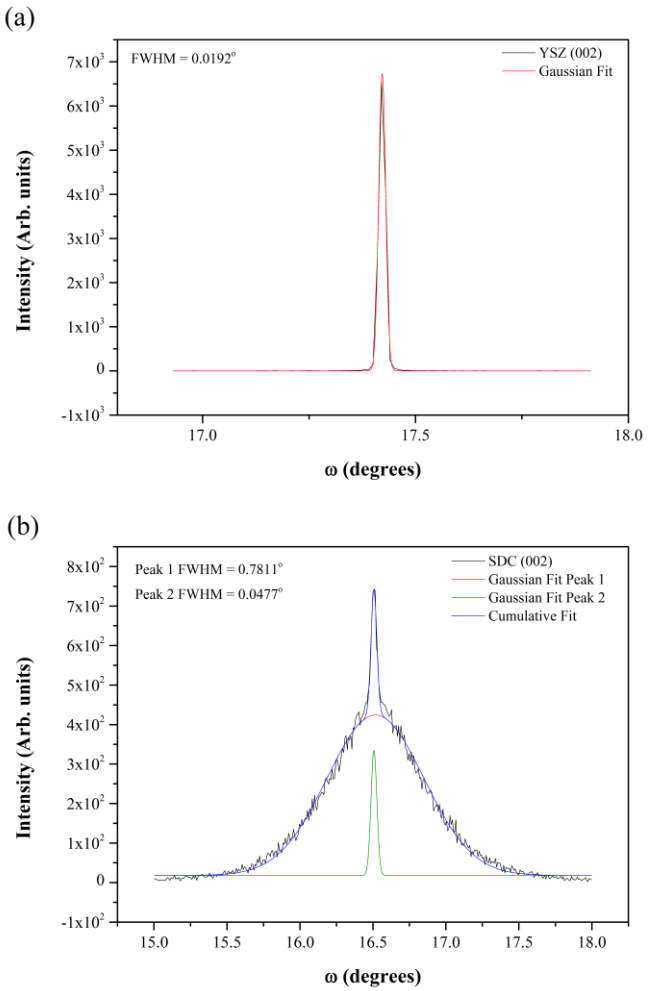

Figure 5.18: Rocking curves of the (a) YSZ and (b) SDC (002) peaks for the 100nm target thickness SDC film.

The full width half maximum (FWHM) can be obtained from Gaussian fits of the omega scans.[15] The YSZ (002) peak has a FWHM of 0.02°. The SDC rocking curve can be described by two Gaussian peaks, one broad peak with a FWHM of 0.78° and a second narrower peak with a FWHM of 0.05°. The narrower peak could be attributed to a crystal truncation rod from the substrate. Additional information on crystal truncation rods is reported by Robinson.[16]

The stability of the 10 layer inks at the sintering temperature was investigated with varying thickness of SDC. The films were cut into quarters with the diamond tipped pen before applying the 10 layer ink. The films were each heated to 100°C for one hour to dry, before sintering at 950°C for one hour. X-ray diffraction patterns were taken to determine the stability and these can be seen in Figure 5.19.

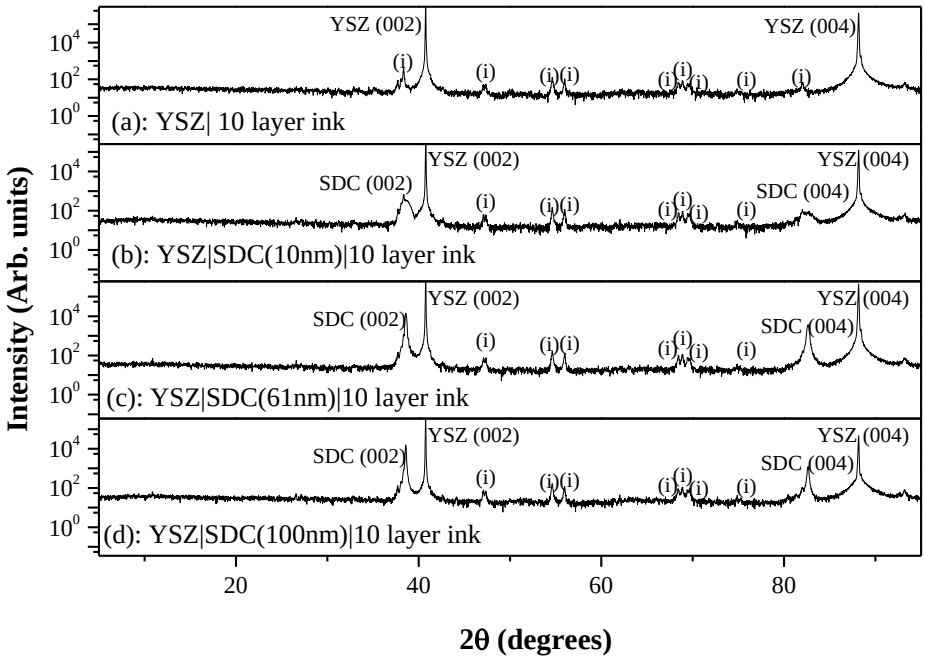

Figure 5.19: XRD patterns having sintered the 10 layer ink at 950°C for one hour with various thicknesses of SDC films. (a) is the YSZ| 10 layer ink control, (b) is the 10nm SDC film, (c) the 61nm SDC film and (d) is the 100nm SDC film. The (i) indicates the 10 layer ink peaks.

From the patterns in Figure 5.19, no additional peaks appear to be present other than the ink peaks. In addition the SDC peaks are still present and no degradation to the SDC film is observable.

The 10 layer ink was also applied to an YSZ substrate as a control (Figure 5.19 (a)). An SDC film is required to prevent the 10 layer ink from coming into contact with the YSZ, as it is known to react in the bulk when the powders are ground together and sintered in a conventional solid state reaction.[6] There is no observable difference between the stabilities of different thickness of SDC.

The 10 layer was dried on the YSZ substrate under the same conditions as before (100°C for 1 hour) and then sintered at 950°C for 1 hour. An XRD pattern was obtained, shown in Figure 5.20 (a). The ink was subjected to 950°C for a further 5 hours, with the resultant XRD pattern shown in Figure 5.20 (b).

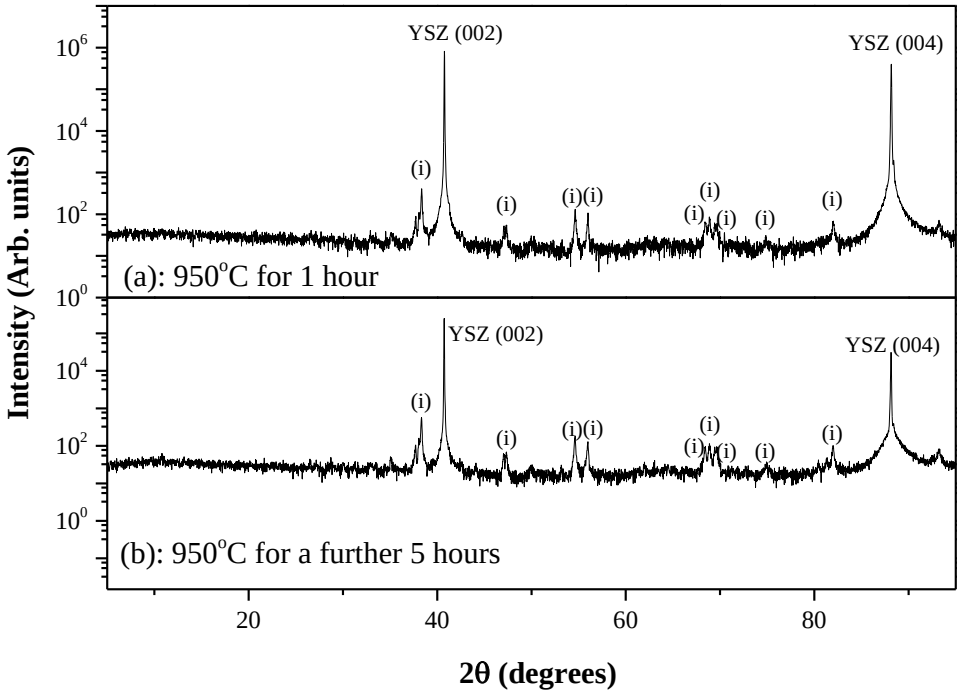

Figure 5.20: XRD of YSZ|10 layer ink control, (a) after sintering at 950°C for 1 hour, and (b) and at 950°C for a further 5 hours.

The SDC films were then subjected to similar stability testing at the sintering temperature (950°C) for 5 hours, and the XRD patterns are shown in Figure 5.21.

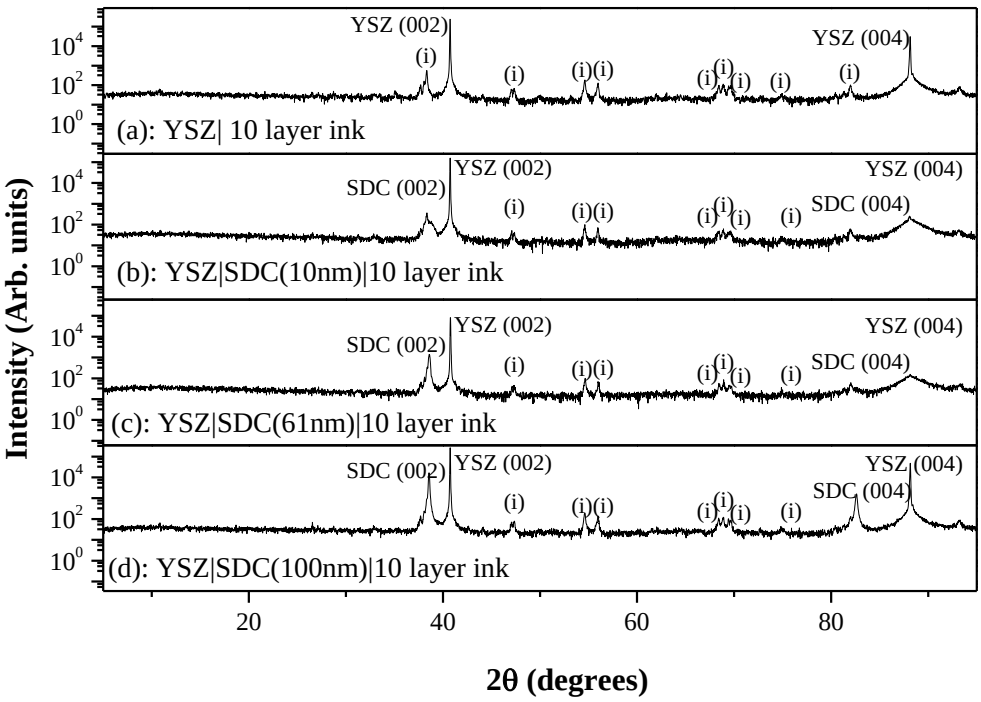

Figure 5.21: XRD patterns after stability testing at 950°C for 5 hours. (a) is the YSZ| 10 layer ink control, (b) is on the 10nm SDC film, (c) 61nm SDC film and (d) is the 100nm SDC film. The (i) indicates the 10 layer ink peaks.

Once again there is no observable difference in the stability of the different thicknesses of SDC at this stage. The stability of the SDC films with the 10 layer inks were also tested at the operating temperature of 600°C for 120 hours (Figure 5.22).

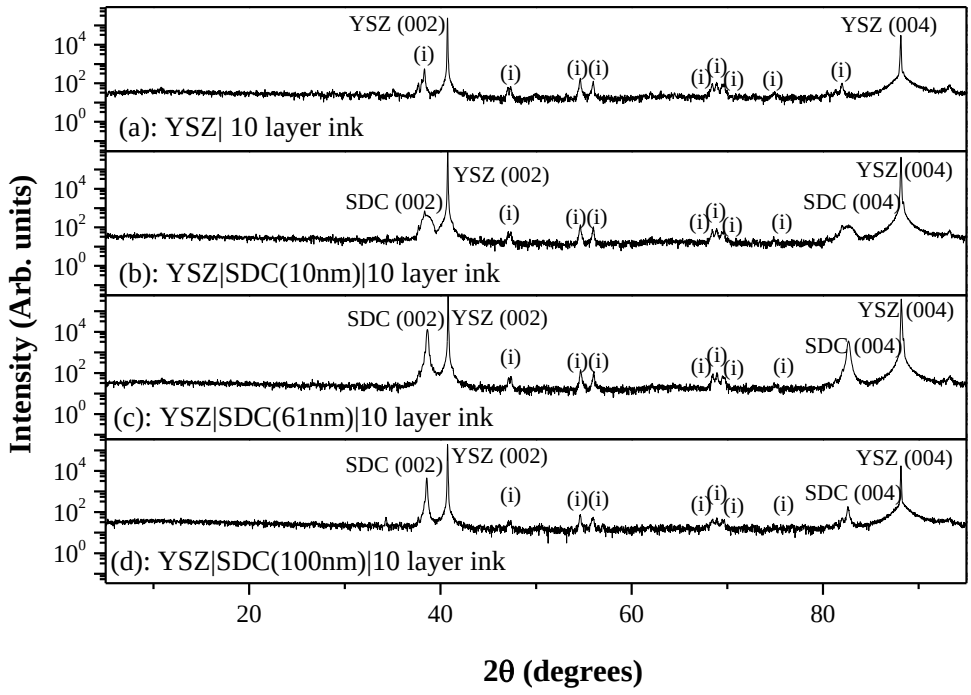

Figure 5.22: XRD patterns from the stability tests at the operating temperature of 600°C for 120 hours. (a) is the YSZ| 10 layer ink control, (b) is on the 10nm SDC film, (c) 61nm SDC film and (d) is the 100nm SDC film. The (i) indicates the 10 layer ink peaks.

Throughout the 10 layer ink stability tests none of the XRD data showed the (004) 10 layer ordering peak, which was visible in the XRD of the ink in Figure 5.14. However the intensity of this peak is quite small, and this is discussed again in more detail (in Section 5.3.2.3) after the stability tests of the 10 layer films which now follows.

5.3.2.2 Stability Tests of the 10 Layer Films

Bilayer films of SDC and 10 layer were also grown for stability tests. As in the ink tests the SDC films were grown to different thicknesses to see if the thickness of the SDC had an impact on the stability of the 10 layer films.

As before the films were grown on the new holder at 975°C, and the XRD patterns for the as deposited films can be seen in Figure 5.23.

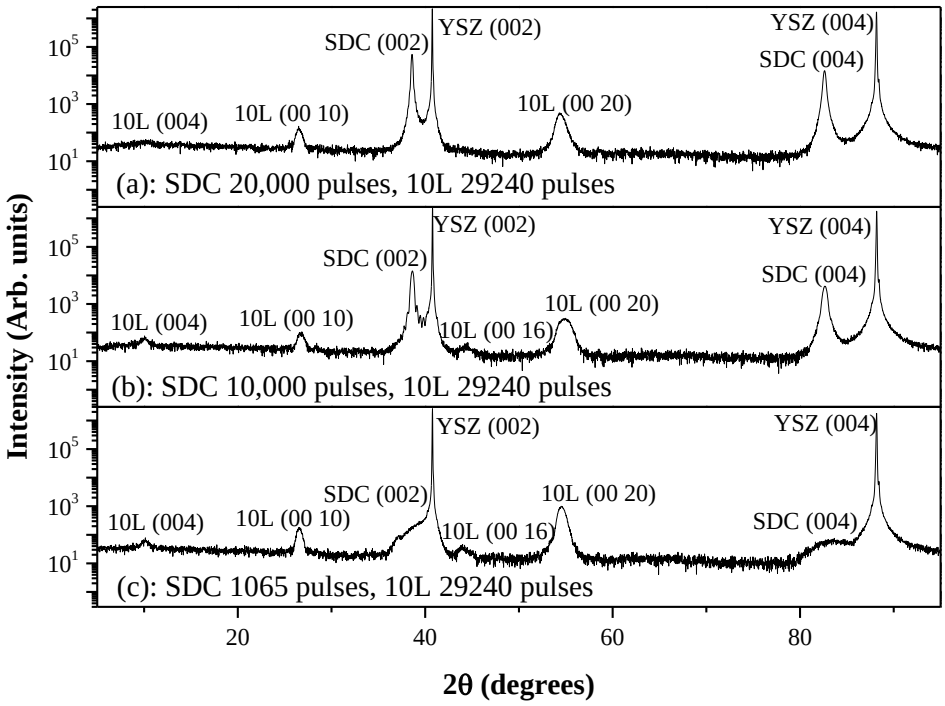

Figure 5.23: XRD patterns of the as deposited SDC 10 layer bilayer films prior to the stability measurements. (a) is SDC deposited with 20,000 pulses and the 10 layer deposited with 29240 pulses, (b) is SDC deposited using 10,000 pulses and the 10 layer with 29240 pulses and (c) is SDC deposited for 1065 pulses and the 10 layer for 29240 pulses.

The films also underwent XRR analysis to determine the thickness of both the SDC and 10 layer films. The patterns were fitted using X'Pert Reflectivity.[14]

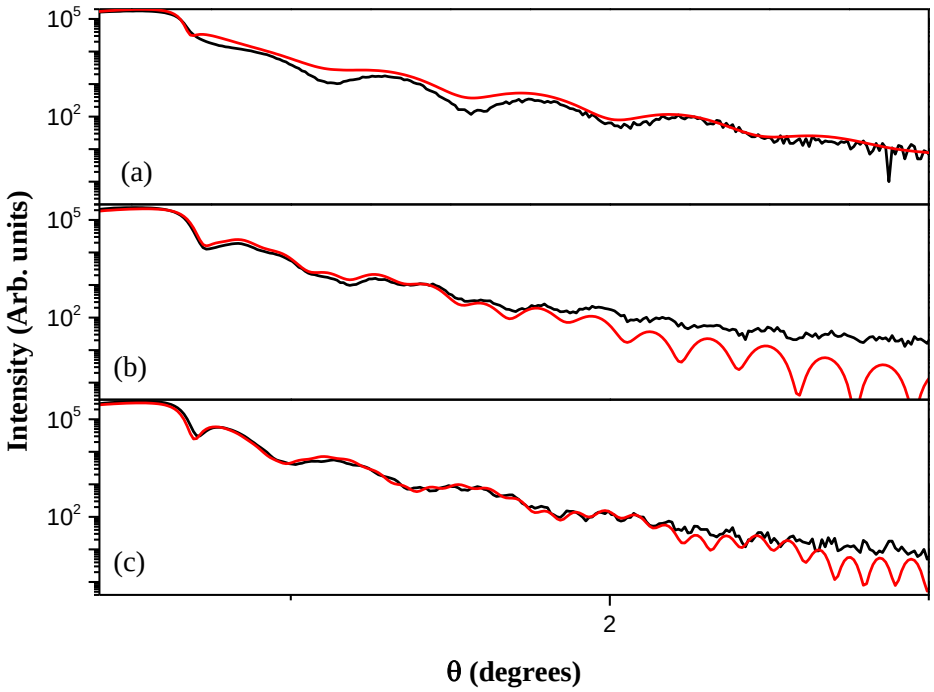

Figure 5.24: XRR patterns from the bilayer films with varying thickness of SDC. (a) SDC is 1065 pulses and 29240 pulses of 10 layer, (b) 10,000 pulses of SDC and 29240 pulses of the 10 layer and (c) 20,000 pulses of SDC and 29240 pulses of the 10 layer. The experimental data is in black with the simulated data overlaid in red for each thickness respectively.

Simulated fits from Figure 5.24 pattern (a) give an SDC thickness of 4.0nm, and a 10 layer thickness of 15.5nm. Pattern (b) has an SDC thickness of 31.5nm and a 10 layer thickness of 15.0nm. Pattern (c) has an SDC thickness of 74.0nm and a 10 layer thickness of 18.0nm.

The films were each cut into quarters with a diamond tipped pen. One quarter from each SDC film was put in a furnace at 600°C for 120 hours. The second

quarter was put in a furnace at 700°C for 120 hours and the third quarter was put in a furnace at 800°C for 120 hours. The XRD patterns for the SDC film deposited with 20,000 pulses can be seen in Figure 5.25, 10,000 pulses in Figure 5.26 and 1065 pulses in Figure 5.27.

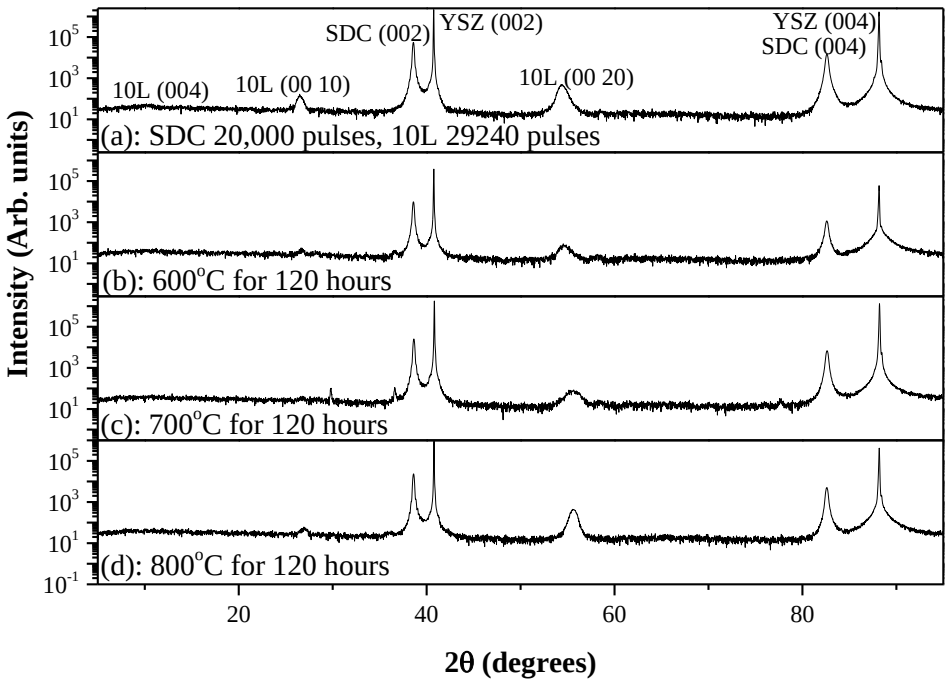

Figure 5.25: XRD of (a) 74.0nm of SDC, and 18.0nm of 10 layer, having been annealed at (b) 600°C, (c) 700°C and (d) 800°C for 120 hours.

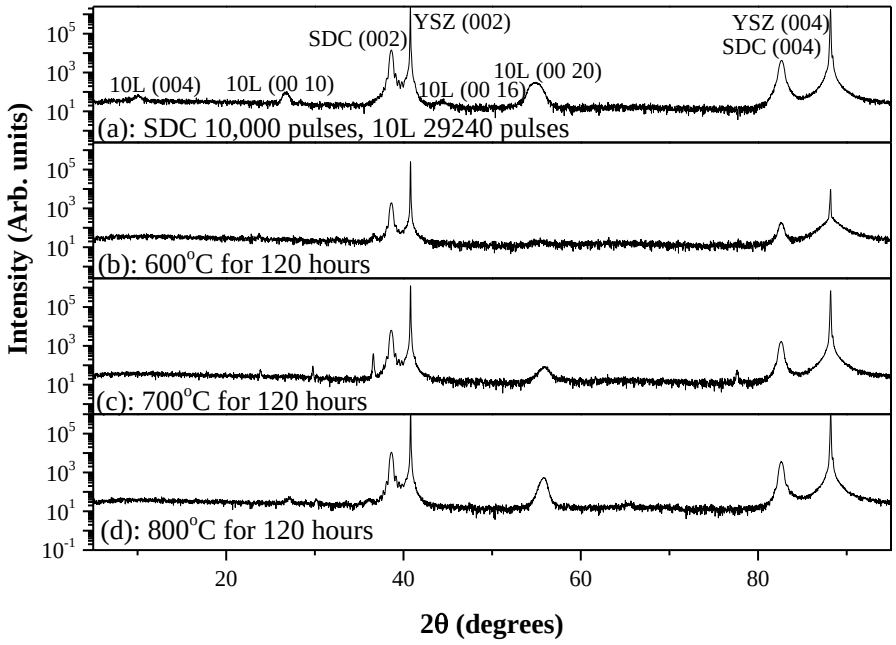

Figure 5.26: XRD of (a) 31.5nm of SDC and 15.0nm of 10 layer, having been annealed at (b) 600°C, (c) 700°C and (d) 800°C for 120 hours..

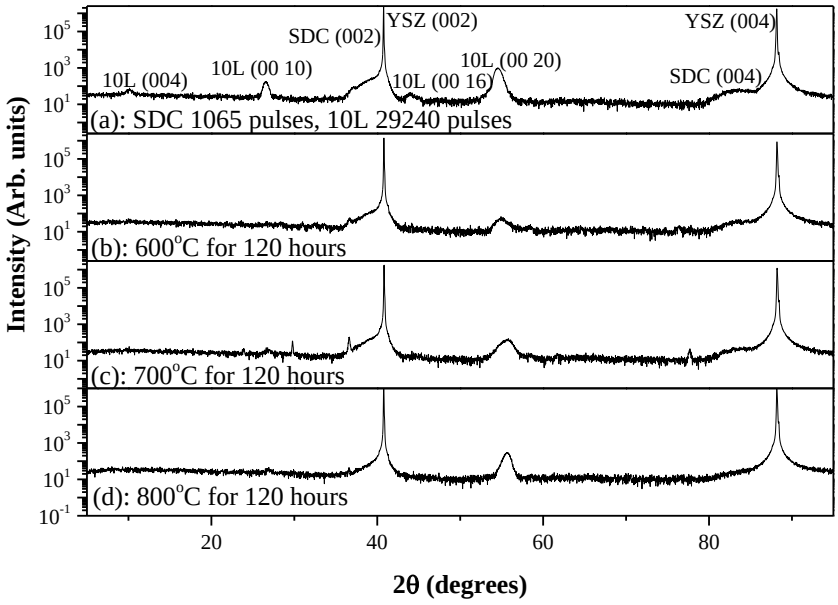

Figure 5.27: XRD of (a) 4.0nm of SDC and 15.5nm of 10 layer, having been annealed at (b) 600°C, (c) 700°C and (d) 800°C for 120 hours.

All the SDC films in Figures 5.25, 5.26 and 5.27 are lacking the (004) 10 layer ordering peak at all temperatures. In addition to this there is a shift in the 10 layer peak position as the temperature increases across all the SDC films.

From the stability testing it was concluded that the thickness of the SDC film does not affect the stability of the 10 layer film for the thicknesses of SDC investigated. However the 10 layer peak positions shift in all cases indicating instability, and therefore the ASR was unable to be measured for these films in this geometry.

5.3.2.3 Further Stability Analysis

Dr. Marco Zanella at the University of Liverpool performed Raman spectroscopy of the 10 layer target, which was used in the deposition of the films, and Darren Hodgeman's 10 layer ink both dried at 100°C and annealed at 600°C for 120 hours. A Renishaw inVia Raman Microscope was used with WiRE software.

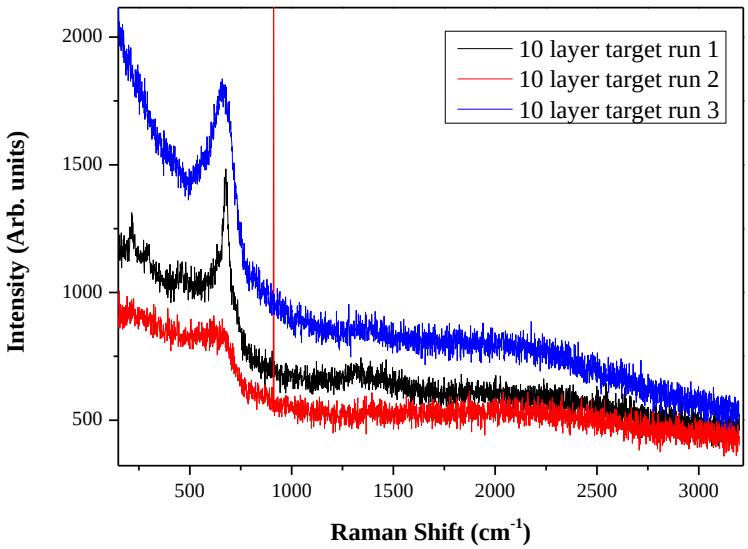

Figure 5.28: Raman spectra from the 10 layer target.

The Raman spectra in Figure 5.28 were taken from the 10 layer target, as synthesised by Dr. Ruth Sayers at the University of Liverpool. The spectra are used as a reference for later Raman spectra, of the 10 layer ink.

XRD patterns of the 10 layer ink were compared both on a glass slide, dried at 100°C, and on a YSZ substrate at 600°C for 120 hours. Close analysis of these patterns highlights that the (004) peak in Figure 5.29 pattern (a) is missing on pattern (b).

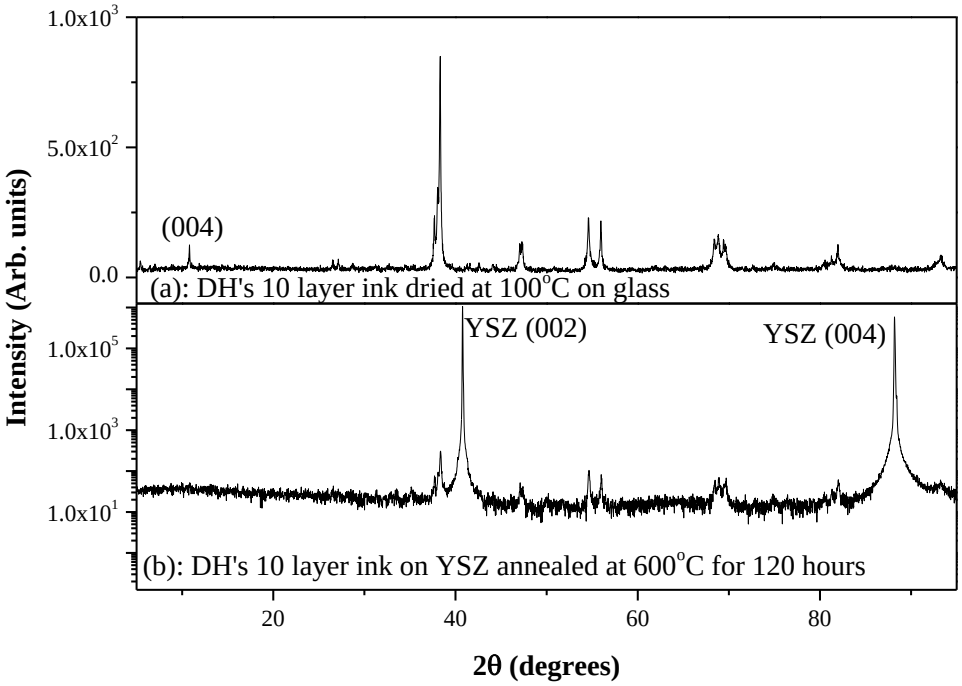

Figure 5.29: XRD data from the 10 layer ink, (a) dried at 100°C on glass and (b) annealed at 600°C for 120 hours on YSZ.

Although the XRD data doesn't show the (004) 10 layer ordering peak, the intensity of this peak is quite small. The Raman data was therefore analysed to see

if the inks were stable but the intensity of the peak was too small to observe in the XRD pattern, or if the ink had indeed degraded.

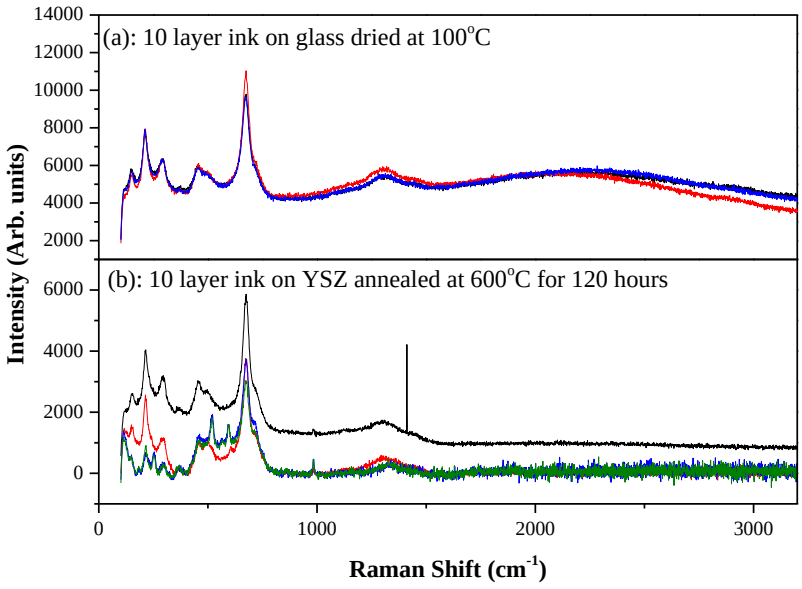

Figure 5.30: Raman data from the 10 layer ink, (a) dried at 100°C on glass and (b) annealed at 600°C for 120 hours on YSZ. Different colours represent repeat runs.

Kosacki *et al*. report on Raman data of single crystal 16 mol% YSZ, and find that there are peaks at 259, 362, 620 and 690 cm^{-1}.[17] The Raman peaks in Figure 5.30, aside from the anomalous artefact at 1410cm^{-1}, while different in intensities are nominally in the same position which suggests that the 10 layer ink hasn't reacted with the YSZ substrate.

In the literature SDC buffer layers are in the order of μm,[11-13] and are much thicker than those we were able to grow for this work. In addition to this an interfacial reaction between YSZ and SDC can form a (Zr, Ce)O_2 based solid-

solution at high temperatures.[10] The stability studies with the SDC and 10 layer films, in Section 5.3.2.2, showed that the 10 layer film was not stable having been annealed at 600°C for 120 hours. In order for the double sided geometry to be grown the initial SDC|10 layer film would be effectively annealed during the growth of the second side at the optimum growth temperature of 850°C. It was therefore decided to no longer pursue this geometry.

5.3.3 Geometry Three

A third and final geometry was studied, to resolve the issues faced with geometries one and two. In collaboration with Dr. Plamen Stanislavov's group at the University of Dublin geometry 3, was designed, see Figure 5.31.

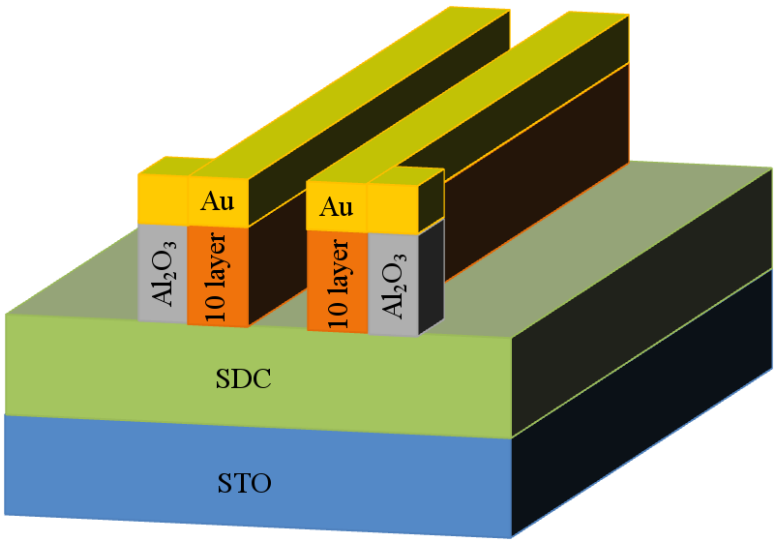

Figure 5.31: Schematic, not to scale, showing geometry 3. The STO substrate is shown in blue, the SDC electrolyte layer in green, the 10 layer in orange. Gold electrodes are shown in yellow, with insulating Al_2O_3 in grey.

The electrodes are patterned by Dr. Plamen Stanislavov's group at the University of Dublin. In Figure 5.31 the additional gold pads to the side of the gold electrodes are deposited on insulating Al_2O_3 which would not contribute to the measurement of ASR, but provide a larger area for attaching wires.

Thin films of the 10 layer material are deposited on SDC, itself deposited on STO (001) single crystal substrates. Both the 10 layer and SDC films were deposited at 850°C, 5Hz and a pO_2 of 10mTorr, with a flow rate of 12.8sccm. The SDC film was deposited for 8,433 pulses with a laser energy of 195mJ to give a target thickness of 100nm. The $Ba_{1.7}Ca_{2.4}Y_{0.9}Fe_5O_{13}$ cathode layer was deposited at 300mJ for 29,240 pulses to give a target thickness of 50nm.

XRD analysis was carried out on both the single layer and bilayer films, shown in Figure 5.32. In this case it was not necessary to use the YSZ substrate, because here the SDC film will be the electrolyte, thereby eliminating the YSZ|SDC interfacial reaction difficulties.

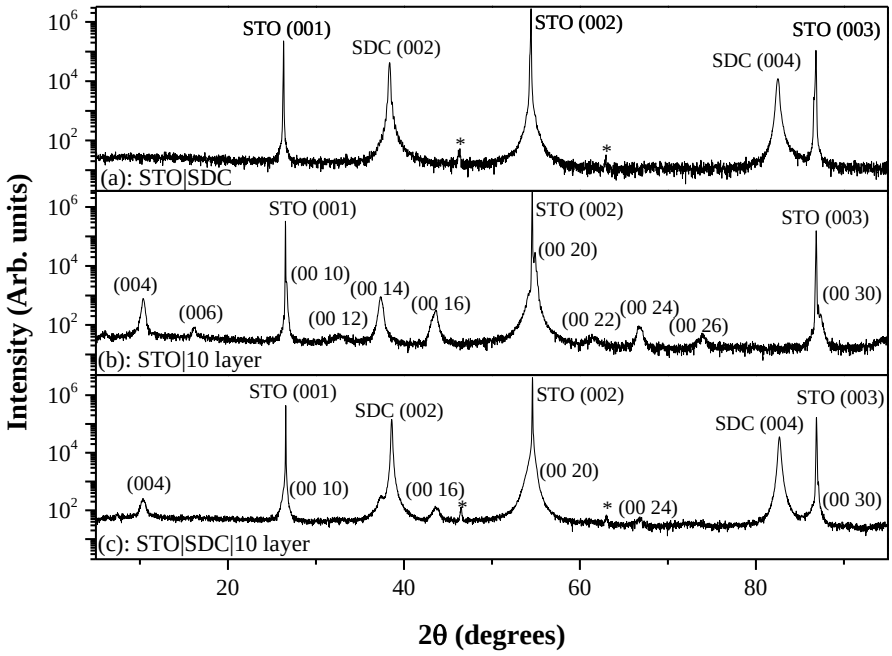

Figure 5.32: XRD patterns of the single and bilayer films on STO (001) substrates, (a) is SDC grown on STO, (b) 10 layer on STO and (c) the SDC| 10 layer bilayer film. Peaks marked with an * are from the sample holder.

From Figure 5.32 (c) it can clearly be seen that there is a combination of the peaks from the XRD patterns in Figure 5.32 (a) and (b). This indicates that oriented films were successfully grown in this configuration. Some of the less intense ordered peaks (eg (006)) are no longer visible, due to the single layer 10 layer film being thicker than that grown on the bilayer film.

XRR was used to determine if the target thicknesses were achieved. The XRR patterns were simulated using X-Pert Reflectivity software, and both the measured and simulated data is shown in Figure 5.33.[14]

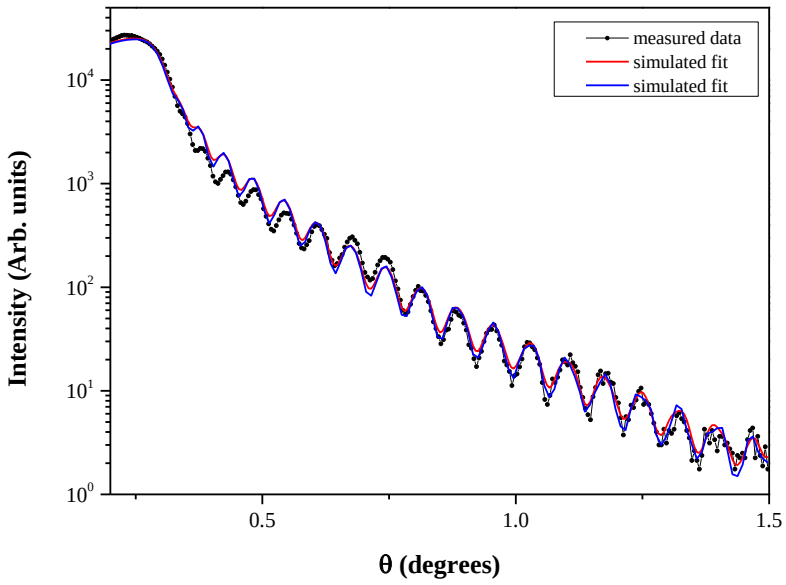

Figure 5.33: XRR measured data in black from the bilayer film, and simulated fits in red and blue.

Two simulations were performed to fit the XRR data as bilayer films are typically difficult to fit exactly and an average fit from multiple simulations gives an indication of the errors involved in the fitting. The red simulated fit shown in Figure 5.33 gives simulated thicknesses of 98nm for the SDC and 59nm for the 10 layer. A roughness of 0.6nm for the SDC and 0.6nm for the 10 layer are also observed from the simulated fit, and the STO substrate is assumed to be perfectly smooth.

The blue simulated fit from Figure 5.33 gives thicknesses of 92nm for the SDC and 59nm for the 10 layer. A roughness of 0.6nm for the SDC and 0.6nm for the 10 layer are also observed, and again the STO substrate is assumed to be perfectly smooth.

The simulated fits give thicknesses that are comparable to the target thicknesses of the films, with the SDC layer slightly thinner than expected at 95 ±3nm and the 10 layer slightly thicker at 59nm.

Rocking curves, or omega scans, of the bilayer films have also been measured by XRD, shown in Figure 5.34. These curves have been fitted using the Gaussian mathematical function in Origin version 8.5.[15]

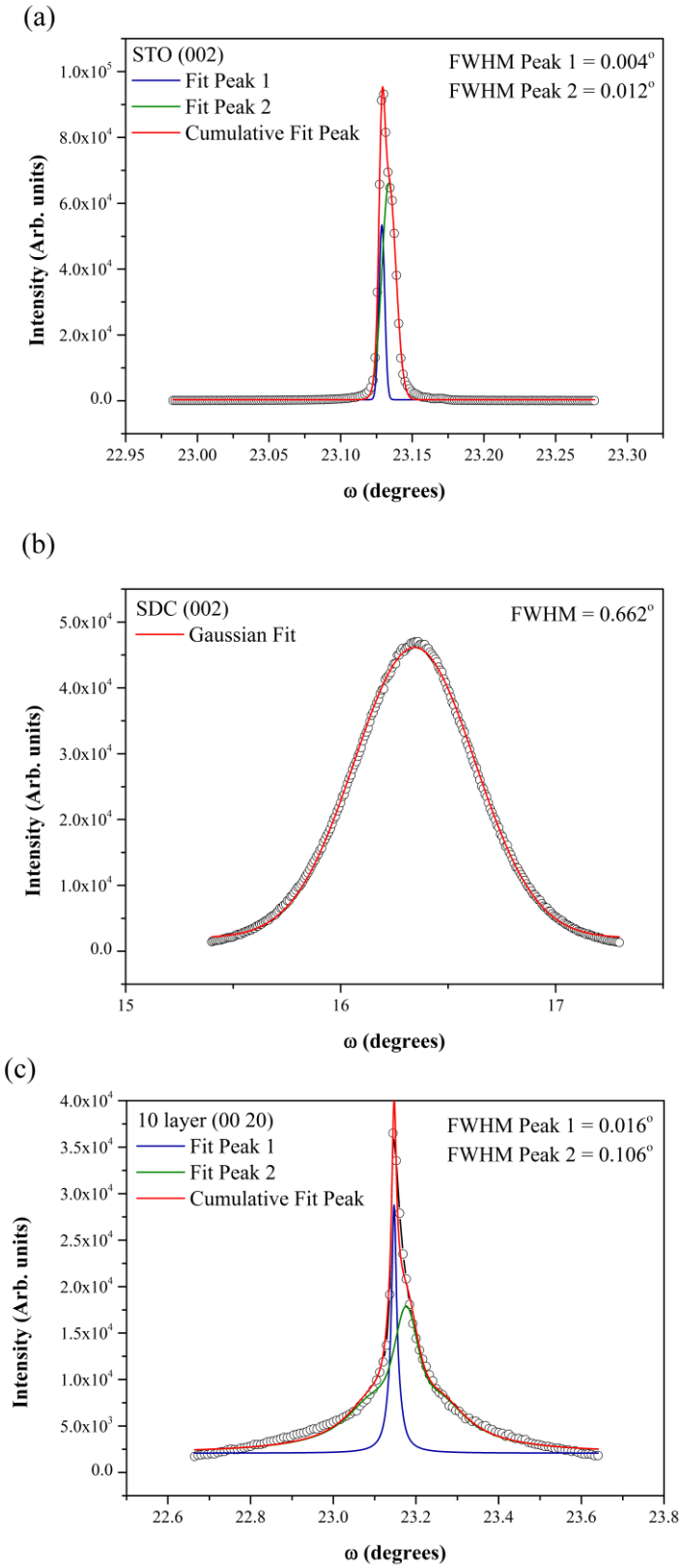

Figure 5.34: Rocking curves of (a) the STO substrate, (b) SDC and (c) 10 layer film.

The FWHM can be fitted from the omega scans and the STO (002) peak has a FWHM of 0.008°, the SDC (002) peak has a FWHM of 0.662° and the 10 layer (00 20) has a FWHM of 0.061°. This shows that the films have good growth coherence.

In addition to the X-ray analysis, atomic force microscopy (AFM) was used to analyse the surface roughness of both the single layer and the bilayer films. The topography images were collected using alternating current atomic force microscopy (ACAFM) mode, and are shown in Figures 5.35, 5.36 and 5.37.

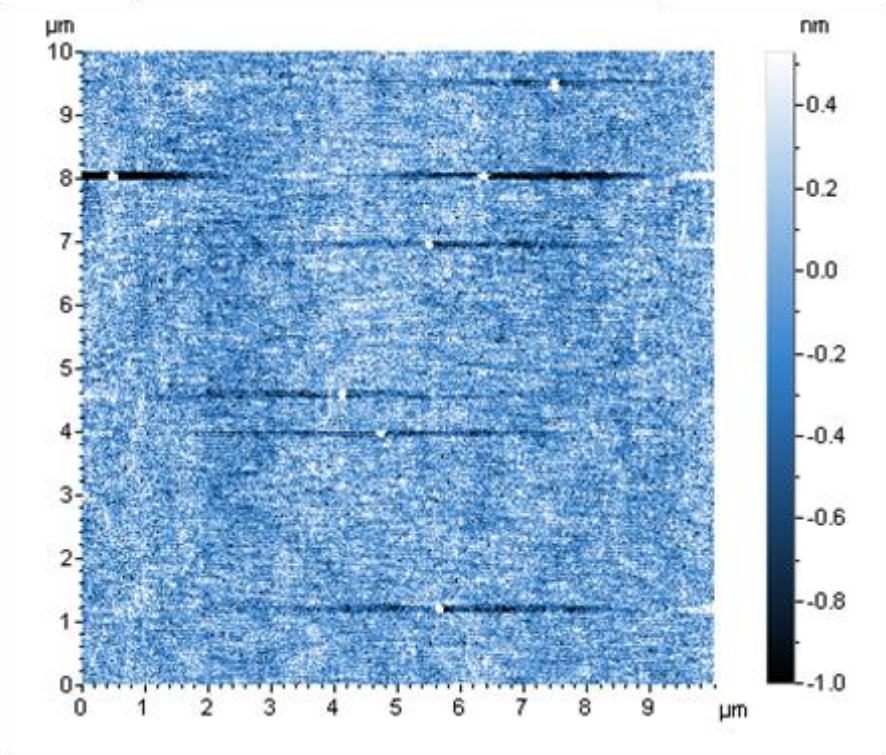

Figure 5.35: AFM of SDC on STO.

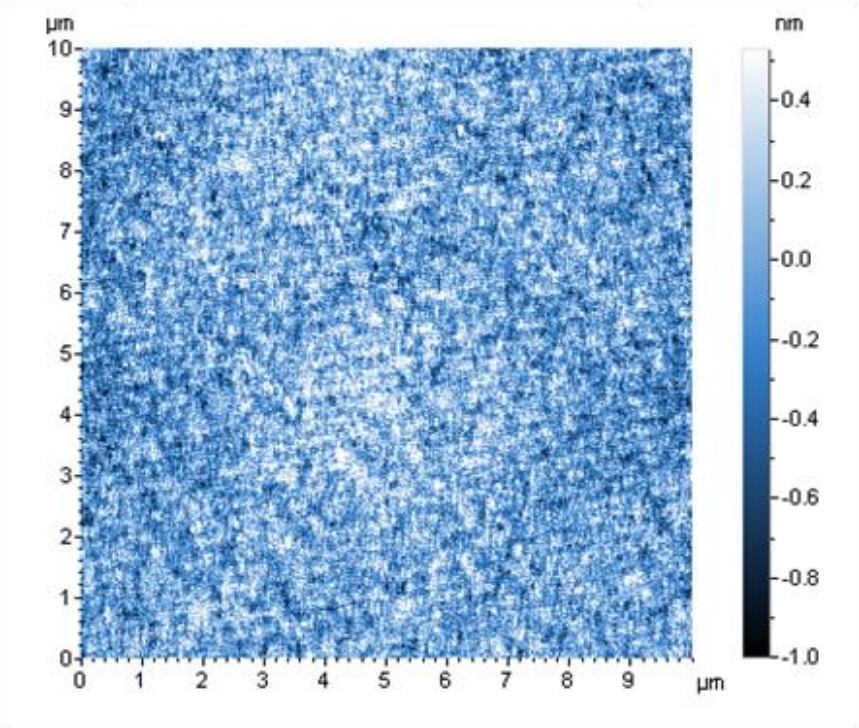

Figure 5.36: AFM of 10 layer on STO.

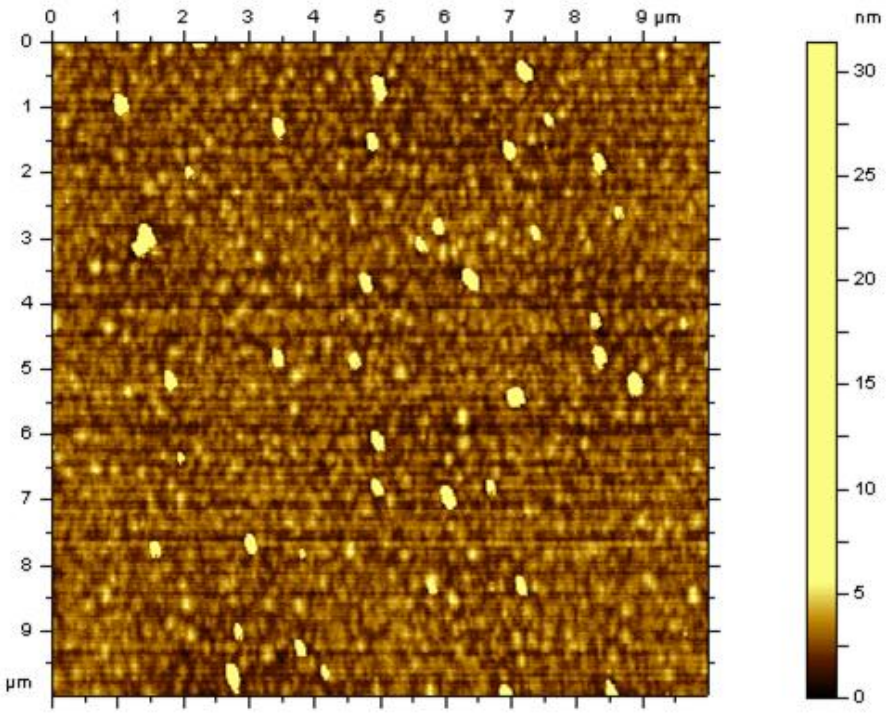

Figure 5.37: AFM of 10 layer |SDC|STO bilayer film surface.

From the AFM topography images the root mean square (RMS) roughness can be obtained, giving a roughness value across the whole image. The single layer SDC on STO has a RMS value of 1.1nm, slightly rougher than the 0.6nm found from the simulated STO|SDC|10 layer XRR bilayer fit, likely due to the artefects present on the surface. The single 10 layer on STO has a RMS value of 0.6nm, the same as calculated from the simulated STO|SDC|10 layer bilayer XRR. The STO|SDC|10 layer bilayer has a RMS value of 1.6nm from the AFM, slightly larger than the combined roughness of 1.2nm from the bilayer XRR simulation due to the artefacts present in the AFM. The darker horizontal features observed in Figure 5.35 are artefacts resultant from the slow reaction of the tip to a high feature.

Stability testing of the bilayer film was also performed, by annealing a film at 600°C for 90mins with a heating and cooling rate of 5°Cmin^{-1}. XRD patterns were taken both before and after annealing, and are shown in Figure 5.38.

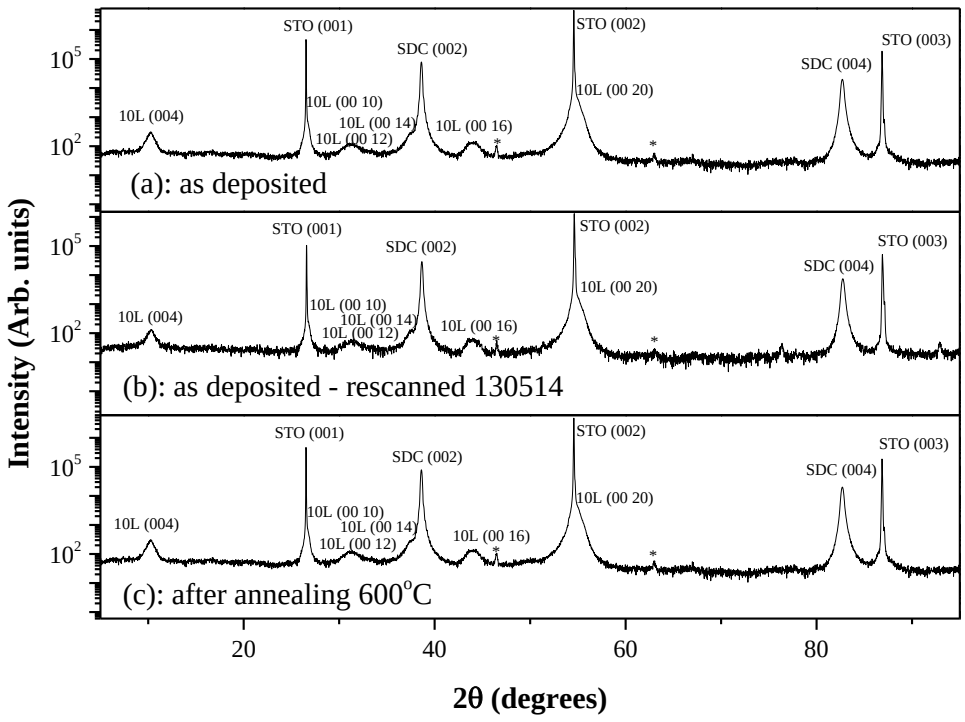

Figure 5.38: XRD data from the bilayer film before (a and b) and after annealing at 600°C (c).

The film was initially grown and X-rayed in October 2013 (Figure 5.38 (a)), and then again in May 2014 when the stability tests were performed. The second XRD is shown in Figure 5.38 (b), and a comparison with Figure 5.38 (a) shows that the film is stable over this period. From the XRD patterns in Figure 5.38, it can be seen that there are no missing or additional peaks present after the film was annealed at 600°C (Figure 5.38 (c)).

In addition to the XRD, Dr. Marco Zanella collected Raman data from the bilayer film before and after annealing, as shown in Figure 5.39. A Reinshaw inVia Raman Microscope was used with WiRE software. A laser with wavelength of 633nm and a range of 100-3200cm^{-1} was used to collect spectra.

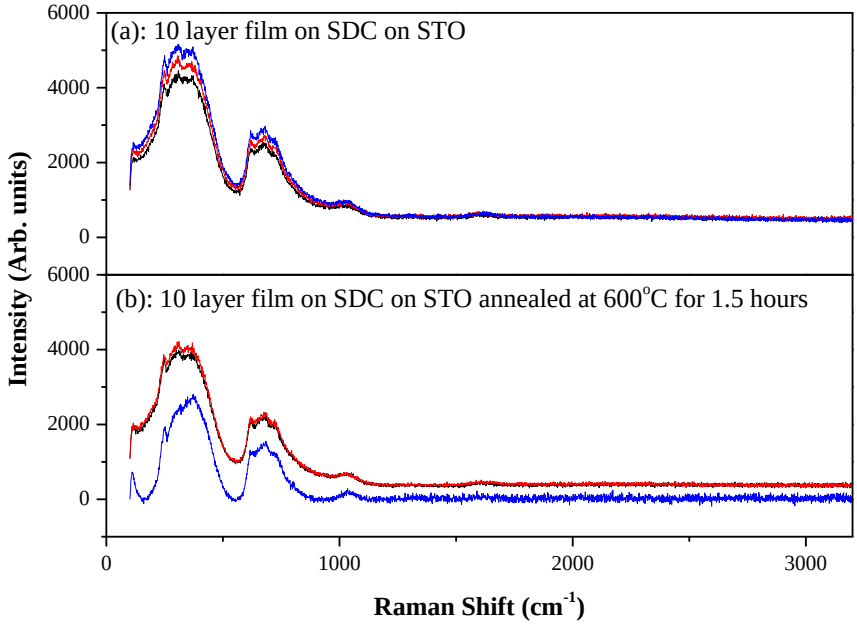

Figure 5.39: Raman spectra of the bilayer film before (a) and after (b) annealing, the repeat runs can be seen in red and blue.

After annealing at 600°C the Raman peaks are still in the same position as the original film, and so the film is deemed stable. The difference in intensity seen in Figure 5.39 (b) between the blue run and the red and black runs is a resulting function from removing the background in the blue spectrum. SDC powder has been found to produce a broad peak in the Raman spectra between 530 and 620cm^{-1} by Wang *et al.*[18] STO single crystals exhibit broad peaks between 200 and 400cm^{-1}, between 600 and 800cm^{-1} and 1050cm^{-1}.[19] This is consistent with the Raman data shown in Figure 5.39.

After growth and analysis, the bilayer film was sent to Dr. Plamen Stanislavov's group at the University of Dublin for plasma etching to pattern the 10 layer film into electrodes. Figure 5.40 shows the electrode design that was sent to Dublin.

Each of the positions on the mask have varying dimensions of the width of the electrode (W) and the distance between the electrodes (D), which are shown in Figure 5.40.

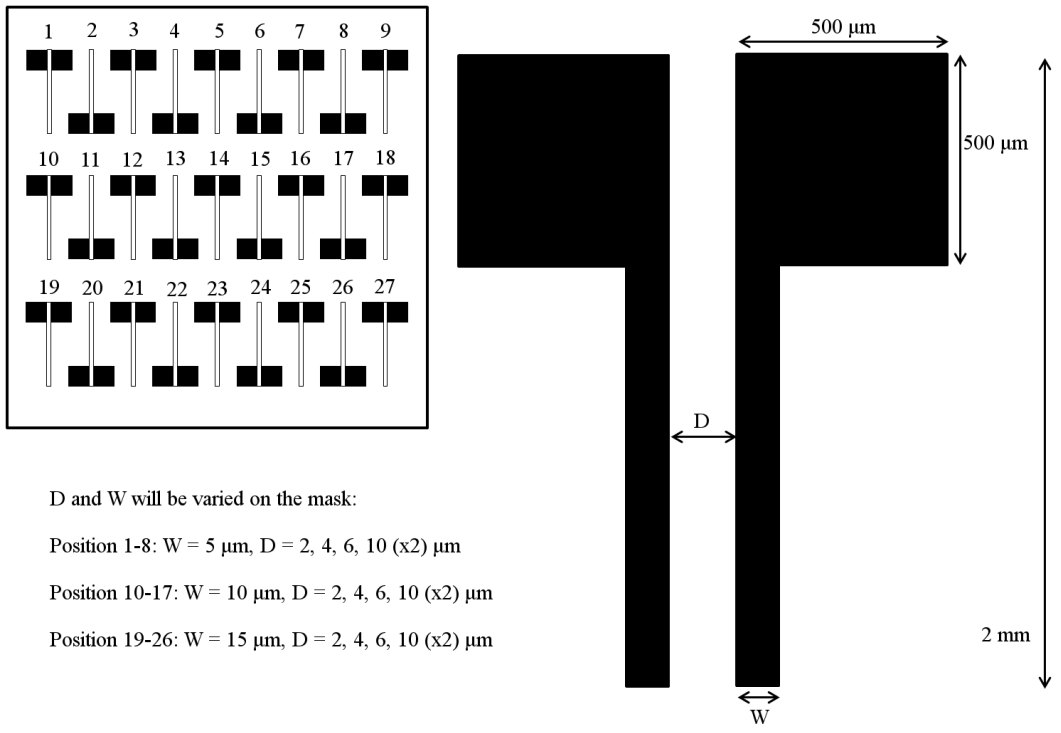

Figure 5.40: Schematic, not to scale, of the electrode arrangement in the top left with an expanded view of an electrode pair with dimensions on the right. Values for D and W are in µm.

Small values for D and W are required to clearly observe the low frequency electrode arc, however this presents a practical challenge as to how small the electrodes can be without causing electrical short circuits or suffering stability issues. It is unknown which specific values of D and W will produce the clearest

arcs for this geometry and so a selection of the best options, based on simulations carried out by Dr. Ming Li at the University of Liverpool (shown in Appendix 2, Figures A2.1 - A2.4), has been chosen.

The impact of the Al_2O_3 insulating layer is also investigated, with positions 9, 18 and 27 possessing wider Al_2O_3 layers as shown in Figure 5.41.

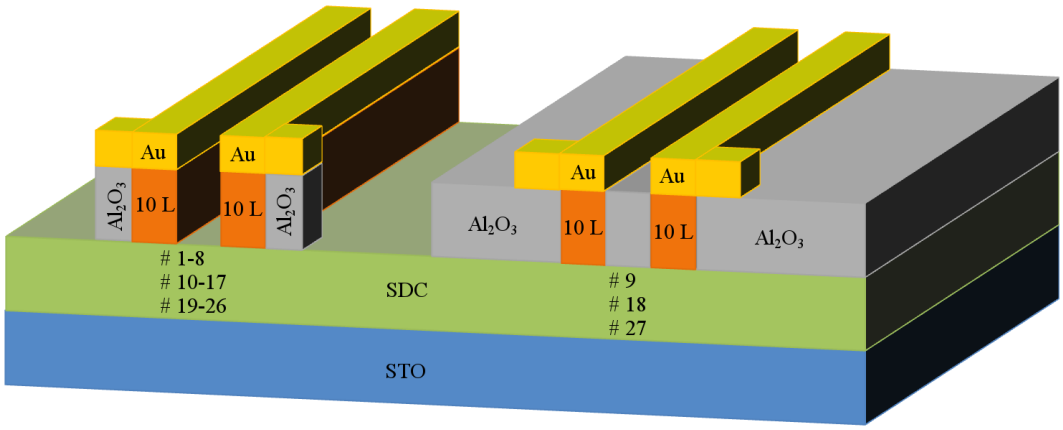

Figure 5.41: The difference in electrode design between the end electrode and the remaining electrodes in each row.

In addition to patterning the STO|SDC|10 layer bilayer film, two blank (001) STO substrates were also patterned. The first STO substrate was patterned with Ti|Au electrodes and the stability of these electrodes was tested. The electrodes were analysed using optical microscopy before and after annealing at 600°C for 38 hours, shown in Figures 5.42 and 5.43.

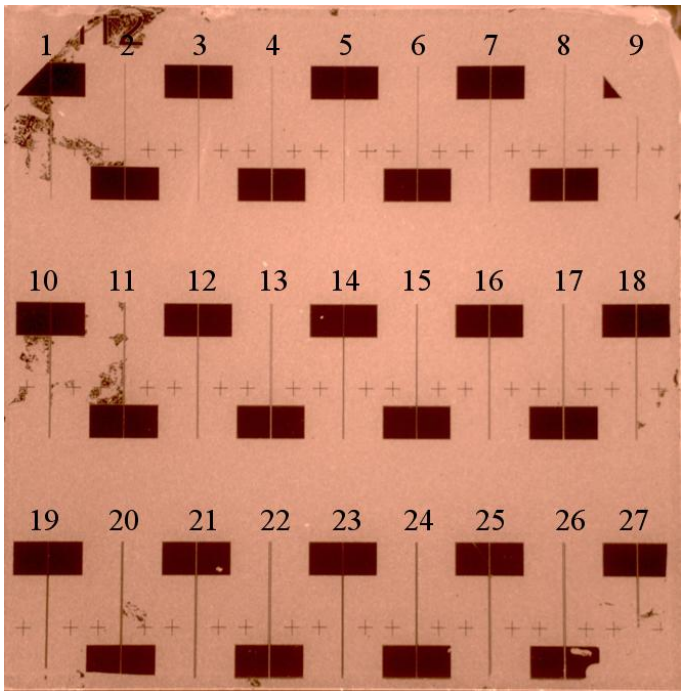

Figure 5.42: Optical microscopy of the patterned STO substrate before annealing. Electrode pairs are numbered following the schematic shown in Figure 5.40.

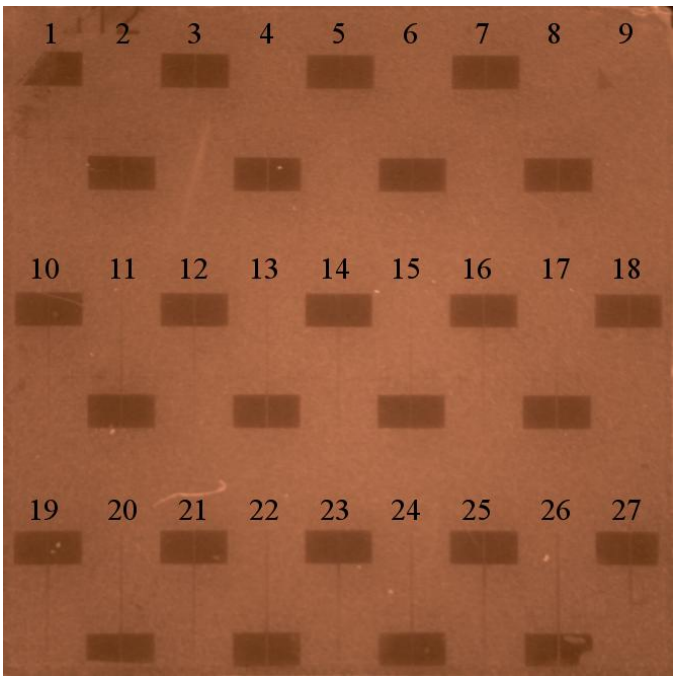

Figure 5.43: Optical microscopy of the STO substrate having been annealed at 600°C for 38 hours. Electrode pairs are numbered following the schematic shown in Figure 5.40.

From the optical microscopy in Figures 5.42 and 5.43 it is clear that the gold has faded having been subjected to annealing at 600°C, being the operating temperature for an SOFC and therefore our target temperature to measure the ASR.

As the gold features have faded, and the gold likely diffused into the substrate, the second STO substrate was patterned with Cr|Pt electrodes to see if these are more stable. Optical microscopy and the Keithly probe station measurements were performed before annealing the sample. The stability was tested at 600°C for 3 hours, and then for a further 36 hours repeating the microscopy after the initial 3 hours and after the further 36 hours. The resultant photographs from the optical microscopy of an example electrode from the top row electrodes can be seen in Figure 5.44.

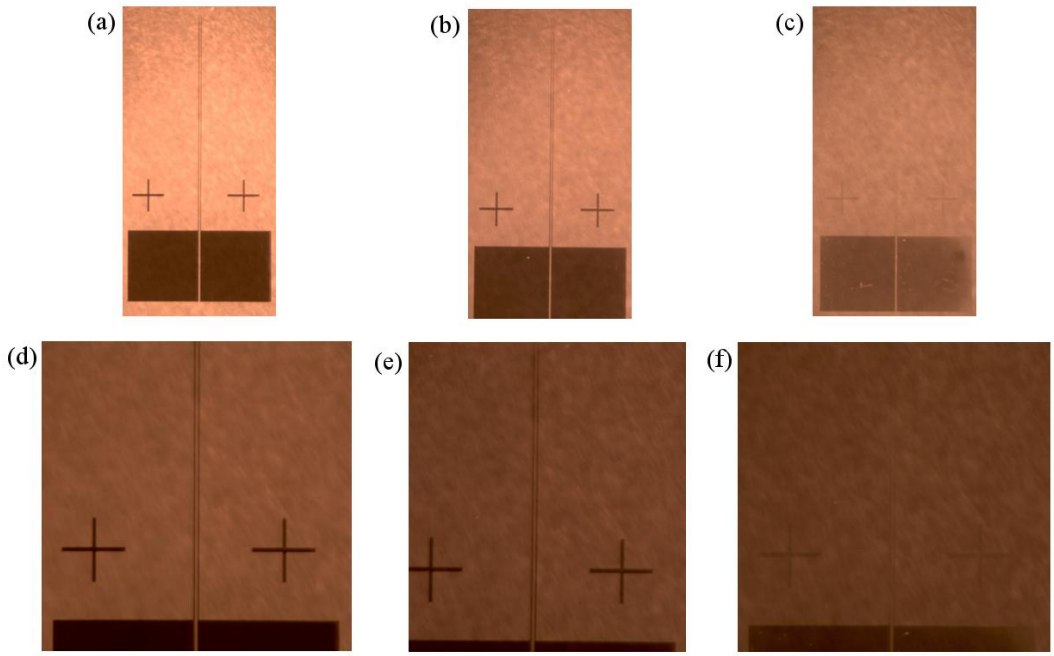

Figure 5.44: Optical microscopy of electrode pair 8 on the top row of electrodes. (a) is as received, (b) after annealing at 600°C for 3 hours, (c) after annealing at 600°C for a further 36 hours. (d), (e) and (f) are zoomed images of (a), (b) and (c) respectively.

As can be seen from Figure 5.44 the top row electrode pairs do fade after 36 hours of annealing, but the electrodes appear intact in the SEM image (shown in Appendix 2, Figure A2.5). Figures 5.45 and 5.46 show the electrode pairs from the middle and bottom rows respectively, which also show similar fading after the prolonged time at temperature.

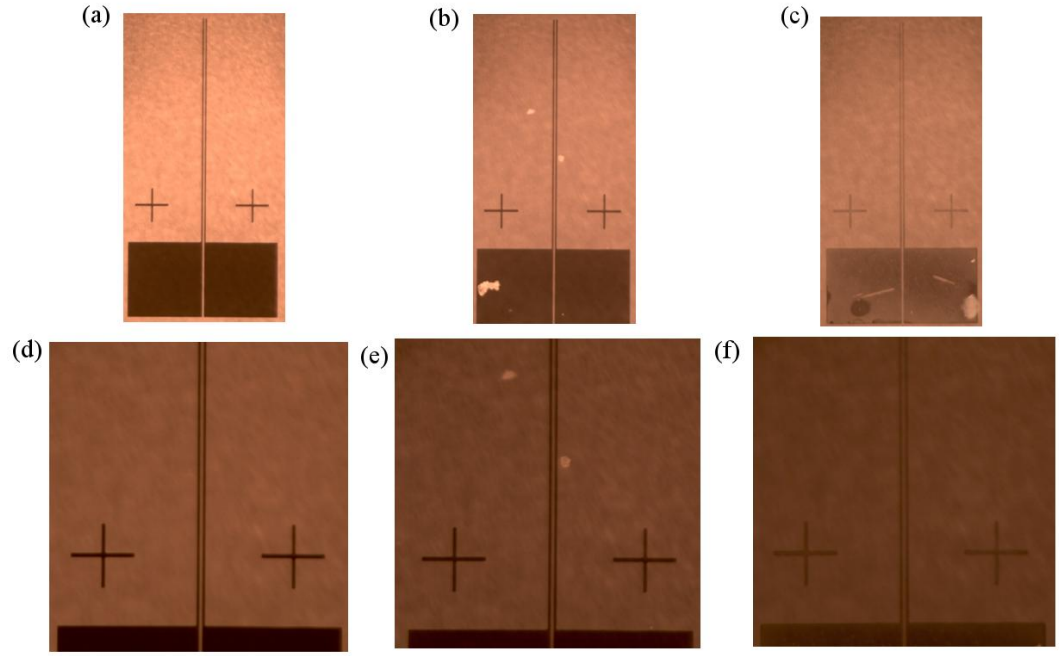

Figure 5.45: Optical microscopy of electrode pair 13 on the top row of electrodes. (a) is as received, (b) after annealing at 600°C for 3 hours, (c) after annealing at 600°C for a further 36 hours. (d), (e) and (f) are zoomed images of (a), (b) and (c) respectively.

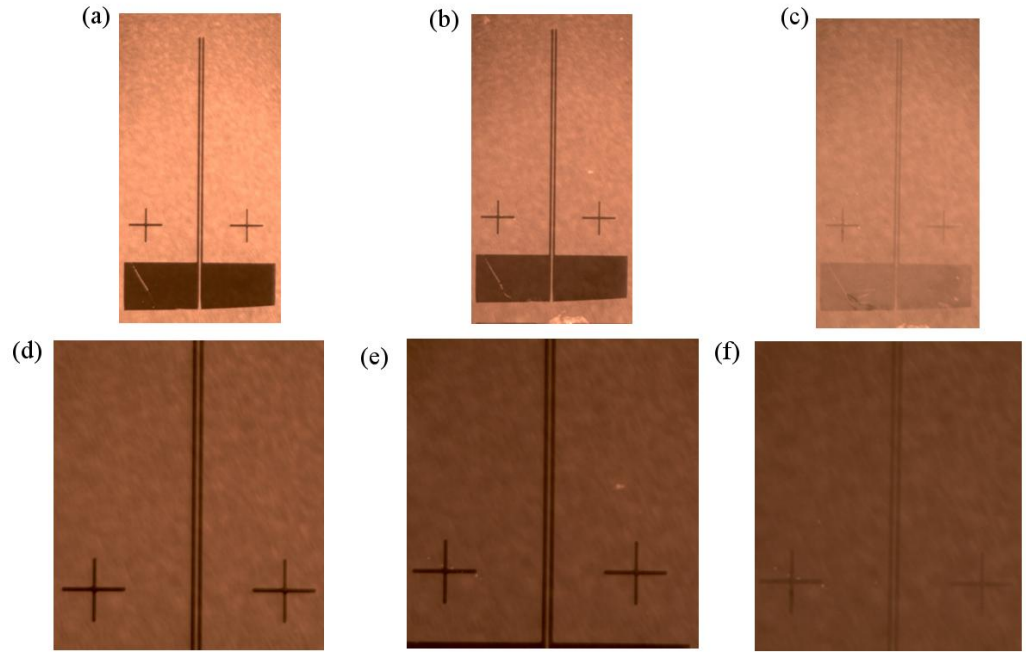

Figure 5.46: Optical microscopy of electrode pair 26 on the top row of electrodes. (a) is as received, (b) after annealing at 600°C for 3 hours, (c) after annealing at 600°C for a further 36 hours. (d), (e) and (f) are zoomed images of (a), (b) and (c) respectively.

At the University of Liverpool 2-probe measurements, like those discussed in Chapter 4 are commonly run, however this new electrode design required a new testing setup, to be designed, that would allow switching between electrodes at 600°C. Therefore whilst the patterning of the electrodes was being optimised at the University of Dublin, work in Liverpool continued to optimise the experimental test setup. Before all 27 electrodes pairs could be measured, a new experimental setup that could measure multiple electrodes was required. The prototype design is shown in the schematic in Figure 5.47.

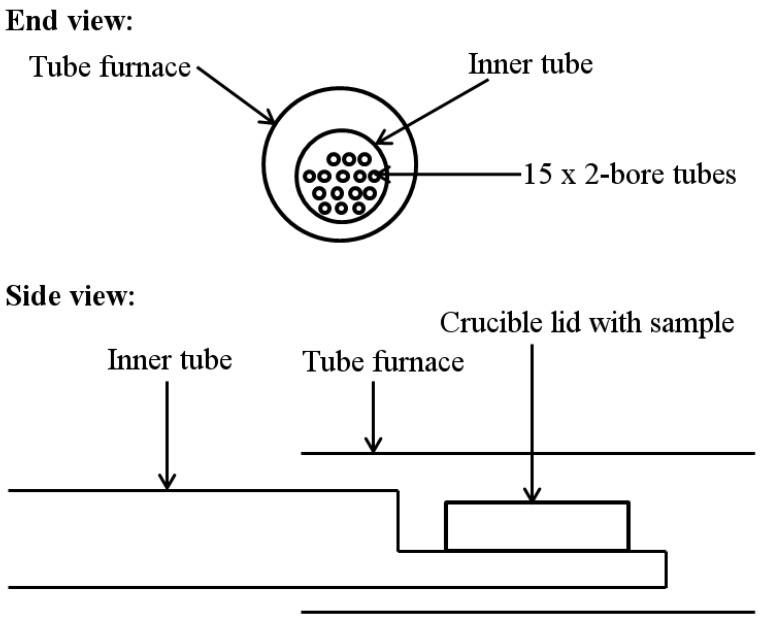

Figure 5.47: Schematic showing the new experimental setup. In addition to the diagram there is also a thermocouple placed through the inner tube.

The ASR experiment was designed to take place in a tube furnace. The inner tube was cut, as a support to hold the crucible lid. Charles Clavering at the University

of Liverpool created a switch to enable the wires coming out of the 2-bore tubes to be connected to the Solatron for measurement, and to enable the switching between electrode positions. Initially a 4 way switch was made, enabling 4 electrode pairs to be tested at a time. Dr. Marco Zanella at the University of Liverpool assisted with the new experimental setup.

The crucible lid was patterned with gold spots to use as contacts to the sample, using the gold sputter coater, as shown in Figure 5.48.

Figure 5.48: showing a substrate sitting inside the well in the crucible lid before and after the lid had been patterned.

Here, the sample holder is used to connect the wires from the electrode pairs, and then into the wires running through the furnace, as shown in Figure 5.49.

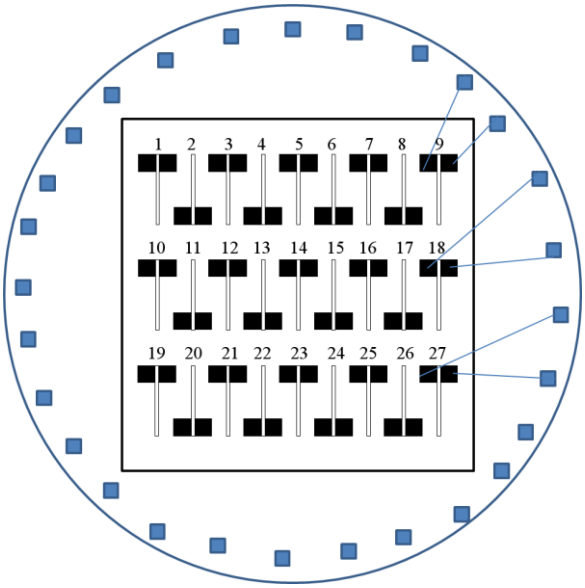

Figure 5.49: Schematic showing how the wires will be connected from the sample to the crucible lid. Pt wires are also attached from the 2-bore tubes to the gold spots to complete the connection.

Initially the attachment of the wires to the crucible lid was tested. The sputtered gold has good adherence to the crucible lid, and didn't come off when scratched.

Gold paste was then used to attach the wires at 600°C, however this connection was weak. The temperature was increased to 750°C, and a thicker layer of the gold was sputtered before the paste was applied and this improved the adherence.

5.3.3.1 Experimental Prototype

The prototype has Pt wire threaded through one 2-bore tube and alumina fish spine beads threaded onto the wires to electrically isolate them and ensure they do not short circuit when they come out of the tube. The prototype is shown in Figure 5.50.

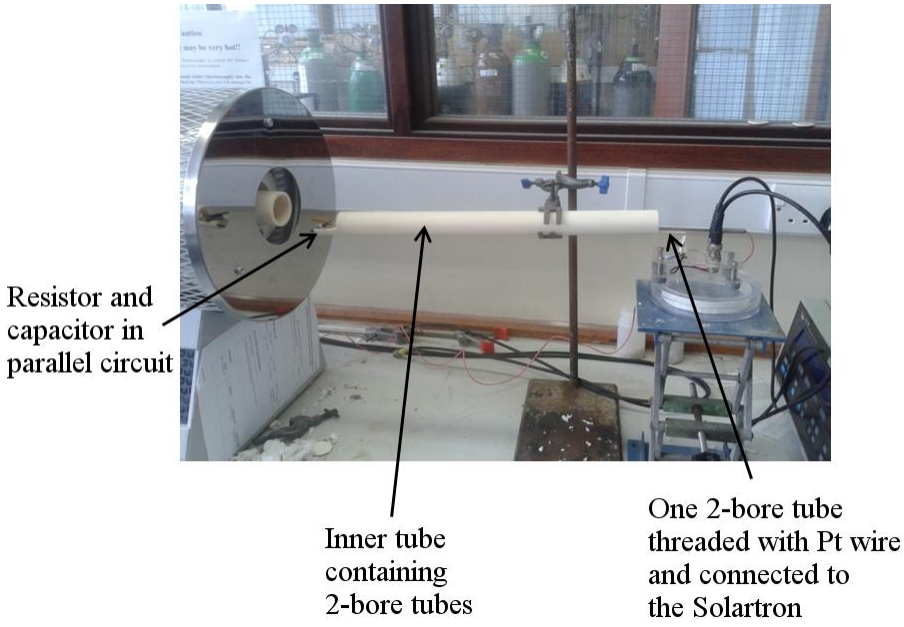

Figure 5.50: Showing the prototype arrangement.

In order to connect the prototype to the Solartron to test the measurements, the setup shown in Figure 5.51 was used.

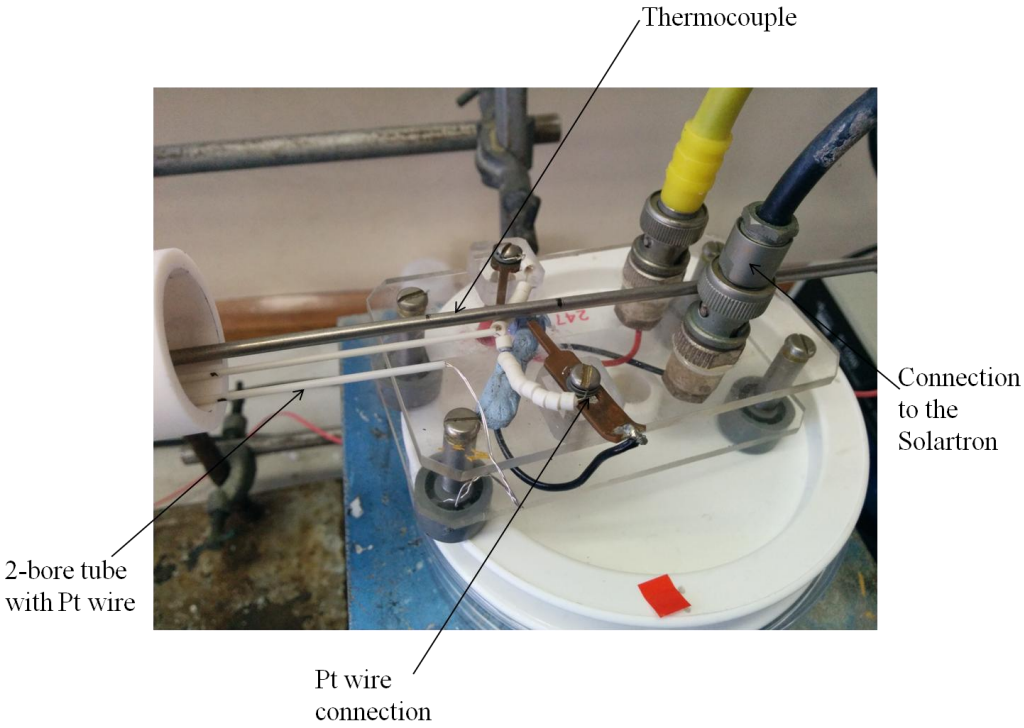

Figure 5.51: Setup connecting the prototype to the Solartron.

The prototype was used to measure the resistance and capacitance of a resistor and capacitors at room temperature in a parallel circuit. A 470Ω resistor with 2 capacitors, one of 200pF and the other of 800pF giving a total of 1nF was used. The AC impedance data can be seen in Figure 5.52. Dr. Ming Li at the University of Liverpool assisted with the AC impedance measurements.

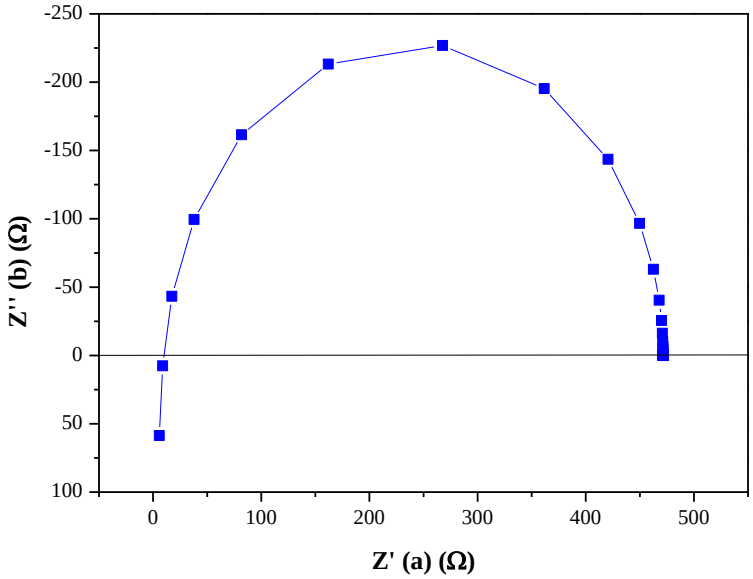

Figure 5.52: Nyquist plot of data taken with a resistor and capacitor in a parallel circuit.

From the Nyquist plot (seen in Figure 5.52) a resistance of 471.5Ω and a capacitance of 1.1nF is obtained. This is in close agreement with the expected 470Ω from the resistor and 1nF from the combination of the capacitors. It was concluded that the prototype worked.

The second stage prototype reduced the number of electrodes on the crucible lid to 8, see Figure 5.53, with a corresponding switch constructed by Charles

Clavering at the University of Liverpool. The electrode count was reduced for this prototype to help avoid short circuits with additional electrodes, and also to make it easier to attach the gold wires using gold paste.

Figure 5.53: New design for an 8 wire configuration.

The prototype will allow the use of 8 wires, and therefore to measure 4 pairs of electrodes.

Although the new experimental setup was primarily designed for measuring the ASR of the 10 layer film, initial conductivity tests were also conducted on the STO|Cr|Pt sample. Firstly gold wires were attached to the substrate pads before being joined to the sample holder shown in Figure 5.54.

Figure 5.54: STO|Cr|Pt sample with gold wires attached.

Once the sample was connected to the sample holder, the sample holder was then connected to the Pt wires running through the furnace.

The sample holder was then placed into the cut out ledge on the alumina tube, as in Figure 5.55.

Figure 5.55: The STO|Cr|Pt sample resting on the sample holder with all the wires connected.

The photograph in Figure 5.56 shows the new experimental setup as used to test electrode pairs 8, 13 and 26 from the STO|Cr|Pt sample.

Figure 5.56: Photograph of the new experimental setup.

At the end of the furnace the Pt wires were connected to the switch. The dimensions of the electrode pairs are shown in Table 5.1.

Table 5.1 Distances and widths of the three electrode pairs measured.

Electrode pair	8	13	26
D (µm)	10	10	10
W (µm)	5	10	15

Impedance arcs were measured from three electrode pairs each with a D of 10µm and with varying W of 5, 10 and 15µm. The electrode pairs were attached to a

switch box at positions 1, 2 and 4 for electrode pairs 8, 13 and 26 respectively. Nyquist plots, taken at 600°C, for these widths are shown in Figures 5.57, 5.58 and 5.59 respectively.

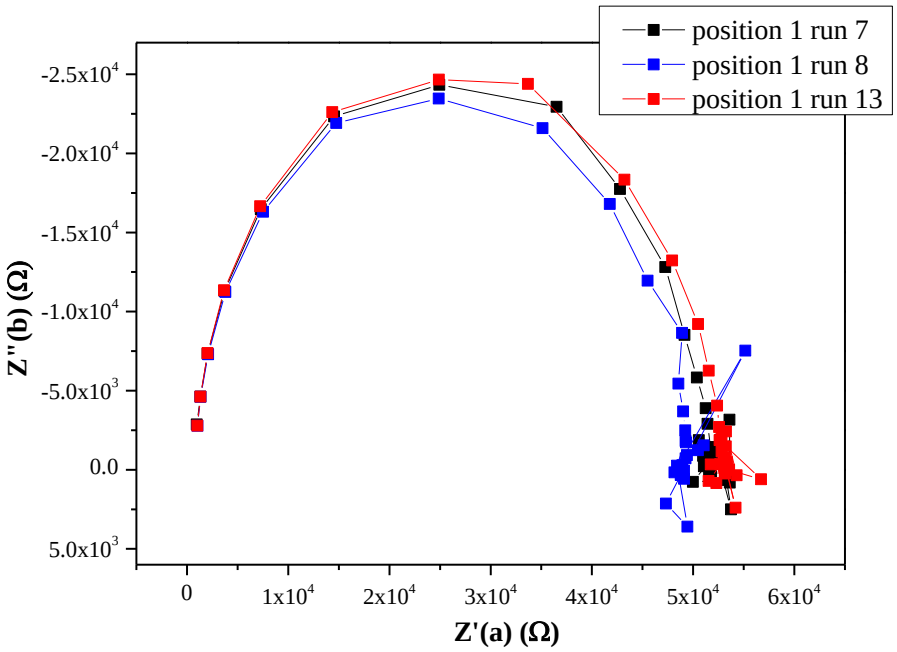

Figure 5.57: Impedance arcs from position 1, electrode pair 26 which had a D of 10μm and a W of 15μm.

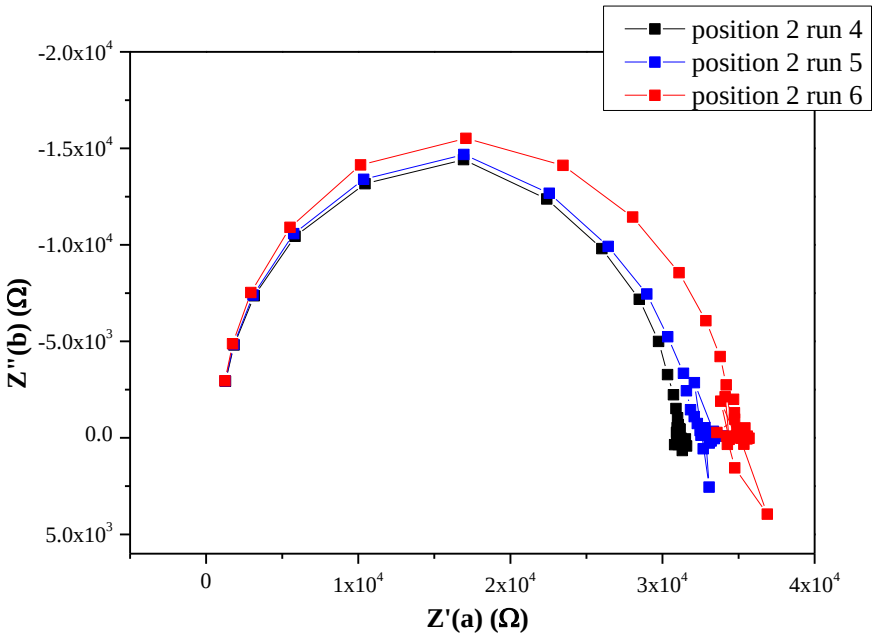

Figure 5.58: Impedance arcs from position 2, electrode pair 8 which had a D of 10µm and a W of 5µm.

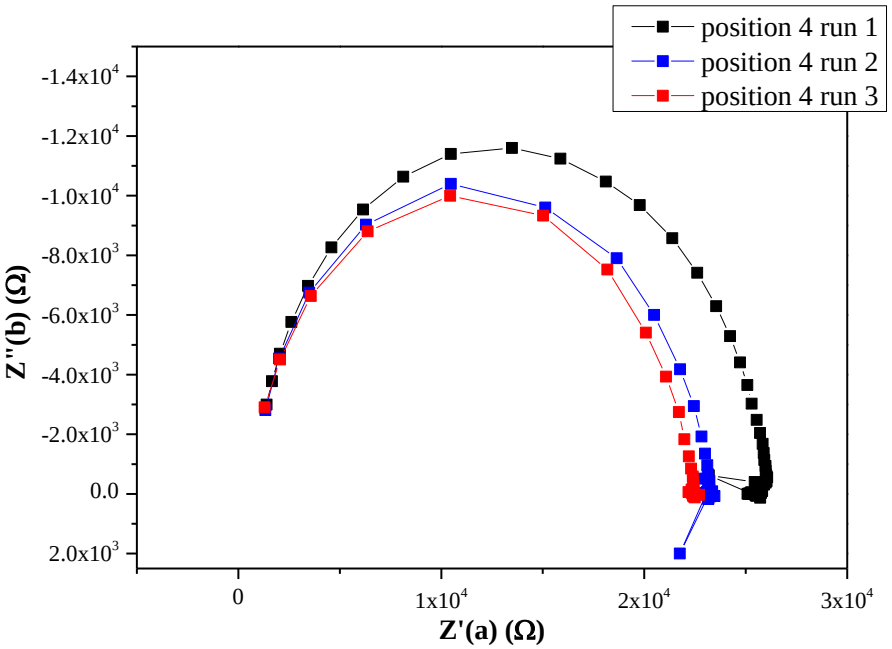

Figure 5.59: Impedance arcs from position 4, electrode pair 13 which had a D of 10µm and a W of 10µm.

The Nyquist plots shown in Figures 5.57, 5.58 and 5.59 are quite comparable in the repeat runs shown in the different colours. Resistances obtained from these arcs using Z-View software fits, were used to calculate the conductivities plotted later in Figure 5.60 including repeat measurements for positions 1 and 4. Unfortunately no arcs were obtained from the repeat of position two, with an open circuit response observed. Upon cooling and removing the sample from the furnace, one of the gold wires for position 2 was found to be broken.

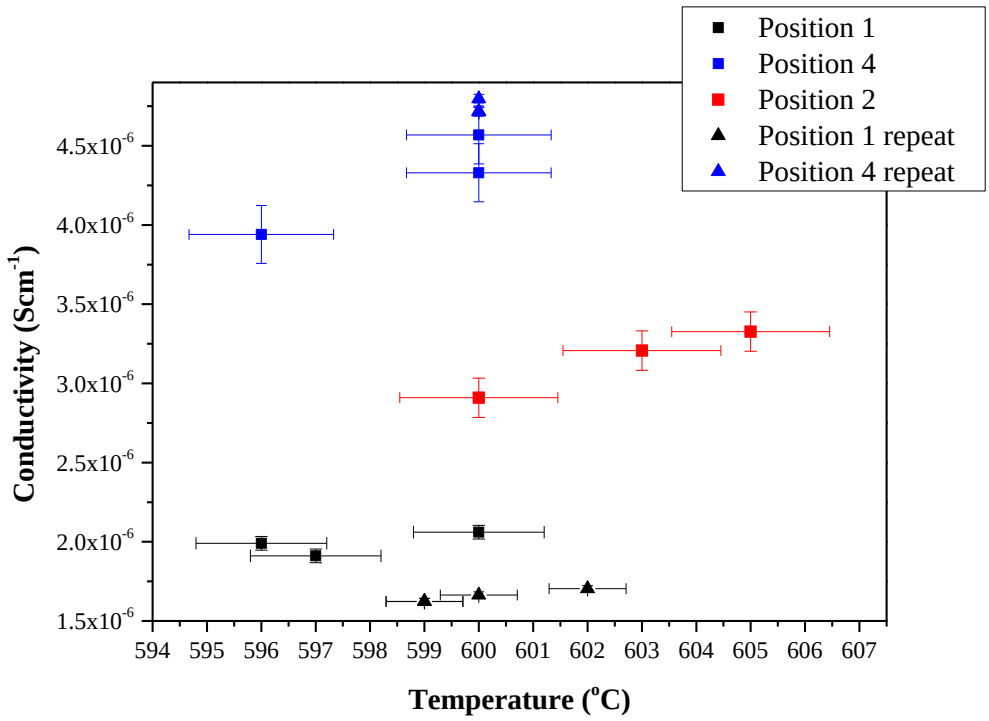

Figure 5.60: Conductivity data from the first run and the repeat measurements from the STO sample.

Mochizuki *et al*. report a range of conductivities from their STO single crystal of $\sigma < 10^{-8}\Omega^{-1}cm^{-1}$ and $\sigma \geq 10^{-3}\Omega^{-1}cm^{-1}$.[20] Our initial σ values of $10^{-6}Scm^{-1}$ from Figure 5.60, are within this range. Mochizuki *et al*. report that σ depends on the

crystal growth conditions, and where in the crystal boule the sample was located.[20] Balachandran *et al*. state that σ is also affected by defects, accidental acceptor impurities, and their related oxygen vacancies.[21] Therefore we can conclude that our value of σ is consistent with the literature for the STO substrates.

Further analysis of the electrodes was performed using SEM, with images shown in Figure 5.61.

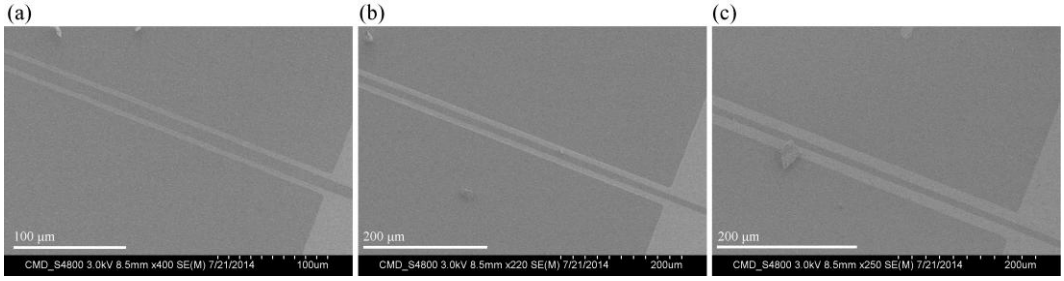

Figure 5.61: (a) SEM after impedance of top row electrode pair 8, (b) SEM after impedance of middle row electrode pair 13, and (c) SEM after impedance of bottom row electrode pair 26.

As can be seen from Figure 5.61 the Cr/Pt electrode pairs are still visible after the impedance, and therefore still stable.

To enable a clearer conclusion to be made the same STO substrate with the Cr/Pt electrodes was cut with a diamond tipped pen for further measurements using an alternative geometry. The symmetrical cell arrangement mentioned in geometry 2 was used with gold paste painted onto each side of the STO substrate covering the Cr/Pt electrodes on one side.

The symmetrical cell testing of the STO substrate with the Cr/Pt electrode was compared to a new 'as received' substrate (from PI-KEM). Both substrates were painted with gold paste (from Koartan) and dried in the furnace for 1 hour at 200°C. Once the first side had dried this process was repeated for the reverse side of the substrates. Gold wire was then adhered to both painted areas using additional gold paste, before drying in the furnace for a further 30mins. The new setup was used to measure the impedance of both STO substrates at 600°C during the same run. The Nyquist arcs for both substrates can be seen in Figures 5.62 and 5.63, with the calculated conductivities in Figure 5.64.

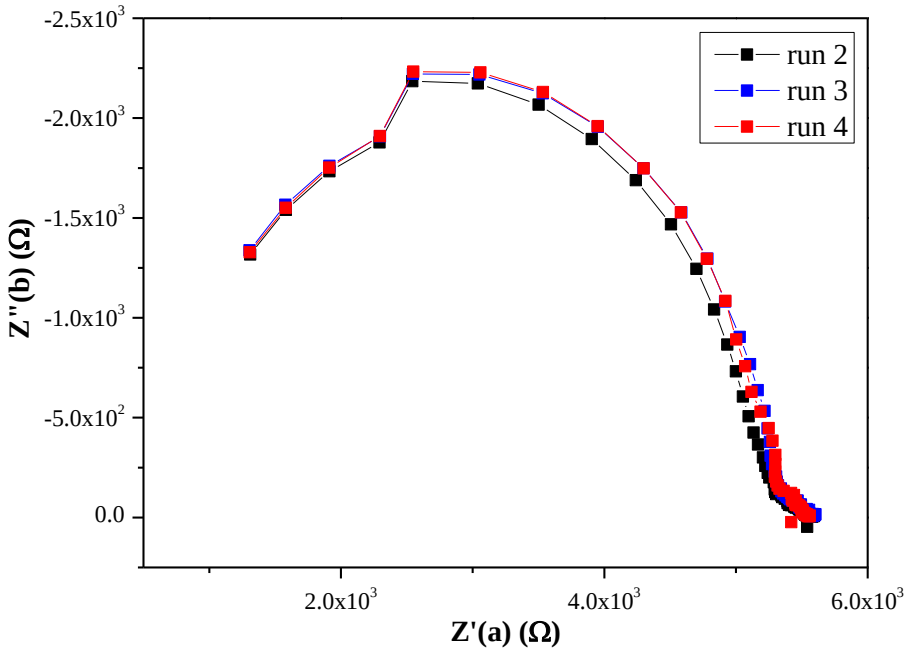

Figure 5.62: Nyquist plot of the STO sample with the Cr/Pt electrodes.

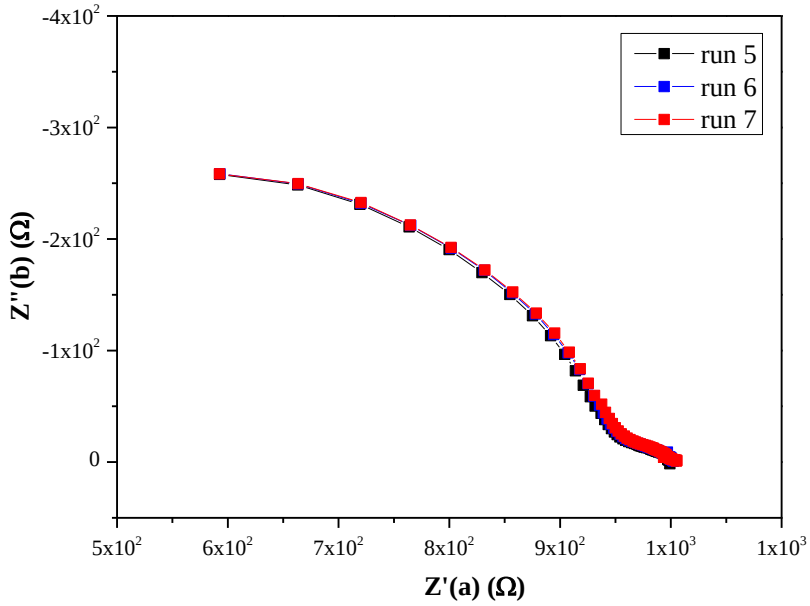

Figure 5.63: Nyquist plot of the STO sample 'as received'.

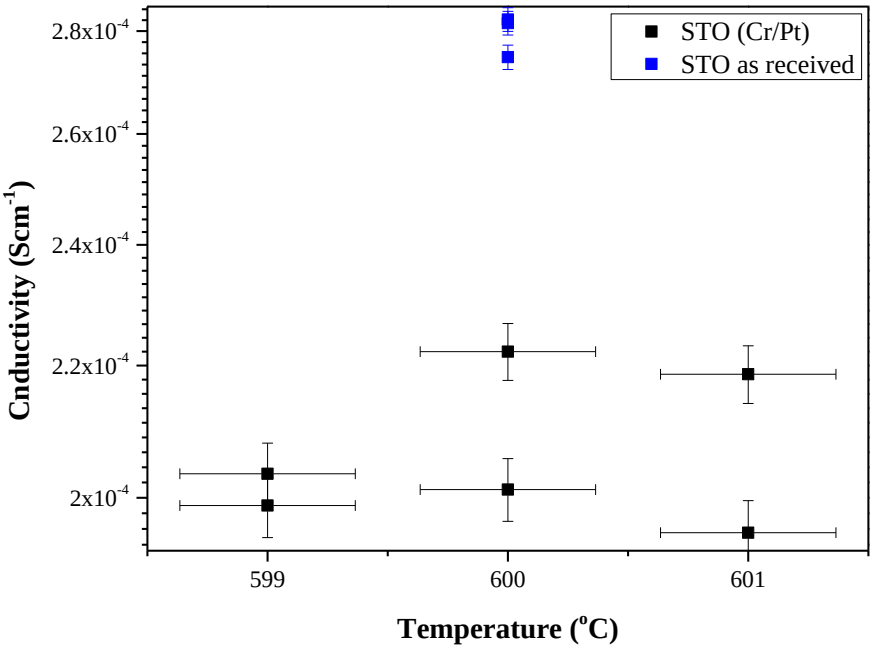

Figure 5.64: Conductivity data from the symmetrical cell geometry of the STO sample with the Cr/Pt patterning in black and the 'as received' sample in blue.

The conductivity data (Figure 5.64) from the symmetrical cell geometry produces values of the order of $10^{-4}Scm^{-1}$, compared to the new geometry 3 which gave values of $10^{-6}Scm^{-1}$. Due to this poorer response the arcs in Figures 5.62 and 5.63 do not show the complete semi-circle shape. There are several possible explanations for this difference in conductivity. Geometry 3 conductivities made the assumption that the current flows through the total thickness of the substrate. Given the substrate is 0.5mm thick and the current follow the path of the least resistance, this is quite unlikely. The relationship between the thickness of the sample and the conductivity is such that decreasing the thickness that the current passes through would increase the conductivity and therefore could be one reason to explain the difference in values from the two geometries. This should not cause problems for thin film measurements though, firstly because the total thicknesses of the films are much less (nm), and so it is a more reasonable assumption to presume the current passes through the full thickness of the film. Secondly, the geometry is going to be used for calculating the ASR, which does not require the cross sectional area, but instead the surface area of the electrodes. A further explanation for the differences in conductivity values could be due to the differences in current flow. To understand more about the current pathways, computational modelling using finite element models (FEM) could be used to determine the probable current pathways.

5.4 Conclusions

Three different geometries for measuring the ASR of the 10 layer films were investigated. The first geometry was halted due to the instability of the 10 layer material at 800°C which was highlighted in the XRD patterns.

The second geometry investigated the stability issues using Darren Hodgeman's 10 layer ink and the 10 layer thin films. The problems of growing SDC on both sides of the substrate were overcome, however it was found that the thickness of the SDC buffer layers were not sufficient to prevent reaction and degradation. In the literature SDC buffer layers are of the order of μm, generally much thicker than those able to be grown for this work. In addition to this an interfacial reaction between YSZ and SDC can form a (Zr, Ce)O_2 based solid-solution at high temperatures.[10] The stability studies with the SDC and 10 layer films showed that the 10 layer film was not stable having been annealed at 600°C for 120 hours. In order for the double sided geometry to be grown the initial SDC|10 layer film would be effectively annealed during the growth of the second side at the optimum growth temperature of 850°C. It was therefore decided to no longer pursue this geometry.

The third and final geometry removed the problem of stability as the films could be grown on a non-electrolyte substrate such as STO. For geometry 3 what was attempted was challenging, as a new setup was required for the measurement of multiple electrodes. Whilst the development of a fully functional 27 pair electrode test station was not successful, a 4 electrode pair testing station was created and

validated. The testing station was found to be not suitable for conductivity measurements of STO due to the unknown quantity of the cross-sectional area. However this should not cause problems for thin film measurements, as the total thicknesses of the films are much less (nm), and also because the geometry will be used for calculating the ASR, which does not require the cross sectional area, but instead the surface area of the electrodes.

Future work for this project should involve the testing of the 10 layer material after measuring other thin film cathodes that have also been measured in the literature such as LSC and LSM to verify the ASR measurement setup.

Further thin film cathodes can then be tested using this equipment in the future at Liverpool. The setup can be developed further so that the full mask pattern can be used.

5.5 References

1 Steele, B. C. H. & Heinzel, A. Materials for fuel-cell technologies. *Nature* **414**, 345-352 (2001).

2 Baqué, L., Caneiro, A., Moreno, M. S. & Serquis, A. High performance nanostructured IT-SOFC cathodes prepared by novel chemical method. *Electrochemistry Communications* **10**, 1905-1908, doi:http://dx.doi.org/10.1016/j.elecom.2008.10.010 (2008).

3 Gemmen, R. S., Williams, M. C. & Gerdes, K. Degradation measurement and analysis for cells and stacks. *Journal of Power Sources* **184**, 251-259, doi:http://dx.doi.org/10.1016/j.jpowsour.2008.06.047 (2008).

4 Fleig, J., Tuller, H. L. & Maier, J. Electrodes and electrolytes in micro-SOFCs: a discussion of geometrical constraints. *Solid State Ionics* **174**, 261-270, doi:http://dx.doi.org/10.1016/j.ssi.2004.07.035 (2004).

5 Plonczak, P., Sørensen, D. R., Søgaard, M., Esposito, V. & Hendriksen, P. V. Electrochemical properties of dense (La, Sr)$MnO_{3-\delta}$ films produced by pulsed laser deposition. *Solid State Ionics* **217**, 54-61, doi:http://dx.doi.org/10.1016/j.ssi.2012.03.043 (2012).

6 Hodgeman, D. W. *New cathodes for intermediate temperature solid oxide fuel cells (IT-SOFCs).* PhD thesis, University of Liverpool, (2014).

7 Simrick, N. J. *et al.* An investigation of the oxygen reduction reaction mechanism of $La_{0.6}Sr_{0.4}Co_{0.2}Fe_{0.8}O_3$ using patterned thin films. *Solid State Ionics* **206**, 7-16, doi:http://dx.doi.org/10.1016/j.ssi.2011.10.029 (2012).

8 Simrick, N. J. *et al.* Micro-fabrication of patterned LSCF thin-film cathodes with gold current collectors. *Solid State Ionics* **192**, 619-626, doi:http://dx.doi.org/10.1016/j.ssi.2010.03.025 (2011).

9 Mutoro, E., Crumlin, E. J., Biegalski, M. D., Christen, H. M. & Shao-Horn, Y. Enhanced oxygen reduction activity on surface-decorated perovskite thin films for solid oxide fuel cells. *Energy & Environmental Science* **4**, 3689-3696, doi:10.1039/c1ee01245b (2011).

10 Qian, J., Tao, Z., Xiao, J., Jiang, G. & Liu, W. Performance improvement of ceria-based solid oxide fuel cells with yttria-stabilized zirconia as an electronic blocking layer by pulsed laser deposition. *International Journal of Hydrogen Energy* **38**, 2407-2412, doi:http://dx.doi.org/10.1016/j.ijhydene.2012.11.112 (2013).

11 Peña-Martínez, J. *et al.* Fuel cell studies of perovskite-type materials for IT-SOFC. *Journal of Power Sources* **159**, 914-921, doi:http://dx.doi.org/10.1016/j.jpowsour.2005.11.036 (2006).

12 Zhou, W., Ran, R. & Shao, Z. Progress in understanding and development of $Ba_{0.5}Sr_{0.5}Co_{0.8}Fe_{0.2}O_{3-\delta}$-based cathodes for intermediate-temperature solid-oxide fuel cells: A review. *Journal of Power Sources* **192**, 231-246, doi:http://dx.doi.org/10.1016/j.jpowsour.2009.02.069 (2009).

13 Lim, Y. H., Lee, J., Yoon, J. S., Kim, C. E. & Hwang, H. J. Electrochemical performance of $Ba_{0.5}Sr_{0.5}Co_xFe_{1-x}O_{3-\delta}$ (x=0.2–0.8) cathode on a ScSZ electrolyte for intermediate temperature SOFCs. *Journal of Power Sources* **171**, 79-85, doi:http://dx.doi.org/10.1016/j.jpowsour.2007.05.050 (2007).

14 X'Pert Reflectivity v. 1.1 (PANalytical B. V. , Almelo, The Netherlands, 2004).

15 v. 8.6 (OriginLab Corporation, 1991-2012).

16 Robinson, I. K. Crystal truncation rods and surface roughness. *Physical Review B* **33**, 3830-3836 (1986).

17 Kosacki, I., Petrovsky, V., Anderson, H. U. & Colomban, P. Raman Spectroscopy of Nanocrystalline Ceria and Zirconia Thin Films. *Journal of the American Ceramic Society* **85**, 2646-2650, doi:10.1111/j.1151-2916.2002.tb00509.x (2002).

18 Wang, S.-F., Yeh, C.-T., Wang, Y.-R. & Wu, Y.-C. Characterization of samarium-doped ceria powders prepared by hydrothermal synthesis for use in solid state oxide fuel cells. *Journal of Materials Research and Technology* **2**, 141-148, doi:http://dx.doi.org/10.1016/j.jmrt.2013.01.004 (2013).

19 Bdikin, I. *et al.* Nanoindentation induced piezoelectricity in SrTiO3 single crystals. *Scripta Materialia* **74**, 76-79, doi:http://dx.doi.org/10.1016/j.scriptamat.2013.11.003 (2014).

20 Mochizuki, S. *et al.* Optical, electrical, and X-ray-structural studies on Verneuil-grown $SrTiO_3$ single crystal: Annealing study. *Physica B: Condensed Matter* **401–402**, 433-436, doi:http://dx.doi.org/10.1016/j.physb.2007.08.205 (2007).

21 Balachandran, U. & Eror, N. G. Electrical conductivity in strontium titanate. *Journal of Solid State Chemistry* **39**, 351-359, doi:http://dx.doi.org/10.1016/0022-4596(81)90270-X (1981).

Chapter 6: Conclusions and Future Work

This thesis has investigated the pulsed laser deposition (PLD) growth of thin films for use as electrolytes and cathodes in solid oxide fuel cell applications. In Chapter 3, both oriented ordered $NdBaCo_2O_{(5+\delta)}$ (NBCO) films and oriented $Sm_{0.2}Ce_{0.8}O_{(2-\delta)}$ (SDC) films were successfully deposited on $SrTiO_3$ (STO) (001) substrates.

The initial aim when depositing the single layer films was also to compare the alternating current (AC) impedance of the single layer with the multilayer films, however instability in the NBCO material prevented this. As the NBCO was designed to be used as a cathode for intermediate temperature - solid oxide fuel cells (IT-SOFCs), its instability in air and oxygen at 600°C shows that it is not fit for purpose. One of our hopes was that in growing the multilayers we could deposit SDC capping layers to improve the stability, however this was also unsuccessful.

Following on from this work, multilayers of the SDC and NBCO films were also grown. A set of multilayer films were deposited with 2nm, 5nm, 10nm and 15nm of each layer.

One of the challenges of these multilayer films was that the NBCO required deposition at 850°C, whereas it was found that the SDC grew with a lower surface roughness at lower temperatures of around 650°C. Combining these films into the multilayer gave the challenge of whether it was better to sacrifice some of the surface roughness of the SDC and use the higher temperature or not. From the transmission electron microscopy (TEM) and EDX data there is likely migration

of Nd into the SDC layers. The interfaces are also less sharp for the multilayer films deposited at the higher temperature for the SDC growth. However, in all cases the SDC growth appears more favourable in the TEM when compared to the NBCO, with some regions even showing Co-metal and fluorite structures potentially attributed to Co-O_x where we would expect to see the perovskite block. Further experiments relating to the work in Chapter 3 could include replacing the NBCO in the multilayer film with another more stable perovskite structure to continue to investigate the relationship between the perovskite and fluorite interfaces.

As the NBCO was not stable enough to carry out reliable impedance measurements a second cathode material, barium calcium yttrium iron oxide (10 layer), $Ba_{1.7}Ca_{2.4}Y_{0.9}Fe_5O_{13}$, was chosen for further study and this work was discussed in Chapter 4.

In Chapter 4, the growth of a strongly cation ordered 10 layer perovskite film with a more complex structure than previous SOFC cathode materials, was grown in thin film form via PLD. The symmetry of the film appears to be tetragonal within the resolution of the measurements employed, as opposed to the orthorhombic symmetry of the bulk phase, which may be attributed to the in-plane structural match between the cubic STO substrate and the grown layer. This complex structure was confirmed by high resolution transmission electron microscopy (HRTEM) data, which shows the faithful reproduction of the cation site ordering from the bulk material, is associated with retention of the A site layering, and the presence of defects associated with faulting in the ordering of the component structural units. The high degree of uniformity and structural perfection of the

grown films averaged over larger areas than those probed by TEM was clear from XRD data, with the narrowest rocking curve peak widths thus far reported for ordered layered SOFC cathode candidate materials.

The self-assembly of the six-site 39Å repeat structure derived from the essentially isotropic perovskite subcell in single-target pulsed laser deposition growth reflects the favourable nature of the A site cation ordering which drives the formation of the structure. The perovskite-based nature of the superstructure makes it distinct from large repeat Aurivillius and Ruddlesden-Popper phases, which are intrinsically layered due to the insertion of fluorite and rock-salt type layers respectively.

The conductivity of these $10a_p$ films is significantly higher than that of the bulk polycrystalline ceramic. The conductivity attained by the film is $30.0 Scm^{-1}$ at 600°C, greater than that of the bulk $3.5 Scm^{-1}$, which is a key temperature for IT-SOFCs.

The enhanced conductivity is assigned to the reduction in the density of grain boundaries and the *a-b* orientation of the film in-plane. This shows that the electronic conductivity can be increased by oriented growth related to the cation stacking sequence. The film growth has thus revealed good intrinsic transport properties of the complex superstructure $Ba_{1.7}Ca_{2.4}Y_{0.9}Fe_5O_{13}$, as the measured conductivity shows that Fe^{3+}-based oxides can have acceptable conductivities for application as IT-SOFC cathodes.

The 10 layer film project could be further studied by measuring the area specific resistance (ASR) of this cathode material as is commonly done for bulk SOFC

cathode materials. Equipment and geometry considerations for measuring the ASR were discussed in Chapter 5.

In Chapter 5, three different geometries for measuring the ASR of the 10 layer films were investigated. The first geometry was halted due to the instability of the 10 layer material at 800°C which was highlighted in the XRD patterns.

The second geometry investigated the stability issues using Darren Hodgeman's 10 layer ink and the 10 layer thin films. The problems of growing SDC on both sides of the substrate were overcome, however it was found that the thickness of the SDC buffer layers were not sufficient to prevent reaction and degradation. In the literature SDC buffer layers are of the order of μm, generally much thicker than those able to be grown for this work. In addition to this an interfacial reaction between YSZ and SDC can form a $(Zr,Ce)O_2$ based solid-solution at high temperatures. The stability studies with the SDC and 10 layer films showed that the 10 layer film was not stable having been annealed at 600°C for 120 hours. In order for the double sided geometry to be grown the initial SDC|10 layer film would be effectively annealed during the growth of the second side at the optimum growth temperature of 850°C. It was therefore decided to no longer pursue this geometry.

The third and final geometry removed the problem of stability as the films could be grown on a non-electrolyte substrate such as STO. For geometry 3 what we attempted was challenging, as a new setup was required for the measurement of multiple electrodes. Whilst the development of a fully functional 27 pair electrode test station was not successful, a 4 electrode pair testing station was created and validated. The testing station was found to be not suitable for conductivity

measurements of STO due to the unknown quantity of the cross-sectional area. However this should not cause problems for thin film measurements, as the total thicknesses of the films are much less (nm), and also because the geometry will be used for calculating the ASR, which does not require the cross sectional area, but instead the surface area of the electrodes.

Extending the work in Chapter 5 should involve measuring the ASR of well-studied thin film cathode materials such as LSC and LSM to verify the equipment, before testing the 10 layer material. Further thin film cathodes can then be tested using this equipment in the future at Liverpool. The setup can also be developed further so that the full mask pattern can be used.

Appendix 1: Supplementary Information for NBCO

A1.1 Additional Information on the Growth of SDC Films

The $Sm_{0.2}Ce_{0.8}O_{(2-\delta)}$ (SDC) deposition conditions were optimized to be as follows: temperature of 630°C, laser energy of 250mJ, a frequency of 5Hz, oxygen flow rate of 20sccm (standard cubic centimetres), and partial oxygen pressure of 1mTorr. However SDC also grows well at 850°C and, as this temperature matches the conditions of the $NdBaCo_2O_{(5+\delta)}$ (NBCO) growth, many of the multilayers included SDC grown at 850°C. (See Chapter 3 for further information on NBCO and details of the multilayer films.)

Having initially studied the growth of SDC on $SrTiO_3$ (STO) (100), SDC was also deposited on alternative substrates to analyse the effect of strain on the SDC films. SDC films were grown on; lanthanum aluminate, $LaAlO_3$, yttrium stabilized zirconia, $Y:ZrO_2$, samarium scandate, $SmScO_3$, dysprosium scandate, $DyScO_3$, see Table A1.1.

Table A1.1: Lattice mismatch between SDC and the various substrates used for the growths.

Substrate	Bulk lattice parameter (Å)	Direct lattice mismatch with SDC (%)	45° cube on cube lattice mismatch with SDC (%)
$SrTiO_3$	**3.91**	**- 28.2**	**+ 1.5**
$LaAlO_3$	3.79	- 30.3	**- 1.5**
$Y:ZO_2$	5.14	**- 5.5**	+ 33.6
LSAT	3.87	- 29.1	**+ 0.3**
$SmScO_3$	4.00	- 26.6	**+ 3.8**
$DyScO_3$	3.95	- 27.5	**+ 2.5**

θ/2θ XRD patterns were collected from the SDC films grown on different substrates and are shown in Figure A1.1.

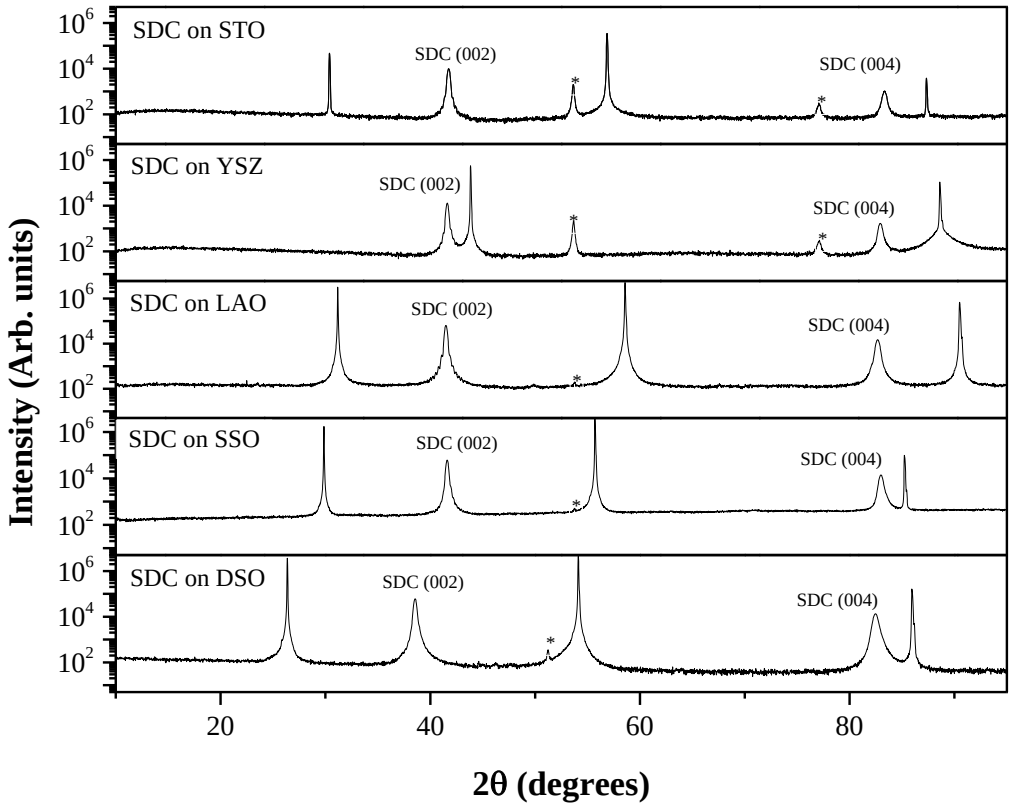

Figure A1.1: XRD patterns of SDC films on different substrates.

Rocking curves were used as a tool to decide on the most suitable substrate to use, and STO was used for the work in Chapter 3.

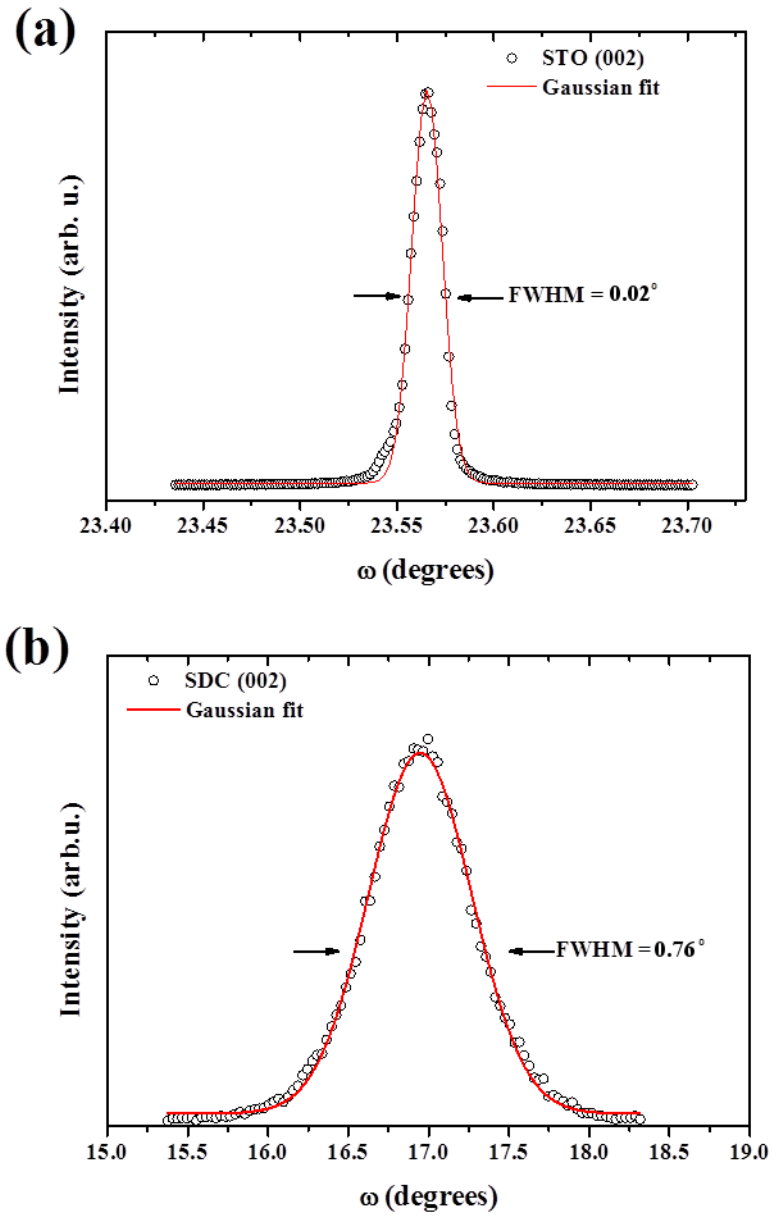

Figure A1.2: Rocking curves of SDC on STO.

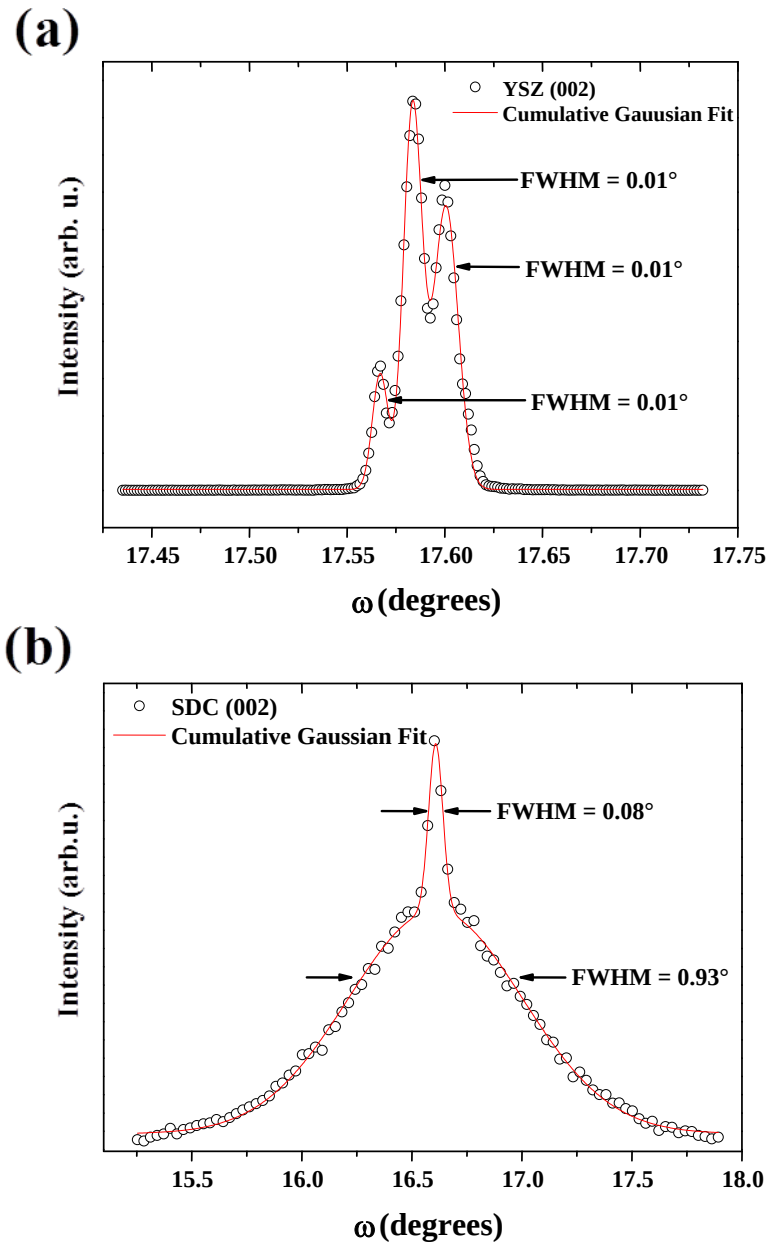

Figure A1.3: Rocking curves of SDC on YSZ.

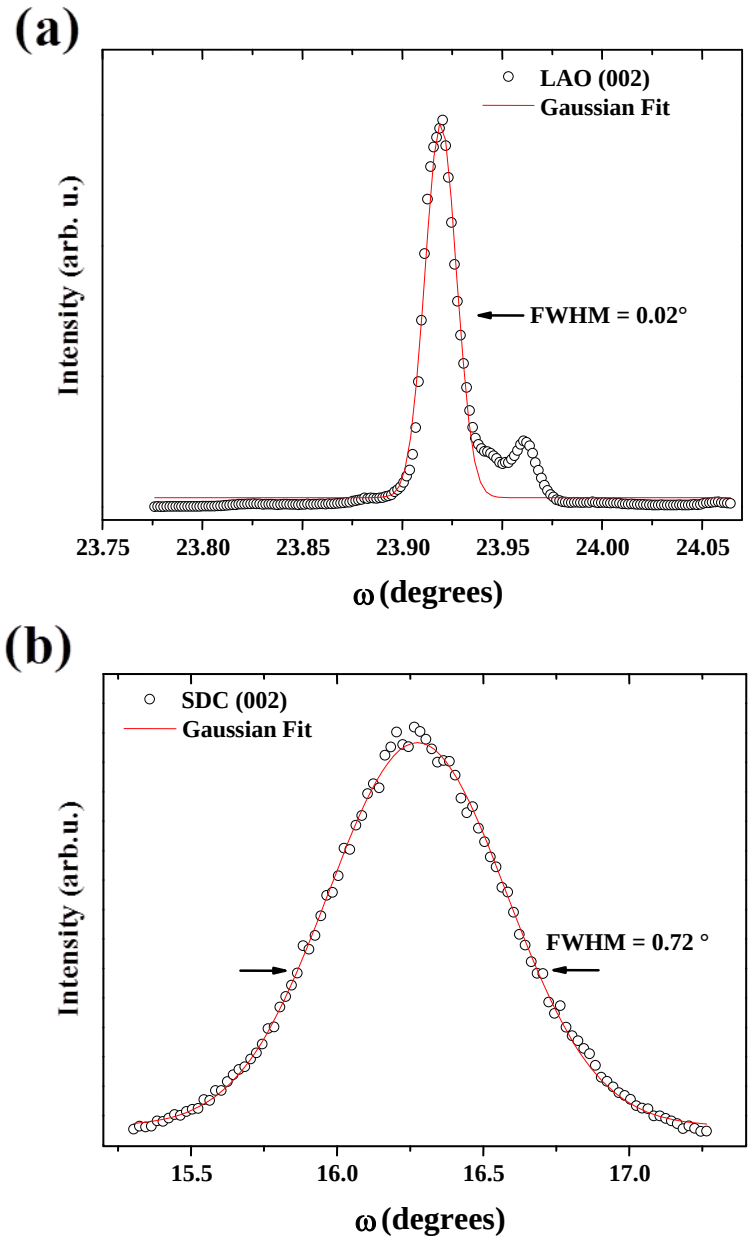

Figure A1.4: Rocking curves of SDC on LAO.

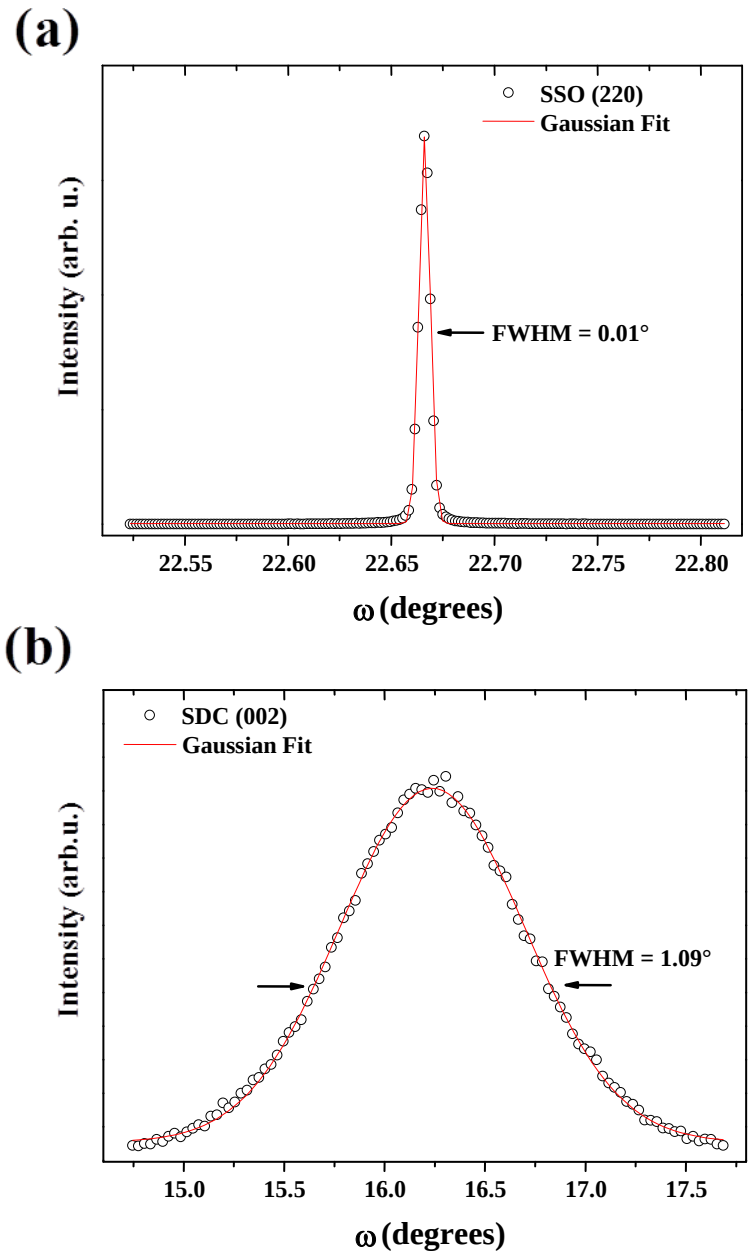

Figure A1.5: Rocking curves of SDC on SSO.

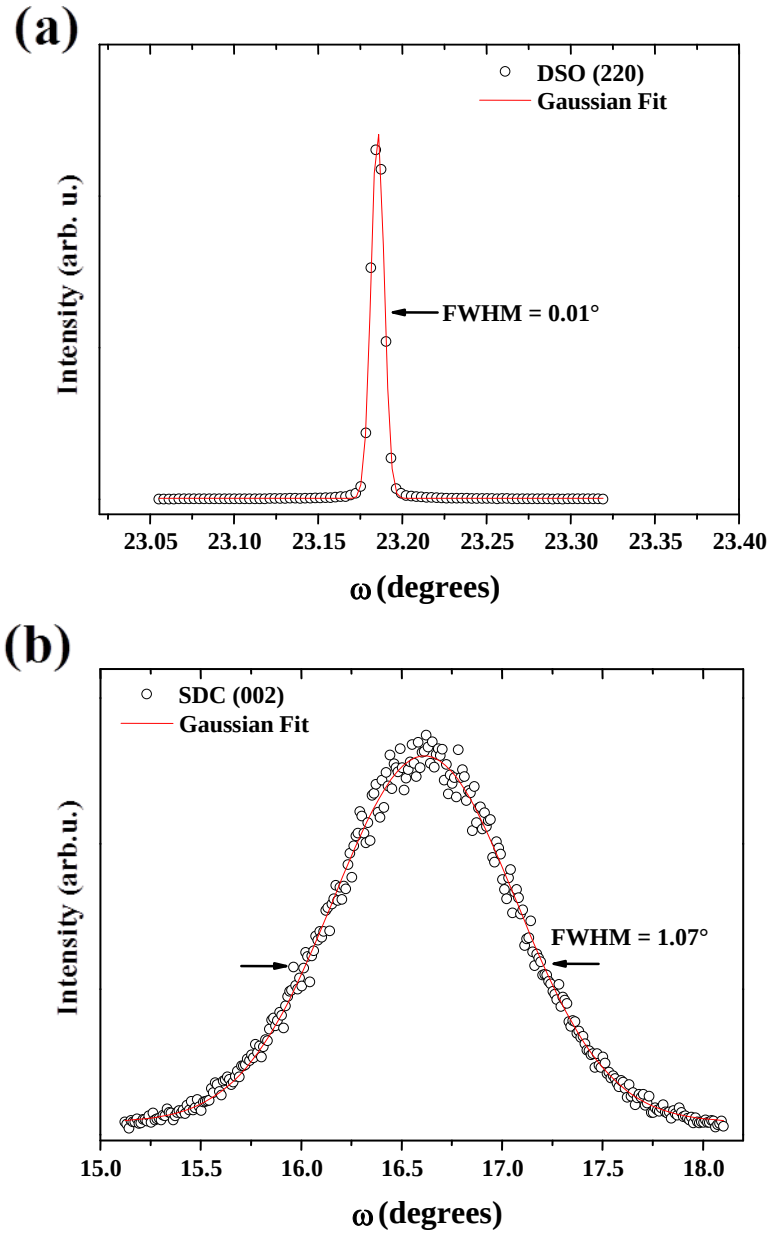

Figure A1. 6: Rocking curves of SDC on DSO.

The full width half maximum (FWHM) observed from each of the growths of SDC on different substrates are summarized in Table A1.2.

Table A1.2: Summary of the FWHM of the SDC films grown on different substrates.

Substrate	FWHM of Substrate (°)	FWHM of Film (°)
$SrTiO_3$	0.02	0.76
$Y:ZrO_2$	0.01	0.50
$LaAlO_3$	0.02	0.72
$SmScO_3$	0.01	1.09
$DyScO_3$	0.01	1.07

To check the orientation of the SDC on STO phi scans around the (113) and (114) peaks respectively were collected.

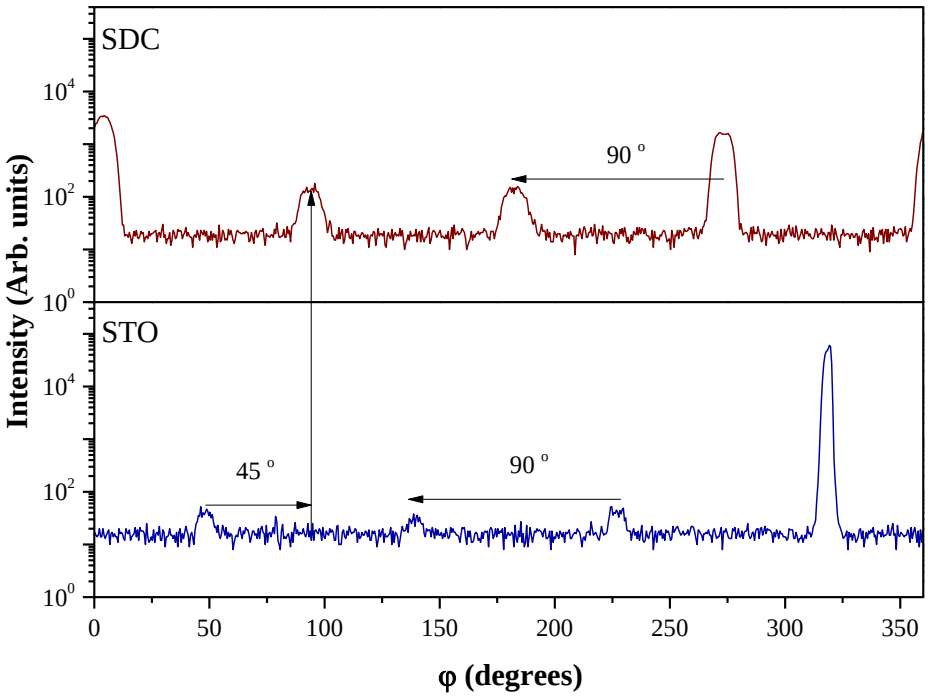

Figure A1.7: XRD phi scans showing the growth direction of SDC with respect to the STO substrate.

Phi scans (Figure A1.7) are off axis scans, and from this we learn that SDC has a 45° cube-on-cube epitaxial relationship to STO. The schematic below (Figure

A1.8) shows a representation of how one unit cell of the SDC (in red) sits across 4 unit cells of the STO (in blue). The ideal lattice parameter for a film grown 45° to cube-on-cube on STO (i.e. one grown with no lattice strain) would be equal to ($\sqrt{2}$ x 3.9Å), i.e. 5.52Å. SDC, however, has a lattice parameter of 5.44Å, and gives a lattice mismatch of 1.5%.

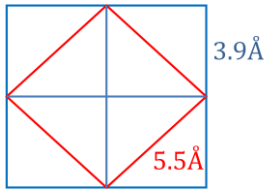

Figure A1.8: Schematic showing the growth direction of SDC with respect to the STO substrate.

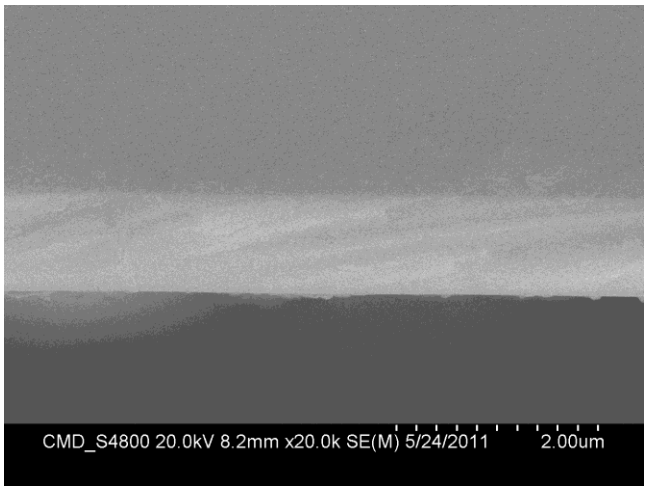

Figure A1.9: SEM image of SDC grown on STO.

From SEM work (Figure A1.9), the thickness of the films could be determined and thus the deposition rate. Table A1.3 indicates the simple ratio between the thickness of the film and the number of pulses required for growth. The thicker

film was analysed via SEM, and so an estimate can be calculated for the number of pulses required to grow the thinner, 5nm, film.

Table A1.3: Data from SEM image.

Thickness (μm)	Thickness (nm)	Pulses
1	1000	25,000
$5x10^{-3}$	5	125

From this initial SEM work we were then able to grow thinner films which were characterised by XRR as shown in Chapter 3.

Table A1.4: Lattice parameters of the SDC films.

Substrate	Bulk lattice parameter (Å)	Lattice parameter of the SDC film (Å)	Best lattice mismatch with SDC (45^{o} cube on cube, and direct) (%)	Experimental lattice mismatch (%)
$SrTiO_3$	3.91	5.42	+ 1.5 (45^{o})	+ 1.9
$LaAlO_3$	3.79	5.44	- 1.5 (45^{o})	- 2.1
$Y:ZrO_2$	5.14	5.47	- 5.5 (direct)	- 6.0
$SmScO_3$	4.00	5.45	+ 3.8 (45^{o})	+ 3.4
$DyScO_3$	3.95	5.44	+ 2.5 (45^{o})	+ 2.4

A1.2 Additional Information on the Growth of NBCO Films

Rocking curves were also carried out on the NBCO films.

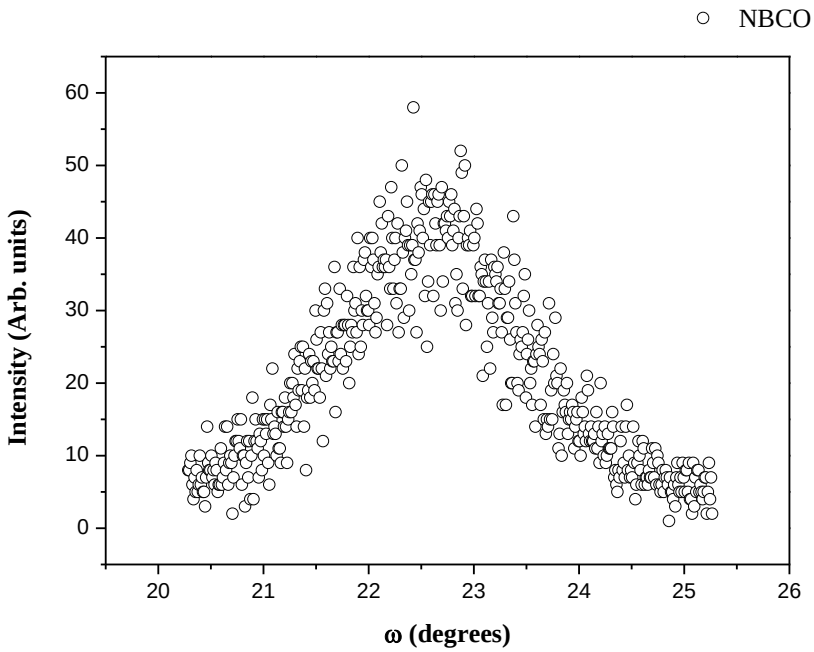

Figure A1.10: rocking curve of the NBCO (002) peak.

The Full width half maximum of the NBCO (002) peak shown in Figure A1.10 is 1.68°.

A1.3 Additional Information on the DIFFaX Analysis

All models were constructed and simulated by Dr. Robert Palgrave at the University of Liverpool.

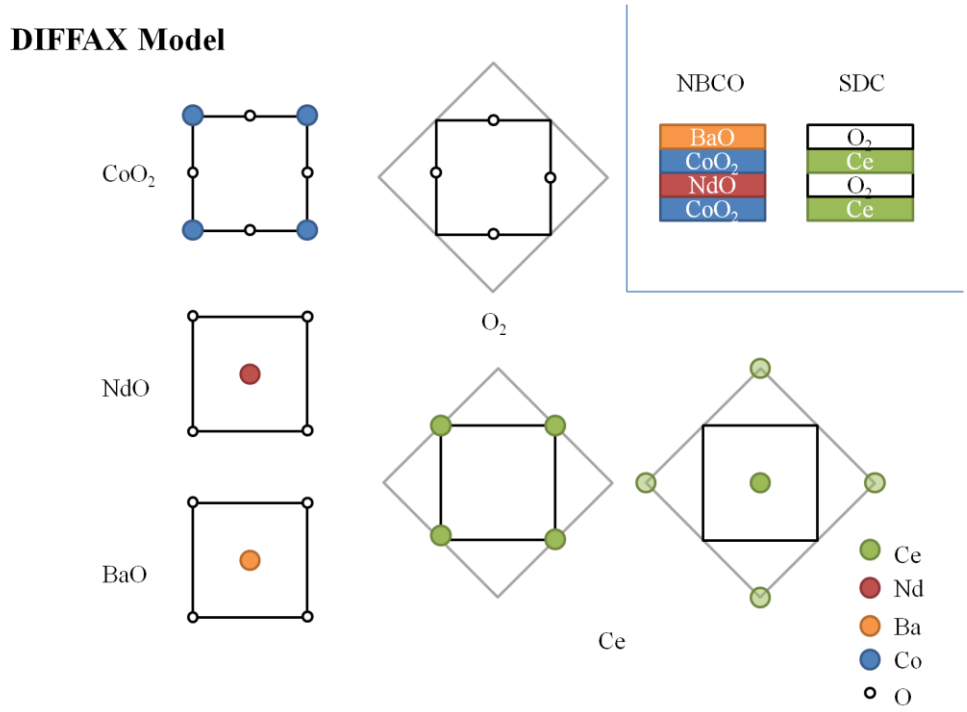

Figure A1.11: Model that was used for the DIFFaX analysis, with the Co shown in blue, Ba shown in orange, Nd in red, O in white and Ce in green.

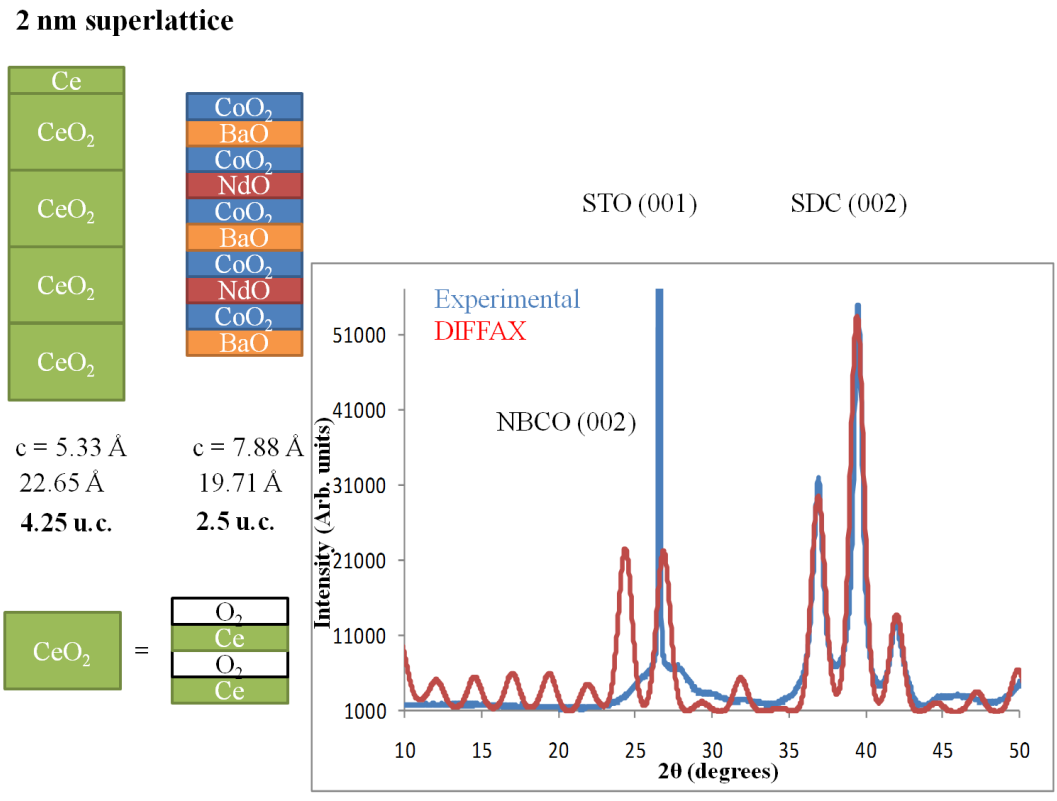

Figure A1.12: 2nm DIFFaX analysis.

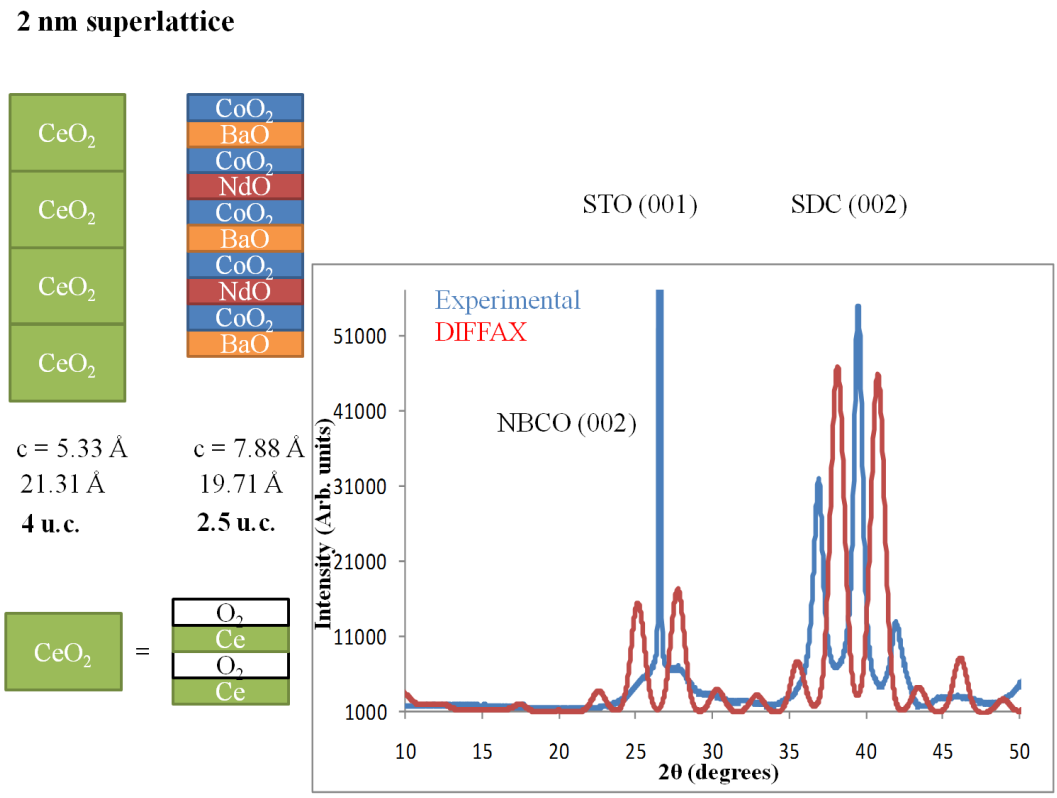

Figure A1.13: 2nm DIFFaX analysis.

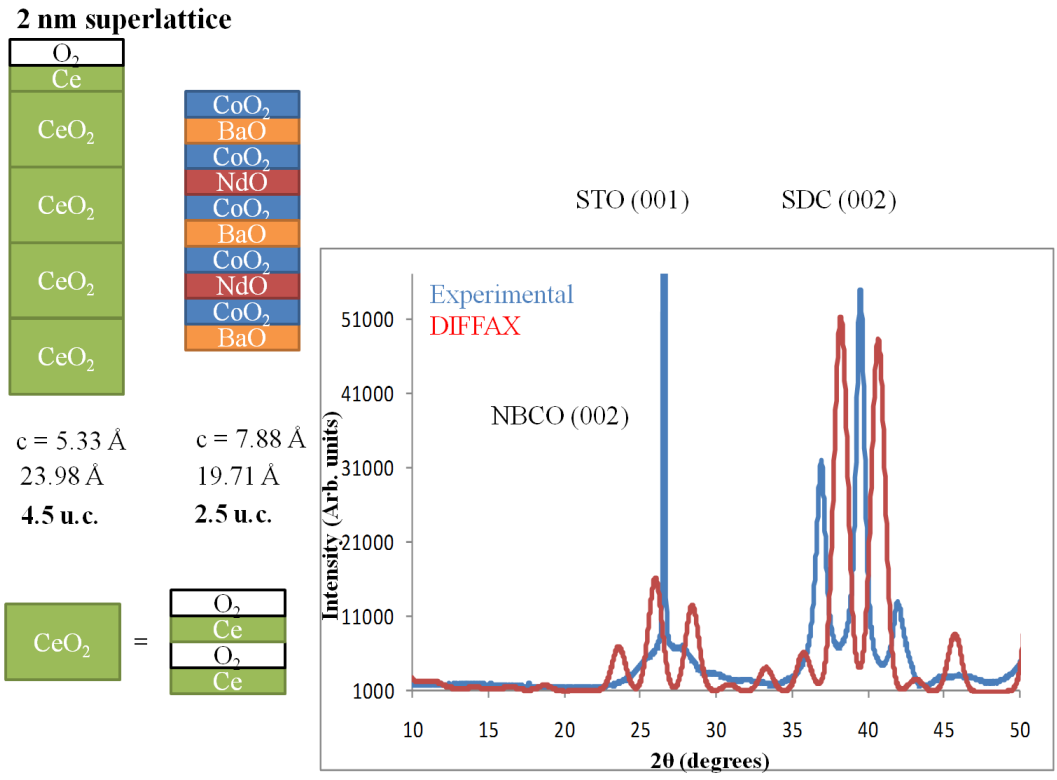

Figure A1.14: 2nm DIFFaX analysis.

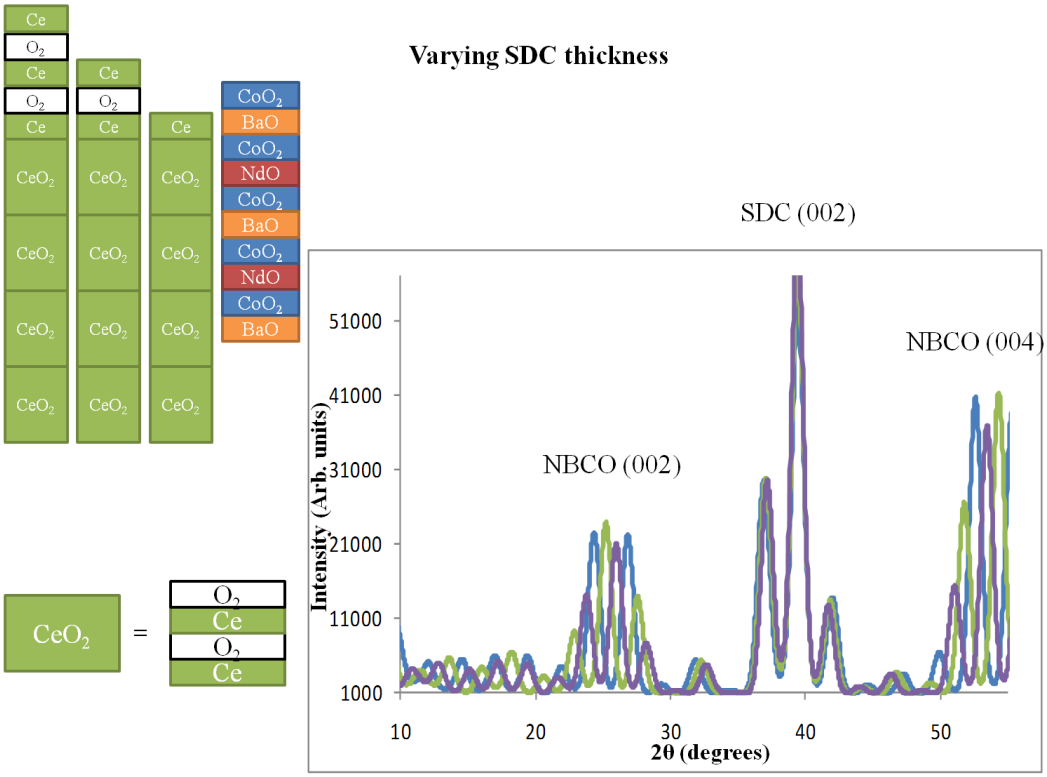

Figure A1.15: Varying SDC thickness DIFFaX analysis.

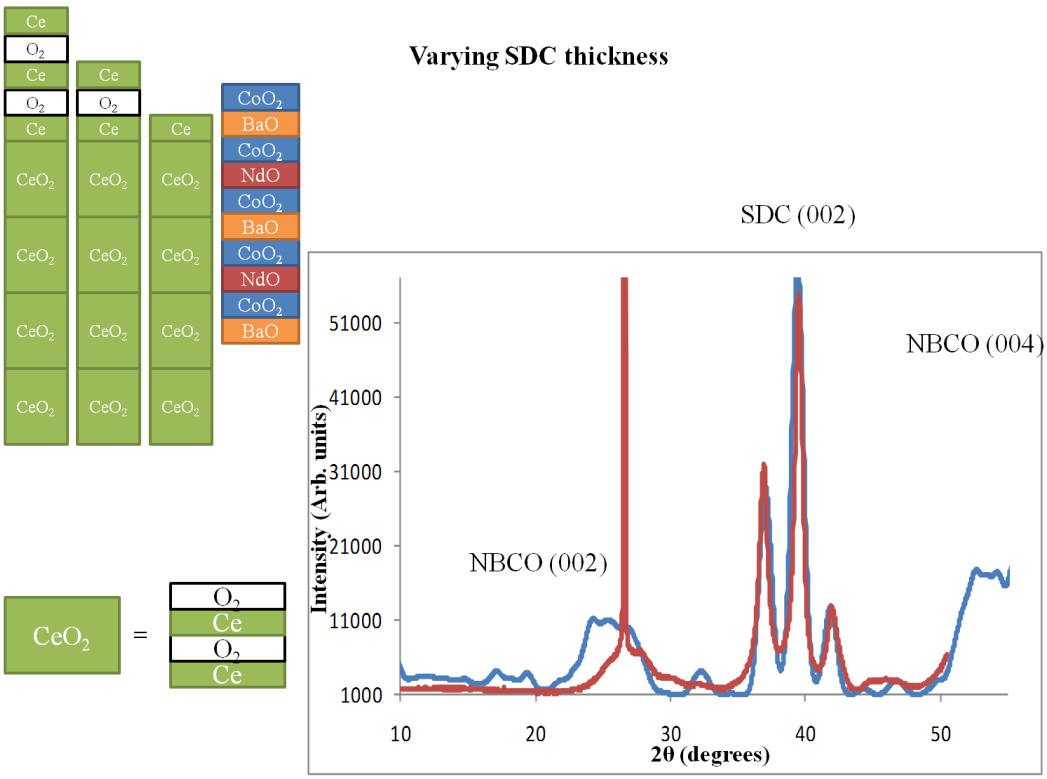

Figure A1.16: Varying SDC thickness DIFFaX analysis.

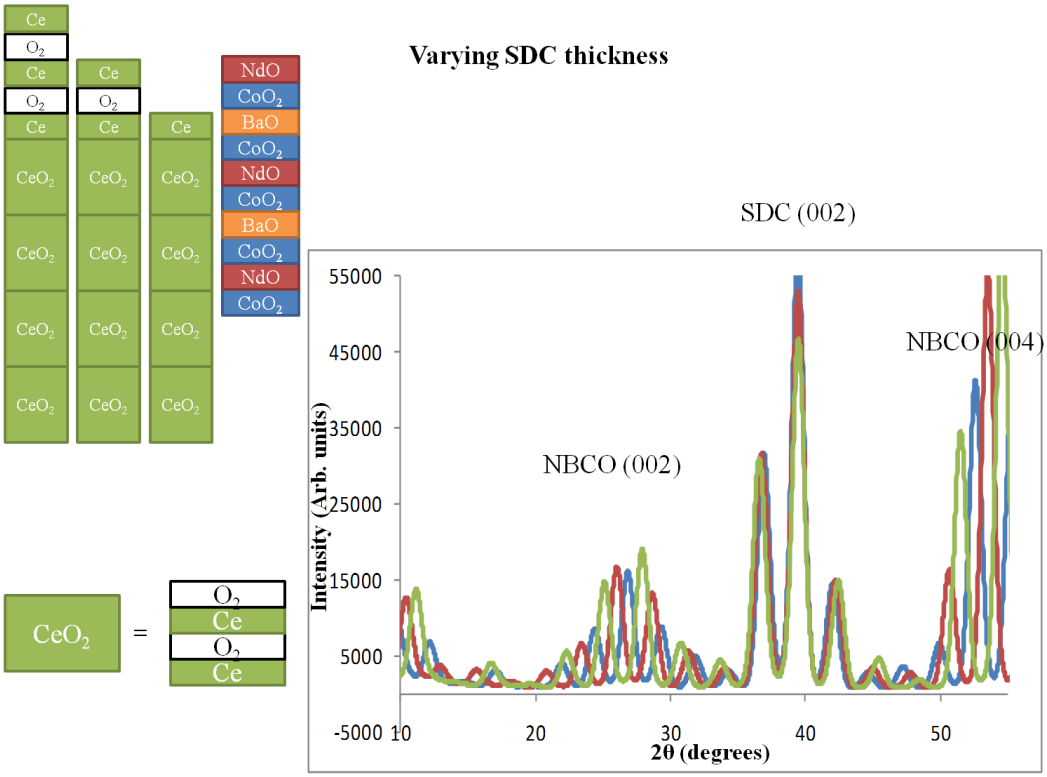

Figure A1.17: Varying SDC thickness DIFFaX analysis.

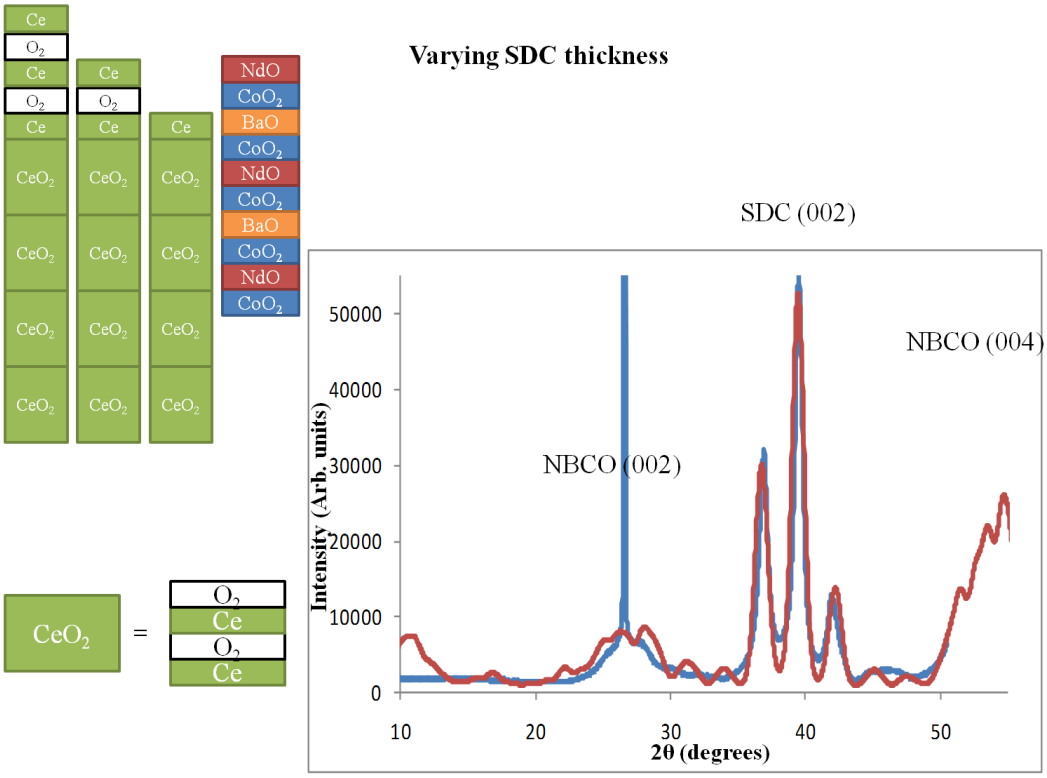

Figure A1.18: Varying SDC thickness DIFFaX analysis.

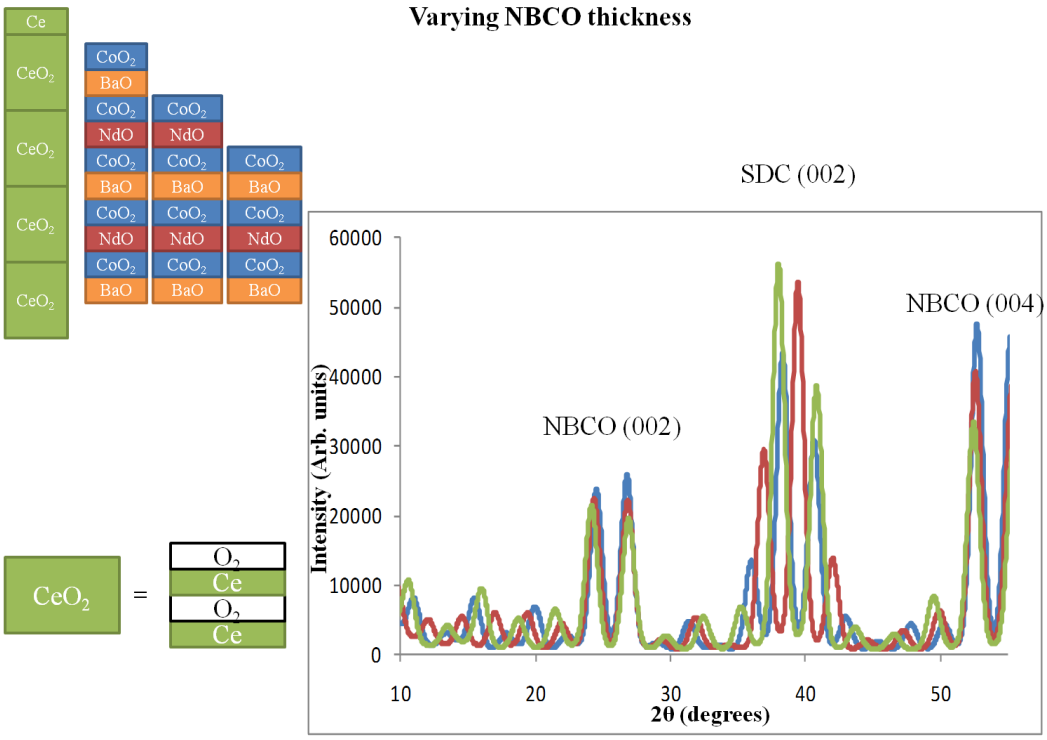

Figure A1.19: Varying NBCO thickness DIFFaX analysis.

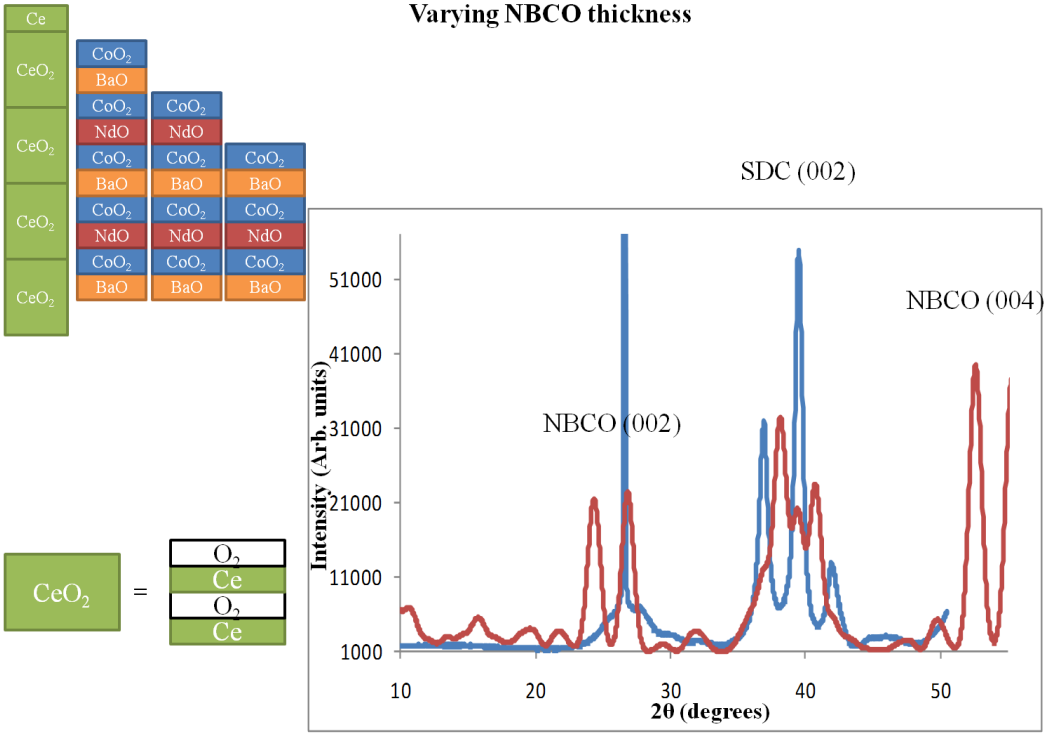

Figure A1.20: Varying NBCO thickness DIFFaX analysis.

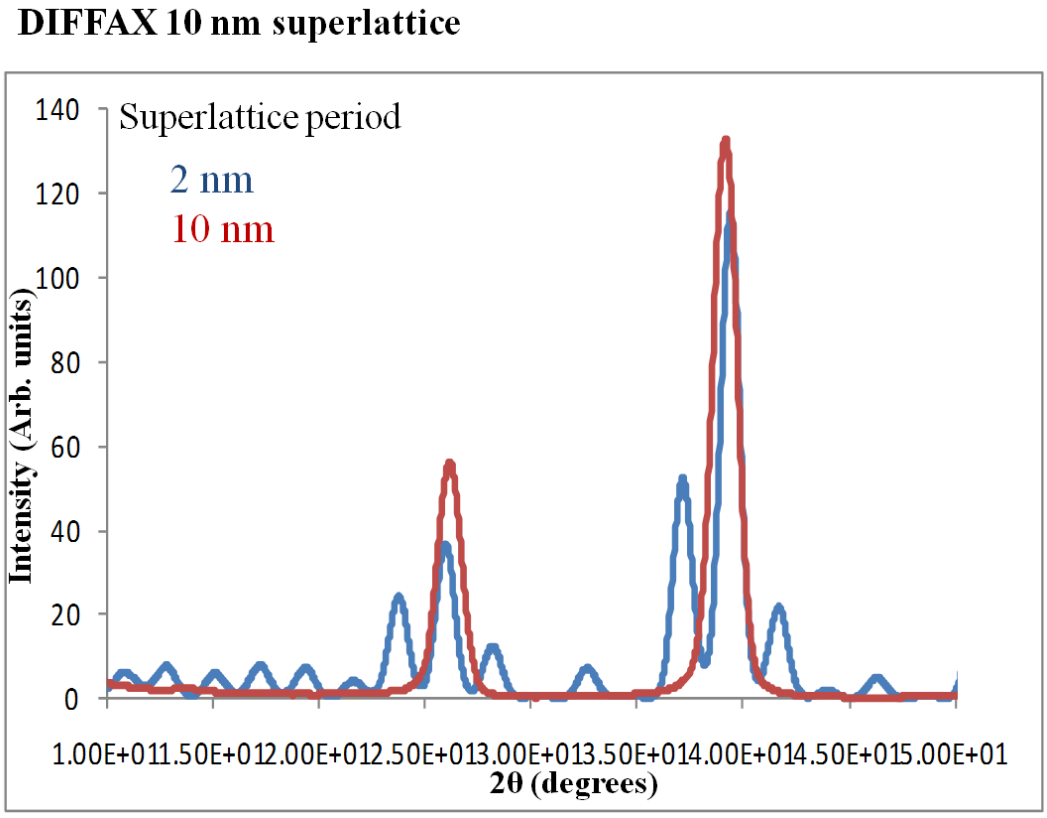

Figure A1.21: 10nm and 2nm DIFFaX comparison analysis.

The DIFFaX simulations suggest that each NBCO layer is uniform in thickness and each SDC layer is of varying thickness.

Appendix 2: Supplementary Information for ASR

A2.1 Simulations for Geometry 3

It is unknown which specific values of D and W will produce the clearest arcs for this geometry and so a selection of the best options, based on simulations carried out by Dr. Ming Li at the University of Liverpool, has been chosen.

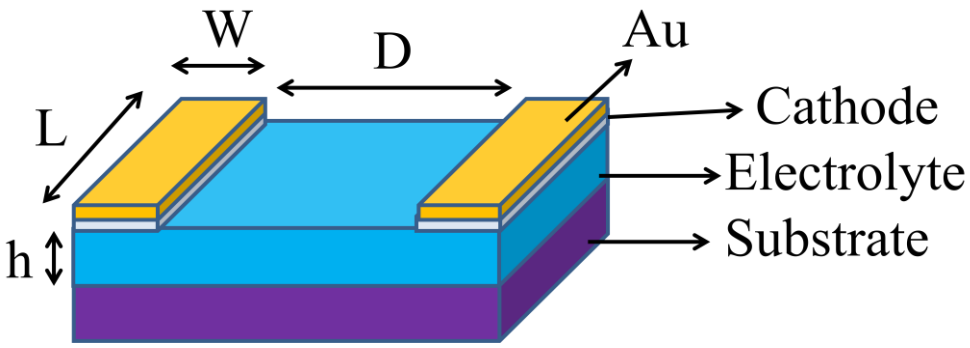

Figure A2.1: Schematic showing the STO|SDC|10 layer geometry used for the simulations. Where (W) is the width of the electrode, (D) is the distance between the electrodes, (L) is the length of the electrode and (h) is the thickness of the electrolyte.

The first simulation assumed the following D=5mm, L=5mm, W= 1mm, h=100nm. In addition the resistivity of the SDC electrolyte was = 100Ωcm and the permittivity of the SDC electrolyte =30. This simulation resulted in the following Nyquist plot.

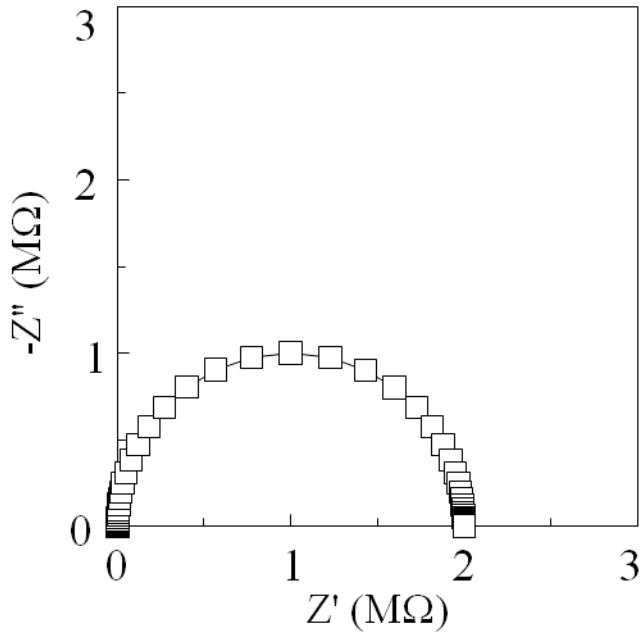

Figure A2.2: Predicted Nyquist plot assuming values of D=5mm, L=5mm, W= 1mm, h=100nm.

The Nyquist plot Figure A2.2 doesn't clearly show a small arc at the low frequency end, indicating that the assumed vales of of D=5mm, L=5mm, W= 1mm, h=100nm are not ideal for obtaining information of the cathode resistance.

Further simulations were carried out, this time with the assumptions of **D=10μm**, L=5mm, W=1mm and h=100nm. In addition the resistivity of the SDC electrolyte was = 100Ωcm and the permittivity of the SDC electrolyte =30. This simulation resulted in the following Nyquist plot.

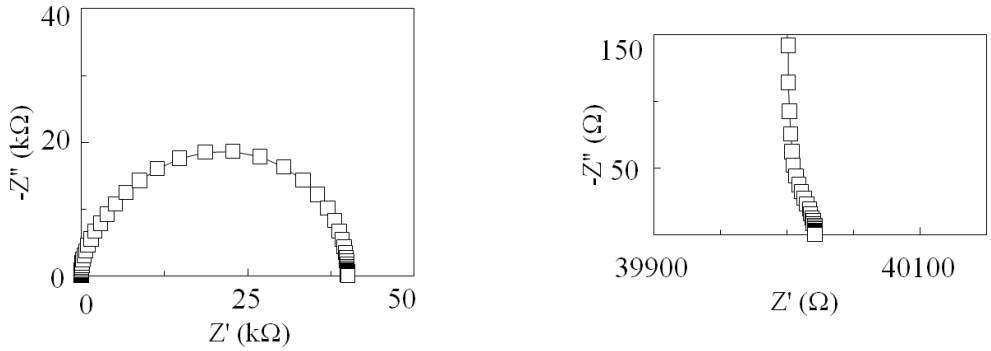

Figure A2.3: Predicted Nyquist plot on the left, with a zoomed in section of the low frequency end on the right, assuming values of **D=10µm**, L=5mm, W=1mm and h=100nm.

The Nyquist plot shown in Figure A2.3 begins to show the electrode arc in the zoomed in image, and therefore further reductions in the electrode sizes were simulated to improve the clarity of the arc.

The simulated arc shown in Figure A2.4 was carried out assuming D=10µm, L=5mm, **W= 10µm** h=100nm.

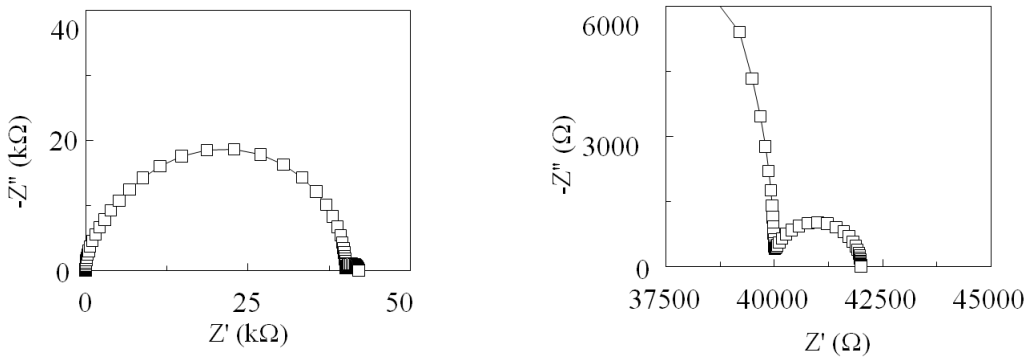

Figure A2.4: Predicted Nyquist plot on the left, with a zoomed in section of the low frequency end on the right, assuming values of D=10µm, L=5mm, **W= 10µm** h=100nm.

Decreasing the values of both D and W to the order of μm allowed the electrode arc to be more clearly visible. In order to ensure the most successful measurement a range of sizes in the μm region were designed for patterning the electrodes.

A2.2 SEM Images of Electrodes for Geometry 3

Top row electrode SEM after annealing at 600°C, showing that the electrode is still intact.

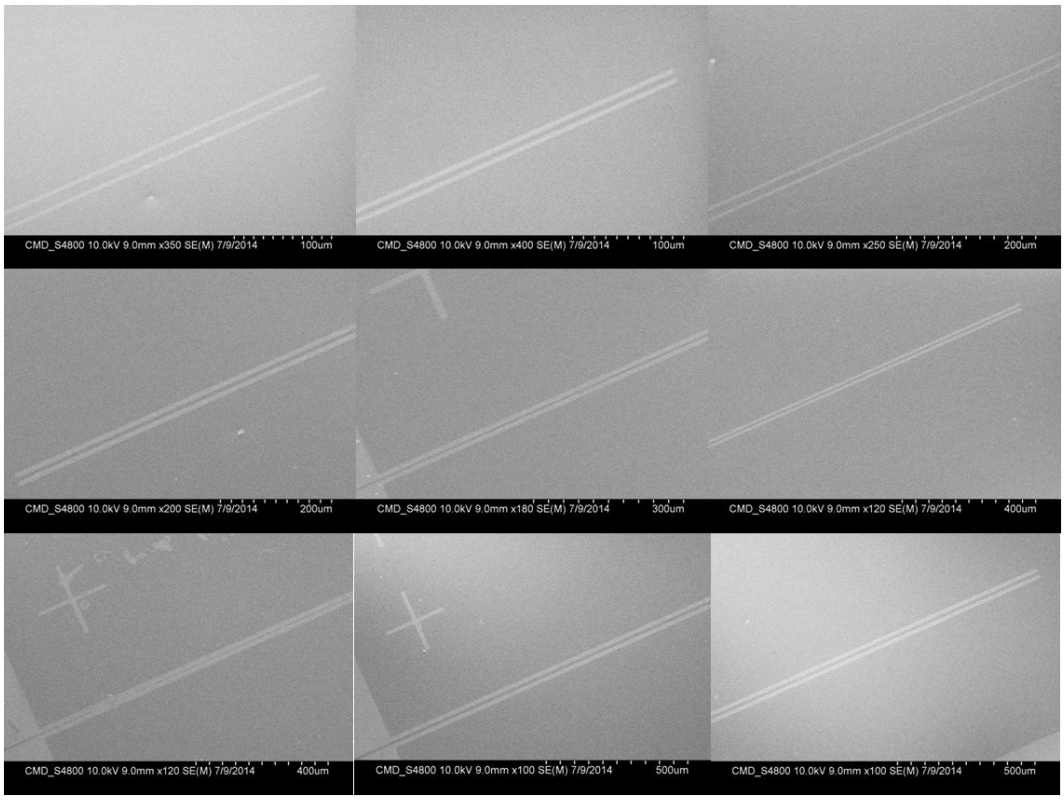

Figure A2.5: SEM images of the STO Cr|Pt electrodes after annealing at 600°C. Top row of images are taken of the top row of electrodes, the middle row of images are the middle row of electrodes and the bottom row of images are from the bottom row of electrodes.